

Extension and improvement of the coupled CFD-DEM approach to describe multidimensional heat transfer and non-spherical particle shape for fluidized systems

vorgelegt von

M.Sc., M.Sc.

Tobias Sebastian Oschmann

von der Fakultät III – Prozesswissenschaften
der Technischen Universität Berlin
zur Erlangung des akademischen Grades

Doktor der Ingenieurwissenschaften
- Dr.-Ing. -

genehmigte Dissertation

Promotionsausschuss:

Vorsitzender: Prof. Dr.-Ing. habil. Jens-Uwe Repke

Gutachter: Prof. Dr.-Ing. Harald Kruggel-Emden

Gutachter: Prof. Dr.-Ing. Viktor Scherer

Tag der wissenschaftlichen Aussprache: 25. Februar 2019

Berlin 2019

Vorwort

Die vorliegende Dissertation entstand im Rahmen meiner Tätigkeit als wissenschaftlicher Mitarbeiter an dem Fachgebiet Mechanische Verfahrenstechnik und Aufbereitung der Technischen Universität Berlin.

Mein besonderer Dank gilt Prof. Dr.-Ing. Harald Kruggel-Emden für die Möglichkeit zur Promotion, sehr gute Zusammenarbeit während meiner Tätigkeit am Fachgebiet sowie die konstruktive und wissenschaftliche Unterstützung während der Erstellung meiner Dissertation. Ebenfalls danken möchte ich ihm für die Übernahme des Hauptreferats.

Prof. Dr.-Ing. Viktor Scherer danke ich für die Übernahme des Zweitreferats sowie für die vorherige Zeit als wissenschaftlicher Mitarbeiter am Lehrstuhl für Energieanlagen und Energieprozesstechnik.

Ebenfalls danken möchte ich allen wissenschaftlichen und technischen Mitarbeitern für die gemeinsame Zeit und das ausgeprägte kollegiale Verhalten am Lehrstuhl für Energieanlagen und Energieprozesstechnik. Besonders hervorheben möchte ich hier meinen jahrelangen Bürokollegen Dr. Bastian Krause. Für die kritische Durchsicht meiner Dissertation möchte ich meinen ehemaligen Arbeitskollegen und Freunden Dr. Peter Fischer, Christoph Pieper, Bogdan Kravets und Frederik Bambauer danken. Zudem danke ich allen wissenschaftlichen Mitarbeitern am Fachgebiet Mechanische Verfahrenstechnik und Aufbereitung für die sehr angenehme Arbeitsatmosphäre und fachlichen Diskussionen während meiner Zeit in Berlin. Hier möchte ich besonders meinen Bürokollegen Frederik Elskamp nennen. Zudem danke ich Kevin Vollmari für die in der Promotion entstandene gute Freundschaft und zahlreichen Diskussion die mich sowohl fachlich als auch persönlich bereichert haben.

Meinen Eltern und meiner Schwester danke ich für die berufliche und private Unterstützung während meiner beruflichen und privaten Laufbahn.

Vor allem gilt mein Dank meiner Verlobten Narudee Suwanwattana für den starken Rückhalt, ihre große Geduld, Motivation und tolle Unterstützung zu jeder Zeit vor und insbesondere während der zeitintensiven Anfertigung meiner Dissertation trotz der großen räumlichen Entfernung zwischen uns. Ebenfalls möchte ich ihr aufgrund ihrer sehr guten Englischkenntnisse meinen besonderen Dank aussprechen für die sprachliche Durchsicht meines Manuskriptes. Meiner Verlobten widme ich diese Dissertation.

Braunschweig, Oktober 2018

Tobias Sebastian Oschmann

Kurzfassung

Die Auslegung und Verbesserung von industriellen Anlagen zur Behandlung granularer Materialien im Bereich der Energie- und Verfahrenstechnik basiert häufig auf den Ergebnissen numerischer Simulationen, da experimentelle Untersuchungen in vielen Fällen aufgrund der Zugänglichkeit der Prozesse an ihre Grenzen stoßen. Die meisten verwendeten numerischen Ansätze für granulare Materialien, auch häufig als Partikelsysteme bezeichnet, setzen eine sphärische Partikelform voraus, obwohl reale Partikel in industriellen Prozessen oftmals nicht-sphärisch sind. Diese Vereinfachung kann insbesondere in Partikel-Fluid Systemen zu starken Abweichungen zwischen in der Simulation prädictiertem und realem Verhalten führen, da hier die Partikelform einen großen Einfluss auf die Bewegung und das thermische Verhalten der Partikel hat. Darüber hinaus beschränken sich viele Simulationen mit Wärmeübertragung auf einfache Modelle, die eine konstante Temperaturverteilung innerhalb eines Partikels annehmen, was eine Annahme ist, die in vielen Fällen unzutreffend ist.

Das Ziel dieser kumulativen Dissertation ist es daher, neue numerische Modelle zum besseren Verständnis des mechanischen und thermischen Verhaltens von Partikel-Fluid Systemen zu entwickeln. Als Modellrahmen wird der gekoppelte Computational Fluid Dynamics - Diskrete Elemente Methode (CFD-DEM) Ansatz verwendet. Innerhalb dieses Ansatzes werden alle Partikelinformationen wie die Translations- und Rotationsbewegung mittels DEM berechnet, wohingegen die Navier-Stokes-Gleichungen einschließlich der Energiegleichung für das Fluid durch die CFD gelöst werden. Die neuen abgeleiteten Modelle zur Berücksichtigung von nicht-sphärischen Partikelformen und / oder Wärmeübertragung sind in 7 Publikationen beschrieben. Zunächst wird der CFD-DEM-Ansatz in seiner aus der Sicht dieser Dissertation einfachsten Form für sphärische Partikel und ohne Wärmeübertragung vorgestellt (Untersuchung I). Anschließend erfolgt eine Erweiterung dieses CFD-DEM-Ansatz in den Untersuchungen II-IV um entsprechende Widerstandskraftmodelle und ein Porositätsmodell, um nicht-sphärische Partikel ohne Wärmeübertragung zu berücksichtigen. Hier werden Simulationsergebnisse entweder mit Experimenten (z.B. Druckverlust), analytischen Lösungen (z.B. Druckverlust, Strahlenbildung und -länge) oder numerischen Ergebnissen aus Veröffentlichungen aus der Literatur verglichen. Des Weiteren wird der Einfluss der Partikelform auf die mechanische Mischung (Untersuchung II-III) oder Strahlenbildung (Untersuchung IV) detailliert untersucht, um die Notwendigkeit der Beschreibung nicht-sphärischer Partikel innerhalb der CFD-DEM zu betonen. Anschließend wird der CFD-DEM-Ansatz erweitert, um Wärmeleitung innerhalb von Partikeln und Wänden räumlich und zeitlich aufgelöst zu berücksichtigen. Dies erfordert auch eine Anpassung der Abbildung anderer Wärmeübertragungsmechanismen wie der Partikel-Partikel und Partikel-Wand Wärmeleitung im Kontakt, dem konvektiven Partikel-Fluid Wärmeübergang sowie dem Wärmeaustausch durch Strahlung. Daher wird in Untersuchung V ein neues dreidimensionales Wärmeleitungsmodell für die Wärmeleitung innerhalb eines Partikels

vorgelegt, das für mehrere Testfälle auf der Partikelebene mit einem etablierten Finite-Volumen-Verfahren und mit einem Modell, das die Temperatur räumlich nicht auflöst, verglichen wird. Darüber hinaus wird eine Verteilungsfunktion für eine realistischere Variation des Wärmeübergangskoeffizienten auf der Partikeloberfläche im CFD-DEM Ansatz realisiert, um den Wärmeübergang resultierend aus der Partikel-Fluid Konvektion zu berücksichtigen (Untersuchung VI). Abschließend wird in Untersuchung VII ein neuer Koppelungsalgorithmus für die Partikel-Wand Wärmeübertragung abgeleitet, um den Wärmeübergang resultierend aus dem Partikel-Wand Kontakt mit dreidimensionaler Wärmeübertragung innerhalb der Wände detailliert zu beschreiben, was insbesondere wichtig ist, wenn Prozesse nach außen nicht als adiabatisch angenommen werden können.

Abstract

The design and improvement of industrial applications involving granular materials in the field of energy and thermal process engineering is often based on the results of numerical simulations as the experimental determination of the key process parameters of interest is frequently hard to conduct due to limited accessibility of the processes. Most used numerical frameworks for granular materials, which are regularly also referred to as particle systems, assume spherical shaped particles although real particle systems, especially in industry, often involve non-spherical particle shapes. This assumption can lead to strong deviations between predictions from simulations and real behavior, especially in particle-fluid systems where the particle shape has a strong influence on the movement and the thermal behavior of the particles. In addition to that, simulations involving heat transfer often rely only on simple models which are limited to solely describe a constant temperature profile within one particle. This assumption is often not valid.

Therefore, the scope of this cumulative dissertation is to derive novel models for a better understanding of the mechanical and thermal behavior of particle-fluid systems. As a model approach the coupled Computational Fluid Dynamics - Discrete Element Method (CFD-DEM) is used. Here all particle related information such as the translational and rotational motion over time are calculated by the DEM whereas the Navier-Stokes equations including the energy equation for the fluid are solved by the CFD. The new derived models for considering non-spherical particles or / and heat transfer are outlined in 7 publications. Firstly, the CFD-DEM approach is presented in its simplest form (from the point of view of this dissertation) for spherical particles and without heat transfer (investigation I). Secondly, in investigations II-IV, this CFD-DEM approach is extended by drag force models and a porosity model to consider non-spherical particles without heat transfer. Here simulation results are either compared against experiments (e.g. pressure drop), analytical results (e.g. pressure drop, rope formation and rope length) or numerical studies from literature. Besides this, the influence of the particle shape is investigated in a detailed manner based on mechanical mixing (investigation II-III) or rope formation (investigation IV) which underlines the importance for describing non-spherical particles within the CFD-DEM. After that, the CFD-DEM approach is extended to represent spatially resolved heat transfer for particles and walls which requires extending the modelling of other heat transfer mechanisms namely particle-particle and particle-wall contact heat conduction, particle-fluid convective heat transfer and radiation. Therefore, investigation V presents a new particle 3D heat transfer conduction model which is compared against an established Finite Volume Method in parts and a model assuming a spatially constant temperature for several test cases. Besides that, a distribution function for a more realistic heat transfer coefficient variation on the particle surface is implemented in the context of the particle interior resolved CFD-DEM approach to consider particle-fluid convective heat transfer (investigation

VI). Finally, in investigation VII a novel particle-wall heat transfer coupling algorithm is derived to describe particle-wall heat transfer due to contact while resolving the temperature field in both particles as well as the walls in three dimensions. The latter approach is especially important if systems under consideration cannot be assumed to be adiabatic.

List of Publications

Articles in peer reviewed journals

1. Oschmann, T., Hold, J., Kruggel-Emden, H.: Numerical investigation of mixing and orientation of non-spherical particles in a model type fluidized bed. *Powder Technol.* 258, 304–323 (2014), <https://doi.org/10.1016/j.powtec.2014.03.046>, Investigation II on page 66
2. Kruggel-Emden, H., Oschmann, T.: Numerical study of rope formation and dispersion of non-spherical particles during pneumatic conveying in a pipe bend. *Powder Technol.* 268, 219–236 (2014), <https://doi.org/10.1016/j.powtec.2014.08.033>, Investigation IV on page 112
3. Vollmari K., Oschmann T., Wirtz S., Kruggel-Emden H.: Pressure drop investigations in packings of arbitrary shaped particles, *Powder Technol.* 271, 109–124 (2015)
4. Pieper C., Oschmann T., Markauskas D., Kempf A., Fischer A., Kruggel-Emden H.: Numerical investigation of third body behavior in dry and wet environments under plane shearing, *Chemical Engineering & Technology*, 2015, Volume 39, 1497-1508. Copyright Wiley-VCH Verlag GmbH & Co. KGaA, Reproduced with permission, <https://doi.org/10.1002/ceat.201500647>, Investigation I on page 47
5. Oschmann T., Schiemann M., Kruggel-Emden H.: Development and verification of a resolved 3D inner particle heat transfer model for the Discrete Element Method (DEM), *Powder Technology* 291, 392-407 (2016), <https://doi.org/10.1016/j.powtec.2015.12.008>, Investigation V on page 146
6. Vollmari K., Oschmann T., Kruggel-Emden H.: Mixing quality in mono- and bidisperse systems under the influence of particle shape: A numerical and experimental study, *Powder Technology* 308, 101 – 113 (2017)
7. Oschmann T., Kruggel-Emden H.: Numerical and Experimental Investigation of the Heat Transfer of Spherical Particles in a Packed Bed with an Implicit 3D Finite Difference Approach, *Granular Matter* 19: 47 (2017), <https://doi.org/10.1007/s10035-017-0711-z>, Investigation VI on page 178

- 8 Oschmann T., Kruggel-Emden H.: A novel method for the calculation of particle heat conduction and resolved 3D wall heat transfer for the CFD/DEM approach, Powder Technology 338, 289-303 (2018), <https://doi.org/10.1016/j.powtec.2018.07.017> , Investigation VII on page 196

Conference Papers

1. Oschmann T., Vollmari K., Kruggel-Emden H., Wirtz S., 2014, Numerical Investigation of Mixing of Non-Spherical Particles in Fluidized Beds and during Pneumatic Conveying, 7th World Congress on Particle Technology, Beijing, China, <https://doi.org/10.1016/j.proeng.2015.01.220>, Investigation III on page 100
2. Vollmari K., Khan M.S., Oschmann T., Kruggel-Emden H., 2014, Numerical and Experimental Investigation of the Pressure Drop in Packings of Spherical and Non-Spherical Particles, 12th International Conference of Numerical Analysis and Applied Mathematics, Rhodes, Greece.
3. Oschmann T., Kruggel-Emden H., 2015, Development and testing of a resolved 3D heat transfer model for the coupled CFD-DEM-approach, The 8th International Conference for Conveying and Handling of Particulate Solids, Tel-Aviv, Israel.
4. Oschmann T., Wirtz S., Kruggel-Emden H., 2016, Investigation of heat transfer in packed/fluidized beds for spherical particles resolved by an implicit 3D finite difference approach, Partec 2016, Nuremberg, Germany.

Conference Poster

1. Vollmari K., Oschmann T., Kruggel-Emden H., 2016, Experimental and Numerical Analysis of Particle Motion in a Laboratory Scale Dual Chamber Fluidized Bed, Partec 2016, Nuremberg, Germany.

Table of Contents

1. Introduction	1
1.1 Thematic classification	4
2. Basic equations and force models	6
2.1 Contact force and torque models	7
2.2 Validation of the implemented non-linear contact model	9
2.3 Determination of friction and coefficient of restitution	10
2.4 Particle-fluid interaction forces	13
3. Non-spherical particles within the DEM	16
3.1 Rotational motion of non-spherical particles	16
3.2 Representation methods of non-spherical particles in the DEM	18
3.3 Contact definition and detection of non-spherical particles	21
3.3.1 Contact detection for super-quadrics	22
3.3.2 Contact detection for polyhedrons	25
4. Heat Transfer within the DEM	30
4.1 Inner particle heat transfer	35
4.2 Numerical approximation of the heat transfer equation in spherical coordinates	38
5. CFD-DEM approach with relevant CFD equations	44
6. Results and Publications	47
I. Numerical investigation of third body behavior in dry and wet environments under plane shearing	47
II. Numerical investigation of mixing and orientation of non-spherical particles in a model type fluidized bed	66
III. Numerical Investigation of the Mixing of Non-Spherical Particles in Fluidized Beds and during Pneumatic Conveying	100
IV. Numerical study of rope formation and dispersion of non-spherical particles during pneumatic conveying in a pipe bend	112
V. Development and verification of a resolved 3D inner particle heat transfer model for the Discrete Element Method (DEM)	146
VI. Numerical and Experimental Investigation of the Heat Transfer of Spherical Particles in a Packed Bed with an Implicit 3D Finite Difference Approach	178

VII. A novel method for the calculation of particle heat conduction and resolved 3D wall heat transfer for the CFD/DEM approach.....	196
7. Conclusions and Perspective	225
References.....	232

1. Introduction

The detailed understanding of the mechanical and thermal behavior of particulate systems is crucial for a resource-conserving and efficient design of plants and components in the field of energy, thermal and mechanical process engineering. Particulate or granular systems which are large assemblies of smaller discrete bodies are either inert or materially convert. Typical inert systems are not chemically reactive such as lumpy heat transfer medium / storage in solar thermal power plants or gasification processes. In contrast to that, materially convert particulate systems are chemically reactive like solid fuels (e.g. coal or biomass) or materials that are used as oxygen carriers in modern processes for CO_2 separation such as the Chemical Looping process [1].

In most industrial applications, the discrete particles of granular systems are often shaped non-spherical and vary in size and character. These properties have a strong influence on the thermal and mechanical behavior, especially in particle-fluid systems where granular systems are transported and converted. Typical common industrial examples are packed beds, fluidized beds, particle-entrained flows, heat exchangers involving granular media or drying of particulate solids which is often performed in rotating drums.

To achieve a better understanding of the mechanical and thermal behavior of particulate systems consisting of non-spherical particles, numerical methods can be used alternatively to experimental investigations. The modeling of particle-fluid systems is possible at different levels of detail and in different frameworks, which is demonstrated in fig. 1.

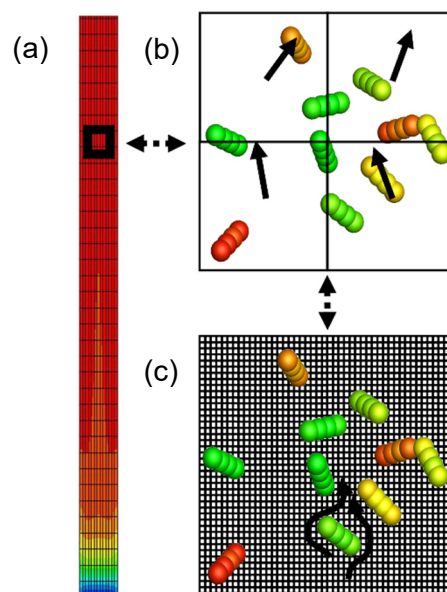


Figure 1: Different degrees of detail for modelling of particle-fluid systems: (a): Continuum model; (b) Discrete Element Method with averaged cell velocity; (c) Discrete Element Method with resolved velocity field [2]

In literature two approaches are widely used, namely the discrete (fig. 1b-c) and the continuum approach (fig. 1a) [3]. Within the continuum approach the solid and gas phase are treated as continuous functions of space and time [4] whereas the motion and interaction of each particle is resolved individually by the discrete approach [3]. Both methods can be used for the description of particle-fluid systems but have specific limitations and drawbacks. The continuum approach is often used in process studies but is not able to consider the effect of microscopic structure of granular flow [5,6]. In contrast to that, the strength of Discrete Element Method (DEM), firstly introduced by Cundall and Strack in 1979 [7], lies in the detailed description of particle scale information such as particle trajectories and forces acting on each particle. This information is often crucial for the understanding of the mechanisms governing in complicated flow behavior and allows to model any dense, static or also moving particle system [8]. However, the DEM is often unsuitable for describing process modelling or macroscopic flow behavior as the computational effort mainly depends of the number of used particles.

To combine the advantages of both methods, the discrete and continuum approach can be linked over coupling algorithms. Here the gas phase of the particle-fluid system, discretized in space by using Finite difference (FD) or Finite Volume or Finite Element methods [3,9,10], is described by the continuum approach [3]. All relevant particle information such as non-spherical shape of single particles and the formation of a complex microstructure are modelled by the DEM. Coupling algorithms generally fall into two categories depending on the grid size, namely unresolved (fig 1b) or resolved simulations (fig. 1c).

The resolved method solves the fluid flow on a much smaller scale than the particle size so that the interactions between particle and fluid can be described as momentum/heat transfer on the particle-fluid interfaces (at this small cells). Possible continuum approaches to solve the flow field on such a scale are the immersed boundary method (IBM) or Lattice Boltzmann Method (LBM) [3]. In contrast to that, the unresolved method solves the Navier–Stokes equations / energy equation on a grid normally larger than the largest particle. Here the particle-fluid interactions are modeled by the available particle and fluid flow properties based on averaged fluid cell values. However, a resolved detailed flow around a particle is usually very computationally demanding and therefore only considered in single cases [11]. Therefore, many investigators focused on the unresolved simulations to describe their particle-fluid systems [8].

As summarized before, the DEM enables the integration of geometrically arbitrary shaped bodies (spherical and non-spherical) and is suitable to describe the microstructure of granular systems and their dynamics. Despite the great flexibility of this method, the computational effort significantly increases with the number of particles which limit the usage of the DEM, especially in case of particle-fluid systems with heat transfer. Because of this, many studies focus

on spherical particles without heat transfer as discussed later. The investigation of non-spherical particles interacting with a fluid and the effects occurring therein, such as heat transfer, mixing or discharge are essential to gain a deeper understanding of the processes influenced by the microstructure. While systems of spherical bodies are widely understood, systems of complex bodies have a much more diverse structure, e.g. due to a different particle orientation. This fact has a direct influence on integral system quantities such as the particle dwell times, the particle flow behavior or the temperature distribution within a particle. Such differences underline the importance to consider non-spherical shaped particles within the DEM to describe industrial processes in sufficient detail. In addition to that heat transfer (also for spherical particles) is mostly modeled by simple approaches with only one constant temperature value per particle which is only valid for certain cases. Especially in cases where unequal temperature distributions occur within one particle these simple methods are not able to describe the system behavior adequately.

The aim of this dissertation is to close this gap and to provide a set of novel methodologies to consider non-spherical particles in particle-fluid systems and heat transfer equations to describe an uneven temperature distribution within a particle. Therefore, the unresolved coupled computational fluid dynamics – discrete element method (CFD-DEM) approach is used as model framework and extended by several methods. For the description of the continuum phase the CFD in form of the commercial software ANSYS Fluent is used whereas the particle phase is described by an existing in-house DEM code written in the programming language FORTRAN.

The cumulative dissertation can be subdivided in 7 chapters. In addition to the introduction, a literature review with a thematic classification is given in the chapter 1. The chapters 2-5 describe the methodology with all relevant equations and give additional information important for all investigations which are outlined in chapter 6.

Chapter 2 begins with a presentation of the DEM basic equations. After that, an overview of existing DEM contact models is given and two contact models, one simple linear contact model for simulations without heat transfer and one more detailed non-linear contact model for all simulations with heat transfer, are chosen for all investigations. In addition to that, both contact models are validated with a reference case from literature. For the calculation of the particle-fluid drag force no general agreement in literature exists for model approaches for the CFD-DEM. Therefore, in the last part of this chapter different particle-fluid force interaction models are discussed, and the considered particle-fluid force model is described. Chapter 3 marks up the challenges for describing non-spherical particles within the DEM. Here model approaches for the rotational motion of particles and the approximation of non-spherical particles are presented. Furthermore, differences between the spherical and non-spherical particle contact detection are shown and two non-spherical contact algorithms are discussed in detail. The topic

heat transfer in the context of the DEM is considered in chapter 4. Firstly, the different possibilities for solving heat transfer within one particle are outlined. As mentioned above, most investigations focus on simple approaches with a constant temperature within a particle which is only valid for some cases. To close this gap a new 3D heat transfer model is derived to solve the heat transfer within one particle and exemplary numerical approximated from the heat equation. The introduced CFD-DEM coupling approach with the most important CFD equations is shown in chapter 5. The investigations which are the focus of this dissertation can be found in chapter 6. Finally, the most relevant results of all investigations are concluded and an outlook for further work is given in chapter 7.

1.1 Thematic classification

The own publications of this cumulative dissertation can be classified in four main topics, see fig 2.

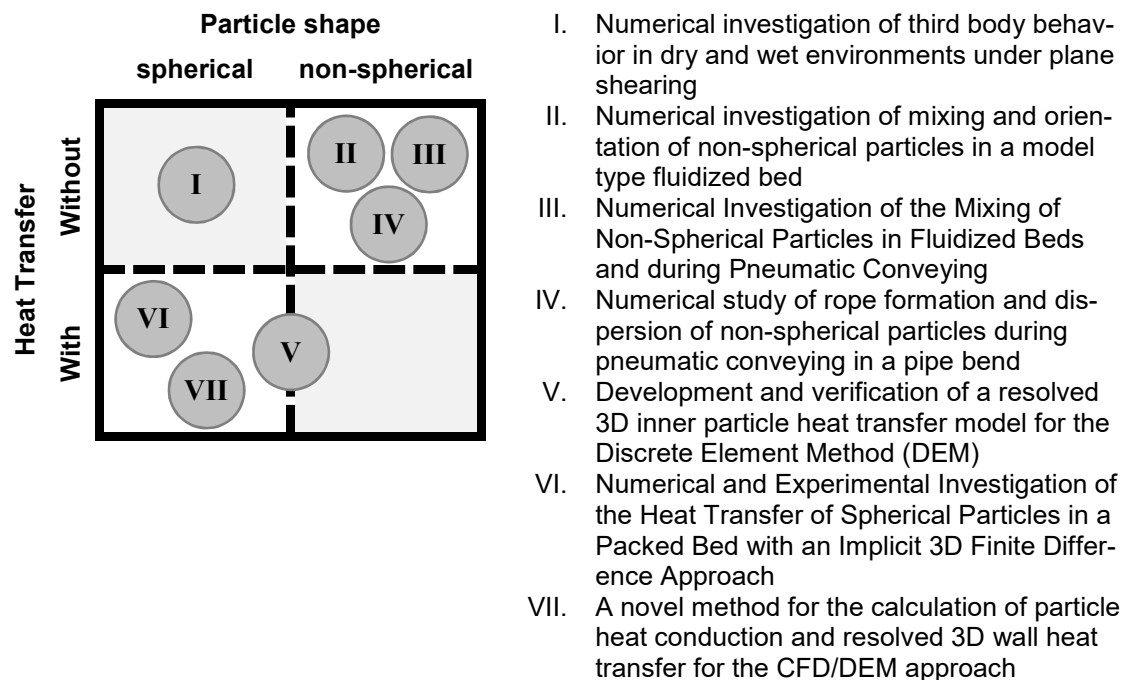


Figure 2: Thematic classification of the own publications

In all studies the coupled computational fluid dynamics – discrete element method (CFD-DEM) approach is used. In the first investigation this approach is presented to model and assess third-body behavior in dry and wet environment under plane shearing. Here spherical particles without modelling the heat transfer are considered. Studies II – IV concentrate on the investigation of arbitrary shaped particles (like e.g. cylinders, cubes, etc.) in a model type fluidized bed or during pneumatic conveying. Again, no heat transfer is solved. In contrast to that, the publications VI and VII investigate the transient heat transfer for spheres in a packed bed and a rotating drum. The last work contains both, spherical and non-spherical shaped particles equally

as an implicit 3D heat transfer model is derived in Cartesian and spherical coordinates to calculate the temperature within a particle in time and space. A survey of the literature indicates that the four main topics were investigated in the past 20 years in different degree of detail, see fig. 3. By far most papers have been published for DEM simulations with spherical shapes and without heat transfer (fig. 3a). The high number of published works of this simplest case (from the view of this dissertation) underlines the importance of DEM in general which rapidly increased in the past 10 years. In case of non-spherical particles without heat transfer (fig. 3b), investigations have only received significant attention the past 7 years. Only a few investigators considered this topic before that time. Although the total amount of publications is less than for simulations without heat transfer with spherical particles (fig. 3a), a more comparable evolution can be seen for DEM simulations with spherical particles and heat transfer (fig. 3c). Here the published investigations continuously increased over the past 20 years. The least progress has been made for DEM simulations with heat transfer and non-spherical particle shape (fig. 3d). In this area, investigators just started with the formulation of new approaches.

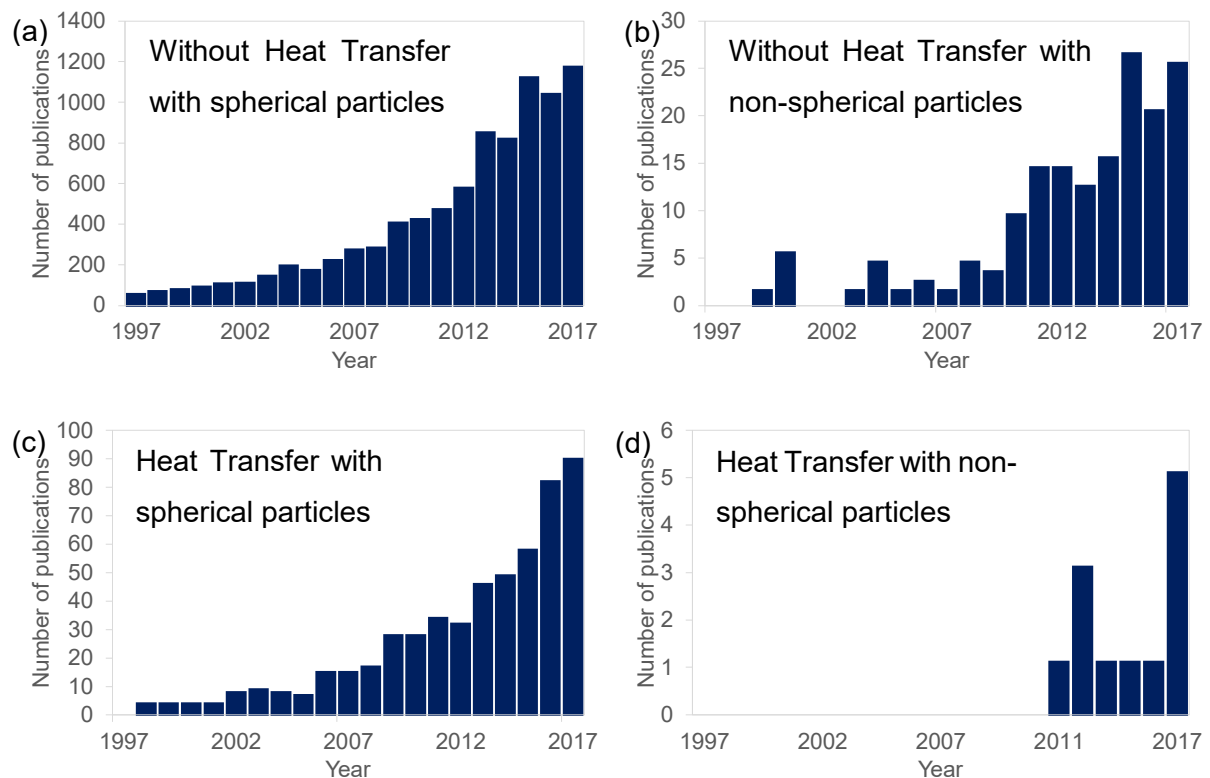


Figure 3: Number of publications concerned with DEM simulations of granular systems in the past 20 years, obtained from Web of Science using following keywords: “discrete element method/model” or “distinct element method/model” or “discrete particle simulation/method/model” or “granular dynamic simulation”. (a): keywords “heat transfer” and “non-spherical” are excluded”; (b): keyword “heat transfer” is included and “non-spherical” excluded; (c): keyword “heat transfer” is included and “non-spherical” excluded”; (d): keywords “heat transfer” and “non-spherical” are included.

2. Basic equations and force models

For the description of the translational and rotational motion of the particles in a granular flow the Discrete Element Method (DEM) is used. In general, the DEM can be subdivided in the “soft sphere” and “hard sphere” approach. Both methods consider the collision behavior between particles differently. In the hard sphere method, also known as Event-Driven DEM, particles are assumed as perfectly rigid bodies which follow a rectilinear motion until a collision occurs. Here only binary collisions are considered which is valid for dilute system without many multi-particle contacts. By contrast, in a soft sphere simulation, also known as Time-Driven DEM, each particle is treated as individual discrete element which interacts with its neighboring particles, walls or the surrounding fluid over time. Collisions are resolved more detailed as the deformation of a particle is considered as an overlap between particles and this overlap is used to calculate elastic, plastic and frictional forces between contacting partners. Therefore, this method is more suited for systems with multiple contacts like the particle-fluid systems considered in this dissertation. All following descriptions regarding the DEM are reduced to the soft sphere DEM approach as all cases consist of multiple contacts and the hard sphere approach is therefore not used. For granular systems the DEM was firstly introduced by Cundall and Strack [7] who presented this approach as an efficient tool for describing such environments. In general, the translational and rotational motion are obtained by integrating Newton’s and Euler’s equations for each particle given in general form for arbitrarily shaped particles

$$m_i \frac{d^2 \vec{x}_i}{dt^2} = \vec{F}_i^c + \vec{F}_i^{nc} + \vec{F}_i^g + \vec{F}_b + \vec{F}_l + \vec{F}_i^{pf}, \quad (1)$$

$$\hat{I}_i \frac{d\vec{W}_i}{dt} + \vec{W}_i \times (\hat{I}_i \vec{W}_i) = \Lambda_i^{-1} \vec{M}_i, \quad (2)$$

with particle mass m_i , particle acceleration $d^2 \vec{x}_i / dt^2$, contact force \vec{F}_i^c , gravitational force \vec{F}_i^g , buoyancy force \vec{F}_b , lubrication force \vec{F}_l , particle/fluid force \vec{F}_i^{pf} , angular acceleration $d\vec{W}_i / dt$, angular velocity \vec{W}_i , external moment \vec{M}_i resulting out of contact or particle/fluid forces, the inertia tensor \hat{I}_i along the principal axis and the rotation matrix converting a vector from the inertial into the body fixed frame Λ_i^{-1} [12]. Non-contact forces (\vec{F}_i^{nc}) such as van der Waals forces, electrostatic forces or liquid bridge forces are not part of this dissertation as most simulations either address dry systems without moisture or/and particles are of large diameters [8]. In the following sections models for the calculation of all remaining forces and external moments are presented.

2.1 Contact force and torque models

As mentioned previously the deformation between two colliding particles is assumed as two rigid bodies which overlap. In general, the contact force can be subdivided in a normal \vec{F}_i^n and \vec{F}_i^t tangential component and is just calculated when the overlap between particles is greater than zero $\delta_n > 0$

$$\vec{F}_i^c = \vec{F}_i^n + \vec{F}_i^t. \quad (3)$$

Various approaches have been proposed in literature. An overview of selected models is given in table 1.

Table 1: Overview of contact force and torque models

Force models	Normal force	Tangential force	Ref.
Linear spring-dash-pot	$\vec{F}_i^n = k^n \delta_n \vec{n} + \gamma^n \vec{v}_{rel}^n$	$\vec{F}_i^t = \min(k^t \vec{\xi}^t , \mu_c \vec{F}_i^n) \vec{t}$	[7]
Non-linear contact model according to Tsuji and Di Renzo	$\vec{F}_i^n = \frac{4}{3} E^* \sqrt{R} \delta_n^{\frac{3}{2}} \vec{n} + \gamma^n \delta_n^{1/4} \vec{v}_{rel}^n$	$\vec{F}_i^t = \min\left(\frac{2}{3} k^t \vec{\xi}^t , \mu_c \vec{F}_i^n \right) \vec{t}$ with $k^t = 8G^* \sqrt{R} \delta_n$ and $\vec{\xi}^t \leq (1/k^t) F^n$	[13–15]
Hysteretic models	$\vec{F}_i^n = \begin{cases} k_1 \delta_n \vec{n}, & \delta_n \geq 0 \\ & \text{(loading)} \\ k_2 (\delta_n - \delta_{n0}) \vec{n}, & \delta_n < 0 \\ & \text{(unloading)} \end{cases}$ $\delta_{n0} = \frac{v_0 (m_{eff})^{\frac{1}{2}} (k_{ul} - k_l)}{k_{ul} (k_l)^{1/2}}$	$\vec{F}_i^t = \begin{cases} \vec{F}_i^t + k_0^t \left(1 - \frac{ \vec{F}_i^t - \vec{F}_i^{*t} }{\mu \vec{F}_i^n - \vec{F}_i^{*n} }\right)^{1/3} \Delta \vec{\xi}^t & \text{if } \dot{v}_{rel}^t \text{ in initial direction} \\ \vec{F}_i^t + k_0^t \left(1 - \frac{ \vec{F}_i^t - \vec{F}_i^{*t} }{\mu \vec{F}_i^n + \vec{F}_i^{*n} }\right)^{1/3} \Delta \vec{\xi}^t & \text{if } \dot{v}_{rel}^t \text{ in opposite direction} \end{cases}$	[16,17]
Torque models	Rolling friction torque $M_r = -k_2 \theta_r - C_r d\theta_r/dt$ $M_r = -\min\{\mu_r \vec{F}_i^n , \mu_r' \omega_n \} \hat{\omega}_n$	Torque from tangential forces $M_t = R \times \vec{F}_i^t$	[18–21]

Force models can be subdivided in linear, non-linear and hysteretic models [22]. In addition to that particle torque models can be accounted for as sum $M_i = M_r + M_t$ for the calculation of the rotational velocity [22]. In contrast to the normal force component, the tangential force always implies a torque M_t . Beside the torque from tangential forces, several rolling friction torque models M_r can be considered, two of them are exemplary shown in table 1. The torque M_r results out of the rolling of a single particle whereas the tangential force implies an additional torque M_t . As M_r is zero or has no significant influence for some particle shapes (e.g. cubes, pyramids: no rolling; cylinders: rolling only in one direction) only the torque M_t is considered in this dissertation. The most frequently employed models in the DEM due to simplicity are the linear ones [23]. In case of the publications “I-IV” the so called linear spring-dashpot

model proposed by Cundall and Strack [7] is used. The normal force \bar{F}_i^n consists of two parts, the elastic repulsion and the viscous dissipation. The elastic repulsion can be understood as an elastic spring whereas the viscous dissipation represents a displacement rate dependent damper. The tangential force is calculated by a linear elastic spring without damper unless the related Coulomb force is exceeded. In contrast to that the relationship between normal force and normal displacement is treated non-linearly for contact models based on the Hertz theory [13]. Originally this approach was just formulated to describe the elastic contact between two spheres in normal direction. To provide a solution for calculation of the tangential component, Mindlin and Deresiewicz [24] derived a model to close this gap. Although such models overcome some limitations of linear viscoelastic models (constant coefficient of restitution and duration of contact) they are more complicated than linear models as the collision time is dependent of the initial normal velocity. High initial velocities may lead to small collision times and therefore to small simulation time steps (high computational effort). To calculate the collision time, the initial velocity must be either initially assumed or adjusted based on experimental data [23,25]. Schäfer et al. [26] presented an equation for calculating the collision time t_n in dependence on the relative normal velocity v_n^i

$$t_n = 3.21 \left(\frac{m_{eff}}{\frac{4}{3}E^*\sqrt{R}} \right)^{2/5} v_n^i^{-1/5}, \quad (4)$$

where $m_{eff} = m_1 m_2 / (m_1 + m_2)$ is the effective particle mass and $E^* = 1 / ((1 - \nu_1^2) / E_1 + (1 - \nu_2^2) / E_2)$ is the effective Young's modulus. In contrast to that the linear spring model obtains a constant collision time independent of the initial normal velocity

$$t_n = \pi \left(\frac{k^n}{m_{eff}} - \left(\frac{\gamma^n}{2m_{eff}} \right)^2 \right)^{-1/2} \quad (5)$$

An alternative to linear and non-linear viscoelastic models form hysteretic models which represent the particles as plastically deformable. A simple hysteretic model was proposed by Walton and Braun [16,17] who used a semi-latched spring force-displacement model in normal direction and an approximation of the Mindlin and Deresiewicz contact theory for the case of constant normal force in tangential direction [8]. Hysteretic models are either linear or non-linear. Here the normal force is calculated with different springs for loading and unloading. Nevertheless, for solving the particle-particle or particle-wall heat transfer by contact conduction (respective models also based on the Hertz Theory), the overlap of non-linear contact models is needed as this overlap bases on real material parameters such as Young's or shear

modulus. In contrast to that, the linear model requires a correction of the overlap as the resulting overlap depends on the used material parameter (collision time, spring stiffness, etc.). For simple cases like a heat transfer case in a packed bed, this can be performed by a calibration with experimental data. In moving systems, a correction of the overlap must be done every time step, which makes it even more unpractical to be used. Therefore the contact force is calculated by the models of Tsuji [15] (normal) and Di Renzo [14] (tangential) in the publications “V – VII” of this dissertation. Both are modifications of the described non-linear contact models. As no non-linear contact model was implemented in the DEM code before this dissertation, the presented non-linear contact model is compared against experiments and the already implemented linear model in the next chapter.

2.2 Validation of the implemented non-linear contact model

To compare linear and non-linear contact models with literature data a simple particle-wall case with different particle impact angles is considered in this chapter [25]. A simple 2D sketch of this setup is shown in fig. 4. Here the collision between an aluminum alloy particle and an aluminum oxide wall is considered. One approach to prove the contact model is to investigate the changing of the translational velocity component v_{x0} or v_{y0} and rotational velocity ω_0 over the full temporal collision time. These quantities can be understood as microscopic collisions properties. The disadvantage of this approach is that measurements on that level are only available in very limited cases, e.g. Van Zeebroeck et. al. [27] in normal direction and Zhang and Whiten [28] or Dintwa et al. [29] in tangential direction. Therefore, only the final macroscopic values of the obtainable properties are used and compared against experiments. Fig. 5 shows the two macroscopic properties tangential coefficient of restitution e^t (fig. 5a) and rotational velocity ω (fig. 5b) in dependency of the impact angle β .

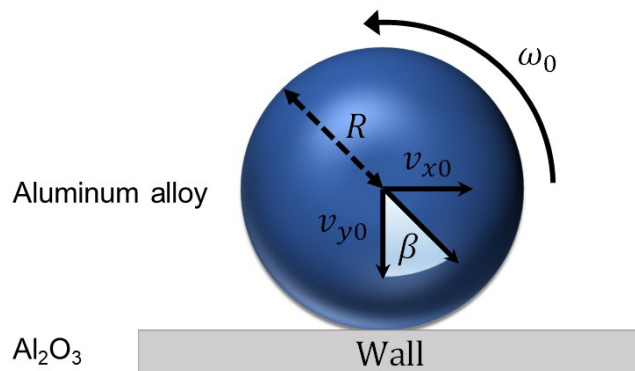


Figure 4: Validation of the implemented non-linear contact model by a particle-wall impact according to [25]

In fig. 5 the implemented non-linear contact model is compared against the linear model [26] and experiments performed by Gorham et al. [30]. The impact angle can be expressed as the arcus tangents of the ratio of the initial velocities v_{x0} and v_{y0}

$$\beta = \arctan\left(\frac{v_{x0}}{v_{y0}}\right), \quad (6)$$

whereas the tangential coefficient of restitution is given by the ratio of the velocities in x direction directly before v_{x0} and after v_{x1} the collision

$$e^t(\beta) = \frac{v_{x1}}{v_{x0}}. \quad (7)$$

The results regarding the tangential coefficient of restitution (fig. 5a) show a better agreement between experiments and simulation for the non-linear model. Only small differences occur for impact angles between 17 and 40 degrees. In the second case (fig. 5b) the final values of the rotational velocity match the experimental results well for the non-linear model whereas larger differences are observable for angles between 15 and 50 degrees for the linear model. To summarize this part, although the non-linear contact model shows a better agreement with the performed experiments both models are in principal able to describe the collision behavior.

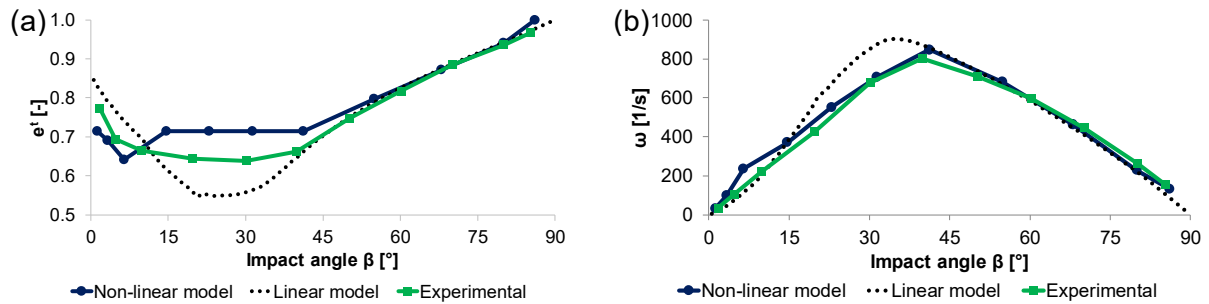


Figure 5: Results regarding the tangential coefficient of restitution (a) and rotational velocity (b) over the impact angle

2.3 Determination of friction and coefficient of restitution

By using the DEM to model particle systems, information for the input parameters friction and coefficient of restitution are needed. The normal k^n and tangential k^t spring stiffness in combination with the damping coefficient determine the maximum overlap for the particle collision. As a guideline, Kruggel-Emden et al. [31] suggested a maximum overlap of 1 % of the particle diameter to avoid alteration of the simulations. In general, two kind of calibration methods are used in literature to determine normal k^n and tangential k^t spring stiffness [32]. The first method is to measure these parameters directly on a single particle level whereas other researchers concentrate on the measurement of the bulk behavior of a group of particles and perform a reverse calibration procedure base on their results, iteratively until the experimental bulk behavior is correctly reproduced. Both methods hold drawbacks so that currently no general solution exists [32]. For the bulk calibration approach, it is not guaranteed that the iteratively determined bulk behavior of one application will also be valid for another application. On

the other hand, the determination of the input parameters on a single particle level (direct measurement approach) is often limited to particle sizes in a range of millimeters as the accuracy of this method decreases for smaller particle sizes [33]. However, at least for determining the coefficient of restitution and sliding friction, the advantage of the direct measurement approach is that the resulting properties can be explicitly determined for two specific contact partners. Especially in polydisperse packings where several particle types with different contact properties exist, the reverse calibration method is not able to consider this as only the whole integral behavior can be determined [32]. In case of rolling friction, it is necessary to use a model as a direct measurement is not available [34,35]. As different contact models are used (investigations without heat transfer: Linear spring-dashpot; investigations with heat transfer: Non-linear contact model, see table 1) and all particle sizes are in the range of millimeters the direct measurement approach is chosen for the determination of the friction and coefficient of restitution. For the calculation of the friction μ_c , the classical friction theory is applied

$$\mu_c = \frac{|\vec{F}_F|}{|\vec{F}_N|}, \quad (8)$$

where \vec{F}_t is the frictional force and \vec{F}_N is the normal force. The classical friction theory is valid for point-point contacts where the effect of the contact area can be ignored [36]. The experimental setup for the measurement of the sliding friction is shown in fig. 6.

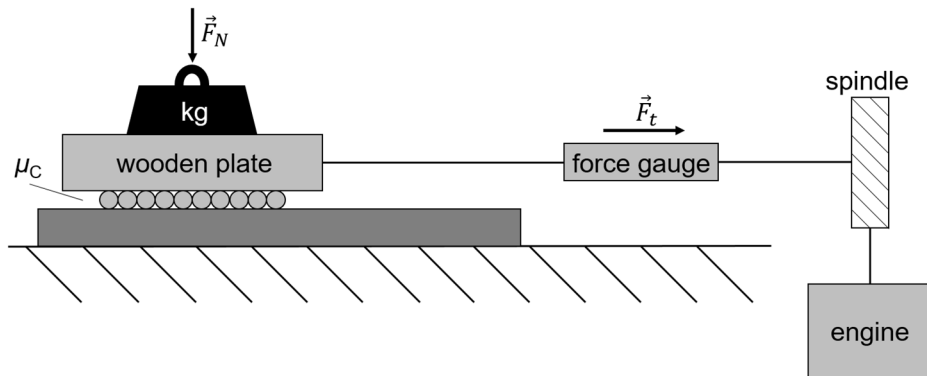


Figure 6: Determination of sliding friction [35]

Here the sliding friction is determined over the force \vec{F}_t which is necessary to drag a sample of particles (of the desired material) glued under a wooden plane over a plate of the material of the second simulation contact partner (in DEM simulations a particle or a wall). The determination of the coefficient of restitution is based on the work of Alonso-Marroquín et al. [37] where the particles are fixed by a rope. A sketch of the experimental setup is exemplary shown in fig. 7.

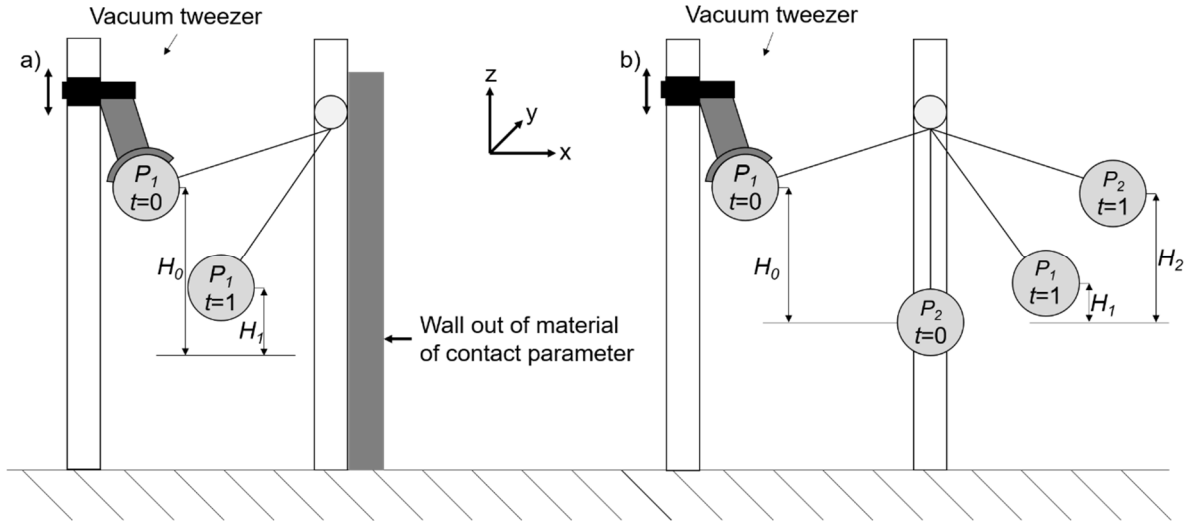


Figure 7: Determination of the restitution coefficient for a) particle-wall and b) particle-particle contacts [35,37].

To minimize the external effects and to guarantee a reproducibility of the experiments, particle P_1 is fixed with a vacuum tweezer and particle P_2 (fig. 7b) is in a non-moving steady state ($t=0$). After switching off the vacuum tweezer, the particle-wall (fig. 7a) and particle-particle collision (fig. 7b) are optically measured with a high-speed camera. For clarity, the moment after the collision is additionally shown and indicated by $t=1$. In case of particle-wall contacts, the heights of P_1 before switching off the vacuum tweezer (H_0) and at the highest point after the rebound (H_1) are evaluated over image processing (written in MATLAB) to calculate the coefficient of restitution e_{pW}^n

$$e_{pW}^n = \sqrt{H_1/H_0}. \quad (9)$$

The particle-particle coefficient of restitution e_{pp}^n is given by

$$e_{pp}^n = (\sqrt{H_2} - \sqrt{H_1})/\sqrt{H_0}, \quad (10)$$

where H_0 and H_1 are the particle heights of particle P_1 before switching off the vacuum tweezer and after the collision at the highest position and H_2 is the maximum height of particle P_2 after the collision. To determine the rolling friction the model of Zhou et al. [18] is used where the calculation of the rolling friction μ_r is simplified as quotient of moment \vec{M}_r and normal force \vec{F}_N

$$\mu_r = \frac{|\vec{M}_r|}{|\vec{F}_N|}. \quad (11)$$

The experimental setup to determine \vec{M}_r is shown in fig. 8.

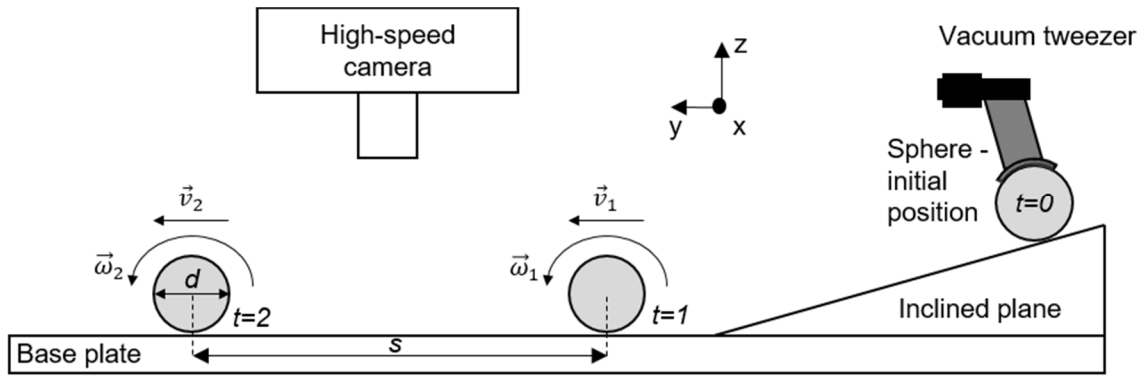


Figure 8: Determination of the rolling friction

Again, a single sphere is fixed at the beginning ($t=0$) by a vacuum tweezer. After switching off the vacuum tweezer the rolling motion of the sphere is recorded by a high-speed camera. By comparing two different moments in time $t=2$ and $t=1$ \vec{M}_r can be calculated as follows

$$|\vec{M}_r| = \frac{(1/2m(v_1^2 - v_2^2) + 1/2\theta(\omega_1^2 - \omega_2^2))}{d/(2s)}, \quad (12)$$

where v_1, ω_1 and v_2, ω_2 are the velocities (translational and rotational) at the moments of time $t=1$ and $t=2$, respectively, m is the particle mass, θ is the mass moment of inertia, d the particle diameter and s is the travelled distances between both moments in time. Under the assumption that the sphere does not slip or bounce on the applied base plate, the angular velocity is equal to the translational velocity so that only s, v_1 and v_2 must be determined via image processing.

2.4 Particle-fluid interaction forces

For the description of the interaction between a particle and its surrounding, fluid particle-fluid interaction forces have to be realized for. In recent years many investigators derived and implemented forces, including particle-fluid drag force, lift forces such as Saffmann, Magnus and Basset force, lubrication force and buoyancy force. The driving force for the fluidization of a granular system is the drag force [8]. In general, two approaches have been used to determine this force in the past. The first one is based on the determination of the drag force by direct numerical simulations (DNS) such as particle resolved CFD based on the solution of the Navier-Stokes equations or the Lattice-Boltzmann method (LBM). Alternatively, drag forces can be evaluated based on pressure drop measurements [8,38,39]. An empirical correlation that bases on experiments and DNS is used for this dissertation and can be found in the investigations I-IV and VI-VII. Instead of calculating the drag and pressure gradient force separately like [11,40], who evaluated the pressure gradient force from the CFD, the combined particle-fluid

force \vec{F}_i^{pf} containing drag force \vec{F}_i^d and pressure gradient force $\vec{F}_i^{\nabla p}$ as introduced by Shimizu [41] is used and calculated by the approach of Di Felice [42]

$$\vec{F}_i^{pf} = \vec{F}_i^d + \vec{F}_i^{\nabla p} = \frac{1}{2} \rho_F |\vec{u}_F - \vec{v}_i| C_D A_{\perp} \varepsilon_F^{1-\chi} (\vec{u}_F - \vec{v}_i) \quad (13)$$

where ρ_F is the fluid density, ε is the local porosity, $(\vec{u}_F - \vec{v}_i)$ is the relative velocity between fluid and particle, C_D is the drag coefficient, and A_{\perp} is the particle cross-sectional area perpendicular to the flow. The used combined particle-fluid interaction forces with the three presented values for the exponent χ are given in table 2. Eq. 13 is based on the combined particle-fluid force on a single particle influenced by the particulate system [43]. The influence of the particle bed on a single particle is considered through a porosity function $\varepsilon_F^{1-\chi}$ [43], with the exponent χ which can vary in dependency of the used model. The simplest form is the model of Wen and Yu who used a constant value of $\chi = 3.7$. Di Felice [42] derived a model where χ is dependent of the Reynolds number. Rong et al. [44] added an additional dependency of the local porosity in their model.

Table 2: Overview of particle-fluid interaction forces

Forces	Correlations	Ref.
Combined particle-fluid force	$\vec{F}_i^{pf} = \vec{F}_i^d + \vec{F}_i^{\nabla p} = \frac{1}{2} \rho_F \vec{u}_F - \vec{v}_i C_D A_{\perp} \varepsilon_F^{1-\chi} (\vec{u}_F - \vec{v}_i)$ <p>a): Wen and Yu: $\chi = 3.7$</p> <p>b): Di Felice: $\chi = 3.7 - 0.65 \exp(-(1.5 - \log(Re))^2/2)$</p> <p>c): Rong: $\chi = 2.65(\varepsilon_F + 1) - (5.3 - 3.5\varepsilon_F)\varepsilon_F^2 \exp(-(1.5 - \log(Re))^2/2)$</p>	[7]
Saffman force	$F_{LS} = 6.46 C_{LS} r^2 \sqrt{\rho_g \eta} \frac{u_r D^*}{\sqrt{D^*}}$ $C_{LS} = \begin{cases} e^{-0.1 Re_p} - 0.3314 \sqrt{\alpha} (e^{-0.1 Re_p} + 1) & Re_p \leq 40 \\ 0.0524 \sqrt{\alpha Re_p} & Re_p > 40 \end{cases}$ $D^* = \nabla u_r + \nabla u_r^T$	[13–15]
Magnus force	$F_{LM} = \frac{1}{2} C_{LM} \pi r^2 \rho_g \frac{\omega_r \times u_r}{ u_r }$ $C_{LM} = 2r \omega_r \begin{cases} 1 & Re_p \leq 1 \\ 0.178 + 0.822 Re_p^{-0.522} & Re_p > 1 \end{cases}$	[16,17]
Basset force	$F_{LB} = \frac{3}{2} d_p^2 \sqrt{\pi \rho_f \mu_f} \left[\int_0^t \frac{(\dot{u} - \dot{v})}{\sqrt{t-t'}} dt' + \frac{(u-v)_0}{\sqrt{t}} \right]$	[18–21]
Lubrication force	$F_l(t) = \frac{6\pi\mu r^2 \vec{v}_{rel}^n }{\delta}$	[45,46]
Buoyancy force	$F_b = \frac{1}{6} \pi \rho_f d_p^3 g,$	[47]

In addition to the combined particle-fluid forces, other forces like lift forces, lubrication forces or buoyancy force can be accounted for. Lift forces can be subdivided in the Saffmann (shear dependent), Magnus force (rotational dependent) and Basset force (acceleration dependent) [11]. Lift forces play generally an important role but are not included for the following reasons. The Basset force is neglected as the gas acceleration of the considered systems is low and the density ratio is small ($\rho_f/\rho_s < 10^{-3}$ in all cases) [8,11]. In addition to that, the equations for the Basset and Saffmann force are derived for a single spherical particle where the influence of the particle shape or orientation is not considered. Further investigations like experimental measurements or DNS are required to account for arbitrary shaped particles. Most investigations considering non-moving granular systems (V-VII; forces are zero) or non-spherical shaped particles (II-IV; no suitable models) so that Basset and Saffmann forces are not considered in this dissertation. Furthermore, lubrication forces are only relevant for systems with liquids such as in investigation I. Nevertheless, the focus here is set to mark up the relevance of the lubrication forces. In the lubrication model given in table 2, the force between two particles is only calculated if the following two conditions are fulfilled. Firstly, the distance δ between both particle surfaces must be less than or equal to the mean radius $\delta \leq (r_1 + r_2)/2$. This restriction ensures that no third particle lies between the regarded particles. Secondly, the lubrication force is only calculated if δ is larger than or equal to the combined roughness of both particles $\delta \geq 2\sigma_s$ (otherwise contact forces apply). In addition to the lubrication force, the density-based buoyancy force, relevant for systems with a high fluid density (like water), can be added to eq. 1. More detailed information about lubrication force and buoyancy force are given in investigation I.

The presented modelling approach of table 2 can be used for dry systems with arbitrary shaped particles if a respective model for the calculation of the drag coefficient is used. In opposite to spheres, the drag coefficient of non-spherical particles can strongly vary with the particle orientation. To provide a model which is valid for arbitrary shaped particles the drag coefficient model (derived by numerical simulations and experiments) of Hölzer und Sommerfeld [48] is used

$$C_D = \frac{8}{Re} \frac{1}{\sqrt{\phi_\perp}} + \frac{16}{Re} \frac{1}{\sqrt{\phi}} + \frac{3}{\sqrt{Re}} \frac{1}{\phi^{3/4}} + 0.42 \times 10^{0.4(-\log(\phi))^{0.2}} \frac{1}{\phi_\perp} \quad (14)$$

with the Reynolds number Re and the sphericity ϕ which is the ratio between the surface area of the volume equivalent sphere and the surface area of the considered particle. The crosswise sphericity ϕ_\perp is the ratio between the cross-sectional area of the volume equivalent sphere and the projected cross-sectional area of the considered particle perpendicular to the flow. The average error of this proposed model is around 14.4 % [48]. The important theoretical foundations of modelling non-spherical shaped particles are described in the next section.

3. Non-spherical particles within the DEM

3.1 Rotational motion of non-spherical particles

The exact description of the rotation of the arbitrary shaped particles is fundamental as rotational motion (see eq. 2) leads to a change in particle orientation which may have a strong influence on the contact detection or the combined particle-fluid force. In non-spherical particle DEM simulations the orientation of the particle can be represented by two approaches (among others): The transformation matrix or via quaternions, a special type of the Euler angles. Table 3 shows the general convention of both approaches and the transformation to and from rotation matrix to the quaternions.

Table 3: Convention of particle rotation and transformation to and from Rotation Matrix

Convention	
Rotation Matrix	Quaternions
$A_i = \begin{pmatrix} i_x & j_x & k_x \\ i_y & j_y & k_y \\ i_z & j_z & k_z \end{pmatrix} = \begin{pmatrix} r_{11} & r_{12} & r_{13} \\ r_{21} & r_{22} & r_{23} \\ r_{31} & r_{32} & r_{33} \end{pmatrix}$	$q_1^2 + q_2^2 + q_3^2 + q_4^2 = 1$
Transformation to rotation matrix [49]	
$A_i = 2 \begin{pmatrix} q_1^2 + q_2^2 - 1/2 & q_2 q_3 - q_4 q_1 & q_2 q_4 + q_3 q_1 \\ q_3 q_2 + q_4 q_1 & q_1^2 + q_2^2 - 1/2 & q_3 q_4 + q_2 q_1 \\ q_4 q_2 + q_3 q_1 & q_4 q_3 - q_2 q_1 & q_1^2 + q_4^2 - 1/2 \end{pmatrix}$	
Transformation from rotation matrix [50]	
$d_1 = 1 + i_x - j_y - k_z \quad d_2 = 1 - i_x + j_y - k_z $ $d_3 = 1 - i_x - j_y + k_z \quad d_4 = 1 + i_x + j_y + k_z $ <p style="text-align: center;">choose i for $d_i = \max(d_1, d_2, d_3, d_4)$</p> $q_i = \pm \sqrt{d_i}/2$	
if $i < 4$	else
$j = i \bmod(3) + 1 \quad k = 6 - j - i$	$q_e = r/4q_4 = [q_1, q_2, q_3]^T$
$q_j = (r_{ij} + r_{ji})/(4q_i) \quad q_k = r_{ik} + r_{ki}/4q_i$	with
$q_4 = (r_{jk} - r_{kj})/(4q_i)$	$r = [r_{23} - r_{32}, r_{31} - r_{13}, r_{12} - r_{21}]^T$

Both approaches have in common that they do not own singularities (every rotation is explicitly defined). Through numerical error propagation over time a rotation matrix may lose the ability of being a rotation matrix which has to be corrected by rescaling this matrix. Quaternions do not hold this problem through the restriction $q_1^2 + q_2^2 + q_3^2 + q_4^2 = 1$. For the transformation of quaternions from rotation matrix a distinction of cases is done based on the maximum value of the d_i for the calculation of the four values $q_1 - q_4$. If the maximum value is d_4 , $q_1 - q_3$ are

calculated based on the three dimensional column matrix q_e , otherwise each value is calculated separately. Quaternions can be described with only three values and the sign of the fourth instead of nine (rotation matrix). As described previously (compare eq. 2), the method applied for the rotational motion of particles within the DEM is based on the work of Munjiza et al. [12]. Here the rotation matrix is used. DEM simulations usually obtain small time steps and small rotations between two time steps. Therefore, a constant angular velocity is assumed during one single time step resulting from a rotation angle $\vec{\psi}_i$ given by [22]

$$\vec{\psi}_i = \Delta t \vec{W}_i = \Delta t \Lambda_i^{-1} \vec{\omega}_i = [\psi_{i,1}, \psi_{i,2}, \psi_{i,3}]^T, \quad (15)$$

while the change of each row of the rotation matrix can be calculated as follows

$$i_{t+\Delta t} = \frac{1}{\bar{\psi}^2} (\bar{\psi} i_t) \bar{\psi} + \left[i_t - \frac{1}{\bar{\psi}^2} (\bar{\psi} i_t) \bar{\psi} \right] \cos(\bar{\psi}) + \frac{1}{\bar{\psi}} (\bar{\psi} \times i_t) \sin(\bar{\psi}), \quad (16)$$

$$j_{t+\Delta t} = \frac{1}{\bar{\psi}^2} (\bar{\psi} j_t) \bar{\psi} + \left[j_t - \frac{1}{\bar{\psi}^2} (\bar{\psi} j_t) \bar{\psi} \right] \cos(\bar{\psi}) + \frac{1}{\bar{\psi}} (\bar{\psi} \times j_t) \sin(\bar{\psi}), \quad (17)$$

$$k_{t+\Delta t} = \frac{1}{\bar{\psi}^2} (\bar{\psi} k_t) \bar{\psi} + \left[k_t - \frac{1}{\bar{\psi}^2} (\bar{\psi} k_t) \bar{\psi} \right] \cos(\bar{\psi}) + \frac{1}{\bar{\psi}} (\bar{\psi} \times k_t) \sin(\bar{\psi}), \quad (18)$$

$$\bar{\psi} = \sqrt{\psi_1^2 + \psi_2^2 + \psi_3^2}. \quad (19)$$

To calculate the change in angular velocity during a single time step it is assumed that the external moments \vec{M}_i applied on a non-spherical particle are acting instantaneously. This means that the angular momentum (after the external impulse has been applied but before the spatial orientation has changed) is equal to the angular momentum at the end of the time step [22]

$$\vec{\pi}_i(t + \Delta t) = \vec{\pi}_i(t) + \vec{M}_i \Delta t, \quad (20)$$

where $\vec{\pi}_i = \Lambda_i \hat{I}_i \Lambda_i^{-1} \vec{\omega}_i$ is the angular momentum. To derive the angular velocity of the next time-step $\vec{\omega}_i(t + \Delta t)$ the inverse rotation matrix Λ_i^{-1} and inertia tensor \hat{I}_i^{-1} are used

$$\vec{\omega}_i(t + \Delta t) = [\Lambda_i(t + \Delta t) \hat{I}_i^{-1} \Lambda_i^{-1}(t + \Delta t)] [\Lambda_i(t) \hat{I}_i \Lambda_i^{-1}(t) \vec{\omega}_i(t) + \vec{M}_i \Delta t]. \quad (21)$$

An arbitrary point within the body \vec{x}_{ik} can be rotated by the rotation matrix and the center of mass \vec{x}_i as [22]

$$\vec{x}_{ik}(t + \Delta t) = \vec{x}_i(t) + \Delta \Lambda (\vec{x}_{ik}(t) - \vec{x}_i(t)). \quad (22)$$

Besides the rotational motion during one-time step, information about the particle orientation in space are needed for the calculation of the cross-sectional area to determine the combined particle-fluid force. To avoid unnecessary recalculation during every time step and to reduce required memory (compared to the rotation matrix), the quaternion approach is taken to save the in MATLAB pre-calculated cross-sectional areas in a lookup table for every particle type (types varying in diameter and shape), see investigation II – section 2.3.1. During one DEM time step the respective particle rotation matrix is then taken and transferred in quaternions. Further information about rotating a particle with the quaternion approach can be found in literature [49].

3.2 Representation methods of non-spherical particles in the DEM

For the geometric description of a non-spherical particle several approaches can be found in literature. The most common approaches in the DEM are the polyhedron, multi-sphere and super-quadrics approach [3,51–53]. An overview of these representation methods with three degrees of approximation accuracy from coarse to fine is given in fig. 9.

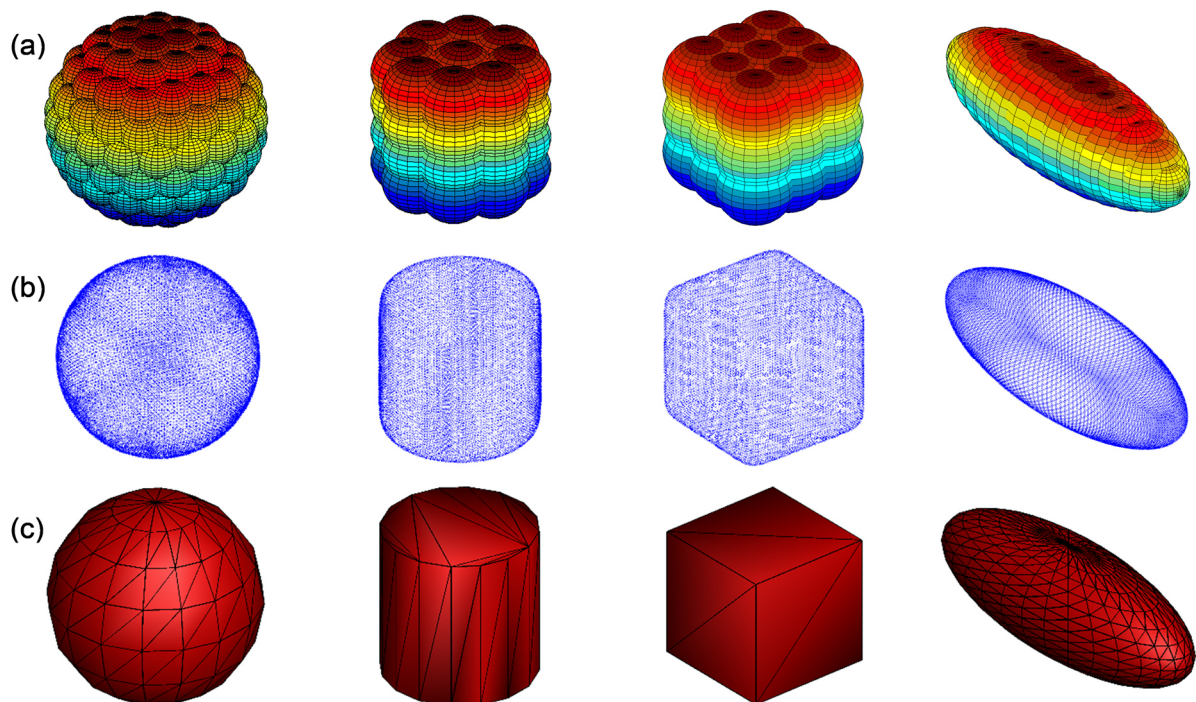


Figure 9: Illustration of four different shapes (sphere, cylinder, cube, ellipsoid) with the different representation methods of non-spherical particles from coarse to fine approximation. (a): Multi-spheres, (b): Super-quadrics described by the discrete function representation (DFR) approach, (c): Polyhedrons, [53].

The easiest by implementation and often fastest method is the multi-sphere method where one non-spherical particle is approximated by a certain number of clumped spheres. This group of spheres can overlap, vary in size and do not change their position to each other during a

contact. The forces and torques acting on that group of spheres are calculated for each single overlapping sphere and are then accumulated relative to the center of mass. These accumulated values are finally averaged as follows

$$\vec{F}_i = \sum_{k=1}^M \sum_{l=1}^N (\vec{F}_{ikl}^n + \vec{F}_{ikl}^t) / j_{ikl}, \quad (23)$$

$$\vec{M}_i = \sum_{k=1}^M \sum_{l=1}^N (\vec{x}_{ikl} - \vec{x}_i) \times (\vec{F}_{ikl}^t / j_{ikl}) \quad (24)$$

with the total number of artificial contacts j_{ikl} , the contact point \vec{x}_{ikl} between two contact partners and the position of the center of mass \vec{x}_i . Each sum represents the artificial contacts (overlapping clumped spheres) of the contact partners (wall or particle) k and j . If contact partner j is a wall only the first sum is needed. The big advantage of this methodology is that it provides a fast and robust algorithm for the contact detection and the determination of contact parameters as conventional methods for spherical particles can be applied [52]. Consequently, this method often provides the fastest simulation speed of all three methods [53]. However, generating an approximation of some real particle shapes, like e.g. the cube of fig. 9, is a big challenge. Due to the geometric abilities of the clumped spheres it is hard to generate a smooth particle surface. As mentioned in investigation II, differences in volume or/and total mass can occur between the real particle and the particle generated by the multi-sphere approach. The mass can be corrected by choosing a higher density. Nevertheless, to represent a smooth particle surface a high number of particles is required which results in two problems. Firstly, the simulation time increases with the number of particles, meaning that the big advantage of being the fastest method decreases. Secondly, many composite particles result in a higher probability for multiple contacts. Without any correction, these multiple contacts may give rise to an unphysical contact behavior [52,54,55]. Using the described averaging method in eq. 23 reduces the error for the normal component \vec{F}_{ikl}^n [55]. However, deviations can still occur for tangential forces as the force is just restricted to an upper limit (Coulomb force, compare table 1).

In contrast to multi-spheres, super-quadrics provide a smooth particle surface. In general form a super-quadric particle can be described through the following equation [52,56]

$$f(x, y, z) = \left(\left(\frac{x}{a} \right)^{\frac{2}{\varepsilon_2}} + \left(\frac{y}{b} \right)^{\frac{2}{\varepsilon_2}} \right)^{\varepsilon_2 / \varepsilon_1} + \left(\frac{z}{c} \right)^{2 / \varepsilon_1} - 1, \quad (25)$$

or the equivalent parametric form

$$x = a(\sin\theta)^{\varepsilon_1}(\cos\vartheta)^{\varepsilon_2}, \quad y = b(\sin\theta)^{\varepsilon_1}(\sin\vartheta)^{\varepsilon_2}, \quad z = c(\cos\theta)^{\varepsilon_1}, \quad (26)$$

with the angles $0 \leq \theta \leq \pi$ and $-\pi \leq \vartheta \leq \pi$, the half lengths a, b, c along the principal axes and the parameters ε_1 and ε_2 which describe the blockiness of the cross-section. ε_1 controls the blockiness of the cross-section in the $x - z$ and $y - z$ plane whereas the $x - y$ plane is controlled by ε_2 . In fig. 9b four respective examples are given of the geometries sphere, ideal cylinder, cube and ellipsoid. A sphere is obtained for $a = b = c = \varepsilon_1 = \varepsilon_2 = 1$. An arbitrarily shaped ellipsoid can be described when only the half lengths are varied ($\varepsilon_1 = \varepsilon_2 = 1$). Cylinders ($\varepsilon_1 = 1, \varepsilon_2 = 0.2$) and cubes ($\varepsilon_1 = 0.2, \varepsilon_2 = 0.2$) are obtained by changing the blockiness parameters. More examples for geometry forms described by the super-quadric approach are given in literature [11,40,51–53]. As summarized by Höhner [53] the blockiness parameters have to fulfill the condition $0 \leq \varepsilon_1 \leq 0.2$ and $0 \leq \varepsilon_2 \leq 0.2$ as the implemented contact algorithms are just defined for convex shaped bodies. Although super-quadrics possess a continuous and smooth surface they have some limitations [52]. Firstly, it is not possible to describe sharp edges and/or flat surfaces which is necessary for the approximation of some real particles. Secondly, with this method it is not possible to describe asymmetries that some natural solids provide (e.g. coal, stones).

One method which can address all these requirements is the polyhedron approach which is used in studies II-V. In this approach a non-spherical particle is described by vertices which are connected over edges to generate triangular surfaces. Therefore, a rigid body consists of a certain number of triangles, edges and vertices. Technically every shape can be approximated through this approach but again due to the limitations of the contact algorithm, only convex shaped particles are valid. A special form of the polyhedron method is the smooth polyhedron method where particles are represented by not sharp-edges. As this special subgroup of the polyhedron method is not used in this dissertation it is not explained in detail. Further information can be found in literature [53,57,58]. In fig. 9c it is shown that some geometries like cubes can be perfectly described by a small number of elements, e.g. 12 triangles, 8 vertices and 18 edges. Other bodies like spheres, cylinders and ellipsoids always show deviations between real and approximated shape which can be reduced by choosing a higher number of triangles, vertices and edges. However, the computational effort rapidly increases with the number of elements. Especially in cases with a high number of particles and/or where many elements are needed to approximate the real shape, the use of this method is often limited. Höhner [53] showed that the simulation time of polyhedron cases is mainly influenced by the number of edges. In case of the multi-sphere approach computational effort increases with the number of composite spheres whereas super-quadrics described by discrete function representation (DFR) are mostly influenced by the number of discrete points which are the number of points used for the contact detection algorithm (explained in the next section). In opposite to spherical particles, contact definition and detection of non-spherical particles are

not always a straightforward procedure. The challenges of the definition of a unique contact point and a time efficient contact detection for non-spherical particles are discussed detailed in the next chapter.

3.3 Contact definition and detection of non-spherical particles

For non-spherical particles approximated by the super-quadric or polyhedron approach, the determination of a contact is comparatively difficult for several reasons. To demonstrate this in a simple 2D example, sketches of relevant contact problems are given in fig. 10.

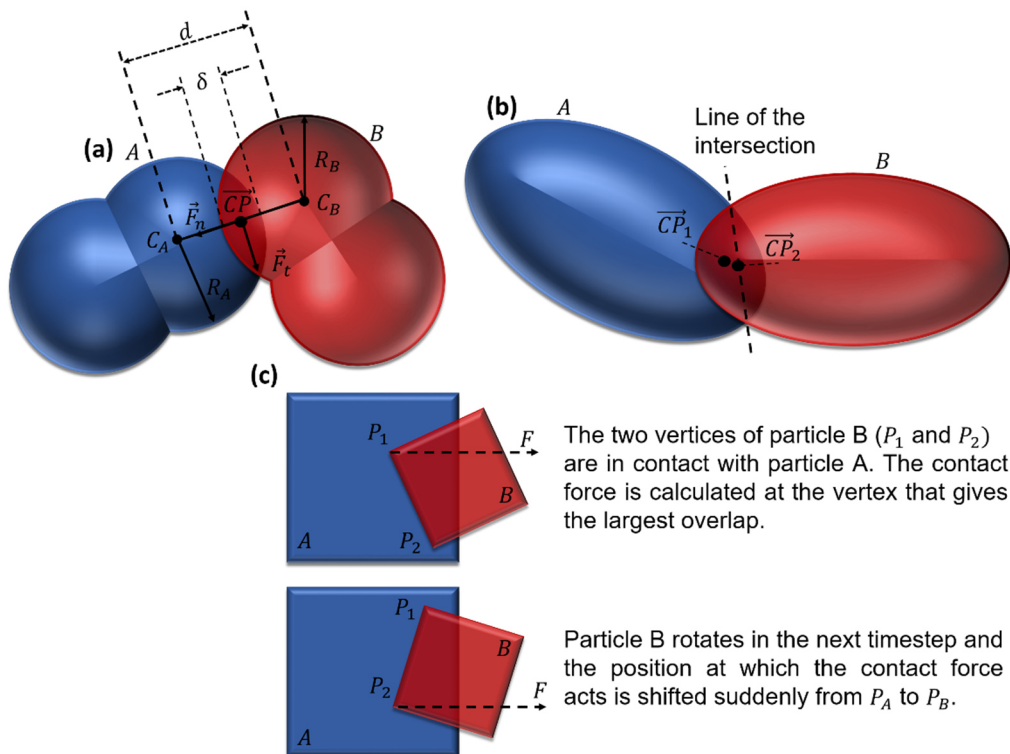


Figure 10: 2D sketch showing schematically the definition of contact parameters: (a) definition of contact point, contact normal and tangential, and contact overlap for two colliding multi-spheres (for clarity the overlap is exaggerated); (b) definition of the contact point for two colliding non-spherical particles; (c) schematic illustration of an issue concerning single-point contact models, showing the sudden shift of the contact point and the direction of the contact force [3]

Within the multi-sphere approach (see fig 9a), contact definition of spherical particles can be adapted easily. Here the overlap between two colliding multi-spheres can be calculated as $\delta = R_1 + R_2 - s$, where R_1 and R_2 are the radius of the overlapping single sphere P1 and P2, respectively, and s is the distance between the center of mass of each single sphere. The contact point can be clearly defined as midpoint of the contact normal line $\overline{P_1P_2}$ which connects both centers of mass. For the multi-sphere method, all values are taken from the overlapping clumped spheres of P1 and P2 to determine a contact and only the calculated forces and moments act on the center of mass for the rotational and translational movement of the multi-

sphere particle. In case of the super-quadric or polyhedron approach for describing non-spherical particles, no clear agreement for the location of one unique contact point can be found [52], see fig. 10b. In a 2D collision of two super-quadric particles for example, the contact point can be defined as the geometric midpoint of the overlapping area or as midpoint of the line of intersection. In addition to that, the definition of the contact normal line $\overline{P_1P_2}$ is not as trivially obtained as for the spherical case. If the contact line does not intersect both centers of mass, e.g. the contact normal is perpendicular to both contacting surfaces and passed through the contact point, the normal component of the contact force produces a moment which results in a rotation. Focusing on one contact point for polyhedrons can lead to an unphysical behavior which is exemplary shown for two different sized squares in fig. 10c. Here the bigger sized particle is fixed in space and it is assumed that the force acts only on those vertices with the largest overlap (P1). In this example, the point with the largest overlap and therefore the point where the force acts directly, shifts from P1 to P2 after one time step due to the rotation of the small particle. To stabilize the contact between two colliding particles and to avoid a sudden change of contact forces multi-point concepts have to be accounted for [52]. A detailed description of the implemented contact detection models for the super-quadric and polyhedron is presented in the following. As the algorithms were implemented by Höhner [53], the next two subchapters correspond to his findings and descriptions.

3.3.1 Contact detection for super-quadrics

For the representation of a contact by using super-quadrics two methods are commonly used, the continuous function representation (CFR) and the discrete function representation (DFR) [52]. As only the DFR approach is implemented in the considered DEM framework [53], the CFR is not explained in detail. Lu et al. [52] summarized a list of authors who used and presented this method. Within the DFR a particle surface is represented by a discrete number of points such as the examples in fig. 9b. The implemented DFR approach is based on the work of Lu et al. [59]. As described in the previous section, the computational effort is mainly influenced by the number of discrete points. However, the accuracy of the DFR method is based on the number of discrete points and distribution of these discrete points over the particle surface [60]. To optimize the distribution and to provide an adequate solution for particle shapes which strongly differ from a spherical shape, the discrete points are adaptively distributed as recommended by Lu et al. [52]. Here a particle is initially surrounded by a box whose edge lengths are equal to the principal axes of the super quadric. In a next step, the discrete points are distributed along the edges of the box which can be either equally distributed or with a distribution function, respectively. Finally, every single discrete point is projected to the particle surface intersection of a line which connects the respective discrete point and the center of mass. This procedure is only required once at the initialization as the points can be described

in a body fixed coordinate system of a particle and therefore be rotated by eq. 22. For the determination of a contact between two particles A and B eq. 25, also known as Inside-Outside function (IO-function), is used. Two particles are in contact when one point of particle A lies in particle B and vice versa. By setting one point of particle B in particle A the following results for the IO-function are possible:

1. $f_A(\vec{P}_B) < 1 \rightarrow$ point \vec{P}_B^{GP} lies in particle A.
2. $f_A(\vec{P}_B) = 1 \rightarrow$ point lies on the surface of particle A.
3. $f_A(\vec{P}_B) > 1 \rightarrow$ point \vec{P}_B^{GP} lies not in particle A.

In contrast to the multi-sphere and polyhedron approach, the implemented super-quadric framework provides only one contact point which is determined with the lowest geometric potential method [61–63]. A simple 2D sketch of two particles with the definition of \overline{CP} is shown in fig. 11.

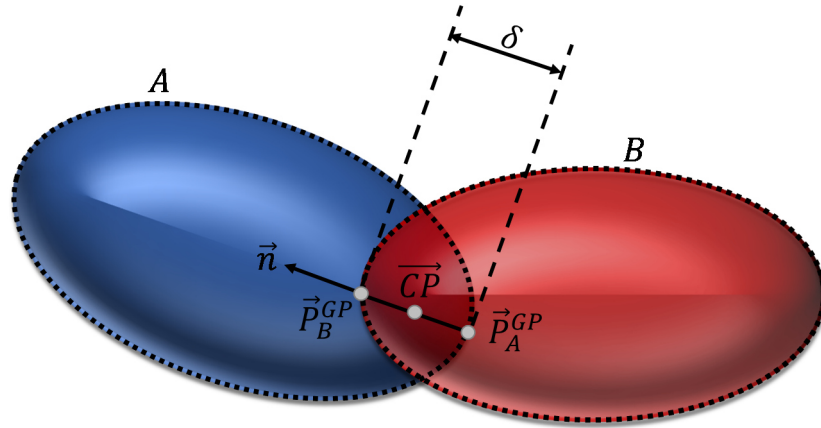


Figure 11: Definition of the contact point \overline{CP} , the contact normal \vec{n} , the overlap δ and both points with the minimal geometric potential \vec{P}_A^{GP} and \vec{P}_B^{GP} , according to [53]. Points on the surface represent discrete points of the DFR method.

\vec{P}_A^{GP} and \vec{P}_B^{GP} are the points with the minimum value for f_A or f_B , respectively. The midpoint of both points with the lowest geometric potential is defined as the contact point \overline{CP}

$$\overline{CP} = \vec{P}_A^{GP} + \frac{(\vec{P}_B^{GP} - \vec{P}_A^{GP})}{2}. \quad (27)$$

In addition to that the obtained points \vec{P}_A^{GP} and \vec{P}_B^{GP} are used for the calculation of the contact normal and overlap δ

$$\vec{n} = \frac{\vec{P}_B^{GP} - \vec{P}_A^{GP}}{|\vec{P}_B^{GP} - \vec{P}_A^{GP}|}, \quad (28)$$

$$\delta = |\vec{P}_B^{GP} - \vec{P}_A^{GP}|. \quad (29)$$

To accelerate the search for the point of the minimal geometric potential (and therefore the simulation speed) Lu et al. [59] provide the so-called contact candidate list which avoids

searching through the whole discrete node array during each time step for existing contacts. Here only a certain number of the spatially closest points to the geometric potential point $\vec{P}_{A,B}^{GP}$ are checked with the IO-function. If one neighbor of $\vec{P}_{A,B}^{GP}$ has a lower geometric potential it becomes the new $\vec{P}_{A,B}^{GP}$ and the candidate list is updated in dependency of the new point. This procedure is repeated until no neighbor holds a lower geometric potential as $\vec{P}_{A,B}^{GP}$. A candidate list is a suitable method for increasing simulation speed as the DEM changes in positions and orientations are generally small due to the small time steps and it can be assumed that $\vec{P}_{A,B}^{GP}$ will not move rapidly from one-time step to another. In accordance to that, Höhner [53] summarized that the candidate list procedure is normally finished after 1-3 updates of $\vec{P}_{A,B}^{GP}$. The best choice for the total number of discrete points within the candidate list depends on the particle shape and the used discretization method [52]. Nevertheless, as a coarse guideline, Höhner [53] suggested a total number of 30 – 50 discrete points in the candidate list to receive the best improvement in simulation speed.

In contrast to non-spherical particles approximated by super-quadrics, walls are described by triangles within the in-house DEM Code to be more flexible in geometric shape. Therefore, some adaption of the particle-wall contact detection must be considered. Again, a candidate list for the discrete points of the particle can be used after a contact occurred. The contact detection consists of three steps. In an initial step the distance d_i between a discrete point \vec{P}_i and the respective wall-plane is checked

$$d_i = (\vec{P}_i - \vec{A}) \cdot \vec{n}_w, \quad (30)$$

where \vec{A} is one arbitrary point of the triangle (\vec{B} or \vec{C} are also possible) and \vec{n}_w is the normal vector of the triangle. Under the assumption that the normal vector \vec{n}_w is pointed in direction of the particle, the distance becomes $d_i < 0$ if a contact occurs. If that condition is fulfilled, it is checked whether the discrete point \vec{P}_i^{proj} projected onto this plane lies in the wall triangle or only in the corresponding plane. \vec{P}_i^{proj} lies in that triangle when the following three conditions are valid

$$[(\vec{B} - \vec{A}) \times (\vec{P}_i^{proj} - \vec{A})] \cdot [(\vec{B} - \vec{A}) \times (\vec{C} - \vec{A})] = 0, \quad (31)$$

$$[(\vec{C} - \vec{A}) \times (\vec{P}_i^{proj} - \vec{A})] \cdot [(\vec{C} - \vec{A}) \times (\vec{B} - \vec{A})] = 0, \quad (32)$$

$$[(\vec{C} - \vec{B}) \times (\vec{P}_i^{proj} - \vec{B})] \cdot [(\vec{C} - \vec{B}) \times (\vec{A} - \vec{B})] = 0, \quad (33)$$

with the three vertices of the triangle \vec{A} , \vec{B} and \vec{C} . However, with eqs. 31-33 particle and wall must not be necessarily in contact, see fig. 12.

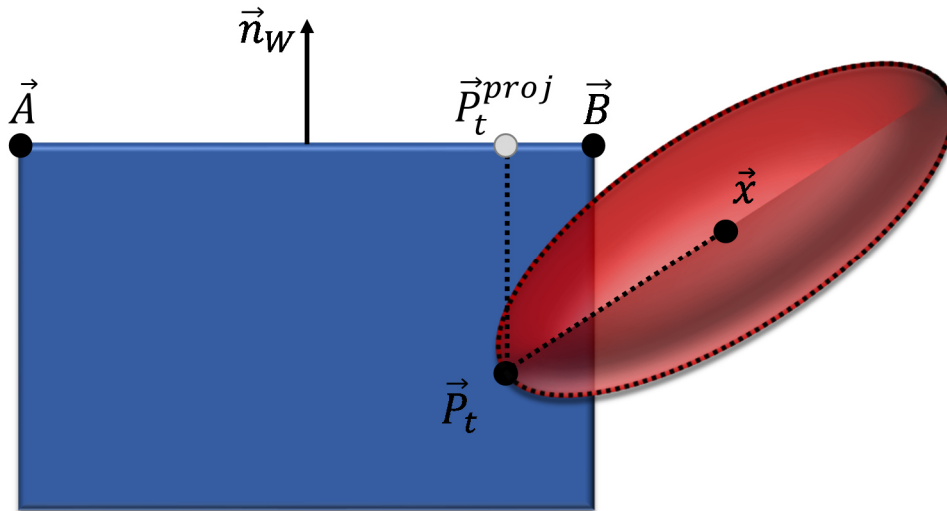


Figure 12: Special case of contact detection between wall and super-quadric which has to be considered [53].

In this shown example, the distance would be $d_i < 0$ and the projected point \vec{P}_i^{proj} fulfills eqs. 31-33, but no real contact exists between particle and the upper wall. To provide an adequate solution to avoid this error it is additionally checked if the line connecting the discrete point \vec{P}_i and the center of mass \vec{x} intersects the triangle which is true when a real contact exists. Again, the contact point is defined as point with the lowest geometric potential whereas the contact vector is equal to the wall normal vector \vec{n}_w if a real contact exist (not fulfilled in fig. 12) [53].

3.3.2 Contact detection for polyhedrons

The contact detection for two three-dimensional polyhedral particles is in general time consuming as the standard algorithm requires a step-by-step assessment of following combinations of possible contacting elements: vertex to vertex, vertex to edge, vertex to face, edge to edge, edge to face or face to face [52]. Even for simple particle geometries like a perfect cube it must be checked if a vertex of one cube falls inside the other or vice versa. In addition to that the respective edges of each contact partner can overlap [64]. Due to this complexity, a widely used method in literature is the common plane algorithm based on the work of Cundall [65]. A schematic three-dimensional example of the implemented common plane algorithm is given in fig. 13a.

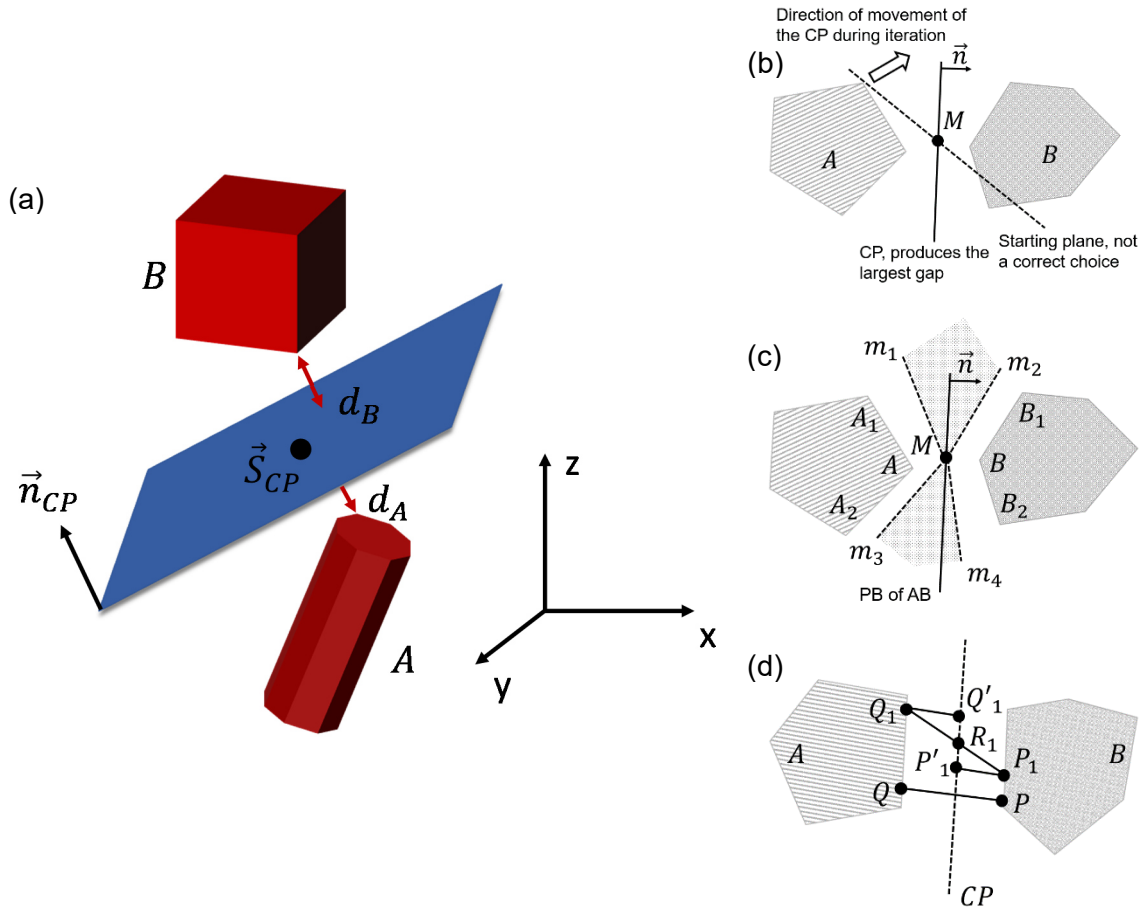


Figure 13 (a): Schematic sketch of the implemented common plane algorithm [53]. Opportunities to find the correct common plane: (b) the conventional iterative algorithm [65,66]; (c) the fast common plane (FCP) algorithm [66]; (d) Shorted Link Method (SLM) [67].

The common plane bisects the space between two particles A and B into a positive and negative half-space. A contact exists if both particles intersect the common plane [3]. A correct placed common plane fulfills following three conditions [52]:

1. The centers of mass of particle A and B are positioned on the opposite sides of the half spaces.
2. d_A and d_B are the shortest distances of the respective particle vertex and the common plane. The following eq. must be true: $d_A = -d_B$.
3. The gap between both possible contact partners, defined as $d_A - d_B$, reaches a maximum. Therefore, no further rotation of the common plane would increase this value. The gap is negative if a contact exists.

The overlap for the calculation of the contact forces is the sum of the absolute values of d_A and d_B whereas the normal vector of the common plane \vec{n}_{CP} is defined as the contact vector. To determine the minimum vertex to common plane distance a loop over all vertices \vec{P}_i of each polyhedron is performed to calculate the distance d_i to a reference point \vec{S}_{CP} of the common plane

$$d_{i,j} = (\vec{P}_{i,j} - \vec{S}_{CP}) \cdot \vec{n}_{NP}. \quad (34)$$

Note that due to the convention of the common plane the determination of the target value for d_A and d_B is different due to the signed distance of the vertices i of particle A and vertexes j of particle B

$$d_A = \min(d_i), \quad (35)$$

$$d_B = \max(d_j). \quad (36)$$

Several approaches for the determination of the correct location of common planes can be found in literature, see fig. 13b-d. All of them have in common that the defined common plane is unique [52,67]. The first and slowest is the so called conventional iterative algorithm [65,66], see fig. 13b. Here a reference point and an initial potential common plane are guessed in a first step. A possible reference point could be the midpoint of line connecting both centers of mass. A possible initial common plane is for example the plane which is perpendicular to that line and intersects the reference point. In a second step this initial guess candidate plane is rotated around the reference point iteratively and compared to the previous candidate plane. If one candidate plane obtains a larger gap it becomes the new common plane. Beside the rotation of the common plane, the reference point is varied such as setting the reference point to the midpoint of the line who connects the closest vertexes between particle A and B. The iteration procedure is done when no candidate plane has a larger gap (with a reasonably accuracy). The efficiency of this iterative method depends on the initial guess of the reference point and the orientation of the plane [52]. A more efficient algorithm is the fast common plane (FCP) algorithm proposed by Nezami et al. [66] which is implemented in the in house DEM code [53]. Nezami et al. [66] summarized that only a few possible orientations for a candidate common plane must be considered. In fig. 13c a simple 2D case is given which demonstrates all possible candidate common planes. For 3D simulations following four types of candidate planes exist [53]

1. The common plane lies in the midpoint M of the line who connects the vertexes with the smallest distance and is perpendicular to that line. This common plane is called initial common plane (marked as PB of AB).
2. The common plane is parallel to minimum one face of particle A or B.
3. The common plane is parallel to one corresponding edges of particle A and B.
4. The common plane is parallel to one corresponding edge on particle A or B.

For this contact detection procedure, the particles are normally initially separated in space. However, Höhner [53] investigated that a separation of both particles (especially for particles

with a high aspect ratio) leads to an error of the real contact geometry which might result in an error for the correct determination of the common plane. Therefore, this part of the original FCP algorithm is not implemented. The last and fastest algorithm for determining the correct position of the common plane is the shortest link method (SLM) [67], see fig. 13d. Here the common plane is perpendicular and set to the midpoint of the shortest line between any two surface points Q / Q_1 (particle A) and P / P_1 (particle B). Nezami et al. [67] figured out that the SLM with the same boundary conditions is 1.5 faster than the FCP and 18 times faster than the conventional iterative method. For future investigations, the author of this dissertation recommends that the SLM should be implemented into the used in-house DEM code and checked if a similar speed-up can be achieved. Beside the implementation of the FCP, Höhner [53] presented modifications which have to be taken into account to avoid an unphysical behavior. This work can be subdivided in a processing of the contact data and a special particle-wall treatment. After a contact between two particles is detected but before the particle-particle contact forces are calculated, it is checked if a real contact exists or just a contact with the common plane. To demonstrate this, a simple particle-particle contact case is considered in fig 14a.

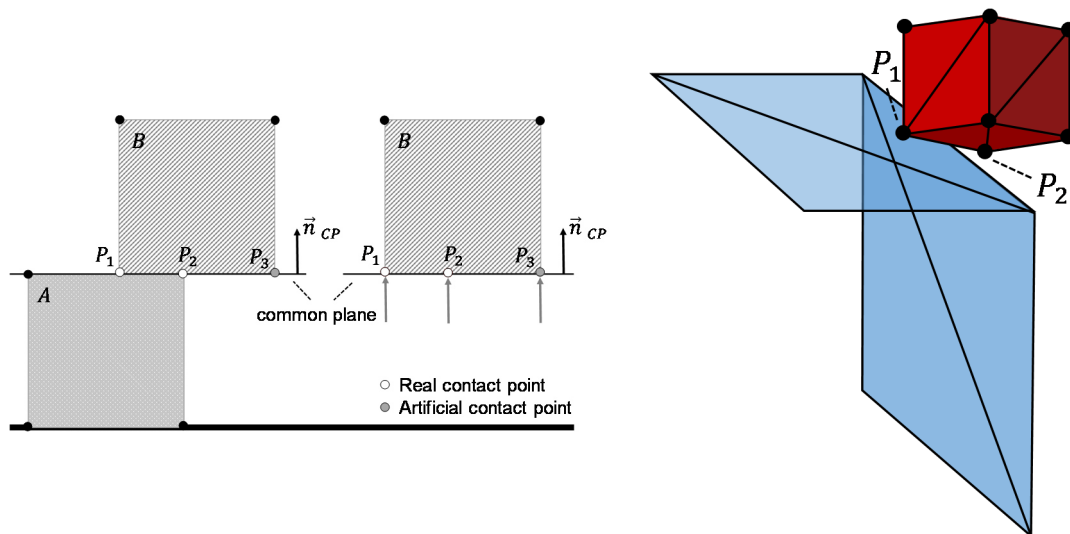


Figure 14: Modifications of polyhedron contact detection algorithms before contact force is calculated implemented by Höhner [53] (a): Deleting artificial contacts; (b): Special case of particle-wall contact.

Here the vertex P_3 of particle B does not lie in particle A and is therefore sorted out for the calculation of the contact forces. To avoid a sorting out of all contacts, which might be sometimes relevant for cases with high aspect ratios or when the wall in fig. 14b is a particle, the intersections of all edges of two particles are additionally defined as a contact point. The particle-wall contact detection between a polyhedron and a wall is similar to the super-quadric case as the vertexes are used as discrete points and checked if they fulfill the three defined

conditions (compare section 3.3.2). However, cases are possible where no vertex is lying inside a wall although a contact exist, see fig. 14b. To fix this error, all three edges of a wall are checked against all faces of the polyhedron. If at least two faces intersect a wall edge, the midpoint of both intersection point is defined as contact point and the distance to one face as overlap. For simplicity, the wall normal vector is treated as contact vector for all particle-wall contacts.

4. Heat Transfer within the DEM

The following section concentrates on the description of heat transfer models in the context of the DEM needed for investigations V – VII. Heat transfer can be generally understood as “thermal energy in transit due to a spatial temperature difference” [68]. Therefore, heat transfer must be accounted for in a DEM simulation if temperature differences occur. Three modes of heat transfer can be defined: conduction, convection and radiation. All three modes are exemplarily shown in fig. 15.

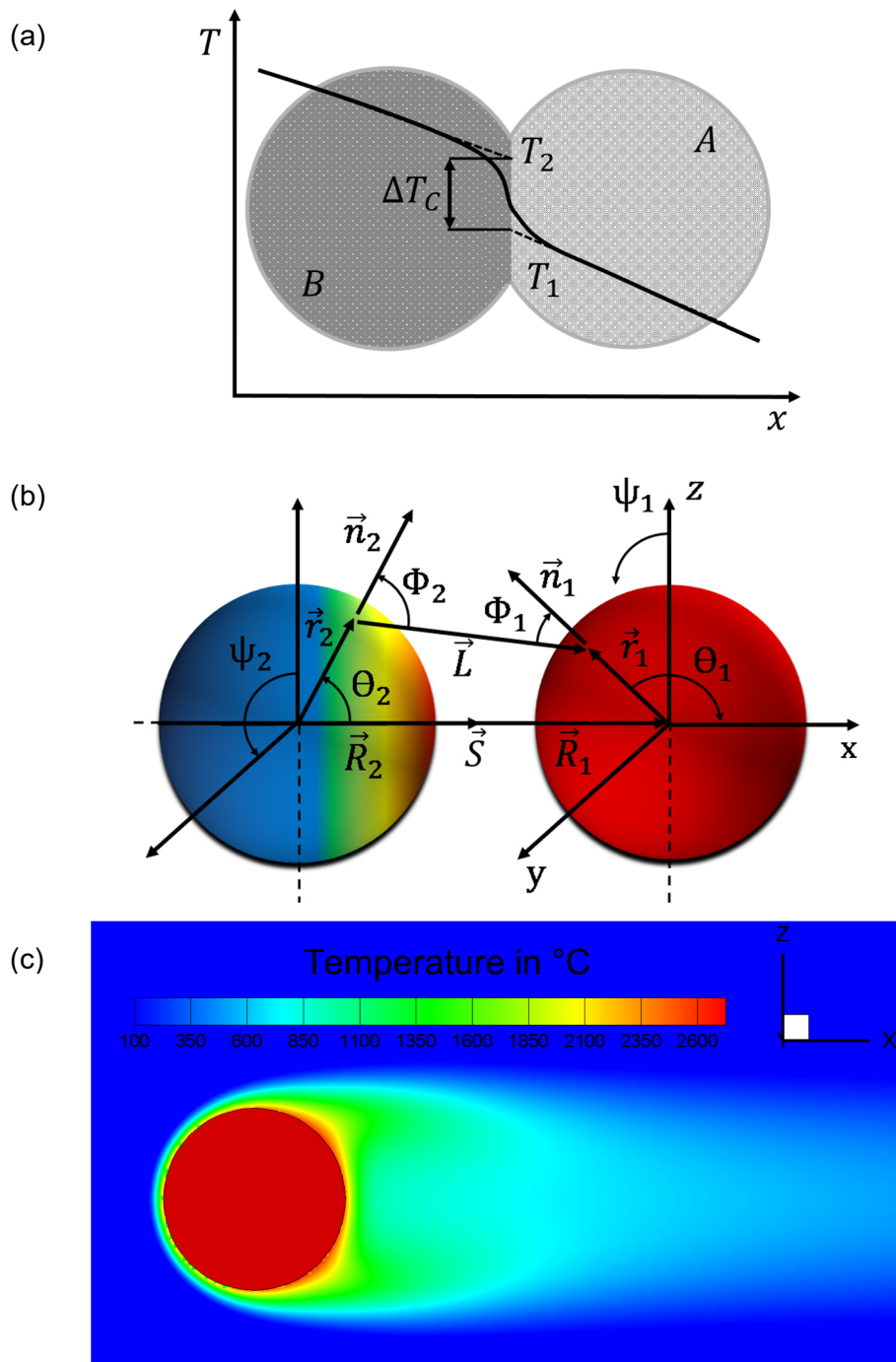


Figure 15: Conduction (a), radiation (b) and convection (c) as heat transfer mechanisms in the DEM, according to [68].

Conduction is defined as the heat transfer that occurs by a temperature gradient in a stationary medium [68]. In case of the DEM the heat transfer mechanism can be subdivided in intra particle / wall or particle heat transfer by conduction, particle-particle, particle-wall and particle-fluid-particle heat transfer by contact conduction. If a body (particle or wall) is surrounded by a moving fluid with a different temperature convective heat transfer will occur. The third and last mode is the radiative heat transfer which is generally understood as heat exchange in form of electromagnetic waves between all emitting surfaces [69]. Zhou et al. [70] summarized that in their simulations the heat transfer is mainly affected by the (1) gas superficial velocity, (2) particle thermal conductivity and (3) bed temperature. To describe the thermal behavior of each individual particle they used the heat transfer coefficient (HTC) which is calculated differently for every heat transfer mechanism as

$$h_{i,conv} = \frac{Q_{i,conv}}{A_i(T_{f,i} - T_i)} \quad (37)$$

$$h_{i,cond} = \sum_{j=1}^{k_i} \left[\frac{|Q_{ij,cond}|}{A_i(T_j - T_i)} \right] + \left[\frac{|Q_{i,wall}|}{A_i(T_W - T_i)} \right] \quad (38)$$

$$h_{i,rad} = \frac{Q_{i,rad}}{A_i(T_{local,i} - T_i)} \quad (39)$$

Here $h_{i,conv}$, $h_{i,cond}$ and $h_{i,rad}$ are the HTCs by convection, conduction and radiation, $Q_{i,conv}$, $Q_{i,cond}$, $Q_{i,wall}$ and $Q_{i,rad}$ are the calculated heat fluxes due to convection, particle-particle conduction, particle-wall conduction and radiation, respectively, A_i is the particle surface area, T_i , T_j , T_W , $T_{f,i}$ and $T_{local,i}$ are the temperatures of particle i , particle j , the wall, fluid and the average temperature of particles and fluid by volume fraction in an enclosed spherical domain and k_i is the total number of particles in interaction. Figs. 16-18 show their calculated HTCs of a packed bed / fluidized bed system (depending on the operational parameters) for the three heat transfer mechanisms conduction, convection and radiation in dependency of the operational parameters gas superficial velocity, particle thermal conductivity and bed temperature. Although the results of figs. 16-18 are only achieved for specific boundary conditions they can be used as a guideline for understanding the dominating heat transfer mechanism of the respective simulation/experimental system. Their used model for the heat transfer by contact conduction is implemented in the in-house CFD-DEM framework. For the heat transfer mechanism convection and radiation newer more detailed models are chosen, see investigation V.

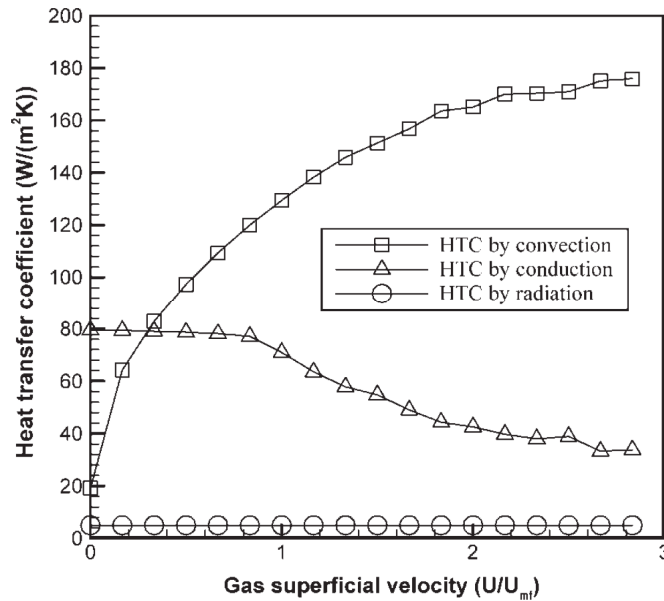


Figure 16: Bed-averaged convective, conductive and radiative heat transfer coefficients as a function of the gas superficial velocity at 100 °C operating temperature [70].

Both, fig 16 and 17 show the average HTC of all particles in a heating process of a packed / fluidized bed. Further information with all relevant data and boundary conditions can be found in the work of Zhou et al. [70]. For clarity, the gas superficial velocity is the quotient of the absolute superficial gas velocity U and the minimum fluidization velocity U_{mf} . The minimal fluidization velocity U_{mf} is defined as the velocity where the packed bed becomes a fluidized bed [71]. Therefore, below the ratio $U/U_{mf} < 1$ the system is called a packed bed whereas the system becomes a fluidized bed for larger values. In fig. 16 the system is heated up from 25°C to a limit of 100°C and U/U_{mf} strongly influences the HTC by convection and by conduction. In general, the HTC by convection increases for higher U/U_{mf} ratios. In opposite to that, the HTC by conduction in the packed bed system is nearly constant but decreases for higher U/U_{mf} values after reaching the fluidized bed state. No significant influence of U/U_{mf} on the HTC by radiation can be found for the applied boundary conditions. Here the contribution of the radiation heat transfer is comparatively low as radiation heat transfer has a minor role on the overall heat transfer for temperatures below 500 °C [72]. To investigate the effect of the bed temperature on the bed-averaged HTCs the system is heated up with a gas inlet temperature of 1000°C and a superficial gas velocity of 3.2 m/s. Bed temperature and HTC variation of each heat transfer mechanism are plotted over time in fig. 17.

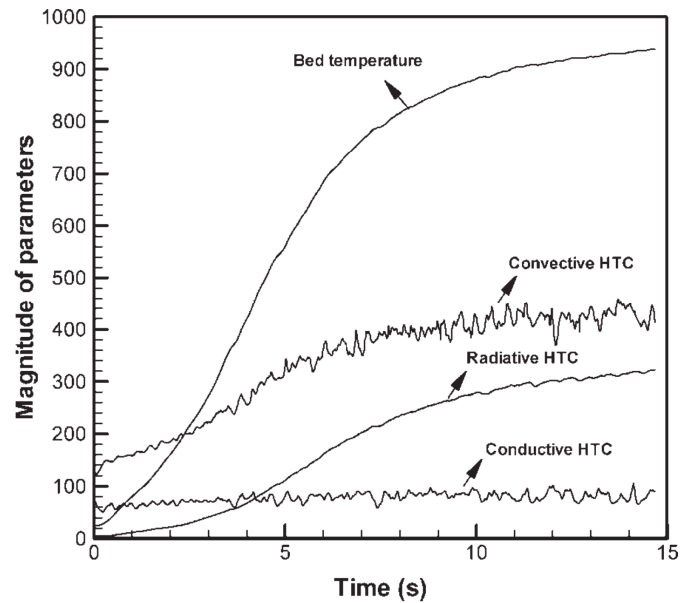


Figure 17: Thermal behavior of bed particles under the condition of gas inlet temperature 1,000°C, and superficial velocity 3.2 m/s [70]

The variable “Magnitude of parameters” is in case of the bed temperature the temperature in K and in case of convective, radiative and conductive heat transfer the HTC. The results indicate that the HTC by radiation increase with time due to the increase of bed temperature. Again, for low bed temperature values the radiation HTC plays a minor role in the overall heat transfer. The conductive HTC is nearly constant over time and therefore insensitive to an increasing bed temperature. Zhou et al. [70] explained the increase in the convective HTC as a consequence of a variation of the gas properties with temperature. The influence of the particle thermal conductivity is presented in fig. 18.

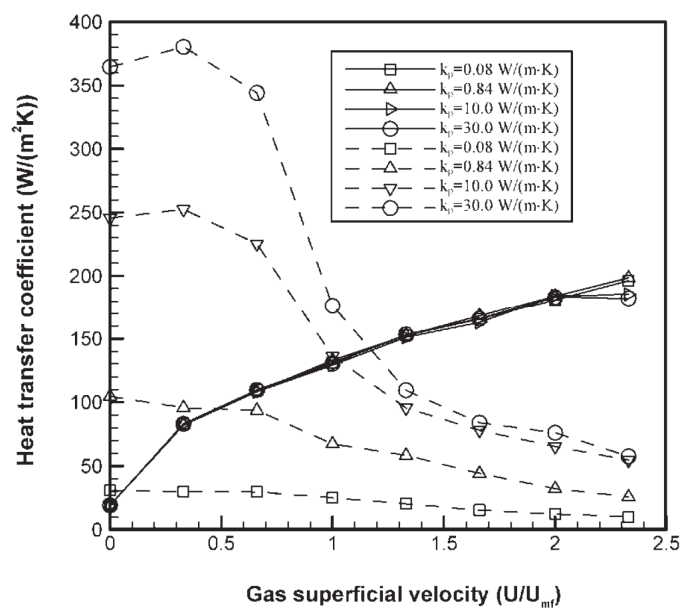


Figure 18: Cooling of a hot sphere in a fluidized bed system [73] with different particle conductivities. Solid line is the heat transfer coefficient due to convection and dashed line due to conduction [70]

In contrast to figs. 16 and 17, fig. 18 considers the cooling of one sphere of nine to that system additionally added approximately 200°C hot spheres. As the system is cooled down and no temperature value is over 500°C, radiation is not analyzed here. Independent of the used particle conductivity, the HTC by conduction decreases and the HTC by convection increases for increasing U/U_{mf} . No significant influences can be observed for a variation of the particle conductivity in case of the convective HTC. In opposite to that, the HTC by conduction increases for higher particle thermal conductivities, especially in the packed bed state ($U/U_{mf} < 1$). Here the overall heat transfer is mainly influenced by the HTC by conduction.

Based on the results of figs. 16 – 18 the considered heat transfer mechanisms of investigation V – VII are chosen. In study VI and VII systems with both low and high particle conductivities and a low superficial velocity $U/U_{mf} < 1$ are chosen. In accordance to fig. 18 the heat transfer mechanism by conduction or convection can be the dominating heat transfer mode. A detailed explanation of the implemented models and the state of the art for the heat transfer mechanism for heat transfer by contact conduction (see investigation V and VII) and convection (see investigation VI and VII) is given in chapter 6. The experimental and numerical setups in investigations VI and VII are always below an operating temperature of 500 °C. Therefore, no radiative heat transfer is considered in that studies. Nevertheless, study V provides an algorithm for particle-particle radiation which can be used for cases with high bed temperatures and a short description of the current research in literature is given in investigation V and in chapter 7. More important and relevant for many in this dissertation investigated systems is the intra particle heat transfer. In the following, solutions for solving intra particle heat transfer within the DEM and a more detailed explanation of the implemented 3D heat transfer model of investigation V-VII is discussed.

4.1 Inner particle heat transfer

In fig. 19 different degrees of detail for the description of the heat transfer within a particle are shown (spherical in fig. 19a and cubic shaped in fig. 19b).

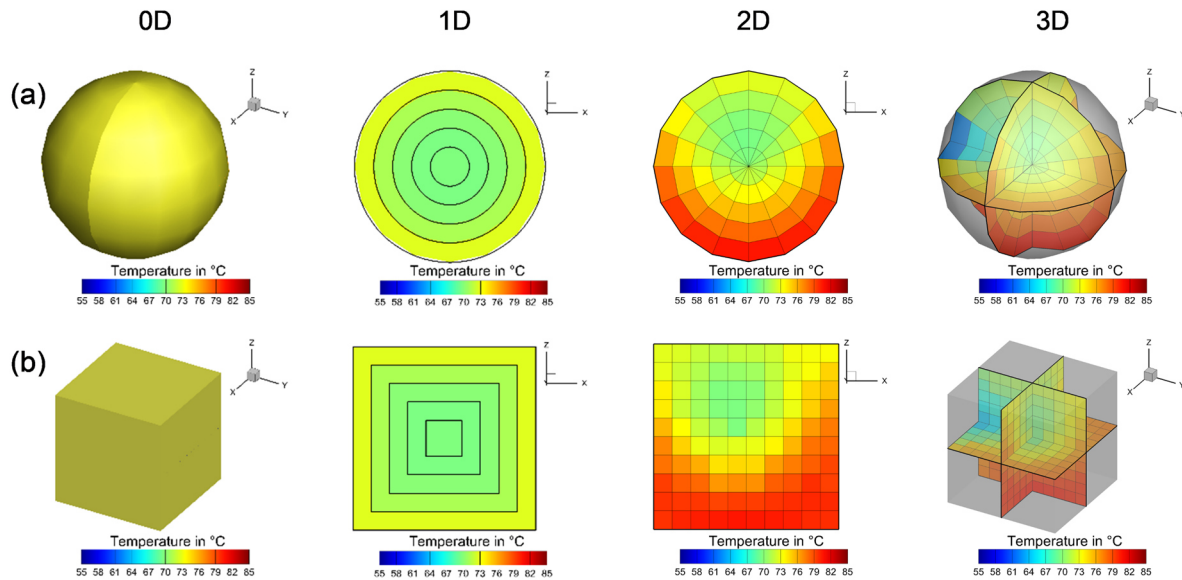


Figure 19: Different degrees of detail for the description of the heat transfer within a spherical particle (a) and arbitrary shaped particle (b).

The simplest form for solving heat transfer within a DEM particle is the 0-dimensional form also known as lumped capacity approach (for more details see investigations V and VII) which means that only one mean temperature value is considered per particle. The drawback of this method is that it can be only used for systems where the temperature distribution within the particle is uniform. If convection is considered this is fulfilled when particles with small Biot numbers $Bi = hL/k \ll 1$ are used. The Biot number is defined as the ratio of the convective heat transfer h , the particle characteristic length L and the thermal conductivity k of the particle. To describe a non-uniform temperature distribution within one particle simple 1D heat transfer models [156,208,260,291,298] or more detailed 2D or 3D heat transfer models [223,268,269] must be considered. Simple 1D heat transfer models are easy to implement and faster than multidimensional models. However, these models are limited to a uniform imposed heat flux such as a constant heat flux due to a constant heat coefficient over the particle surface. For a 3D description of the heat transfer due to a contact of two solids and for imposing a local varying heat transfer coefficient a 3D model is needed as the local imposed heat fluxes can vary in space and time.

The three-dimensional temperature field within a particle can be expressed by the heat equation (here in spherical coordinates) with constant properties and no internal heat generation [274] as follows

$$\frac{1}{\alpha} \frac{\partial T}{\partial t} = \frac{\partial^2 T}{\partial r^2} + \frac{1}{r} \frac{\partial T}{\partial r} + \frac{1}{r^2 \sin \theta} \frac{\partial}{\partial \theta} \left(\sin \theta \frac{\partial T}{\partial \theta} \right) + \frac{1}{r^2 \sin^2 \theta} \frac{\partial^2 T}{\partial \phi^2} \quad (40)$$

where $\alpha = k / (\rho c_p)$ is the thermal diffusivity with the particle thermal conductivity k , density ρ and particle specific heat capacity c_p , t is the solution time, T is the node temperature and r , θ and ϕ are the spherical coordinates in radial, polar and azimuthal directions. Eq. 40 can only be analytically solved in single cases such as a one-dimensional heat transfer problem with constant properties and a specific convection boundary condition [74]. To obtain a general solution this equation must be solved numerically [75]. For this purpose, the work of Özisik [76] provides several finite-difference schemes which are applicable for the general numerical solution of eq. 40. The provided schemes [76] are usually simpler to formulate than finite volume or finite element schemes, are of good accuracy [77] and allow geometric flexibility through the usage of different numerical grid generation techniques. To solve eq. 40 by a finite difference scheme, it must be first decided if the differential equation should be solved implicitly or explicitly. Both possibilities are shown in fig. 20 for a simple 1D temperature problem.

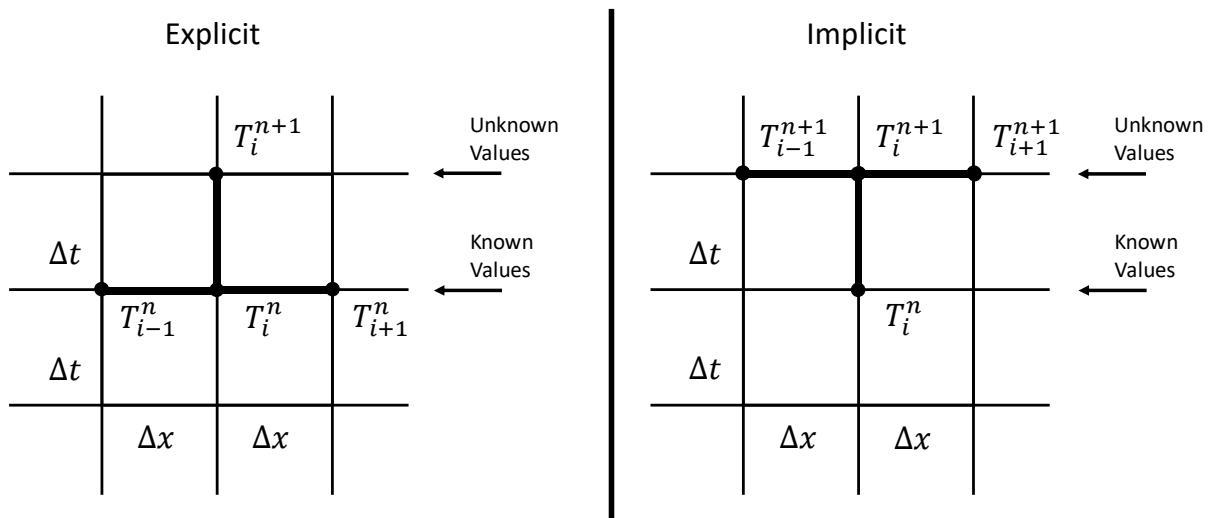


Figure 20: Comparison between simple explicit and simple implicit scheme for the finite difference method [76].

In this example the aim of both schemes is to solve the node temperature of the next time step T_i^{n+1} . In case of the simple explicit scheme this is achieved by using the current node temperature T_i^n and the respective neighbor temperature nodes T_{i-1}^n and T_{i+1}^n . The advantage of the explicit scheme is that this formulation provides an algebraic relation with an equal number of knowns and unknowns which can be directly solved if all boundary conditions are known. However, to obtain meaningful results like a nondivergent or a nonoscillatory solution following restriction must be fulfilled [76]

$$\left(\frac{\alpha\Delta t}{(\Delta r)^2} + \frac{\alpha\Delta t}{(\Delta\theta)^2} + \frac{\alpha\Delta t}{(\Delta\phi)^2}\right) \leq \frac{1}{2} \quad (3D \text{ heat transfer in spherical coordinates}), \quad (41)$$

where Δt is the used time step and Δr , $\Delta\theta$ and $\Delta\phi$ are the grid distances between two nodes. Because of this stability criterion, the maximum size of the time step is restricted. Especially in 3D cases where three terms instead of one (1D heat transfer) influence the stability often small-time steps Δt are required which may increase the computational time significantly. An alternative method which is unconditionally stable for all time and space intervals is the simple implicit method [68]. Here the temperature node T_i^{n+1} is determined by using the unknown neighbor values $T_{i-1}^{n+1}, T_{i+1}^{n+1}$ of the next time step and the known value T_i^n . The scheme is referred implicit as the equations of the nodal temperatures of each time level are simultaneously solved [76]. Under the assumption that the heat transfer problem provides M unknown node temperatures, the simultaneously solving of M unknown temperatures is more complex than the directly calculation of each equation by using the explicit scheme. Nevertheless, as the implicit scheme is unconditionally stable, the time step for solving the heat transfer within the particle can be chosen often higher than for the explicit scheme to save computational effort. This reduction in computational time is often only accompanied with a little loss in accuracy [68]. Due to the opportunity of choosing a high time step, the time step of the implicit scheme is chosen independent of the mechanical DEM time step, which allows a further reduction of the computational effort in certain cases. Therefore, the implemented 3D model for investigations V-VII is derived by an implicit finite difference scheme. However, it should be noted that the value for Δt cannot be too high to obtain a sufficient accuracy. Beside the simple explicit and implicit scheme other finite differences scheme such as the Crank-Nicolson, combined or three-time level scheme exist which combine the accuracy of the explicit and the stability of the implicit scheme [76]. However, this additionally schemes are way more complex than the simple methods for the integration of three-dimensional heat transfer as the equation contain more variables. Especially in cases with a high number of nodes more storage and simulation time are required to solve all nodal temperatures. Therefore, these schemes are not integrated into the DEM. The numerical derivation of eq. 40 is exemplary shown in the following section.

4.2 Numerical approximation of the heat transfer equation in spherical coordinates

For the sake of clarity eq. 40 is rearranged as in [76]

$$\frac{1}{\alpha} \frac{\partial T}{\partial t} = \frac{\partial^2 T}{\partial r^2} + \frac{2}{r} \frac{\partial T}{\partial r} + \frac{1}{r^2} \frac{\partial^2 T}{\partial \theta^2} + \frac{\cot \theta}{r^2} \frac{\partial T}{\partial \theta} + \frac{1}{r^2 \sin^2 \theta} \frac{\partial^2 T}{\partial \phi^2}, \quad (42)$$

where $T \equiv T(r, \theta, \phi)$, $0 \leq r \leq b$, $0 \leq \theta \leq \pi$, $0 \leq \phi \leq 2\pi$. In addition to that, it is defined that the distance between two nodes is always equidistant. The derivatives of eq. 42 can be approximated by a Taylor series expansion which can be also used non-equidistant grid distances [76]. The time or space derivative $\partial T / \partial \tau$ is discretized at the next time step ($n+1$) with a first-order accurate forward differencing formula as

$$\left. \frac{\partial T}{\partial \tau} \right|_{i,n+1} = \frac{T_i^{n+1} - T_i^{n+1}}{d\tau} + O(\Delta\tau), \quad \text{with } \tau = t, r, \theta \quad (43)$$

and a second-order accurate central difference formula for the space derivative

$$\left. \frac{\partial^2 T}{\partial \delta^2} \right|_{i,n+1} = \frac{T_{i-1}^{n+1} - 2T_i^{n+1} + T_{i+1}^{n+1}}{d\delta^2} + O[(\Delta\delta)^2], \quad \text{with } \delta = r, \theta, \phi. \quad (44)$$

The “order of” notations “ $O(\Delta\tau)$ ” and “ $O[(\Delta\delta)^2]$ ” describe the truncation error by the finite difference approximation. In easier words this error characterizes the difference between the derivative and its finite-difference representation which is in case of $O(\Delta\tau)$ [76]

$$O(\Delta\tau) = \frac{\Delta\tau}{2} T''(\tau_0) + \frac{(\Delta\tau)^2}{6} T'''(\tau_0) + \dots, \quad (45)$$

and in case of $O[(\Delta\delta)^2]$

$$O[(\Delta\delta)^2] = \frac{(\Delta\delta)^2}{12} T''''(\delta_0) + \dots \quad (46)$$

The derived numerical equations are valid for all nodes in the region $0 < r < M$ where 0 is the center of mass of the sphere and M the particle surface where boundary conditions are prescribed. The problem of eq. 42 is that it has an apparent singularity at $r = 0$ as the center of T_0 holds no explicit neighborhood relationship like the remaining nodes (more than six neighbors are possible). To account for this singularity in the calculation of the next temperature

T_0^{n+1} eq. 42 is replaced only for the location $r = 0$ (for $r \neq 0$ the equation is not replaced) by the Cartesian formulation as in the 2D example in the work of Özisik [76]

$$\frac{1}{\alpha} \frac{\partial T}{\partial t} = \nabla^2 T(r, \theta, \phi) \quad \text{where } \nabla^2 T = \frac{\partial^2 T}{\partial x^2} + \frac{\partial^2 T}{\partial y^2} + \frac{\partial^2 T}{\partial z^2} \text{ for } r = 0. \quad (47)$$

In a next step, for the approximation of $\nabla^2 T$ all temperature nodes T^{n+1} for $r = 1$ are taken to calculate the temperature at the origin T_0^{n+1} (for $r = 0$)

$$\nabla^2 T|_{r=0} = \frac{\sum_{i=1}^m \sum_{j=1}^n (T^{n+1}(r = 1, \theta_i, \phi_j) - T_0^{n+1})}{(\Delta r)^2} + 0[(\Delta r)^2], \quad (48)$$

where m and n are the total number of nodes in θ and ϕ direction. Beside the origin region T_0 an additional relation for all nodes lying on the particle surface at $r = M$ must be formulated to consider the different heat transfer mechanism acting on a particle. In this dissertation boundary conditions of second and third kind are used. Due to specific convention of the spherical coordinates, only boundary conditions in radial direction must be accounted for. Similar as described in the work of Özisik [76] a fictitious node outside of the particle at $M + 1$ is generated to allow the usage of a second-order accurate central-difference approach. As boundary conditions can only appear in radial direction, this problem can be illustrated with a simple radial 1D example, see fig. 21.

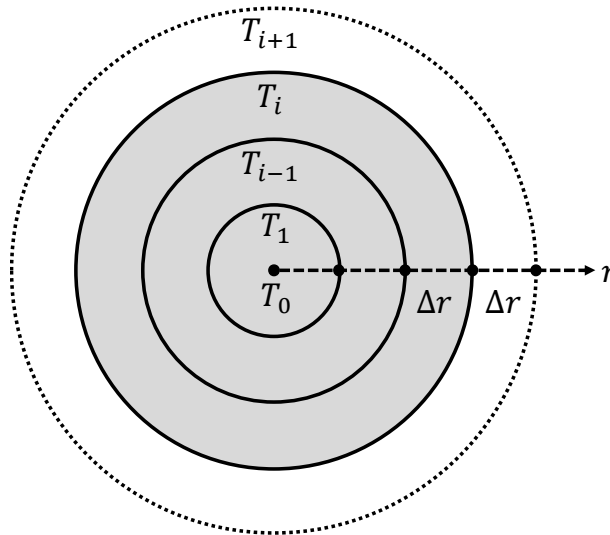


Figure 21: Fictitious node $i + 1$ at fictitious temperature T_{i+1}^{n+1} according to [76]

In the shown example each node is represented by a circle and all circles hold the same distance Δr . Circles inside the particle are represented by a dashed line whereas the fictitious

node T_{i+1} is represented by a dotted circle. For the calculation of particle-fluid convection, the Robin boundary condition (third kind) is taken

$$k \frac{\partial T}{\partial r} + hT_i = hT_{\infty,B} = \text{Known}, \quad (49)$$

where T_i is the boundary node temperature, T_{∞} is the ambient fluid temperature and h is the local heat transfer coefficient (calculated by distribution function, see investigation VI and VII) between particle and fluid. With the formulation of a fictitious node T_{i+1} eq. 49 can be approximated by finite difference as follows

$$k \frac{T_{i+1}^{n+1} - T_{i-1}^{n+1}}{2dr} + hT_{i+1}^n + 0[(\Delta r)^2] = hT_{\infty}. \quad (50)$$

For the calculated heat fluxes resulting out of radiation and conduction heat transfer between two bodies, the Neumann boundary condition (second kind) is used

$$k \frac{\partial T}{\partial r} = q_B = \text{Known}. \quad (51)$$

with the respective implicit finite difference approximation

$$k \frac{T_{i+1}^{n+1} - T_{i-1}^{n+1}}{2dr} + 0[(\Delta r)^2] = q_B, \quad (52)$$

where q_B describes the imposed heat flux. After considering all relations of eqs. 42-52 the heat transfer problem involves n equations with an equal number of unknown temperature nodes T_i^{n+1} and known temperature nodes T_i^n . To solve this set of equations simultaneously the heat transfer problem can be expressed as a linear set of equations [68]

$$[A][T] = [C], \quad (53)$$

where $[T]$ is the vector of all unknown temperature values T_i^{n+1} and $[C]$ the term which contains all numerical values of the nodal temperatures T_i^n (both hold the length M). The $M \times M$ coefficient matrix $[A]$ involves the relationship between all nodes in the following form

$$[A] = \begin{pmatrix}
 1 & 2 & 2 & 2 & 2 & \dots & 0 & 0 & 0 & 0 & 0 \\
 0 & 3 & 2 & 2 & 2 & & 0 & 0 & 0 & 0 & 0 \\
 0 & 2 & 3 & 2 & 2 & & 0 & 0 & 0 & 0 & 0 \\
 0 & 2 & 2 & 3 & 2 & & 0 & 0 & 0 & 0 & 0 \\
 0 & 2 & 2 & 2 & 3 & & 0 & 0 & 0 & 0 & 0 \\
 \vdots & & & & & \ddots & & & & & \\
 0 & 0 & 0 & 0 & 0 & & 4 & 0 & 0 & 0 & 2 \\
 0 & 0 & 0 & 0 & 0 & & 0 & 4 & 2 & 2 & 2 \\
 0 & 0 & 0 & 0 & 0 & & 0 & 2 & 4 & 2 & 2 \\
 0 & 0 & 0 & 0 & 0 & & 0 & 2 & 2 & 4 & 2 \\
 0 & 0 & 0 & 0 & 0 & & 2 & 2 & 2 & 2 & 4
 \end{pmatrix} \quad \text{where} \quad \begin{array}{l}
 1 = \textit{origin node} \\
 2 = \textit{neighbor node} \\
 3 = \textit{inner node} \\
 4 = \textit{boundary node}
 \end{array} \quad (54)$$

In this example the number of shells is $r = 4$, $\Delta\theta = \pi/4$ and $\Delta\phi = 2\pi/8$. For the solution of eq. 53 direct and iterative methods for finding an inverse matrix $[A]^{-1}$ can be used [78]. Typical direct method for solving a linear set of equations are the Gaussian, Gaussian-Jacobi elimination, Cholesky and QR decomposition [78,79]. All direct methods have in common that they provide an exact solution of eq. 53. However, direct procedures are rarely used for solving huge linear sets of equation as they are not able to consider the specific shape of the coefficient matrix $[A]$ in an efficient way. As can be seen in eq. 54 $[A]$ contains many zero values (up to 99 % [78], here $\sim 80\%$ of all coefficients) which are not needed for solving the linear set of equations. Direct procedures use the whole matrix with zero values which may exceed the available disk space. In addition to that, a huge matrix solved by direct methods often result in high unacceptable computation times. Meister [78] demonstrated that the calculation of a $M \times M$ Matrix with $M = 1000$ takes five minutes and 30 seconds when the Gaussian elimination method is used and one multiplication or division takes 10^{-6} seconds. In opposite to that, indirect algorithms are a suitable solution for solving linear sets of equations with a huge coefficient matrix. In general, iterative algorithms find a numerical approximated solution for the exact solution of $[A]^{-1}[C]$. A numerical approximation of eq. 53 decreases the computation time significantly and is often sufficient if the numerical error is in the same order as the numerical error made by the numerical approximation of eq. 42. To provide acceptable computational times the iterative Biconjugate gradient stabilized method (BI-CGSTAB) [80] is used. The big advantage of this algorithm in opposite to others such as the Conjugate Gradients-Squared (CG-S) is that it provides a smooth convergence behavior. In contrast to direct approaches the BI-CGSTAB allows the usage of a so called row-indexed sparse storage mode [79]. Within this scheme only about two times of the number of nonzero matrix elements of eq. 54 must be stored which reduced the required storage for saving the coefficient matrix rapidly (in eq. 54 about approximately $\sim 60\%$ less storage requirement). To explain the row-indexed sparse storage mode scheme a simple $M \times M$ matrix with $M = 5$, zero and nonzero values is considered [79]

$$[A] = \begin{pmatrix} 3 & 0 & 1 & 0 & 0 \\ 0 & 4 & 0 & 0 & 0 \\ 0 & 7 & 5 & 9 & 2 \\ 0 & 0 & 0 & 0 & 2 \\ 0 & 0 & 0 & 6 & 5 \end{pmatrix}. \quad (55)$$

This simple coefficient matrix is represented within the row-indexed sparse storage mode by two rows called *sa* (real values) and *ija* (integer values), see table 4. Following storage rules are counting:

1. In a first step all diagonal matrix values are stored for *sa* in a chronological order, in this example $k = 1 - 5$. Note that here also nonzero diagonal values are stored (here for the $k = 4$) which is one drawback of this method. Nevertheless, in typical heat transfer problems all diagonal matrix values are nonzero.
2. The next value for $sa(M + 1)$ is an arbitrary value, here referred as x .
3. In a next step all nonzero values are stored in *sa*, ordered by rows and within one row by columns
4. After filling the *sa* row, the index k of the first off-diagonal value of each row is stored for *ija*. If all off-diagonal values of one row are zero, $ija(k)$ is one greater than the previous $ija(k - 1)$ value.
5. The first value for $ija(k = 1)$ is always $M + 2$.
6. At $ija(k = M + 1)$, *ija* is always one value greater than the index k of the last off-diagonal value.
7. The remaining $ija(M + 2)$ values correspond to the respective column in the coefficient matrix.

The final resulting sparse matrix for eq. 55 is shown in table 4. The indexed storage of the sparse matrix is optimized for the single multiplication with a vector and therefore suitable for use in the BI-CGSTAB algorithm [78,79].

Table 4: Indexed storage of sparse matrix, exemplary shown for eq. 55 [79]

<i>index k</i>	1	2	3	4	5	6	7	8	9	10	11
<i>ija(k)</i>	7	8	8	10	11	12	3	2	4	5	4
<i>sa(k)</i>	3	4	5	0	5	x	1	7	9	2	6

The approximation of the heat equation in a Cartesian formulation is analogous to the described procedure except of two differences. Firstly, no singularity occurs for the Cartesian formulation, so that all nodes within the particle can be approximated by a central difference

and forward difference formula. Secondly, boundary conditions can appear in all three directions (x , y , z) which must be considered during the approximation.

So far, all chapters concentrated on the description of the relevant models and methods regarding DEM simulations. However, in all investigations the CFD is coupled with the DEM to describe the particle-fluid interaction force, the particle-fluid convective heat transfer or the particle-wall heat transfer by conduction. In addition to that both the fluid movement and the intra wall heat transfer are described on the CFD side. Therefore, the coupling algorithm is described, and all relevant equations are given in the next chapter.

5. CFD-DEM approach with relevant CFD equations

As described previously the CFD-DEM approach is used in all considered investigations. The DEM calculates the particle motion, particle-fluid interaction and all heat transfer mechanisms acting on a particle. In contrast to that, the description of the fluid phase and the heat transfer through a solid (wall) region is represented by the CFD. As CFD software the commercial package ANSYS Fluent is used. The implemented coupling algorithm for the exchange of all relevant data between CFD and DEM (when mechanical particle-fluid interaction and heat transfer by convection is considered) is exemplary demonstrated in fig. 22. An explanation for setting the heat flux resulting out of particle-wall heat transfer by conduction can be found in investigation VII. To describe the exchange accurately three different grids named DEM grid, transfer grid and CFD grid are used. First the porosity is calculated on the DEM grid which size is larger than the largest particle within the DEM. A detailed explanation about the porosity calculation and the underlying algorithm is given in investigation II. DEM cells which lie inside a particle (colored blue) obtain a porosity of $\varepsilon < 1$ whereas cells which lie outside hold a porosity value of $\varepsilon = 1$ (colored white). Instead of the calculation as a cell-based value, the particle velocity v_p and particle fluid friction coefficient β are determined per particle. When intra particle 3D heat transfer with convection boundary condition is considered, the respective surfaces A_N , temperatures T_N and the heat transfer coefficients α_N are transferred to the corresponding transfer cell of the temperature node lying on the particle surface. As the CFD environment provides different mesh types such as structured or unstructured meshes and the CFD cells must not correspond in space with the DEM grid an additional transfer grid finer than the DEM and CFD grid is used. The transfer grid whose cells are sub cells of the DEM grid is used to assign and coordinate the corresponding DEM properties to the CFD and vice versa. The DEM properties are differently written on the transfer grid based on the data type (cell based, particle based, or node based). As the transfer grid cells are sub cells of the DEM grid, cell-based values are directly set to the linked transfer grid cells which are lying in one DEM cell. In opposite to that, particle-based values are assigned to that sub cells whose cell centers are lying in one particle. When one sub cell lies in more than one particle, the particle-based values are averaged over the number of particles (referred as $\bar{\beta}$ or \bar{v}_p). The temperature node-based values are directly written to the corresponding transfer cell and are summed if more than one node lies inside one transfer cell. To transfer the DEM data onto the transfer grid to the CFD, a transfer grid cell is linked to one CFD cell if the transfer grid cell center is lying in that CFD cell. In a next step, all nonzero particle-based and cell-based values of the transfer grid cells in one CFD cell are averaged to one value and then written to that CFD cell. In contrast to that, the node-based values onto one transfer grid are summed to the corresponding CFD cell. The DEM information are considered within the Navier-Stokes equations and energy equations in the solid (wall) and fluid region as source terms to calculate the kinematic

and thermodynamic properties of the next time step. The new obtained values for the fluid properties (velocity u_f , density ρ_f dynamic viscosity η_f and temperature T_f) and the wall temperature T_s are then written to the linked transfer grid cells (exemplary colored green and golden). Finally, all CFD values onto the transfer grid cells lying in one DEM cell are read by the DEM and averaged to one DEM cell-based value to consider the surrounding fluid or the contacting wall. This procedure is repeated every coupling time step which is commonly taken 100 times larger than the mechanical DEM time step in each investigation. The connection between transfer grid and CFD cells must only be updated every coupling iteration when the CFD mesh is moved such as for the rotating drum in investigation VII.

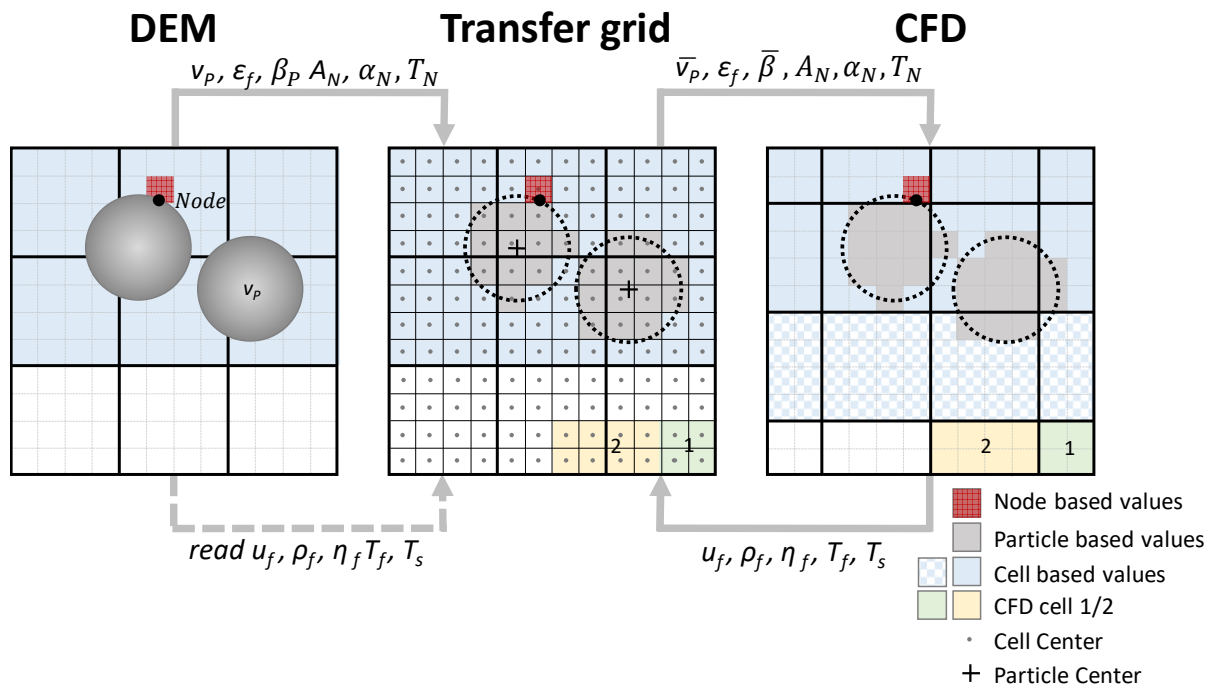


Figure 22: Transfer grid for the coupling of the DEM and CFD including heat transfer and particle-fluid force interaction, according to [81]

All CFD equations relevant for the CFD-DEM approach are listed in table 5. Most equations are explained in the considered investigations such as the energy transport equation (solid region) in investigation VII or the equations of continuity and momentum in investigation I – IV. No detailed description is given for the energy equation of the fluid phase. Therefore, this part concentrates on the explanation of this equation. The energy transport equation of the fluid phase is relevant for all particle systems with a surrounding fluid where the convective heat transfer mechanism is utilized (investigation VI and VII). Within the energy equation the first three terms on the right-hand side describe the energy transport by conduction, species diffusion and viscous dissipation, respectively [82]. In the CFD-DEM framework the viscous dissipation term is neglected as the Brinkman number is below 1 ($Br \ll 1$) with $Br \approx 2.22E - 05$ for all investigations. The Brinkman number is defined by

$$Br = \frac{\mu_f u_f^2}{k_f \Delta T}, \quad (56)$$

with the dynamic viscosity μ_f , the fluid velocity, thermal conductivity k_f and the wall-fluid temperature difference ΔT . The remaining variables of the energy transport equation are the total Energy E , the fluid density ρ_f , the local pressure p , the effective thermal conductivity k_{eff} , the diffusion flux of species \vec{J}_j , the energy source term S_h and the fluid viscous stress tensor $\bar{\tau}$.

Table 5: Relevant CFD equations for the CFD-DEM approach

Solid phase	Fluid phase
Energy transport equation:	Equation of continuity:
$\frac{\partial}{\partial t}(\rho h) + \nabla(\vec{v}(\rho h)) = \nabla(k\nabla T) + S_h$	$\frac{\partial(\varepsilon_f \rho_f)}{\partial t} + \nabla(\varepsilon_f \rho_f \vec{u}) = 0$
Energy source term:	Equation of momentum:
$S_h = \frac{\dot{Q}}{V}$	$\frac{\partial(\varepsilon_f \rho_f \vec{u})}{\partial t} + \nabla(\varepsilon_f \rho_f \vec{u} \vec{u}) = -\varepsilon_f \nabla p + \nabla(\bar{\varepsilon}_f \bar{\tau}) + \varepsilon_f \rho_f \vec{g} + \vec{f}_{int}$
	Fluid viscous stress tensor:
	$\bar{\tau} = \eta_e [(\nabla \vec{u}_f) + (\nabla \vec{u}_f)^{-1}]$
	Volumetric momentum source term:
	$f_{int_j} = \bar{\beta}_j (u_j - \bar{v}_j)$
	Energy transport equation:
	$\frac{\partial}{\partial t}(\rho_f E) + \nabla(\vec{u}_f(\rho_f E + p)) = \nabla \left(k_{eff} \nabla T - \sum_j h_j \vec{J}_j + (\bar{\tau} \vec{u}_f) \right) + S_h$
	Energy source term:
	$S_h = \frac{\dot{Q}}{V} = \frac{\alpha_p A_p (T_p - T_f)}{V}$

6. Results and Publications

Additional information for investigation VI and VII: The Infrared camera (emissivity and transmission) is calibrated with an initial packed bed case where the packed bed was heated up to a constant temperature measured by thermocouples.

I. Numerical investigation of third body behavior in dry and wet environments under plane shearing

Christoph Pieper¹, Tobias Oschmann¹, Darius Markauskas¹, Andreas Kempf², Alfons Fischer³, Harald Kruggel-Emden^{1*}

¹Ruhr-Universitaet Bochum, Universitaetsstrasse 150, 44780 Bochum, Germany

²Universitaet Duisburg-Essen, Carl-Benz-Strasse 199, 47057 Duisburg, Germany

³Universitaet Duisburg-Essen, Lotharstrasse 1, 47057 Duisburg, Germany

*Corresponding author

Email: kruggel-emden@leat.rub.de, Tel.: 0049 234 32 27362, Fax: 0049 234 32 14 227

The following accepted manuscript appeared as journal version in "Pieper C., Oschmann T., Markauskas D., Kempf A., Fischer A., Kruggel-Emden H.: Numerical investigation of third body behavior in dry and wet environments under plane shearing, Chemical Engineering & Technology, 2015, Volume 39, 1497-1508. Copyright Wiley-VCH Verlag GmbH & Co. KGaA, Reproduced with permission." and may be found at <https://doi.org/10.1002/ceat.201500647>.

Abstract

This paper presents a coupled Discrete Element Method and Computational Fluid Dynamics (DEM-CFD) approach to model and assess third body behavior in dry and wet environments under plane shearing. DEM is used to model the granular media, while the fluid side of the system is simulated with CFD, which is based on the Finite Volume Method. The applied model is extended to consider buoyancy as well as lubrication effects. The third body is confined and compressed between two walls which are sheared in opposite direction with a constant velocity. The influence of different shear velocities, fluid viscosities and gravity orientations on particle and fluid rheology is investigated. Obtained results of both dry and lubricated systems are compared regarding velocity and porosity distribution across the gap, sliding friction and particle interaction.

Keywords: DEM-CFD, lubrication force, sliding friction, third body, tribology

1. Introduction

Over the past 15 years the perception of mixed friction and wear has changed enormously [83]. High-resolution experiments at very low wear rates (below 10 nm/h) and high-resolution computer simulations have shown that a 10-100 nm thin layer can form from wear particles,

components of the lubricant and the ambient medium [84–90]. This particle layer was already described in the 1970s and 1980s by Play and Godet [91,92] and is now called "tribomaterial". The "Tribomaterial" develops under extreme plastic deformation of the near-surface solid-body layers with the formation of nano-/microscopic structures (nano-/microcrystals). In the contact area one can distinguish an entrance and exit zone, with different roughness and a spatial expansion that is highly dependent on the contact geometry. The nano-/microscopic wear particles are formed over the entire contact zone. The particles are then channeled towards the exit zone where they often concentrate; the size of the outlet zone correlates with the imposed load [91]. Depending on the considered application, the contact zone features the phenomena of, - adhesion, abrasion, surface disruption, tribochemical reactions, turbulent transport of the detached wear particles - and subsequently, the mixing of possible intermediate materials (for example oil, pseudosynovial fluid, impurities) and the ambient medium (e.g. combustion residues, salts) [84–89].

Through the formation of the tribomaterial a new nanostructured metal-organic composite is created. This tribomaterial separates the moving solids and balances the displacement of surfaces by high shear rates, resulting in the desired very small wear rates (e.g. for hip joint prostheses, cogwheels, or piston rings).

The emergence and behavior of tribomaterials in simplified systems has already been described with Molecular Dynamic Simulations (MD) and was verified in experiments [83,93,94]. The MD simulations are capable of showing the different behavior of dry and lubricated contacts on small spatial and temporal scales. For dry contacts, e.g. for tungsten/tungsten-carbide-contact pairs, material transfer was detected in a nanoscopic range. This does not occur in lubricated systems, resulting in a significantly lower force required for the relative movement of the contact partners [94]. These results were also confirmed for pairings of tungsten and diamond-like carbon [93].

Despite these successes with MD simulations, the long-term behavior (time scales beyond pico seconds) and the properties of the tribomaterials on the multiple-particle scale (larger than a few nano meter) are still unknown. Due to the importance of durable lubricated tribosystems, further research from the particle technology perspective is of great importance and promises considerable progress in the fields of mechanical engineering, manufacturing and medical technology and beyond.

Due to the MD simulations limitation to the smallest length and timescales, alternative numerical approaches are required that provide insight into the tribomaterial even under load and in conditions with difficult experimental access. Adequate simulation approaches consider the viscous flow of the particle-laden fluid, taking account of the particle interaction. This can be achieved by the coupling of Computational Fluid Dynamics (CFD) with the Discrete Element Method (DEM), which describes the microscopic and nanoscopic particles [8,95,96].

The Discrete Element Method (DEM) is a Lagrangian description form [97] to investigate the dynamic behavior of particulate systems numerically. Single particles are typically assumed to be spherical as this simplifies their contact detection and reduces the runtime [23]. The focus of previous DEM studies regarding wear in tribological systems, consisting of two bodies in contact and the tribomaterial as third body, was mostly limited to dry contacts, and did not require a DEM-CFD coupling.

The earliest numerical DEM studies of tribological systems were conducted by Elrod & Brewe [98] in 1991. They investigated the behavior of tribomaterials under shear stress between two parallel moving roughened plates. The simulations were carried out in 2D and showed important aspects of the motion of the tribomaterial, including coagulation, velocity- and stress distributions. The work of Ghaouti et al. [99] aimed in a similar direction for the shear strain of tribological systems under controlled stress and expansion. As the two contact surfaces were also modelled with DEM particles, it was possible to simulate the actual wear process for the first time. Based on this work [98,99] the influence of the chosen contact force model, adhesive forces and particle size was investigated by Seve et al. [100] and Iordanoff et al. [101]. The simulated behavior of the third body was also observed in experiments, but difficulties were encountered when deriving a quantitative description of the material parameters [101].

The actual initial formation of the tribomaterial and the dependencies of the process were shown for the first time in 2004 with DEM investigations. The studies confirmed the experimentally determined and often disregarded relationship between wear and friction [102].

Iordanoff et al. [103] observed different flow states of the granular material, which greatly affect the coefficient of friction on a macroscopic scale and depend on the adhesiveness of the tribomaterial. Qualitatively, these observations were in line with experimental observations. These theoretical investigations [98–103] were applied by Renouf et al. [104] to study rolling wear in wheel/rail configurations.

In recent times, coupled methods for describing wear in tribological systems are becoming increasingly popular. Apart from connecting the DEM to CFD as proposed here, the DEM can also be coupled with the Finite Element Method. The FEM and DEM domains can be spatially combined or the FEM can be used for the detailed description of the deformation, stresses and breakage of individual particles [105]. The DEM/FEM approach was firstly applied on sheared systems by Kabir et al. [106], who achieved a good agreement with pure DEM investigations, but at a much greater numerical complexity [106]. Further applications of the DEM by Tong et al. [107] investigated the influence of structured surfaces on cleavage wear and on erosion wear [108].

The influence of surface roughness in contact pairings was first investigated by Jerier and Molinari in DEM studies of the normal contact [109]. By a homogenization approach, the elastic properties of solids were modelled realistically and the relationship between load and resulting

contact surface described accordingly [109]. Lately, the coupling of FEM and DEM has been applied to simulate the contact partners of the tribological system with an FEM approach and the third body in a DEM framework [110–112]. Progress is also made in the experimental validation of DEM investigations: Payrebrune and Kröger [113] showed good agreement between numerical and experimental results for macroscopic particles.

While the most previously described simulations address dry contacts, there is much less research on tribological systems where the particles are surrounded by a fluid. Examples include the use of the DEM-CFD approach to model wear in pneumatic transport through pipe elbows [114], Couette flows in particle/fluid systems [115] or the interaction of structured surfaces with particle-laden flows [116].

The aim of the present study is to provide a first insight into the lubrication effect of particles in sheared systems through a coupled DEM-CFD approach, providing a basis for further investigation. As previous studies employing the DEM merely investigate dry tribological systems, combining the DEM with CFD is a first step towards understanding the impact of wet environments on the third body. Note that although particles in tribological systems are in the size of a few μm or even nm , deliberately larger sized particles are considered here to reduce the numerical stiffness of the system. Converting the investigated tribological system to smaller dimensions is planned in future research. The non-negligible influence of lubrication on particle collisions and therefore the employed contact model within the DEM has long been established [45,46,117–122]. For this reason the lubrication force model described by Tomac and Guitierrez [46] was incorporated into the DEM. In addition, a model for the shear rate dependent sliding friction coefficient [117,118] was included. To isolate the lubrication effects on the sheared system, the study and mostly neglects gravity. In specific cases where gravity is considered, the buoyancy force acting on the particles is also realized in the DEM [123].

It is however important to note that while DEM and DEM-CFD simulations are well applicable to tribological systems and can provide important insight into third body behavior of tribological systems, simplifications are made regarding particle size, shape and important interaction mechanisms. The obtained results are therefore of qualitative nature and merely provide a basis for further and more detailed investigation, cf. [96,101,113].

2. Methodology

This study focuses on the differences in the third body behavior in wet and dry particle systems. The particle motion is described with the Discrete Element Method (DEM), which is extended with a lubrication- and buoyancy force model for the wet system. The sliding friction coefficient acting between lubricated particle/particle and particle/wall collisions is also adjusted. The fluid side of the wet system is modelled with Computational Fluid Dynamics (CFD), which is coupled

with the DEM. Both governing equations of DEM and CFD are outlined in the following two subsections.

2.1 Discrete Element Method

In the employed Discrete Element Method, the translational and rotational motion of every particle is calculated with Newton's and Euler's equations of motion and can be written as

$$m_i \frac{d^2 \vec{x}_i}{dt^2} = \vec{F}_i^c + \vec{F}_i^{pf} + \vec{F}_i^g + \vec{F}_b + \vec{F}_l \quad (1)$$

$$\hat{I}_i \frac{d\vec{W}_i}{dt} + \vec{W}_i \times (\hat{I}_i \vec{W}_i) = \Lambda_i^{-1} \vec{M}_i, \quad (2)$$

where m_i is the particle mass, $d^2 \vec{x}_i / dt^2$ the particle acceleration, \vec{F}_i^c the contact force, \vec{F}_i^{pf} the particle/fluid force, \vec{F}_i^g the gravitational force, \vec{F}_b the buoyancy force and \vec{F}_l is the lubrication force. The second equation gives the angular acceleration $d\vec{W}_i / dt$ as a function of the angular velocity \vec{W}_i , the external moment resulting out of contact of particle/fluid forces \vec{M}_i , the inertia tensor along the principal axis \hat{I}_i and the rotation matrix converting a vector from the inertial into the body fixed frame Λ_i^{-1} .

The contact forces originating from particle/particle or particle/wall collisions are separated into a normal and tangential component. A linear spring damper model is used to obtain the normal component of the contact force

$$\vec{F}^n = k^n \delta \vec{n} + \gamma^n \vec{v}_{rel}^n, \quad (3)$$

with the spring stiffness k^n , the virtual overlap δ , the normal vector \vec{n} , the damping coefficient γ^n and the normal velocity in the contact point \vec{v}_{rel}^n [23]. The coefficients of normal restitution between particles e_{pp}^n and particles and walls e_{pw}^n together with the employed time step directly determine the spring stiffness k^n and the damping coefficient γ^n . A linear spring limited by the Coulomb condition is employed to calculate the tangential component of the contact force

$$\vec{F}^t = \min(k^t |\xi^t|, \mu_c |\vec{F}^n|) \vec{t}, \quad (4)$$

where k^t is the stiffness of a linear spring, μ_c is the friction coefficient in both wet and dry environment, ξ^t is the relative tangential displacement and \vec{t} is the tangential unit vector [25]. As values for the friction coefficient are different for lubricated and dry contacts, friction is addressed separately in the following.

To improve the representation of particle/particle and particle/wall collisions in lubricated environments, the corresponding friction coefficients are revised, which are usually experimentally obtained constant material dependent values. Joseph and Hunt [117] observed that the sliding

friction coefficient in submerged systems is lower compared to a dry environment, especially at low tangential velocities. A thin liquid layer between the particles prevents direct contact. With increasing shear rates a point is reached at which the rough particles lock with the fluid in the gap resulting in friction coefficients similar to those of dry systems. The coefficient of friction μ_c is directly related to the shear strain of the system $(\mu_0 |\vec{v}_{rel}^t| / r E^*)^{2/7}$. Here μ_0 is the dynamic viscosity at reference pressure, \vec{v}_{rel}^t the relative tangential velocity, r the mean particle radius and E^* the reduced modulus calculated from the Young's moduli E_1, E_2 and Poisson's ratios ν_1, ν_2 of the two bodies in contact

$$E^* = \left[\frac{1 - \nu_1^2}{E_1} + \frac{1 - \nu_2^2}{E_2} \right]^{-1}. \quad (5)$$

This correlation is shown in Fig. 1 for water and glycerol-water mixtures with viscosities of 0.001 Pa·s, 0.0025 Pa·s and 0.0045 Pa·s. The three plotted friction curves are described with polynomials which are incorporated into the DEM with two additional assumptions. First, if the shear strain surpasses the highest plotted value, the friction coefficient of the lubricated system is automatically assumed equal to that of a dry environment, namely $\mu_c = \mu_{dry} = 0.4$ in this study. Second, if the shear strain value drops below the lowest plotted value, the friction coefficient is assumed to be zero.

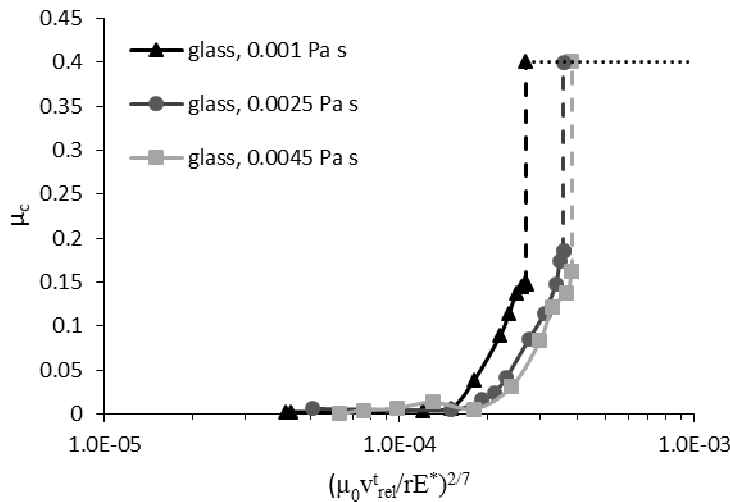


Fig. 1: Coefficient of sliding friction plotted against the shear strain of the system for glass particle-wall collisions in water and glycerol-water mixtures according to Joseph and Hunt [117].

2.1.1 Lubrication Force

The employed lubrication force model is based on the elasto-hydrodynamic theory, which was used to develop a theoretical two-particle collision model by Davis et al. [124]. Based on this

model Tomac and Gutierrez [45,46] conducted DEM-CFD simulations with a contact model that considers the fluid lubrication effects between two approaching particles.

When two particles approach each other in an incompressible fluid, the thin liquid layer between the particles acts like an additional damper in normal contact direction. The kinetic energy is dissipated and the relative particle velocity decreases. This effect intensifies the closer the particles move towards each other. The resulting lubrication force acting on the particle is defined as

$$F_l(t) = \frac{6\pi\mu r^2 |\vec{v}_{rel}^n|}{\delta}, \quad (6)$$

with the fluid dynamic viscosity μ , mean particle radius r , relative velocity of the two approaching particles \vec{v}_{rel}^n and the distance between particle surfaces δ . A sketch of the particle properties and variables required for its calculation is given in Fig. 2. The lubrication force is only calculated if two conditions are met. First, the distance between the particle surfaces δ has to be smaller than the mean radius of the two particles

$$\delta \leq \frac{r_1 + r_2}{2}. \quad (7)$$

This eliminates the possibility of a third particle influencing the process. The second condition is that δ has to be larger than the combined roughness of the two particles

$$\delta \geq 2\sigma_s, \quad (8)$$

as they follow the regular contact regime once they come into direct contact. If both conditions are met the lubrication force is added to the particle's equation of motion. Only the normal component of the contact force is affected by the lubrication force. The tangential component is treated as described in Eq. (4).

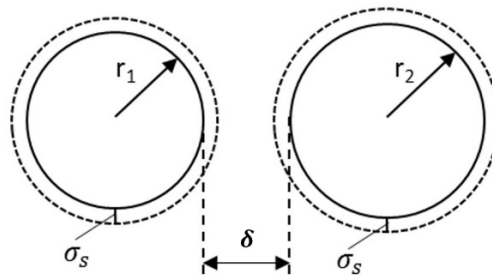


Fig. 2: Sketch of particle properties and variables required for lubrication force calculation.

2.1.2 Buoyancy Force

Buoyancy is a density-based force acting on an immersed particle in opposite direction to gravity. The following model is used in this study to account for this phenomenon (c.f. [123])

$$F_b = \frac{1}{6}\pi\rho_f d_p^3 g, \quad (9)$$

with the fluid density ρ_f , the particle diameter d_p , and gravitational acceleration g . The buoyancy force is added to the translational equation of motion, see Eq. (1).

2.2 Governing Equations of Fluid Dynamics

The fluid phase of the model is described with the commercial Computational Fluid Dynamics (CFD) software FLUENT, which is based on the Finite Volume Method. The domain is divided into equally large cubic cells, in which the mean fluid properties are calculated and then transferred to the DEM. The fluid flow around individual particles is not resolved. The governing equations of continuity (10) and momentum (11) are solved as follows:

$$\frac{\partial(\varepsilon_f \rho_f)}{\partial t} + \nabla(\varepsilon_f \rho_f \vec{u}_f) = 0, \quad (10)$$

$$\frac{\partial(\varepsilon_f \rho_f \vec{u}_f)}{\partial t} + \nabla(\varepsilon_f \rho_f \vec{u}_f \vec{u}_f) = -\varepsilon_f \nabla p + \nabla(\bar{\varepsilon}_f \bar{\tau}) + \varepsilon_f \rho_f \vec{g} + \vec{f}_{int}. \quad (11)$$

Here \vec{u}_f is the physical fluid velocity, ρ_f is the density, p is the pressure, \vec{f}_{int} is the volumetric particle/fluid interaction momentum source employed in each CFD cell, ε_f is the local fluid porosity and $\bar{\tau} = \mu [(\nabla \vec{u}_f) + (\nabla \vec{u}_f)^{-1}]$ is the fluid viscous stress tensor where μ is the effective dynamic viscosity calculated with a standard laminar model in this study. The particle interaction momentum \vec{f}_{int} is given component wise as $f_{int,j} = \bar{\beta}_j (u_{f,j} - \bar{v}_j)$, where \bar{v}_j is the fluid cell averaged particle velocity and $\bar{\beta}_j$ is the fluid cell averaged particle/fluid friction coefficient with $j=x, y, z$.

The particle/fluid force \vec{F}_i^{pf} consists of two main components, namely the drag force \vec{F}_i^d and the pressure gradient force $\vec{F}_i^{\nabla p}$, see Eq. (12). Numerous models are available for the calculation of these forces. The approach used in this study is the very popular model by Di Felice [42] which is given as

$$\vec{F}_i^{pf} = \vec{F}_i^d + \vec{F}_i^{\nabla p} = \frac{1}{2}\rho_f |\vec{u}_f - \vec{v}_i| C_D A_{\perp} \varepsilon_f^{1-\chi} (\vec{u}_f - \vec{v}_i), \quad (12)$$

with the drag coefficient C_D , the cross-sectional area perpendicular to the flow A_{\perp} and the correction factor χ . Eq. (12) can be rearranged to account for the particle/fluid friction coefficient $\vec{\beta}_i$ as follows

$$\vec{\beta}_i = \frac{1}{2} \rho_f C_D A_{\perp} \varepsilon_f |\vec{u}_f - \vec{v}_i| \left((1 - \varepsilon_f) \frac{1}{v_i} \varepsilon_f^{(1-\chi)} \right). \quad (13)$$

The correction factor χ is defined by the Reynolds-number $Re = \varepsilon_f \rho_f d_p |\vec{u}_f - \vec{v}_i| / \mu$ and written as

$$\chi = 3.7 - 0.65 \exp(- (1.5 - \log(Re))^2 / 2), \quad (14)$$

with the diameter of a spherical particle d_p and the fluid dynamic viscosity μ . There are different models available for the calculation of the drag force coefficient C_D , the one employed in this study is a correlation for spherical particles by Dallavalle [125] which reads

$$C_D = \left(0.63 + \frac{4.8}{\sqrt{Re}} \right)^2. \quad (15)$$

3. Numerical Setup and Operating Parameters

The examined system has a size of 0.09 x 0.03 x 0.078 m³. The third body is modelled with 1944 spheres, separated equally into three diameter size groups of 4.8 mm, 5.0 mm and 5.2 mm to reduce crystallization effects, resulting in an over-all porosity of $\bar{\varepsilon} = 0.3939$. The top, bottom and sides (in the X / Z plane) of the system are walls. The top and bottom wall can only move along the X-axis and are sheared in opposite directions with a constant velocity throughout the simulations. The side walls remain fixed and the coefficient of friction between wall and particle is $\mu = 0$ at all times. In order to simulate an infinite domain a periodic boundary condition is employed in X direction. This and other system properties are displayed in Fig. 3.

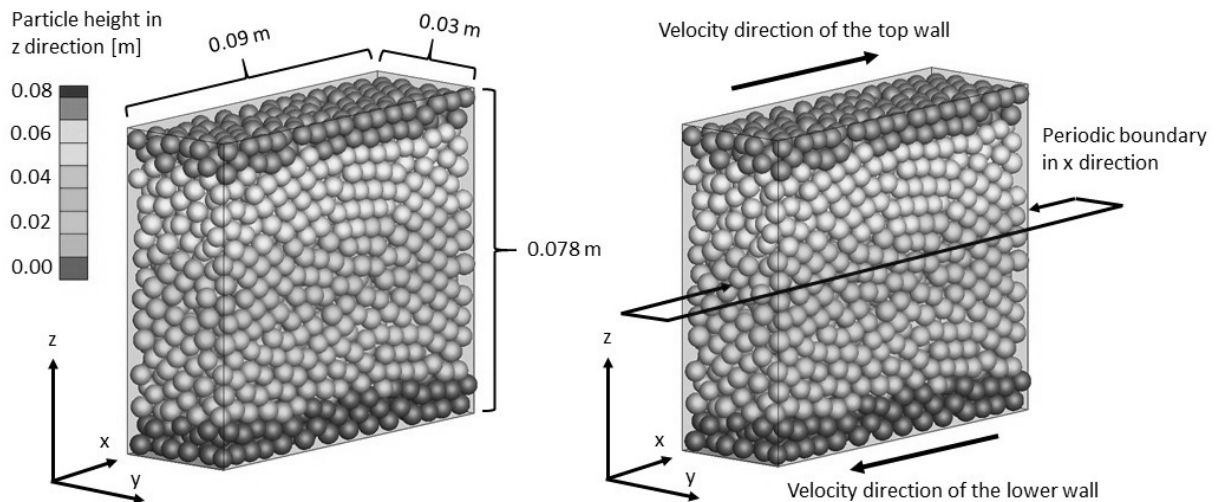


Fig. 3: Numerical setup and system properties.

The properties of the particles used in the simulations correspond to the rough glass particles used by Joseph et al. [126], their properties are shown in Tab. 1.

The system is split into equally large DEM and CFD cells, namely 15 in X direction, 5 in Y direction and 13 in Z direction, resulting in a total of 975 cubic cells with sides of 0.006 m. The CFD time step is set to $1 \cdot 10^{-3}$ s and the corresponding DEM time step to $1 \cdot 10^{-5}$ s. The coefficients of restitution between particles and particles and walls are the same and differ for wet and dry systems (see Tab. 1). The Coulomb friction coefficient μ_c between both particles and particles and walls is set to $\mu_c = 0.4$ for dry systems and automatically adjusted according to the relations shown in Fig. 1 for wet simulations. The spring stiffness k^n and k^t as well as the damping coefficient γ^n are calculated from the chosen time step and the coefficient of restitution. (Table 1)

Tab. 1 Particle properties including the particle diameter d_p , quantity n , volume V_p , density ρ_p , Young's modulus E , Poisson's ratio ν , the asperity height σ_s and the coefficient of restitution.

d_p [mm]	n [-]	V_p [m ³]	ρ_p [kgm ⁻³]	E [GPa]	ν [-]	σ_s [μm]	e [-]
4.8	648	5.80E-08	2540	60	0.23	0.1305	0.95
5.0	648	6.55E-08	2540	60	0.23	0.1305	0.95
5.2	648	7.36E-08	2540	60	0.23	0.1305	0.95

For the base case of the study the simulated fluid is a glycerol-water mixture, assumed incompressible with a density of 998.2 kgm⁻³ and a viscosity of 0.0025 Pa·s. A no slip condition is set between the fluid and the top/bottom wall and a free slip condition for the two side walls. Due to the low Reynolds number the flow is safely assumed to be laminar.

At the start of every simulation the particles are inserted and compressed until the required porosity is reached. Afterwards they have two seconds to settle until the top and bottom walls start to shear. The total simulation duration is 15 seconds. Sliding friction coefficients, particle and fluid velocities, porosity distribution and mean particle forces are investigated by varying operational and simulation parameters starting from a base case. In the wet base case the walls move into opposite directions with a speed of 0.1 ms⁻¹, gravity is not considered and the viscosity of the fluid is 0.0025 Pa·s. In the first simulation series, the strain rate is varied by altering the wall velocity to 0.4 ms⁻¹ and 0.05 ms⁻¹ for both the dry and wet system. The second simulation series investigates the influence of different viscosities (0.001 Pa·s and 0.0045 Pa·s). In the third and last series, the effect of gravity is examined, both in -Z and X direction for dry and wet systems. An overview of the investigated parameters is given by Tab. 2, where the bold font marks base case. All in all 7 simulations of the wet cases and five simulations of the corresponding dry case were conducted. (Table 2)

Tab. 2 Investigated operational and simulation parameters.

1. Wall shear velocities [ms ⁻¹]	2. Fluid viscosities [Pa·s]	3. Gravity orientation [-]
0.05	0.001	-Z direction

0.1	0.0025	Without gravity
0.4	0.0045	X direction

4. Results and Discussion

In the following section the results of the conducted simulation series are presented and analyzed. First the sliding friction coefficients between particles and walls are assessed, followed by the fluid and particle velocities. Furthermore, results of the porosity distribution and the findings of the mean particle forces are presented.

4.1 Sliding Friction Coefficients

The sliding friction coefficient of every particle in contact with the top or bottom wall is considered for every plotted time step ($t_s = 0.02s$) and then averaged. The findings are displayed in Fig. 4.

Fig. 4a shows that the friction coefficient decreases with lower shear rates. When the walls move at 0.4 ms^{-1} , the friction coefficient settles around a value of $\mu_c = 0.35$, whereas the base case (0.1 ms^{-1}) has a mean friction coefficient of about $\mu_c = 0.31$, while the low shear case (0.05 ms^{-1}) yields a friction coefficient of just $\mu_c = 0.27$. The results show that the friction coefficient of the entire particle system increases as the shear strain increases. The friction coefficient of dry systems is of course unaffected and remains at $\mu_c = 0.4$.

The evaluation of the second simulation series (Fig. 4b) reveals that in the examined sheared system small changes in fluid viscosity have little to no influence on the coefficient of friction. Here higher differences in viscosity need to be considered to obtain significant deviations in μ_c . This was not possible within the boundary of this study, due to the lack of reliable experimental data needed for the calculation of the sliding friction in wet environments. Additional investigations like the one done by Joseph and Hunt [117] leading to results as given in Fig. 1 would be necessary.

The results of the third simulation series (Fig. 4c) show that gravity in the -Z direction (normal to the moving walls) has no notable effect on the friction coefficient due to the compressed state of the particles and the buoyancy force acting in opposite direction to gravity. However, when gravity is considered in X direction and therefore acts parallel to the moving plates, the mean coefficient of friction first drops to a value as low as $\mu_c = 0.2$ and then stabilizes at a mean value of about $\mu_c = 0.34$, which is than in the base case without gravity. This behavior can be explained by the change in particle movement caused by the gravity force: the particles in contact with the top wall reach the wall velocity of 0.1 ms^{-1} between the 4 second and 6 second mark. As the friction coefficient is highly dependent on the relative tangential velocity

between particle and wall, this causes the drop in friction coefficient. After 6 seconds the particles are accelerated even further and reach velocities of up to 0.2 ms^{-1} . This, together with the high difference in tangential velocity between the particles and the bottom wall cause the coefficient of friction to increase to the stated value. The higher fluctuation of the friction coefficient is most likely explained by the particle movement at the bottom wall. Here, the particles are affected by both the wall and the remaining third body, which move in opposite direction. Hence, the relative tangential velocity between the particles and the bottom wall is not constant throughout the simulation. It is also important to mention, that the flow around individual particles is not resolved within the conducted simulations.

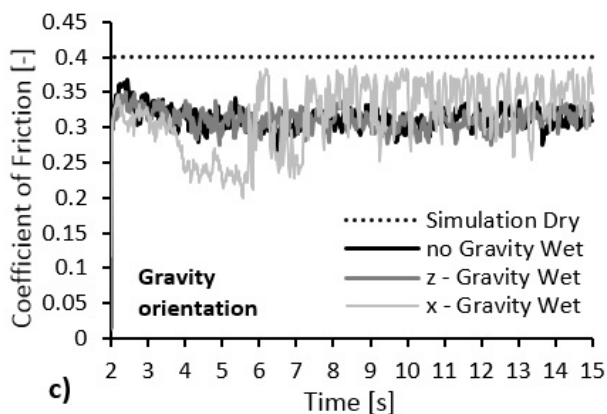
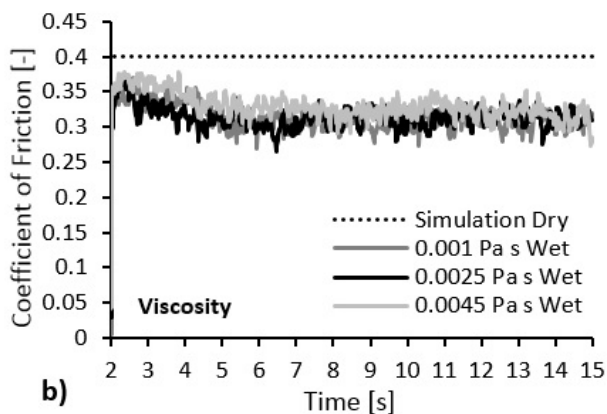
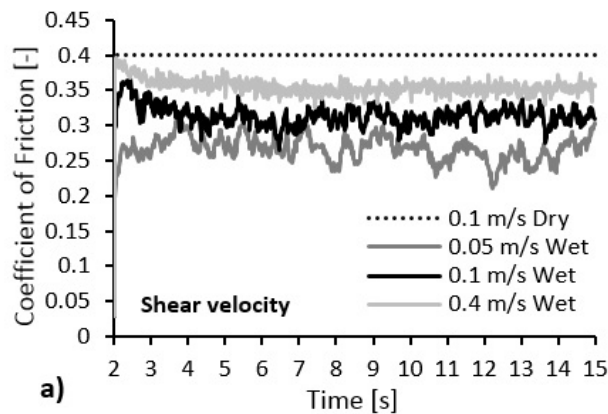


Fig. 4: Mean coefficient of friction between particle and wall plotted against time for different a) shear velocities, b) fluid viscosities and c) gravity orientations.

4.2 Particle and Fluid Velocities

The findings of the particle and fluid velocity observations are presented in Fig. 5. The figures display the mean particle and fluid velocity in X direction plotted against the system height of both wet and dry systems. The velocities are averaged between the 5 second and 15 second mark of the simulation. As the particle movement in the investigated time frame is still subject to small fluctuations, the plotted curves are not completely smooth.

The results of the three employed shear velocities (Fig. 5a-c) show that the differences in particle velocity between wet and dry systems increases with lower shear velocities. This trend is in line with the reduced friction described in Sect. 4.1. As the coefficient of friction between particle and wall decreases, the slip between the two increases, resulting in the observed difference between wall and particle velocity. The particle and fluid velocities in the wet system are very similar in each of the three simulations as it is governed by the particle motion in the domain.

Increasing the fluid viscosity leads to a flattening of the velocity curve (as shown in Fig. 5d-f). The reason for this behavior is not directly apparent and further investigation is required to attain a better understanding of the third body.

The findings of the third simulation series (Fig. 5g-i) reveal very different results in all three cases. When gravity is considered in -Z direction, the particles are drawn toward the bottom wall. As a consequence they are increasingly affected by the velocity of the lower wall. In addition, they start to form denser packings, resulting in an eventual contact loss between the upper wall and the particles in the dry system around the 13 second mark. In the wet system these effects are greatly reduced due to the buoyancy force acting in opposite direction of gravity. Details on the forces acting on the third body are given in Sect. 4.4. The formation of a dense and structured particle packing in the dry simulation in comparison to the random arrangement of the suspended particles in the wet system is shown in Fig. 6. As a result of these effects, the entire particles in the dry simulation start to move in the same direction as the bottom wall after about 13 seconds and the shearing process ceases.

If gravity is oriented in X direction, almost the entire particles move in the same direction after about 6 seconds of simulation, reaching velocities of up to 0.2 ms^{-1} . The particles in the wet simulation show a higher average velocity after 15 seconds, which is probably related to the decrease in particle and particle/wall friction discussed in Sect. 4.1. Although the bottom wall continues to move in the opposite direction of the main part of the third body, only particles in direct contact are sporadically affected.

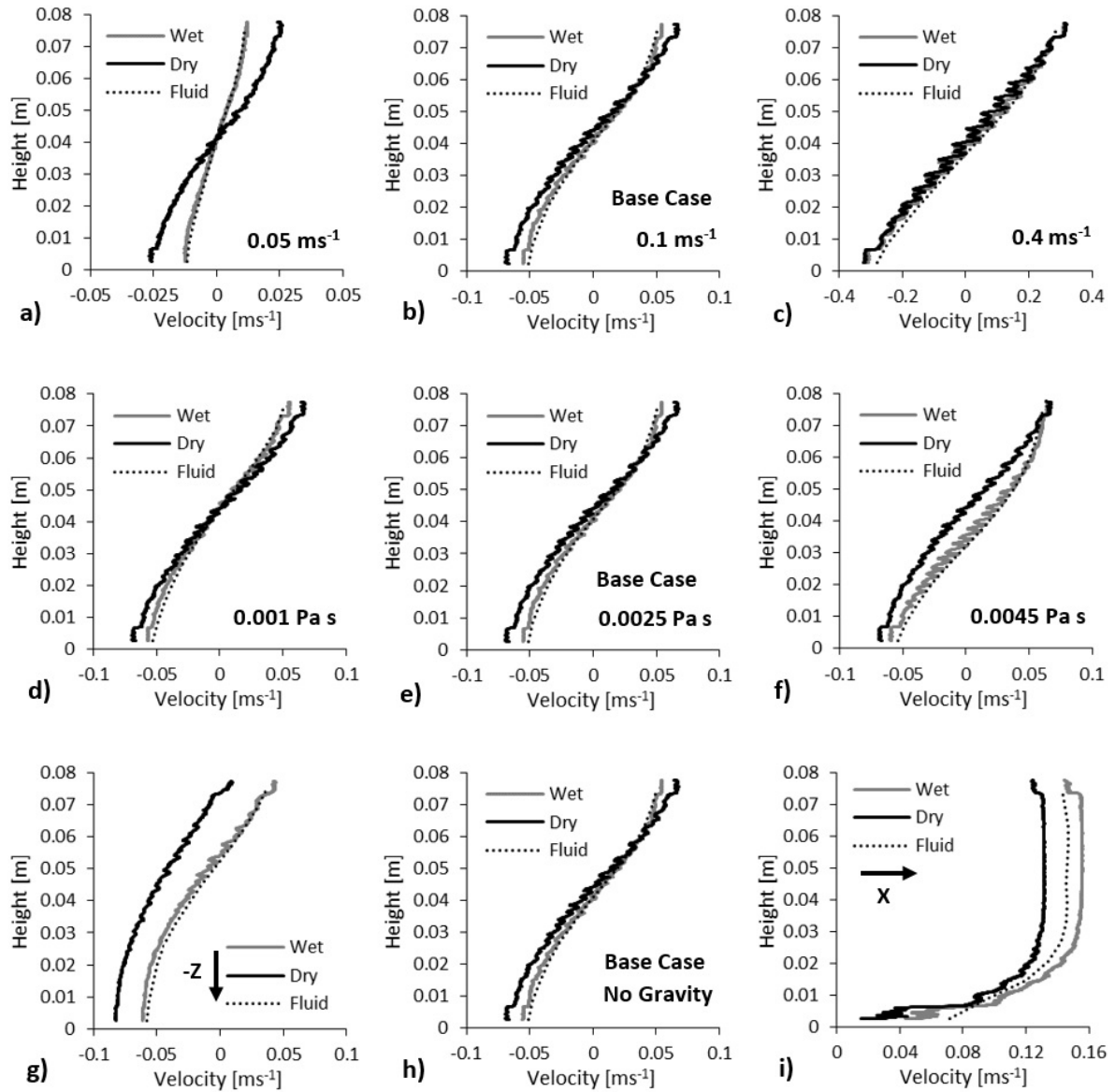


Fig. 5: Mean particle and fluid velocities plotted against the system height for different shear velocities (a,b,c), fluid viscosities (d,e,f) and gravity orientations (g,h,i).

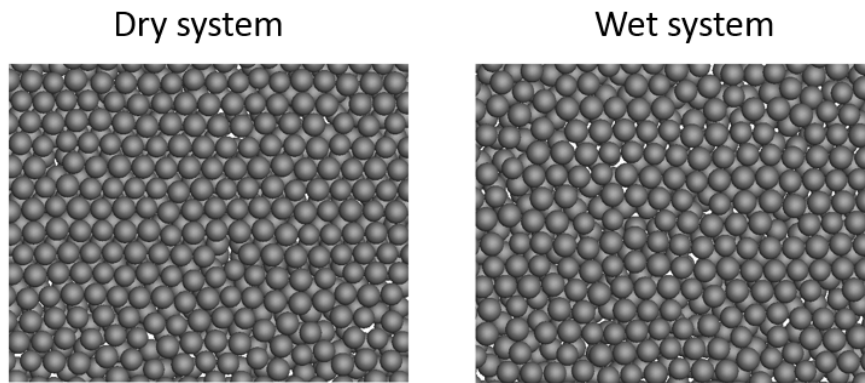


Fig. 6: Comparison between particle structures in a center cut of the dry and wet system under $-Z$ gravity after 13 seconds of the simulation.

4.3 Porosities

The mean porosity distributions averaged between the 5 seconds and 15 second mark are given in Fig. 7. The porosity is averaged over the X domain of the system and only the cells in the middle of the Y axis are considered to avoid a wall influence. Again, both dry and wet simulations are considered. The qualitative trend of all conducted simulations shows that the average cell porosity at the top and bottom wall is significantly higher compared to the rest of the gap. This is expected, due to the high energy particle wall collisions.

The qualitative porosity distribution is very similar in the dry and wet base case (Fig. 7a). Lowering the wall velocity (Fig. 7b) results in a small reduction of particle porosity at the walls whereas an increase in shear strain (Fig. 7c) leads to higher local porosities in close proximity to the walls.

The different fluid viscosities considered (Fig. 7d) show little influence on the porosity distribution, but the effect of significantly higher or lower viscosities would require further investigation. If gravity is considered in $-Z$ direction (Fig. 7e), the porosity close to the top wall increases, especially in the dry simulation. This is explained by the third body behavior described in Sect. 4.2. As the over-all porosity remains the same, the mean porosities across the gap decreases. With gravity oriented in X direction (Fig. 7f), the local porosities of both wet and dry simulations at the lower wall are significantly higher. As the third body moves opposite to the shearing direction of the lower wall, high energy particle/wall collisions take place, increasing the porosity. As the wet system has a higher mean velocity after 15 seconds of simulation, the porosity is slightly higher with a value of 0.52 at the lower wall.

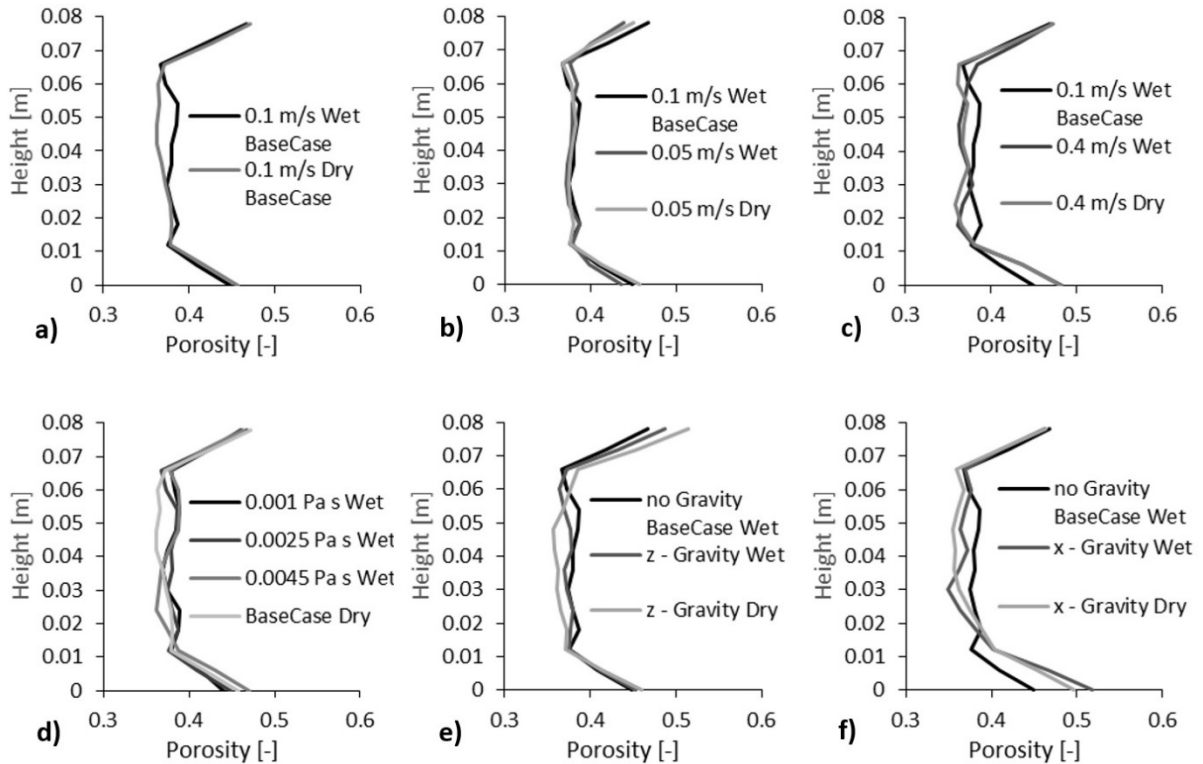


Fig. 7: Dry and wet system porosities plotted against the system height.

4.4 Mean Particle Forces

The mean forces acting on a single particle are presented in Fig. 8 for all lubricated simulations. The displayed results are intended to provide a better understanding of the third body behavior within the system investigated in this study. Displayed forces include the particle contact force, particle/fluid force, particle lubrication force, wall lubrication force, buoyancy force and gravity force. The presented data is to be regarded as a qualitative assessment.

The results show that the average particle contact force is significantly higher compared to the other forces in all conducted simulations. A reduction in shear velocity to 0.05 ms^{-1} (Fig. 8b) shows that the particle/fluid force as well as the particle and wall lubrication forces decrease compared to the base case. This is explained by the fact that the relative velocities between the particles in the system are also reduced. The opposite effect can be observed when the shear velocity is increased to 0.4 ms^{-1} (Fig. 8c). Higher particle velocities also induce higher particle/fluid forces, which can also be seen when comparing Fig. 8a and Fig. 8c.

Lowering the fluid viscosity to $0.001 \text{ Pa}\cdot\text{s}$ (Fig. 8d) shows a reduction in particle/fluid force as well as particle and wall lubrication forces. This was expected considering the viscosity and velocity influence on lubrication (Eq. (6)) as well as the Reynolds number. The particle contact

force remains very similar. Employing a higher viscosity of 0.0045 Pa·s (Fig. 8e) reveals opposite effects. Here, the particle/fluid force, wall lubrication force and particle lubrication force increase in comparison to the base case.

When gravity is considered in -Z direction (Fig. 8f), the individual forces remain very similar. The introduced buoyancy force acting on the glass particles is lower compared to gravity, resulting in the third body behavior discussed in the previous sections. If gravity is considered in X direction (Fig. 8g), the particle contact force significantly decreases after 6 seconds of simulation. As previously discussed, the entire third body starts to move in the same direction, causing the relative velocity between particles and the resulting contact force to drop. The wall lubrication force increases due to the higher relative velocities between particles and walls. The particle/fluid force also rises after 6 seconds, due to the velocity difference between particles and fluid shown in Fig. 5i.

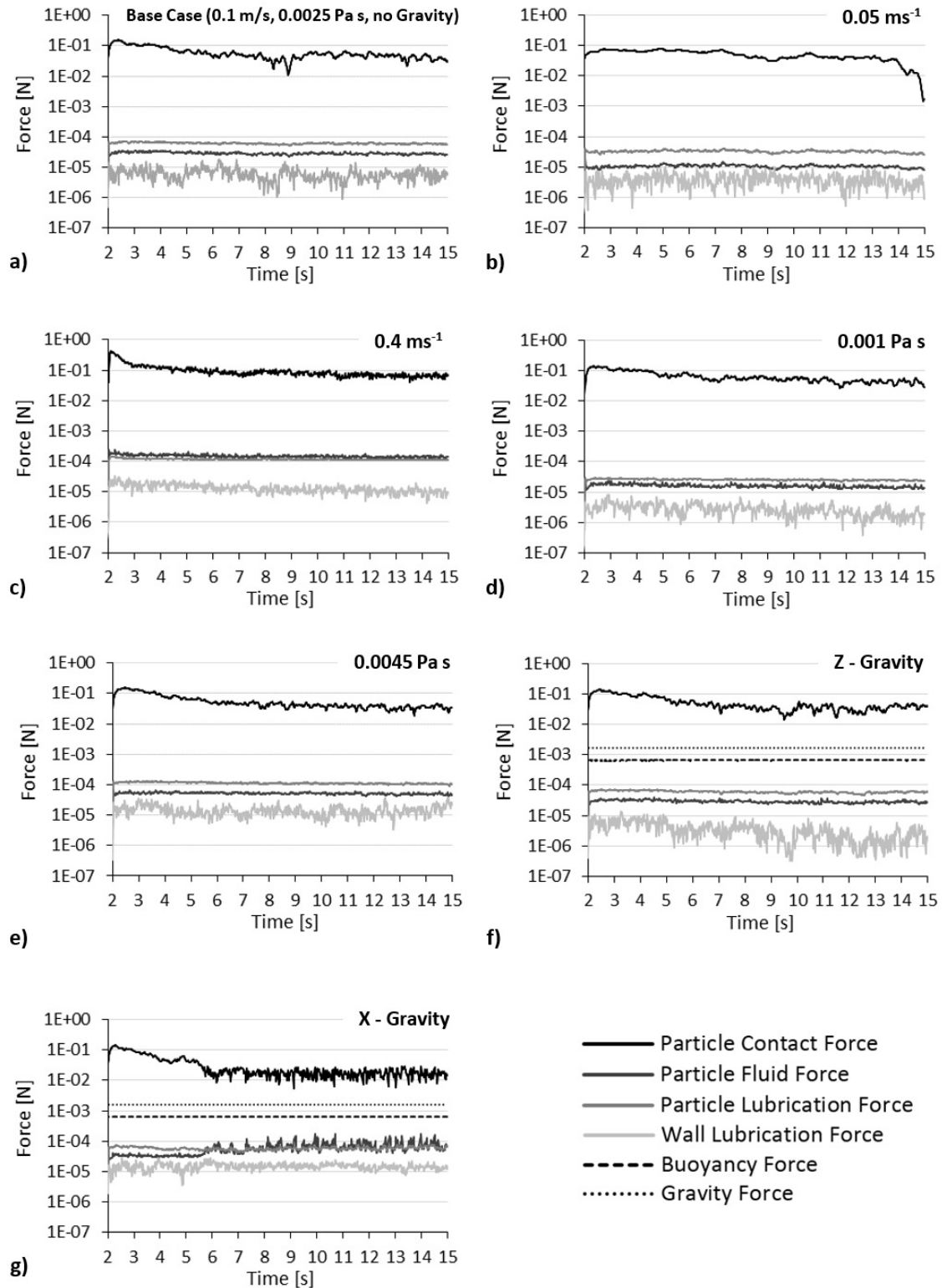


Fig. 8: Mean forces acting on individual particles for the a) base case, shear velocities of b) 0.05 ms^{-1} and c) 0.4 ms^{-1} , fluid viscosities of d) 0.001 Pa s and e) 0.0045 Pa s and gravity orientations in f) Z- and g) X- direction.

5. Conclusions

A numerical study of the third body behavior in wet and dry environments has been conducted based on the coupled DEM-CFD approach. The applied model was extended to consider buoyancy as well as lubrication effects. The system behavior was assessed by altering parameters like shear velocity, fluid viscosity and gravity orientation. Considering the limits of the investigated system the following qualitative conclusions can be made:

- The shear rate greatly affects the third body behavior. Low wall velocities result in a reduction of sliding friction between particles and walls, causing different particle and fluid velocity developments in dry and wet systems. Under high shear rates the friction coefficient of lubricated systems is almost equal to that of dry systems but the local porosity close to the moving walls is increased. High wall velocities induce an increase in lubrication- and particle/fluid force whereas low wall velocities have the opposite effect.
- The different fluid viscosities investigated in this study only show a marginal effect on the behavior of the third body. Although higher viscosities lead to an increase in lubrication forces, these are still not high enough to directly influence the particle packing. Here additional studies with significantly higher fluid viscosities are advisable to accurately assess the impact of this parameter.
- The study showed that gravity in connection with buoyancy plays an important role in moderately compressed sheared systems. The formation of structured and denser particle systems is facilitated when gravity is directed perpendicular to the shear plane in dry environments. In wet systems the buoyancy force counteracts this effect.
- The influence of sliding friction on the third body is significantly higher compared to the lubrication forces within the boundaries of this investigation. Increasing the fluid viscosity or the particle compression (reducing the system porosity) is necessary for detailed analysis and could possibly change this relation.

The obtained results indicate that the employed DEM-CFD approach is capable to generate plausible data on the behavior of sheared particulate systems in both wet and dry environments. It is a promising method to describe and analyze tribological systems. This study provides a first step towards modeling the complex third body behavior in lubricated sheared systems. For future improvement additional and precise data on particle/particle and particle/wall interactions in different fluids is required. The described observations are of qualitative nature and still require verification by further numerical investigations and experiments.

Acknowledgements

The financial support by the DFG – KR 3446/6-1 is gratefully acknowledged.

II. Numerical investigation of mixing and orientation of non-spherical particles in a model type fluidized bed

T. Oschmann, J. Hold, H. Kruggel-Emden*

Ruhr-Universitaet Bochum, Universitaetsstrasse 150, D-44780 Bochum, Germany

*Corresponding author: Email: kruggel-emden@leat.rub.de; Tel.: 0049 234 32 27362, FAX.: 0049 234 32 14 227

The following accepted manuscript appeared as journal version in Oschmann, T., Hold, J., Kruggel-Emden, H.: Numerical investigation of mixing and orientation of non-spherical particles in a model type fluidized bed. Powder Technol. 258, 304–323 (2014) and may be found at <https://doi.org/10.1016/j.powtec.2014.03.046>.

Abstract

A numerical investigation of mixing in a model type fluidized bed is performed based on the three-dimensional discrete element method coupled with computational fluid dynamics (CFD). Particle motion is represented by the discrete element approach applying clustered spheres as well as polyhedrons for the particle shape representation. On the CFD-side fluid flow around individual particles is not resolved, but averaged over cells larger than the particles. Various elongated particle shapes are considered including cylinders, plates and cuboids. Comparisons to spherical particles are made. Thereby, the main focuses are mixing which is assessed by the Lacey index, bed height progression and averaged particle orientation. The investigated particle/fluid systems are rich in detail. Large deviations are obtained for the different particle shapes considered. Mixing as well as bed height progression is also strongly influenced by the particle shape. Especially the shape representation accuracy has strong influence on the results as mass and projection area get altered. Significant variations can be obtained for the preferred particle orientations taken up in regions close to the vessel walls in contrast to the interior of a fluidized bed which clearly limits the ability to evaluate processes inside fluidized beds based on visual observations from the exterior only.

1. Introduction

The basic mechanisms of particle mixing in fluidized beds are scientifically well understood and closely linked to bubble formation and motion. In the wake of a rising bubble particles are transported upwards; in the close vicinity of a bubble particles are locally moving downwards resulting in an overall convective circulation in the vertical direction of the fluidized bed [127–129]. Large scale vertical circulation patterns form out due to bubble/wall interaction which triggers a particle downflow close to the walls and up in the center of the fluidized bed [130]. Horizontal mixing is induced by horizontal motion as well as interaction of bubbles [131,132]. Especially at the fluidized bed surface horizontal mixing is strong due to splashing [128].

So far no generally applicable simple physical or empirical models exist to predict the influence of operating parameters on the mixing in a fluidized bed [95,133]. To close this gap different simulation approaches like two fluid models [134] based on the kinetic theory of granular flow [135] or discrete element approaches (DEM) coupled with continuum models to resolve the fluid flow field (CFD) [133] are applied. Two fluid models despite many effort to improve their accuracy [136–138] are still limited in representing basic flow features [139] as well as mixing and segregation [140]. Combinations of the discrete element method (DEM) coupled with CFD [133,141] are well applicable to particle/gas systems especially when particle sizes are roughly of the same order as the system size. In recent years DEM/CFD approaches have been even extended in few cases to include complex shaped particles [11,40,142–145] and prove powerful for the investigation of related flow features.

The combined DEM/CFD-method was firstly applied by Tsuji et al. [146] to model a two-dimensional fluidized bed of spherical particles. Obtained results were rich in detail regarding phenomena like mixing as well as circulating particle motion. Quantitatively the onset of bubble formation and pressure fluctuations matched experimental observations. Later Hoomans et al. investigated the influence of DEM-collision parameters and compared obtained DEM/CFD-results with experimental investigations involving spherical glass beads resulting in a good match [147]. Xu and Yu [141] simulated the gas/solid flow in fluidized beds and were capable of observing several dynamic flow features attributed to fluidized beds on different scales from the system scale down to the single particle level. Rhodes et al. [133] firstly considered mixing of uniform spherical particles in fluidized beds by a DEM/CFD-approach. Based on the Lacey Index [148] they investigated the dependency of mixing on operational parameters such as fluid velocity, particle size and density. An internally circulating two-dimensional fluidized bed was considered by Bin et al. [149] clearly identifying the increased lateral mixing compared to a conventional fluidized bed. Limtrakul et al. [150] analyzed particle motion by the DEM/CFD-approach for uniform and bidisperse spherical particles. Experimental findings on the particle circulation as well as on operational parameters enhancing mixing were confirmed. Depending on the differences in particle size and density segregation was observed for certain operational parameters. The first three dimensional fluidized particle system was modeled successfully by Feng et al. [151] where the particle motion was considered in 3-D and the fluid motion was still simplified in 2-D. Based on a weighted Lacey mixing index [148] differently sized fluidized particles were investigated in a bidisperse system. Special attention was given to the influence of the initial packing state on the mixing dynamics. The conditions leading to mixing and segregation in the particle system were analyzed. Mixing was identified as fast and segregation as a gradual process. On the particle level the phenomena leading to mixing and segregation were investigated. Strong fluctuations in the spatial and temporal distribution of particle/particle forces and particle/fluid forces were identified. At the same time the influence of the coupling

framework of the particle and the fluid phase within the combined DEM/CFD-framework on mixing and segregation processes was also addressed by Feng and Yu [152]. Two schemes were analyzed theoretically and compared against experimental data on segregation in gas/particle systems favoring the scheme applied in the works [151],[141] and others.

In full 3-D mixing of spherical particles was firstly considered by Chaikittisilp et al. [153] for inclined fluidized beds. Good agreement between experimental investigations and simulations were found pointing out that an inclination of 10° triggers the best mixing compared to other alignments. Nakamura et al. [154] firstly addressed mixing in rotating fluidized beds based on the DEM/CFD-method. Rotating fluidized beds are favorable for the fluidization of fine particles as adhesive forces could be overcome by the combination of drag and centrifugal forces. Obtained experimental results indicated an excellent agreement with numerical results and an empirical mathematical correlation on mixing was proposed for rotating fluidized beds.

More recently micro phenomena related to mixing were addressed. Tian et al. [155] focused on the phenomena triggering mixing in systems with inclined distributor plates or uneven gas feed and identified different convective, diffusive and shear mixing mechanisms. Feng and Yu [156] extended their earlier work [151] on spherical bidisperse particles addressing a wide range of gas velocities. Mixing and segregation mechanisms were identified on the particle level and discussed regarding their influence on flotsam and jetsam particle fractions. Mixing and segregation of equally sized spherical particles with varying density were addressed by Di Renzo et al. [157] by a DEM/CFD-approach and a map of the mixing/segregation in dependence on the fluid velocity and the density ratio was derived. The influence on mixing of immersed objects like tubes which are of importance to fluidized beds in which heat is extracted was investigated by a DEM-LES-scheme by Gui et al. [158]. Zhao et al. investigated flow structure formation and mixing by the DEM/CFD-method in downers [159] and combinations of risers and downers [160] by 2-D simulations. A good agreement was found when comparing obtained numerical results to experimental investigations. The mixing was identified to be strongly related to the initial flow configuration at the inlet in downers and strong backmixing was encountered in risers. Residence time distributions which were derived are rather wide in risers and narrower in downers.

With several DEM/CFD-simulations being performed in 2-D, Feng and Yu [161] addressed differences between 2-D and 3-D by comparative investigations and identified large quantitative deviations in the mixing and segregation kinetics. At the same time other authors addressed mixing in fluidized systems like e.g. spouted beds [162]. Similarly to the investigation by Tian et al. [155], Zhang et al. identified convective, diffusive and shear mixing as relevant mechanisms. The spouting gas velocity mainly induces convective and shear mixing. An increased fluidization velocity reduces convective and shear mixing, but enhances convective mixing which also increases the overall mixing in the fluidized system. Contrary to fluidized

beds spouted beds are attributed to the formation of dead zones which influence overall particle motion.

More recently, extending an earlier work, Gui and Fan evaluated mixing in fluidized beds of spherical particles based on a fractal and entropy analysis [163]. A 2D-investigation of mixing patterns in a bubbling fluidized bed was performed by Norouzi et al. [130] and validated against 3-D radioactive particle tracking technique. The 2-D model reproduces axial diffusivity well while radial diffusivity is reproduced one order of magnitude lower than in the experiments, confirming results obtained by Feng and Yu [161]. Liu et al. [164] derived a DEM/CFD-framework relying on a coupling of the commercial CFD-code Fluent with a non-commercial DEM-scheme, focusing on bubble/particle interaction and its influence on mixing. A fluidized bed with internal recirculation was addressed by Fang et al. [165]. Within the fluidized bed different mixing stages were identified over time. Mixing was assessed based on the Lacey index [148] and the fluidized bed with internal recirculation revealed a better mixing than obtained with conventional fluidized beds. Other recent investigations involving the DEM/CFD-methodology in the context of mixing addressed systems of binary particles with spherical particles varying in density and size [166], large scale investigations involving systems with millions of particles [167] or rotating fluidized beds as investigated earlier by Nakamura et al. [154] but with an inclined injection of air applied as fluidizing agent [154].

Despite many investigations involving spherical particles, so far only few particle/gas-systems were studied with the DEM/CFD-methodology involving complex shaped bodies. The fluid/particle interaction of monodisperse particles in a fluidized bed was addressed by Zhong et al. [142] for cylindrical particles approximated by clustered spheres [54,55] and general flow features in the simulations matched those in corresponding experiments. As fluid/particle forces only drag forces derived from the model of Tran Cong et al. [168] were taken into account; this model [168] is not intended for the use in dense particle systems as the influence of the void fraction is not appropriately considered. Hilton et al. [40] analyzed systems of monodisperse fluidized superellipsoids within a DEM/CFD-framework. As drag force model, the approach of Hölzer and Sommerfeld [48] was coupled with a model for the representation of the void fraction by Di Felice [42]. Other particle/fluid forces than the drag force were neglected. Hilton et al. [40] was able to show that the pressure drop during the onset of fluidization calculated from the sphericity corrected Ergun equation [38] significantly differs from results where the drag force of particles is based on the cross sectional area of the individual particles. In a further study Hilton and Cleary [11] investigated the pneumatic transport of monodisperse superellipsoids using the DEM/CFD-method. The drag force was modeled by the same approach as in [40]. The influence of the rotation of the flow field on the particle motion was considered by interpolation. In addition to the drag force rotational drag and, Magnus and Saffman lift forces were considered based on models available for spherical particles. Hilton and Cleary [11] were

able to detect different flow modes and the dependencies for their transition. Based on the modeling framework proposed earlier [11,40] Hilton and Cleary also investigated raceway formations resulting from gas injected into a particle bed consisting of complex shaped objects [169]. A similar model framework to that of Hilton et al. [40] was also applied by Zhou et al. [143] to investigate the behavior of prolate and oblate ellipsoids in a fluidized bed. Orientation of cylindrical particles during fluidization in a riser was addressed in a Monte Carlo (DSMC) by Cai et al. [170]. Results indicate that orientation strongly depends on the position in the riser and less on air velocity or aspect ratio. A DEM/CFD-framework for modeling corn shaped particles represented by clustered spheres was proposed recently [144] and applied to a spouted bed and validated against experiments. In a further study it was successfully applied to mixing of non-spherical particles for the first time [145].

Although mixing was widely investigated in fluidized beds involving spherical particles for a wide range of operational parameters within the DEM/CFD-method, it is considered for particle/gas systems of particles of complex shape only in singular cases [145]. Even coupled modeling frameworks involving non-spherical shapes were applied only for few studies [11,40,142–144,169]. The general applicability and sensitivity of these frameworks still has to be reliably tested [143]. Orientation during fluidization has only been studied for a limited number of complex particle shapes [95,170]. To extend the knowledge on these important aspects in fluidized systems the current study is performed focusing on the orientation and mixing of volume equivalent cuboidal and cylindrical particles. Operational parameters as well as simulation parameters like the representation accuracy and the shape representation method are addressed.

2. Methodology

The coupled DEM/CFD-method is used in the investigation here. The particle motion is represented within the DEM-framework, where the fluid phase is represented by solving the volume averaged Navier-Stokes equations. Thereby, the flow around individual particles is not resolved [8].

2.1 DEM for complex shaped particles

The discrete element method is routinely utilized for the modeling of systems of particles with spherical shape [95]. When the discrete element method is used to represent non-spherical particles, the translational and rotational motion is obtained by integrating Newton's and Euler's equations of each particle [171]

$$m_i \frac{d^2 \vec{x}_i}{dt^2} = \vec{F}_i^c + \vec{F}_i^{pf} + \vec{F}_i^g \quad (1)$$

$$\hat{I}_i \frac{d\vec{W}_i}{dt} + \vec{W}_i \times (\hat{I}_i \vec{W}_i) = \Lambda_i^{-1} \vec{M}_i, \quad (2)$$

with particle mass m_i , particle acceleration $d^2 \vec{x}_i / dt^2$, contact force \vec{F}_i^c , particle/fluid force \vec{F}_i^{pf} , gravitational force \vec{F}_i^g , angular acceleration $d\vec{W}_i / dt$, angular velocity \vec{W}_i , external moment resulting out of contact or particle/fluid forces \vec{M}_i , the inertia tensor along the principal axis \hat{I}_i and the rotation matrix converting a vector from the inertial into the body fixed frame Λ_i^{-1} . The equations for translational and rotational motion are solved by explicit integration schemes [171]. A flexible approach to model complex shaped particles in the discrete element method is the multi-sphere [54] or polyhedron method [55]. In the multi-sphere method arbitrary sized spheres are clustered to resemble the desired complex particle shape. In the polyhedron method a triangular surface mesh is applied to represent the desired particle shape and a common plane algorithm is used for contact detection of the individual vertexes representing the particle surface [172]. In both methods contact force laws are applied as used for spherical particles [54,55]. In case of multiple contacts an averaging of forces and moments over the number of contact points can be performed [55]. Further details on the contact schemes involving clustered spheres and polyhedrons can be found in [173–175].

The normal component of the contact forces is obtained from a linear spring damper model

$$\vec{F}^n = k^n \delta \vec{n} + \gamma^n \vec{v}_{rel}^n, \quad (3)$$

where k^n is the spring stiffness, δ the virtual overlap, \vec{n} a normal vector, γ^n a damping coefficient and \vec{v}_{rel}^n the normal velocity in the contact point [95]. Both k^n and γ^n determine the coefficient of normal restitution between particles e_{pp}^n as well as particles and walls e_{pw}^n . For the calculation of the tangential forces a linear spring limited by the Coulomb condition is used

$$\vec{F}^t = \min(k^t |\vec{\xi}^t|, \mu_c |\vec{F}^n|) \vec{t}, \quad (4)$$

where k^t is the stiffness of a linear spring, μ_c is the friction coefficient, $\vec{\xi}^t$ is the relative tangential displacement and \vec{t} is the tangential unit vector [25]. Rotational friction is neglected in the investigation here.

2.2 CFD for fluid phase

The fluid phase is described with Computational Fluid Dynamics (CFD) in an Eulerian framework, in which the interior of the fluidized bed is meshed in equal cells. The fluid velocity is addressed as a spatially averaged quantity per cell. The CFD-framework passes the fluid properties and the velocity vector of the fluid to the discrete element method. The equation of continuity (5) and the equation of momentum (6) are solved

$$\frac{\partial(\varepsilon_f \rho_f)}{\partial t} + \nabla(\varepsilon_f \rho_f \vec{u}_f) = 0, \quad (5)$$

$$\frac{\partial(\varepsilon_f \rho_f \vec{u}_f)}{\partial t} + \nabla(\varepsilon_f \rho_f \vec{u}_f \vec{u}_f) = -\varepsilon_f \nabla p + \nabla(\varepsilon_f \bar{\tau}) + \varepsilon_f \rho_f \vec{g} + \vec{f}_{int}, \quad (6)$$

where \vec{u}_f , ρ_f and p are the fluid velocity, density and pressure. \vec{f}_{int} is the volumetric particle/fluid interaction applied in each CFD cell, ε_f is the local fluid porosity and $\bar{\tau}$ is the fluid viscous stress tensor $\bar{\tau} = \mu_e \left[(\nabla \vec{u}_f) + (\nabla \vec{u}_f)^{-1} \right]$ with μ_e the effective viscosity determined from the standard k- ε turbulent model [176]. The particle/fluid interaction \vec{f}_{int} is given component wise as $f_{int_i} = \bar{\beta}_i (u_i - \bar{v}_i)$, where \bar{v}_i is the fluid cell averaged particle velocity and $\bar{\beta}_i$ is the fluid cell averaged particle/fluid drag coefficient with $i=x, y, z$.

2.3 Drag force calculation

The particle/fluid force \vec{F}_i^{pf} consists of all individual particle/fluid forces such as drag force \vec{F}_i^d , pressure gradient force $\vec{F}_i^{\nabla p}$ and forces due to fluid shear stress or the deviatoric stress tensor $\vec{F}_i^{\nabla \tau}$ acting on a particle i written as

$$\vec{F}_i^{pf} = \vec{F}_i^d + \vec{F}_i^{\nabla p} + \vec{F}_i^{\nabla \tau} \quad (7)$$

Under the assumption of parallel flow the rotational motion of particles as well as the particle/fluid stress term can be neglected [40] leading to $\vec{F}_i^{\nabla \tau} = 0$. The drag force \vec{F}_i^d and the pressure gradient force $\vec{F}_i^{\nabla p} = \beta_i (\vec{u}_F - \vec{v}_i) / \varepsilon_F$ [177] can be combined to $\vec{F}_i^d + \vec{F}_i^{\nabla p} = \vec{\beta}_i V_i (\vec{u}_F - \vec{v}_i) / (\varepsilon_F (1 - \varepsilon_F))$ after some transformation following Shimizu [41], where V_i is the particle volume. For the calculation of the drag force \vec{F}_i^d and the combined drag and pressure gradient force $\vec{F}_i^d + \vec{F}_i^{\nabla p}$ various models are available [8]. Very popular and widely used for spherical particles and also applicable for non-spherical particles is the approach by Di Felice [42], where the force for an isolated spherical particle is calculated and altered by the influence of surrounding particles. The respective force reads

$$\vec{F}_i^{pf} = \vec{F}_i^d + \vec{F}_i^{\nabla p} = \frac{1}{2} \rho_F |\vec{u}_F - \vec{v}_i| C_D A_{\perp} \varepsilon_F^{1-\chi} (\vec{u}_F - \vec{v}_i) \quad (8)$$

where C_D is the drag coefficient, A_\perp is the cross-sectional area perpendicular to the flow and χ a correction factor. Equation (8) can be rewritten in terms of the particle/fluid drag coefficient as

$$\beta_i = \frac{1}{2} \rho_F C_D A_\perp \varepsilon_F |\vec{u}_F - \vec{v}_i| (1 - \varepsilon_F) \frac{1}{V_i} \varepsilon_F^{(1-\chi)}, \quad (9)$$

where V_i is the particle volume χ is calculated as a function of the particle Reynolds-number $Re = \varepsilon_F \rho_F d_p |\vec{u}_F - \vec{v}_i| / \mu_F$ as

$$\chi = 3.7 - 0.65 \exp(-(1.5 - \log(Re))^2 / 2) \quad (10)$$

with d_p the diameter of a volume equivalent spherical particle and μ_F the fluid viscosity.

Rong et al. [44] recently suggested an improved correction factor based on a Gaussian distribution which in addition to the Reynolds number Re takes the porosity ε_F into account

$$\chi = 2.65(\varepsilon_F + 1) - (5.3 - 3.5\varepsilon_F)\varepsilon_F^2 \exp(-(1.5 - \log(Re))^2 / 2), \quad (11)$$

thereby reducing the maximal error of the drag force from 25 % to 15 % in packings of spheres.

The drag coefficient C_D of a single particle (spherical or non-spherical) can be derived from detailed resolved flow simulations [178–180] or from correlations such as Ganser [181] or Hölzer und Sommerfeld [48]. Due to its simplicity and general applicability the model by Hölzer und Sommerfeld [48] is popular and can be written as

$$C_D = \frac{8}{Re} \frac{1}{\sqrt{\phi_\perp}} + \frac{16}{Re} \frac{1}{\sqrt{\phi}} + \frac{3}{\sqrt{Re}} \frac{1}{\phi^{3/4}} + 0.42 \times 10^{0.4(-\log(\phi))^{0.2}} \frac{1}{\phi_\perp} \quad (12)$$

where ϕ_\perp is the crosswise sphericity which is the ratio between the cross-sectional area of the volume equivalent sphere and the projected cross-sectional area of the considered particle perpendicular to the flow. The sphericity ϕ is the ratio between the surface area of the volume equivalent sphere and the surface area of the considered particle.

Instead of applying the equation (8) or (9) in combination with (10) or (11) for the calculation of the combined drag and pressure gradient force $\vec{F}_i^d + \vec{F}_i^{\nabla p}$ or the particle/fluid drag coefficient $\vec{\beta}_i$ the combination of Ergun [38] and Wen and Yu [182] can be used which neglects particle orientation [40] and can be written as

$$\vec{\beta}_i = \begin{cases} 150 \frac{(1-\varepsilon_F)^2}{\varepsilon_F d_p^2} \mu_F + 1.75 \frac{(1-\varepsilon_F) \rho_F}{d_p} |\vec{u}_F - \vec{v}_i|, & \text{for } \varepsilon_F \leq 0.8 \\ \frac{3}{4} \rho_F C_D \frac{(1-\varepsilon_F) \varepsilon_F^{-1.7}}{d_p} |\vec{u}_F - \vec{v}_i|, & \text{for } \varepsilon_F > 0.8 \end{cases} \quad (13)$$

This approach also allows for the combination of the drag and pressure gradient force [41]. The non-sphericity of particles is considered by the diameter of a volume-equivalent sphere d_p . The drag coefficient C_D is dependent on the particle Reynolds number and is calculated as

$$C_D = \begin{cases} \frac{24}{Re} (1 + 0.15 Re)^{0.687}, & Re < 1000 \\ 0.44, & Re \geq 1000 \end{cases} \quad (14)$$

Detailed information about the coupling algorithm can be found in [183].

2.3.1 Determination of the projection area

For spherical particles the cross-sectional area A_{\perp} perpendicular to the flow required for equations (8 and 9) or the crosswise sphericity ϕ_{\perp} needed for equation (11) can be readily calculated. For clustered overlapping spherical particles or polyhedra which are used to represent the complex shaped particles in the investigation here iterative procedures are applicable [40]. Due to computational reasons the cross-sectional area A_{\perp} of each particle is calculated in advance and is tabulated in dependence on three symmetric Euler parameters and the sign of the fourth parameter [50]. All four symmetric Euler parameters squared sum up to one. For clustered spheres the individual spheres are mapped on the xy-, yz- and xz-plane. Based on a 2D-Cartesian grid whose size is chosen in dependence on the projected particle size with a resolution of 100x100 cells it is checked for all grid cell centers if the respective point is lying within one of the sphere projections. Based on the accumulated grid area the total projection area is calculated. Two examples for the calculation of the projection area of a clustered sphere particle with varying orientation are given in fig. 1. The same is done for polyhedrons. The method was validated for a single sphere and has an error of less than 0.08 percent when applied for the calculation of the respective projection area. In the simulations the orientation of each particle is tracked based on a rotation matrix. From this matrix the symmetric Euler parameters are derived which allow the look up of the projection area A_{\perp} and calculation of the crosswise sphericity ϕ_{\perp} .

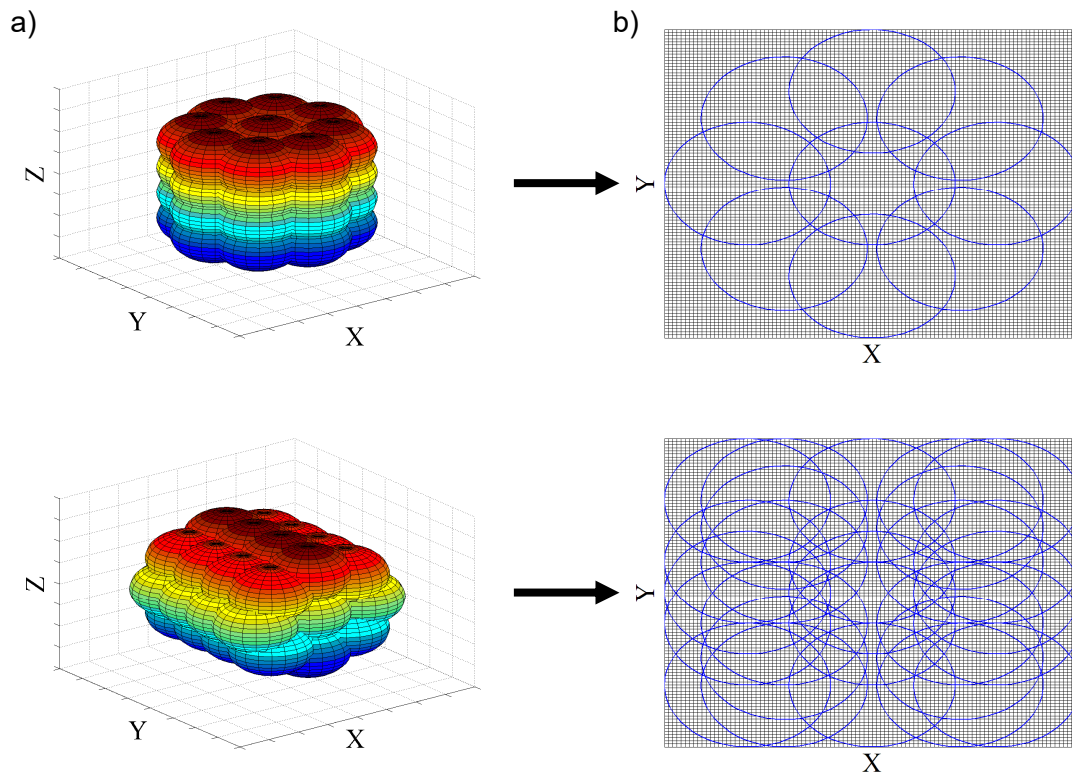


Fig. 1: Two examples for the calculation of the projection area, a) clustered sphere particles with specific orientation, b) the resulting projection areas for the x,y-plane calculated for a grid resolution of 100x100.

2.3.1 Determination of porosity

The porosity is calculated each time step. A fine Cartesian subgrid is used with a single cell size of $1 \times 10^{-9} \text{ m}^3$ which is 1000 times smaller than a single particle cell. Based on the subgrid cell centers it is checked if a particular center lies within part of a particle. If this is the case the respective subcell is considered as fully filled with solid. Based on the ratio of the overall CFD-cell volume V_{CFD} minus the solid volume V_{sol} of the respective subcells to the overall CFD-cell volume the fluid porosity is calculated as

$$\varepsilon_F = \frac{V_{CFD} - V_{sol}}{V_{CFD}}. \quad (15)$$

3. Simulation conditions

3.1 Simulation setup and parameters

The considered simulation setup is a fluidized bed with a quadratic base area as shown in fig. 2.

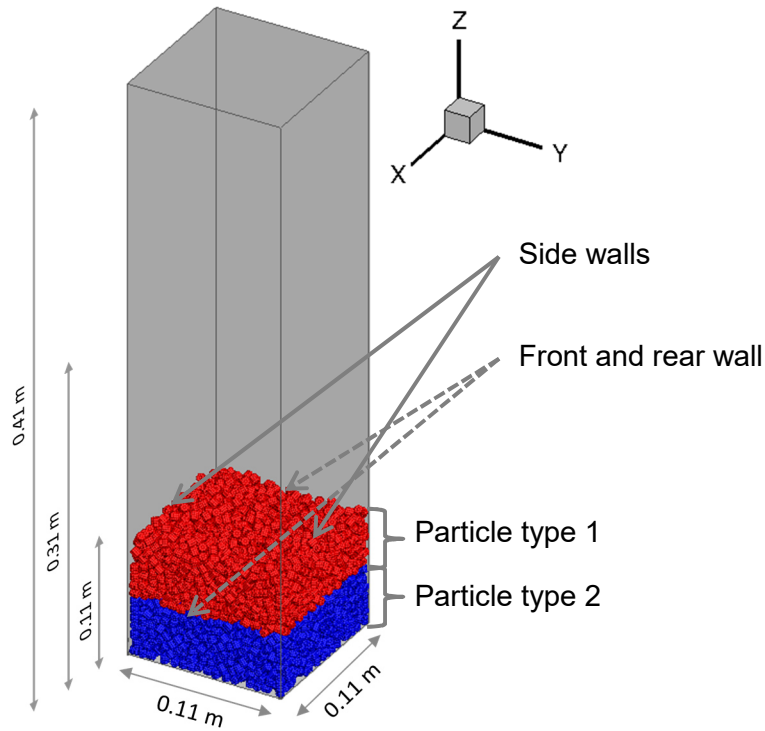


Fig. 2 Schematic diagram of the simulation setup.

A gaseous fluidizing agent is passed into the vessel from the bottom. The base area of the fluidized bed is 0.11 m x 0.11 m - its height is 0.41 m. Particles are placed within the vessel and settle under gravity. The pressure drop over the particle bed can be obtained numerically as averaged difference between the topmost and lowermost CFD-cell layer. An overview of the applied particle shapes consisting of spheres, cylinders and cuboids is given in tab. 1 including information on the particle sizes, aspect ratios along x-, y- and z-axis, on the particle sphericity as well as information on a particle orientation vector (black arrow) initially aligned with the z-axis.

Despite of their varying shape the particles applied are of equivalent volume to a 7 mm diameter sphere. The particle bed consists of 4500 particles and simulations are performed for $t=10$ s.

Table 1: Particle shapes and sizes applied in the simulations. The arrow represents an orientation vector later used in the investigations where AR denotes the aspect ratio

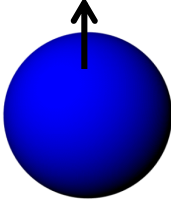
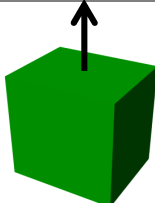
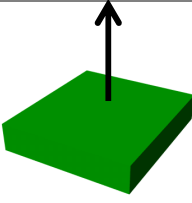
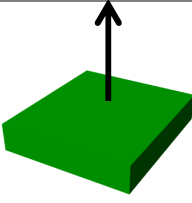
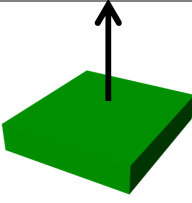
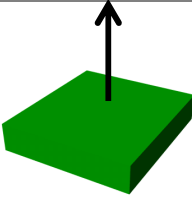
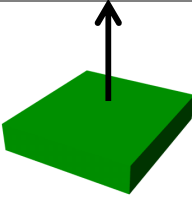
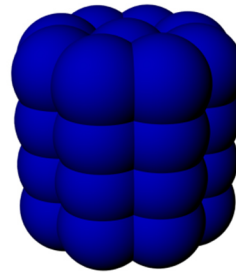
Shape	Sphere						Cylinder					
												
Size in mm	7	7	7	6	6	6	14.3	4	4	25.4	3	3
Axes AR	1	1	1	1	1	1	1	0.28	0.28	1	0.12	0.12
Sphericity		1			0.91			0.75			0.61	
Shape	Cuboid											
												
Size in mm	6	6	5	2	9	10						
Axes AR	1	1	0.83	0.2	0.9	1						
Sphericity		0.80			0.60							

Table 2: Particle, particle-wall and fluid properties of the base-case (left) and cylinder shape (bottom right) approximated by the clustered-sphere method (top right)

Particle properties	
Approximated Shape	Cylinder
Approximation method	Clustered spheres
Number of spheres	36
Density	1380 kg/m ³
Projection area 0°	2.61E-05 m ²
Projection area 90°	3.42E-05 m ²
Spring stiffness	1.00E+05 N/m
Damping coefficient	88888 kg/s
Friction coefficient	0.12
Coefficient of restitution	0.913
Particle-Wall properties	
Spring stiffness	1.00E+05 N/m
Damping coefficient	88888 kg/s
Friction coefficient	0.19
Coefficient of restitution	0.88
Fluid properties	
Density	1.225 kg/m ³
Dynamic viscosity	1.79E-05 N/sm ⁻²



Mixing and particle orientation are investigated in dependence on varying operational and simulation parameters starting from a base-case outlined in tab. 2. The geometric shape considered is an ideal cylinder of 6 mm length and 6 mm diameter approximated as a cluster composed of 36 individual spheres (tab. 2). As material, polyoxymethylene (POM) is considered in the simulations. The spheres applied for the clustered particles have a diameter of 2.4 mm and

are positioned so that they tangent the cylinder surface leading to a total volume approximation accurateness of 81.4 %. This makes the approximated particle shape by weight lighter than the real cylindrical particles. The friction and restitution coefficients were determined according to procedures described by Höhner et al. [175] and Hold [43] on the single particle level, respectively. Spring stiffness and damping coefficient determine the maximum overlap for the particle collision. Kruggel-Emden et al. [31] suggested a maximum overlap of 1 % of the particle diameter to avoid alteration of the simulations. Values for the spring stiffness and the damping coefficient in tab. 2 lead to overlaps smaller than 1 % of the particle diameter. The fluidizing agent is air with a superficial velocity of 3 m/s. The drag force is calculated based on the approach by Di Felice [42] as given by equation (8 and 10).

Starting from the base-case one parameter is altered at a time. An overview over the performed variations is provided in table 3. Variations include the gas inlet velocity, the layer arrangement if particles are colored, the particle aspect ratio, the particle density, the sphere quota (cylinders are placed atop spheres if both shapes are present), the cluster and polyhedron approximation accuracy, the drag force model, the CFD-grid accuracy and the particle shape.

Table 3: Variation of the operational parameters

1. Case	2. Case	3. Case	4. Case
Gas inlet velocity:	Layer arrangement:	Particle aspect ratio:	Particle density:
<ul style="list-style-type: none"> ▪ $v_z = 2$ m/s ▪ $v_z = 3$ m/s ▪ $v_z = 4$ m/s 	<ul style="list-style-type: none"> ▪ x-vector ▪ y-vector ▪ z-vector 	<ul style="list-style-type: none"> ▪ aspect ratio = 1 ▪ aspect ratio = 0.28 ▪ aspect ratio = 0.12 	<ul style="list-style-type: none"> ▪ $\rho = 1380$ kg/m³ ▪ $\rho = 1691$ kg/m³ ▪ $\rho = 2380$ kg/m³
5. Case	6. Case	7. Case	8. Case
Sphere quota:	Cluster accuracy:	Polyhedron accuracy:	Drag force model:
<ul style="list-style-type: none"> ▪ 0 % spheres ▪ 50 % spheres ▪ 100 % spheres 	<ul style="list-style-type: none"> ▪ 36 spheres ▪ 12 spheres 	<ul style="list-style-type: none"> ▪ 8 edges ▪ 16 edges 	<ul style="list-style-type: none"> ▪ Di Felice [42] ▪ Ergun [38] ▪ Rong et al. [44]
9. Case	10. Case		
Grid accuracy (cells):	Variation of shape:		
<ul style="list-style-type: none"> ▪ fine (11x11x41) ▪ medium (7x7x26) ▪ coarse (4x4x15) 	<ul style="list-style-type: none"> ▪ plate ▪ cuboid 		

3.2 Assessment of mixing and particle orientation

The degree of mixing is evaluated based on the local state of homogeneity of a number of samples in which particles are colored by two distinct colors. Initially 50% of the particles are of the first color; 50 % of the second color. In the following chapters the nomenclature type 1 and 2 will be used to describe the two particle colors, see fig. 2. Particles are charged in two layers depending on the particle position in x-, y- and z-direction. The normalized variance is used to classify the mixing quality known as the Lacey mixing index [148]

$$M = 1 - \frac{s^2 - s_r^2}{s_0^2 - s_r^2}, \quad (16)$$

where s_0^2 represents the completely unmixed and s_r^2 the stochastically mixed state. The actual variance s^2 can take up values between these two states. A mixture index of $M = 0$ thus classifies an unmixed system where a completely mixed system comprises a mixing index of $M = 1$. As outlined in [151] the mixing index is influenced by the sample size. A sample size of one particle leads to a value of zero for the mixing index even for a fully-mixed fluidized bed. Otherwise by choosing a sample size including all particles the mixing index will obtain values equal to one. To avoid these extremes the sample size in the investigation here consists of 70 particles and samples are drawn 100 times. These sampling parameters are appropriate to evaluate the mixing behavior over time in the fluidized bed studied here. As a boundary value the mixing index can approach the value of one for a perfectly mixed system. To characterize the initial unmixed-state the mixing index is set to zero for $t=0$ s.

In addition to the mixing behavior the particle orientation is tracked within the simulations. This is done based on an orientation vector which is initially aligned with the z-axis (comp. tab. 1) and moves/rotates with the particles over time. As parameter the projection of the orientation vector on the x-y-, x-z- and y-z-plane is calculated. The orientation is then evaluated based on the minimum of the clockwise or anticlockwise angle between the x- or y-vector and the projection of the orientation vector on the respective x-y-, x-z- and y-z-plane [143].

3.3 Experimental, analytic and numerical validation

To validate the numerical DEM/CFD-framework for clustered and polyhedron shaped particles, a comparison of experimental, analytical and numerical results on the pressure drop for spherical particles is performed. As reference, the pressure drop in a fixed bed for fluid velocities of 0.4 to 2.4 m/s is investigated. The fluid velocity is increased by intervals of 0.2 m/s from the minimum value of 0.4 m/s. Particles are considered which are made of polyoxymethylene (POM) and are spherical with a diameter of 7 mm.

The analytical results are based on the Ergun equation [38], which describes the pressure loss for spheres in a fixed bed

$$\Delta p = 150 \frac{(1 - \varepsilon_F)^2 H_0 \mu_F u_F}{\varepsilon_F^3 d_p^2} + 1.75 \frac{(1 - \varepsilon_F) H_0 \rho_F u_F^2}{\varepsilon_F^3 d_p} \quad (17)$$

where d_p is the sphere diameter, μ_F the dynamic viscosity, ρ_f the fluid density and u_F the superficial velocity. The fluid porosity is obtained as $\varepsilon_F = 0.4$ and the bed height as $H_0 = 0.11 \text{ m}$ from experimental investigations. The pressure drop for the minimum fluidization velocity (lift off pressure) can be obtained analytically as

$$\Delta p = (\rho_p - \rho_F)g(1 - \varepsilon_F)H \quad (18)$$

where H is the mean bed height after reaching a fluidized state.

The experimental fluidized bed is of the same dimensions as the setup in the simulations shown in fig. 2. The experimental setup and its main components are shown in fig.3. The walls consist of antistatic polycarbonate. Three pressure tapping points are available to measure the pressure drop over the particle bed. The particle bed is placed atop a perforated plate with a passage of 37 percent Flow straighteners adjusts the flow and induce a fully-developed flow profile. The superficial velocity is measured at the air inlet compressor.

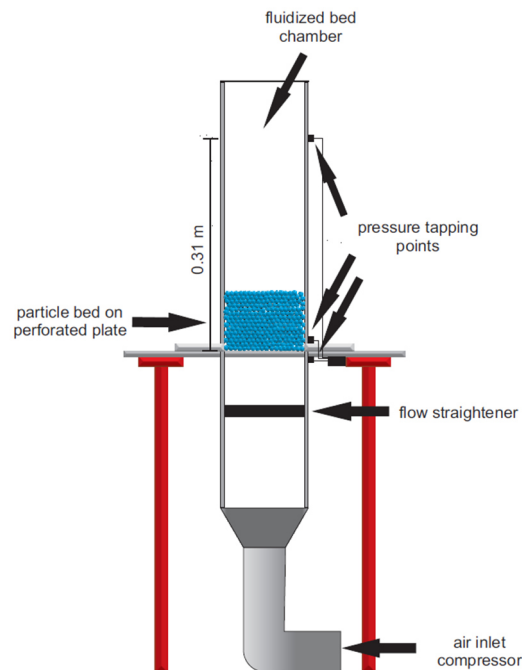


Fig. 3: Experimental setup used for the pressure drop measurements.

Results on the pressure drop in simulations and experiments are plotted in fig. 4 including deviations obtained from average values.

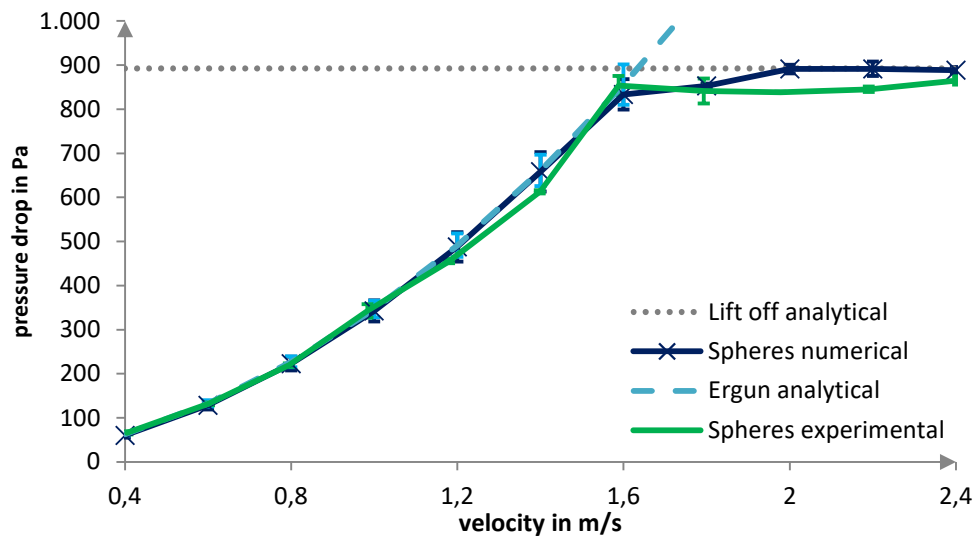


Fig. 4: Pressure drop of spheres plotted against the superficial gas velocity in simulations and experiments; bars indicate maximal and minimal deviations from the average values.

The pressure drop of the spheres in the simulations agrees well with the value reported from the Ergun equation [38] for a porosity of $\varepsilon_F = 0.4$ and the experimentally obtained pressure drop. The lift off pressure (equ. 18) also matches well. The results obtained from the simulations and experiments reveal increasing deviations from the mean pressure drop with increasing gas velocity due to differences in the developing packing structure. The obtained results underline the validity of the derived DEM/CFD-framework.

4. Results and discussion

4.1 Variation of gas inlet velocity

In the first variation the influence of the gas inlet velocity on the mixing of cylindrical particles as outlined in tab. 2 (base-case) is investigated at three velocities of 2 m/s, 3 m/s and 4 m/s which were chosen larger than the minimum fluidization velocity which varies between 1.2 – 1.6 m/s depending on the initial bed porosity. Results are shown in fig. 5a for the degree of mixing M and the average height of particles of color 1 and 2 in fig. 5b, 5c and 5d over time with the inlet surface being the reference.

The results indicate that an increase in the gas velocity leads to an improved mixing. The fastest and most complete mixing is obtained for the largest gas velocity. The mixing index M increases from the totally unmixed state of initially $M=0$ rapidly and then converges to a constant value of $M \approx 0.95-1$ within 3 - 5 s. At gas velocities close to the minimum fluidization velocity a totally mixed state is not fully obtained. This observation is confirmed by comparing the

average heights of the two particle types 1 and 2 at different fluid velocities as shown in figs. 5b, 5c and 5d. Starting from the densely packed state the particle bed is lifted entirely during the first 2 s of the simulation with the particles reaching a fluidized state thereafter. Thereby, a larger fluid velocity results in a larger bed height. A state of complete mixing is characterized by an equal bed height of particles of type 1 and 2 which is observed for fluid velocities of 4 m/s and 3 m/s. At 2 m/s the particle bed is only partially fluidized leading to a constant difference in the average height of particles of type 1 and 2. Bed height oscillations are very homogenous at velocities of 2 m/s and 3 m/s. At velocities of 4 m/s the fluidized system starts to perform a slugging motion which results in inhomogeneous fluctuations of the bed height (fig. 5b).

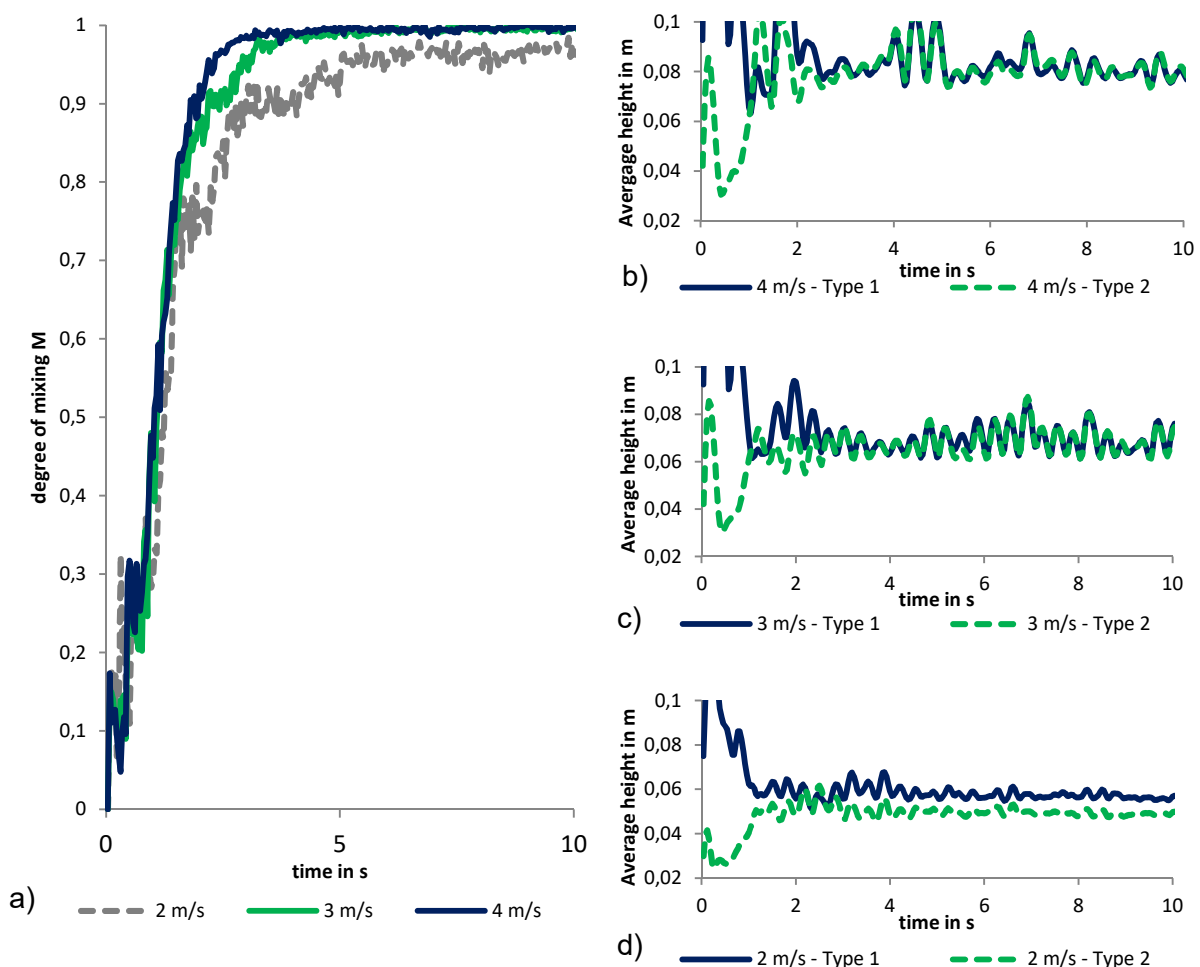


Fig. 5: (a): Degree of mixing M plotted against time and averaged particle heights of colors 1 and 2 for gas velocities: (b) 4 m/s, (c) 3 m/s and (d) 2 m/s.

In addition to the mixing behavior at different gas velocities the typical orientation of the investigated cylinders is represented in fig. 6 where orientation is calculated in accordance to [143]. Figs. 6a, 6c, 6e and 6g show results at gas velocities of 2 m/s, figs. 6b, 6d, 6f and 6h outline results obtained at gas velocities of 4 m/s, respectively. The particle orientation in the outer perimeter (1 cm inwards from the front and rear walls) of the fluidized bed is given in figs. 6a

and 6b. The orientation in the outer perimeter (1 cm from the side walls) is shown in figs. 6c and 6d. Results indicate that particles take up preferred orientations which are aligned parallel to the outer walls with 0° , 90° and 180° . The total number of particles that take up these orientations increases over time as particles line up side by side or atop of each other.

A comparison for the front/back walls in figs. 6a and 6b and side walls in figs. 6c and 6d indicates that at low gas velocities a larger number of particles can be found in the vicinity close to the walls. For clarity for the the front and back walls (figs. 6a and 6b) as well as side walls (figs. 6c and 6d) the x-axis is the principal axis to which the orientation vector is referred to. In case of low gas velocities more particles assume a preferred orientation of 0° and 180° (in sum) at the side walls and of 90° at the front/rear wall. Graphical examples for a single particle close to a front or side wall are illustrated in 4a and 4c, respectively. Larger gas velocities result in lower numbers of particles aligning close to the walls. Additionally, the number of these particles remains constant over time. A preferred overall orientation forms in the system with differences in the number of particles aligned parallel to the front and rear walls as well as side walls. Investigations over a number of initial bed setups (not shown in fig. 6) indicate that the preferred orientation is taken up randomly.

Time averaged data on the orientation with respect to the x-y-surface for the inner region at least 1cm away from the vessel walls of the fluidized bed is shown in figs. 6e and 6f at 2m/s and 4m/s, respectively. At lower gas velocities an influence from the outer regions into the interior of the bed is observable. This behavior is dismantled at larger gas velocities (4 m/s) where all orientations are equally distributed as it is the case for spheres where this behavior is independent of gas velocity.

Distributions in figs. 4g and 4h calculated for the x-z-plane indicate that at low gas velocities particles orient mainly aligned with the main flow direction, whereas at larger gas velocities no preferred orientation is taken up for cylinders of an aspect ratio of 1.

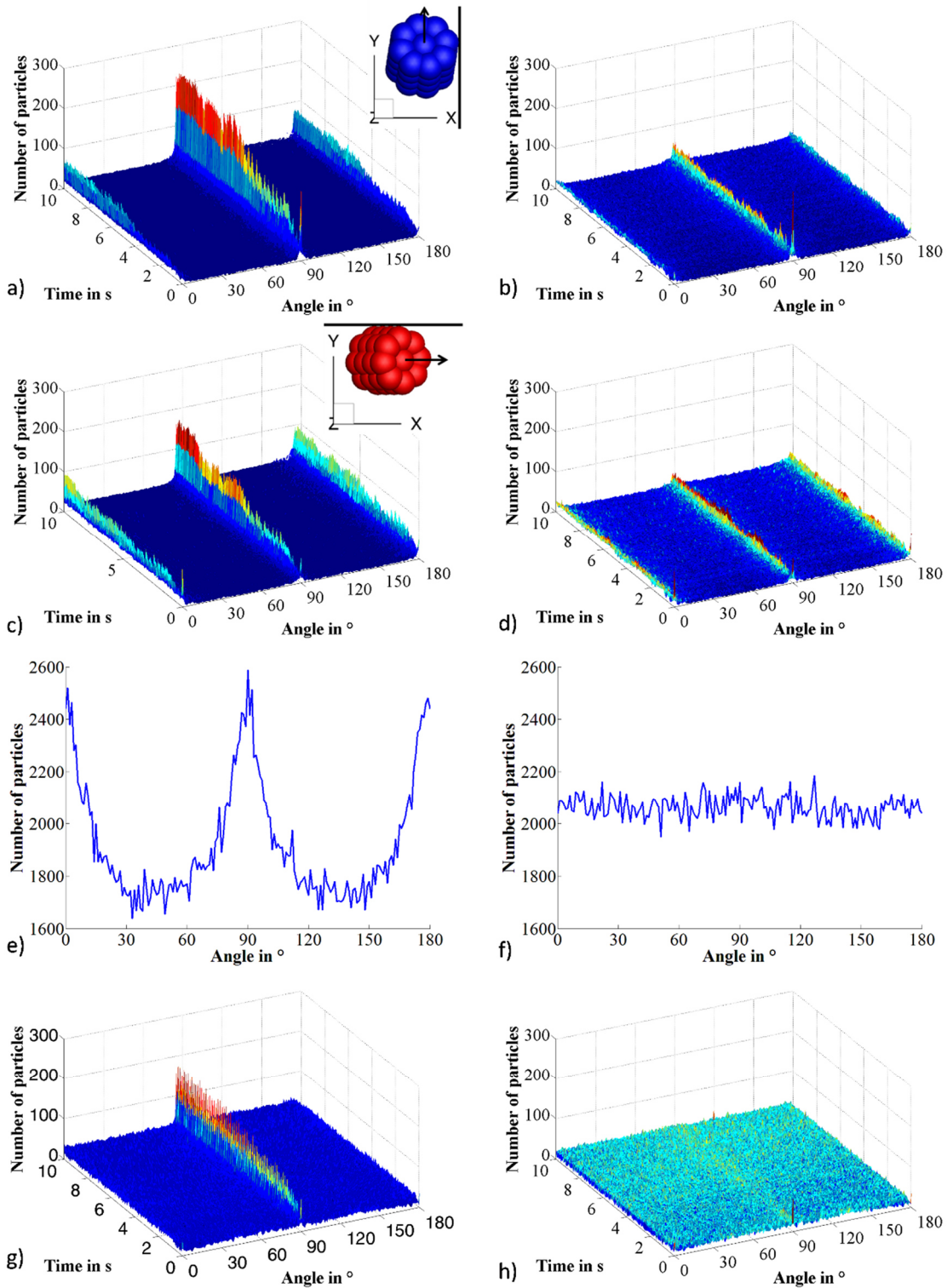


Figure 6: Distribution of the particle orientation for gas velocities of 2 m/s (a, c, e, g) and 4 m/s (b, d, f, h): (a, b) Orientation in the outer perimeter close to the front and rear wall, (c, d) close to the side walls based on the projection onto the x-y-plane over time, (e, f) time summarized orientation in the inner region based on the projection on the x-y-plane and (g, h) orientation over time in the inner region based on a projection on the x-z-plane.

4.2 Variation of the layer arrangement

In addition to the investigation on mixing behavior caused by different fluid velocities the mixing of differently orientated layers is analyzed in the second numerical variation which is performed at a gas velocity of 2 m/s. For this investigation the particles are colored in dependence on the x-, y- and z-coordinate (coloring in two fractions along the z-coordinate represents the base-case). Based on the actual particle position, particles are colored differently in case that their position is larger or smaller than the average value along the respective axis. Obtained results on mixing are shown in fig. 7.

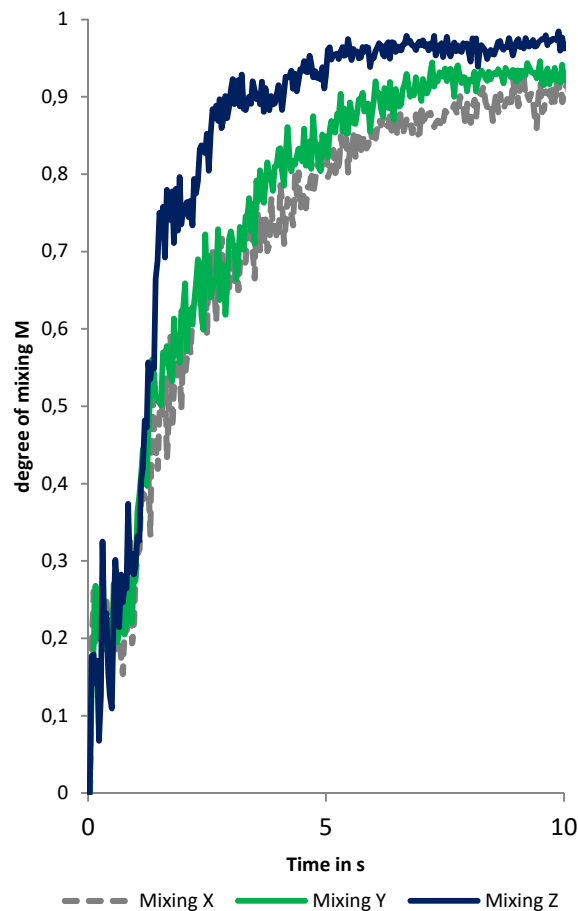


Fig. 7: Degree of mixing M plotted against time

The most intense mixing occurs vertically in the bed. In the horizontal directions mixing is slower; differences exist between x- and y-direction due to the formation of an overall particle alignment in the fluidized bed. No totally mixed state is obtained in the x- and y-direction as already observed for the z-direction at low gas velocities of 2 m/s.

4.3 Variation of the particle aspect ratio

The influence of the particle aspect ratio is studied by altering the aspect ratio from 1 to 0.28 (particle diameter 4 mm and length 14.3 mm) and further to 0.12 (particle diameter 3 mm and length 25.4 mm) while maintaining a constant particle volume. Particles are fluidized with a gas velocity of 3 m/s and represented by clustered spheres. Results on the mixing index M and the average heights of two differently colored vertical particle layers are shown in fig. 8.

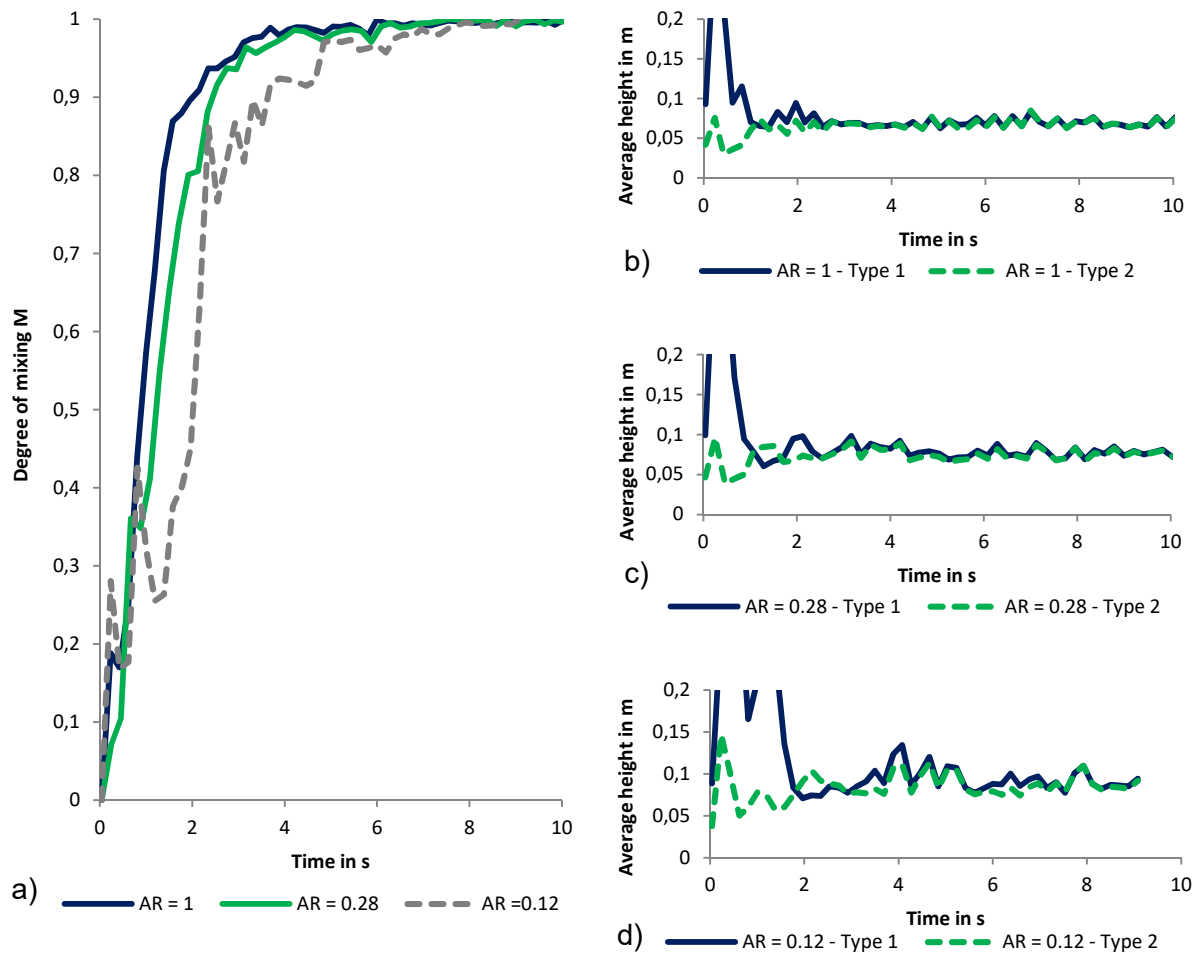


Fig. 8: (a): Degree of mixing M plotted against time and averaged particle heights of colors 1 and 2 for different particle aspect ratios: (b) 1, (c) 0.28 and (d) 0.12.

The results (fig. 8a) indicate that a decreasing particle aspect ratio leads to less intensive mixing if the same gas velocity is applied. Although, the same final mixing index is reached, the mixing progresses slower. The averaged bed heights of the two particle color fractions shown in figs. 8b, 8c and 8d increase with decreasing aspect ratio which is a result of a larger drag force component. The larger drag force value is caused through an increased surface area perpendicular to the flow when particles are aligned vertically in the fluidized bed. The projection area in horizontal direction decreases with a lower aspect ratio and aligned with this decreases the number of particles taking up preferred orientations (see fig. 9 e-f and fig. 13 f).

Therefore, more particles exist with a larger crosswise area in comparison to the base-case. Fluctuations of the averaged heights in figs. 8b and 8c are rather smooth whereas smaller aspect ratios lead to abrupt oscillations due to strong differences in the overall particle surface area resulting out of changes in orientation.

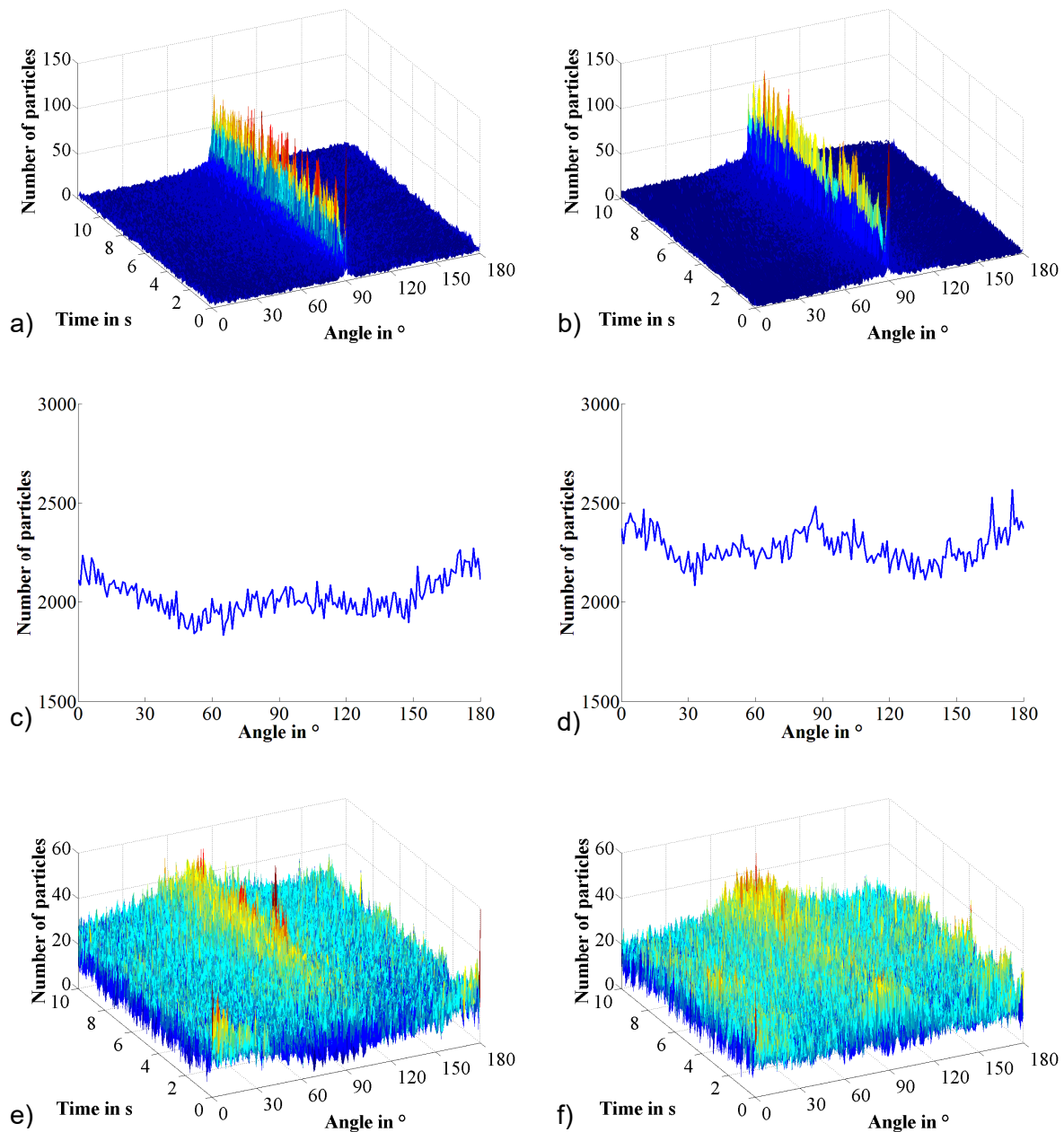


Fig. 9: Distribution of the particle orientation for particle aspect ratios of 0.12 (a, c, e) and 0.28 (b, d, f) : (a, b) Orientation in the outer perimeter close to the front and rear wall, (c, d) time summarized orientation in the inner region based on the projection on the x-y-plane and (e, f) orientation over time in the inner area based on a projection on the x-z-plane.

Results on the obtained orientations of particles with an aspect ratio of 0.12, 0.28 are shown in fig. 9 and can readily be compared against the obtained results for cylindrical particles of an aspect ratio of 1 shown in fig. 13 b, d, f. Figs. 9a – 9e refer to aspect ratios of 0.12 and figs. 9b – 9f to aspect ratios of 0.28, respectively. The particle orientations in the region close to the

front and rear wall is outlined in figs. 9a and 9b. For the two aspect ratios considered, preferred orientations of 90° are taken up by the cylindrical particles in contrast to tendencies observed for particles of aspect ratio of 1 to also take up orientations of 0° or 180° to some extent. Additionally, the number of particles with an orientation parallel to the walls does not change significantly over time (figs. 9a, 9b). In the inner region of the fluidized bed particles with very low aspect ratios are not clearly oriented with 0° , 90° and 180° although weak maxima are still to be identified (figs. 9c and 9d). In contrast to particles of aspect ratio of 1, particles with 0.28 and 0.12 obtain more equally distributed orientations with a weak peak at 90° indicating an upright position when the orientation vector is projected into the x-z-plane (figs. 9g and 9h).

4.4 Variation of density

The density of the particles was investigated in case 4. Densities were chosen with 1380 kg/m^3 in accordance to polyoxymethylene (POM), 1691 kg/m^3 and 2380 kg/m^3 . The density of 1691 kg/m^3 compensates for the volume underrepresentation by clustering spheres as done in the base-case configuration (tab. 2).

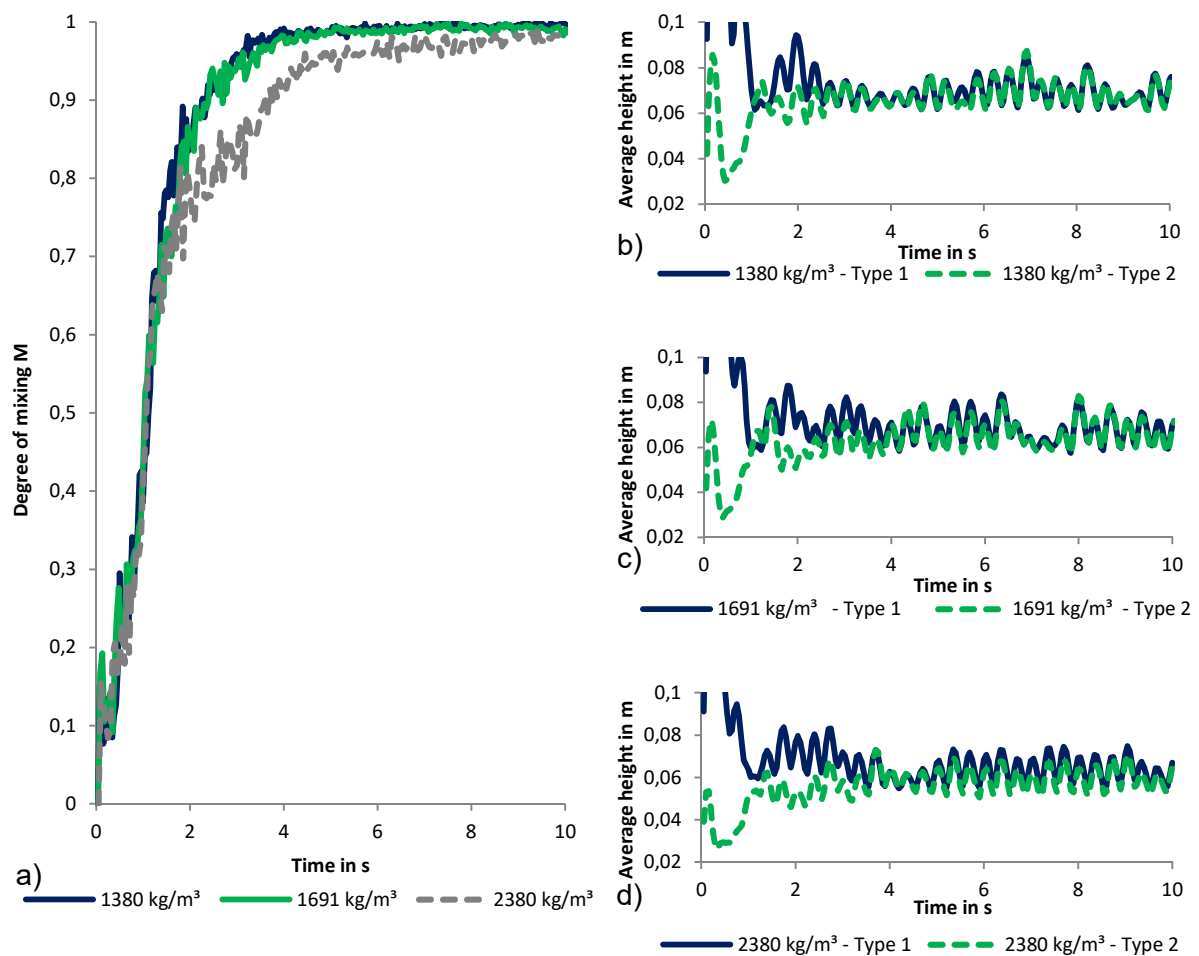


Fig. 10: (a): Degree of mixing M plotted against time and averaged particle heights of colors 1 and 2 for different particle densities: (b) 1380 kg/m^3 , (c) 1691 kg/m^3 and (d) 2380 kg/m^3 .

The degree of mixing M is shown in fig. 10 as well as the average heights of two differently colored vertical particle layers. A change in density from 1380 kg/m^3 to 1691 kg/m^3 which compensates for the volume misrepresentation of the base-case in comparison to an ideal cylinder does not alter the mixing behavior in the fluidized bed significantly (fig. 10a). At densities of 2380 kg/m^3 the particles mix significantly slower. Final degrees of mixing M obtained are equal independent of the densities of the particles. The progression and absolute value of the averaged heights for densities of 1380 kg/m^3 and 1691 kg/m^3 are alike. The enhanced density of 2380 kg/m^3 leads to lower final averaged particle heights and in comparison to lower densities heights of particle type 1 and 2 converge at a later point in time.

4.5 Variation of the sphere quota

In the fifth investigation the sphere quota is varied for the base-case configuration where gas at a velocity of 3 m/s is inserted into the fluidized bed. The cylindrical particles are replaced by 50 % and 100 % by volume equivalent spheres. By replacing the cylindrical particles by 100 % with spheres mixing is progressing slower as shown in fig. 11a.

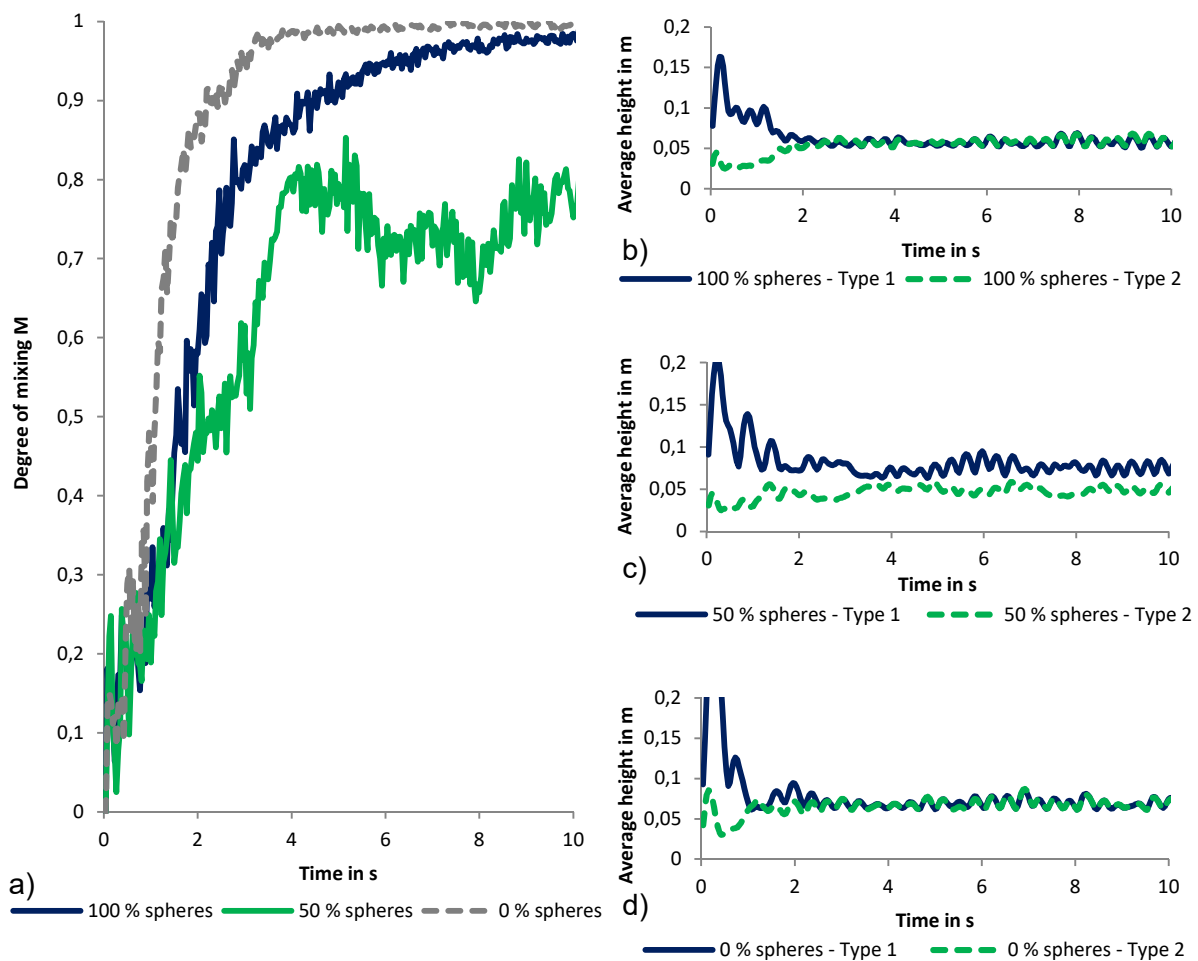


Fig. 11: (a): Degree of mixing M plotted against time and averaged particle heights for the simulations with (a) 100 %, (b) 50 % and (c) 0 % spheres.

A possible explanation is the larger surface area of cylindrical particles in comparison to spheres. This leads to larger particle/fluid forces which enhance mixing in contrast to spherical particles. A mixture of spheres and cylindrical particles does not obtain a state of complete mixing as visible from fig. 11a where final values for the mixing index M are obtained with only 0.7 - 0.8. The averaged heights obtained for spheres converge quickly (fig. 11b) and converge to smaller values than the cylinders with a larger surface area (fig. 11d).

The averaged particle height plotted in fig. 11c reveals the reason for the slow and incomplete mixing visible in fig. 11a. Spheres and cylinders tend to segregate due to differences in the surface areas and obtain non-equal averaged particle heights.

4.6 Variation of the cluster approximation accuracy

The influence of the approximation accuracy on mixing and the orientation for the base-case configuration in case of clusters is investigated in the following at a fluid velocity of 3 m/s. Results are shown in fig. 12 for a particle representation with 36 spheres in contrast to a cluster consisting of only 12 spheres of larger diameter with $d = 3.5$ mm. The coarse approximation matches the original cylinder volume by 76.04 % in comparison to the base-case with 81.4 %.

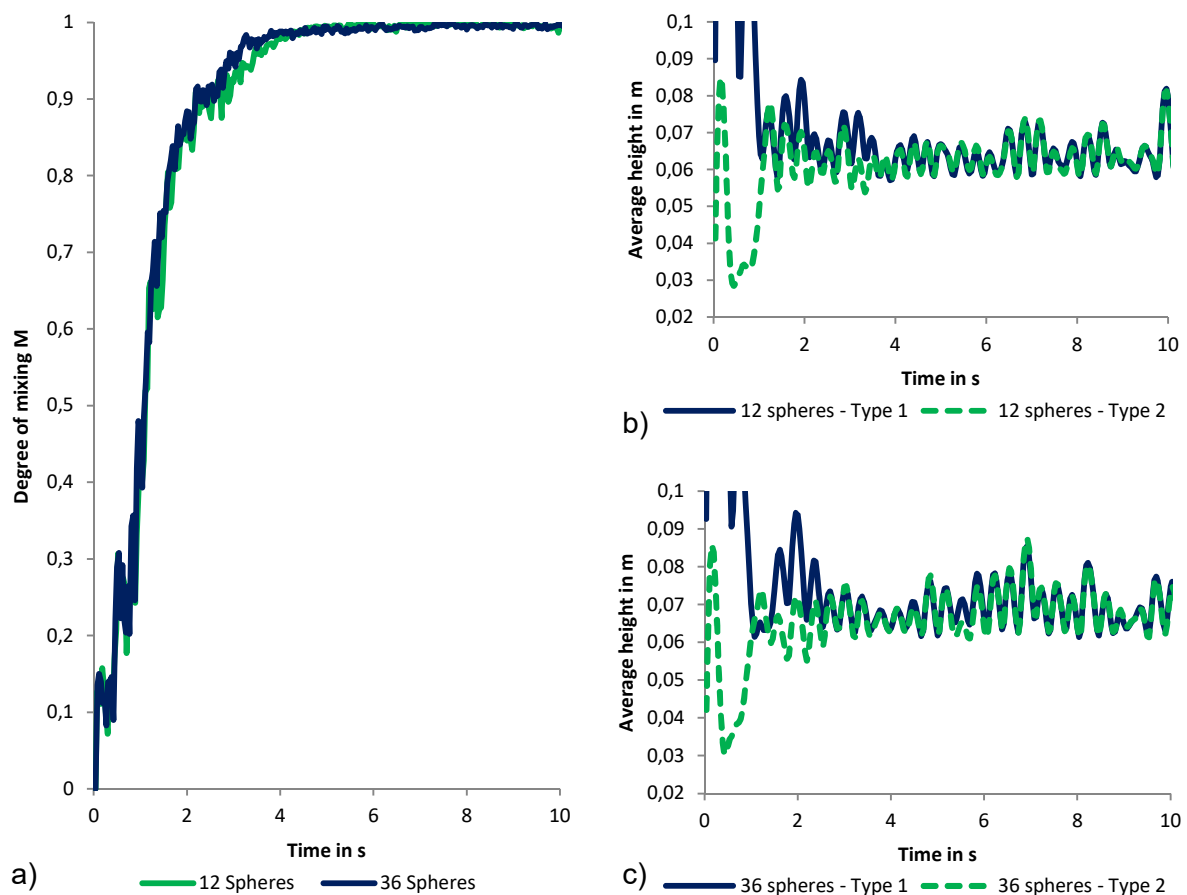


Fig. 12: (a): Degree of mixing M plotted against time and averaged particle heights for cylinders represented as clusters consisting of: (b) 12 and (c) 36 spheres.

Results in fig. 12a reveal no significant differences in terms of the degree of mixing for the two levels of detail used for the approximation. The average particle heights are elevated for a more accurate cylinder approximation because of larger calculated projection areas.

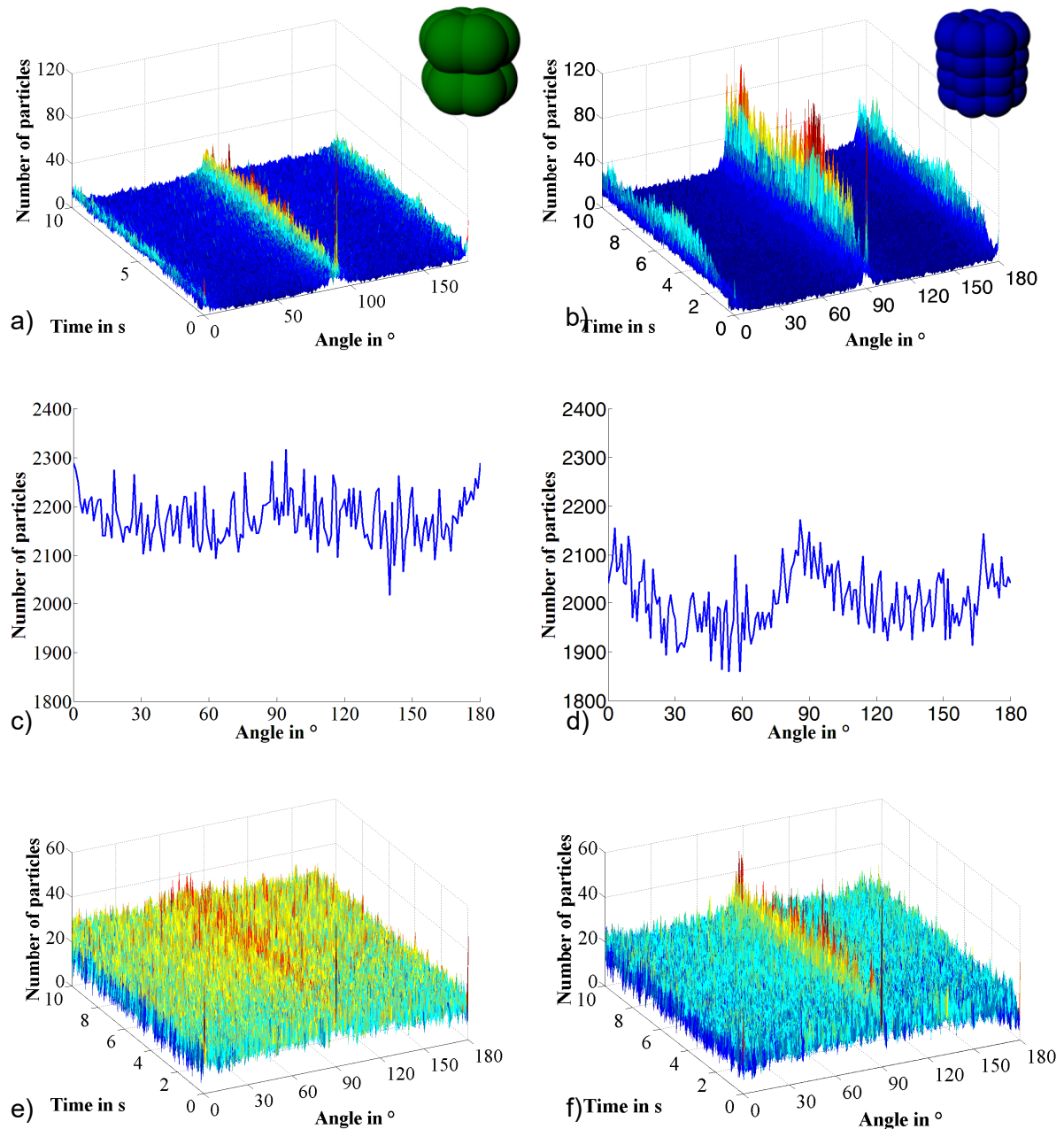


Fig. 13: Distribution of the particle orientation for particle approximations with 12 (a, c, e) and 36 (b, d, f) spheres: (a, b) Orientation in the outer perimeter close to the front and rear wall, (c, d) time summarized orientation in the inner region based on the projection on the x-y-plane and (e, f) orientation over time in the inner area based on a projection on the x-z-plane.

Significant differences, however, are observable for the distribution of the orientations, as outlined in fig. 13. In the outer regions along both front, rear and side walls which are not shown in fig. 13 the coarse multi-sphere cylinder has much less pronounced peaks at 0° , 90° and 180° compared to the more accurately represented cylinder shape. Intermediate values be-

sides 0° , 90° and 180° are much more common for the coarse cluster approximation. Additionally, orientations perpendicular to the walls are nearly as common as orientations aligned to the wall (fig. 13a). In contrast to lower and larger gas velocities (comp. figs. 6a – 6d) the number of particles aligned with the walls are undergoing changes due to dynamic particle regrouping processes. In the center of the fluidized bed the orientation of the coarsely represented particles is nearly equally distributed (fig. 13c). In contrast more accurately represented particles still have preferred orientations even at gas velocities of 3 m/s which are in alignment with one of the wall orientations of 0° , 90° or 180° (fig. 13d). During fluidization detailed approximated particles are mainly in an upright position as shown in fig. 13f. In contrast coarsely approximated particles are mainly equally distributed. Upright positions are more common than other orientations, but distribution maxima are much less pronounced (fig. 13e).

4.7 Variation of the polyhedron approximation accuracy

In addition to the investigation on the cluster approximation accuracy, cylinders were represented by polyhedrons on different levels of detail, see fig. 15 top for a gas velocity of 3 m/s.

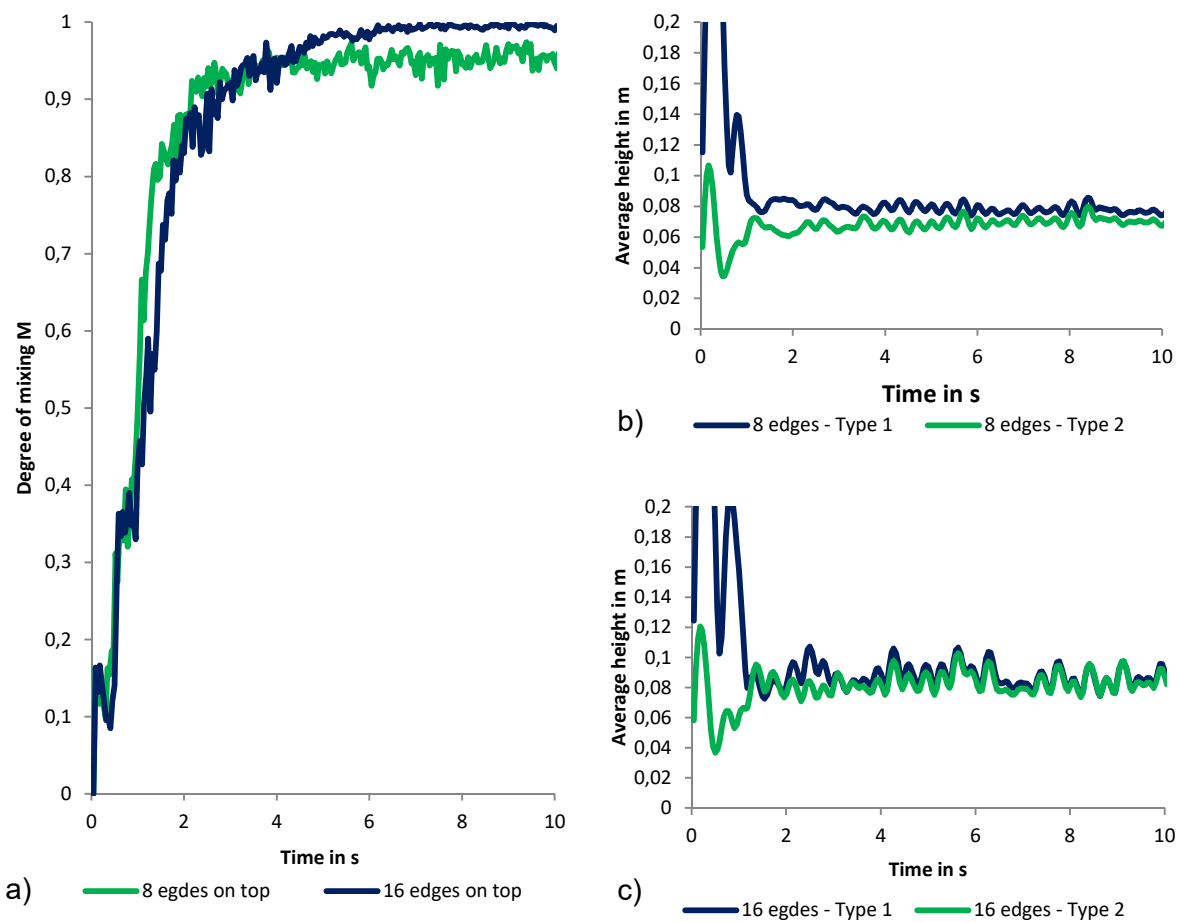


Fig. 14: (a): Degree of mixing M plotted against time and averaged heights for: (b) a rough cylinder approximation with 8 edges and (c) a fine cylinder approximation with 16 edges.

The first polyhedron consists of 8 edges in circumferential direction and the second one is approximated with doubled precision by 16 edges. The layout of the polyhedron with 8 edges is designed analogously to the cluster consisting out of 36 spheres grouped in 4 layers. Polyhedrons have the advantage that nearly every shape can be illustrated and edges are angular in contrast to those of clustered spheres. On the other hand, the computational effort is significantly larger compared to simulations involving clustered spheres, which is a result of the time consuming iterative contact detection during calculation [55]. The 8 edges approximation matches the original cylinder volume by 90 %, the 16 edges approximation by 97.44 %. Obtained results on mixing are depicted in fig. 14.

Up to a time of 2 s, the simulation results on the degree of mixing M of both polyhedron approximations progress similarly (fig. 14a). Mixing is slower than compared to the clustered sphere approximations (fig. 12a) which could be a result of the more accurate volume representation of the polyhedron-shaped particles resulting in a larger mass of the particles in the simulations. Initially the 8 sided polyhedrons mix slightly quicker than the 16 edges polyhedrons which may be also a result of the weight difference. After a time of 4 s the 16 sided polyhedrons continue to mix and a fully mixed state is obtained at a time of 6 s. In contrast the polyhedrons consisting of 8 edges in circumferential direction mixing stagnates at a mixing degree of $M=0.95$ which is a result of their blockiness. The averaged bed heights of particles of type 1 and 2 for the two shape accuracy levels are shown in figs. 14b and 14c. Both, the mass and the cross sectional area of the clustered sphere particles is lower than that of the polyhedron particles. The first parameter leads to an increased, the second decreases the obtainable bed height. In total the bed heights of the polyhedron shaped particles are larger (figs. 14b and 14c) than the heights of the clustered spheres (figs. 12b and 12c). The slow convergence of the two heights in fig. 14b underlines the slow mixing of the particles in the fluidized bed.

The distribution of the particle orientation over time close to the front and rear wall is shown in figs. 15a and 15b. Both cases indicate preferred orientations for the angles 0° , 90° and 180° which are in good agreement with the clustered-sphere simulations. In contrast to the clustered spheres the coarse approximation in case of polyhedrons leads to an inclined number of particles orienting aligned with the walls. In the interior of the bed (figs. 15c and 15d) particles take up positions well aligned with the results of the clustered-spheres consisting of 36 sub-spheres in case of an projection of the orientation vector onto the x - y -plane. No significant differences are observable in the distribution between the approximation with 8 and 16 edges. In contrast significant results are visible for the number of particles taking up an upright position in the bed. In case of a coarser approximation the number of polyhedrons standing upright is larger compared to a case where the approximation is chosen finer.

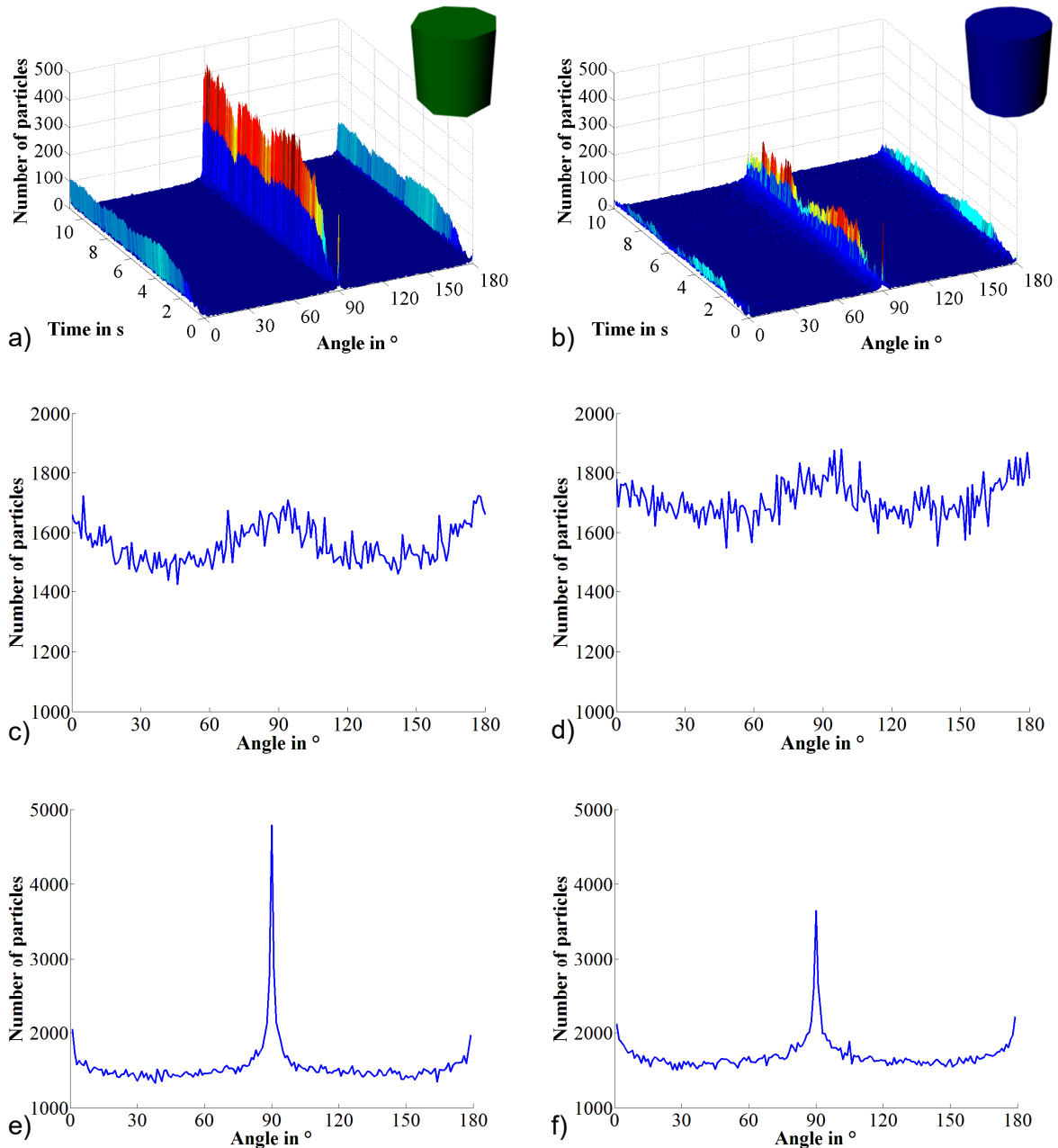


Fig. 15: Distribution of the particle orientation for particle approximations with 8 (a, c, e) and 16 (b, d, f) edges: (a, b) Orientation in the outer perimeter close to the front and rear wall, (c, d) time summarized orientation in the inner region based on the projection on the x-y-plane and (e, f) summarized orientation in the inner area based on a projection on the x-z-plane.

4.8 Variation of the drag force models

To investigate the influence of the drag force model on mixing the approach by Di Felice [42] (see Eqs. 9 and 10) and Rong et al. [44] (see Eqs. 9 and 11) in combination with the single particle force model by Hölzer and Sommerfeld [48] (see Eq. 12) and the combination of Ergun [38] / Wen and Yu [182] (see Eqs. 13 and 14) are applied for a gas velocity of 3 m/s. Results in terms of mixing are shown in fig. 16.

The progression of the degree of mixing M for the drag force model by Di Felice [42] and Rong et al. [44] in combination with [48] show a good agreement (fig. 16a). However, deviations occur by using spheres with a volume-equivalent diameter. In this case it takes significantly more time ($\Delta t=2$ s) until the system completely mixes. This is due to the fact that particles take up different orientations with varying cross sectional areas for [42],[44],[48] in contrast to [38],[182] applied to volume equivalent spheres. The variations resulting from [42],[44],[48] enhance mixing. The development of the average heights is very similar for the first two models [42],[44],[48] (figs. 16b and 16c). The third model [38],[182] obtains lower averaged heights (fig. 16d). It should be noted that under the boundary conditions considered here the results of the models by Di Felice and Rong et al. are only deviating minimally. No interpretation on the exactness of the models is possible through the investigations performed here. Additional experimental investigations are required to elaborate this.

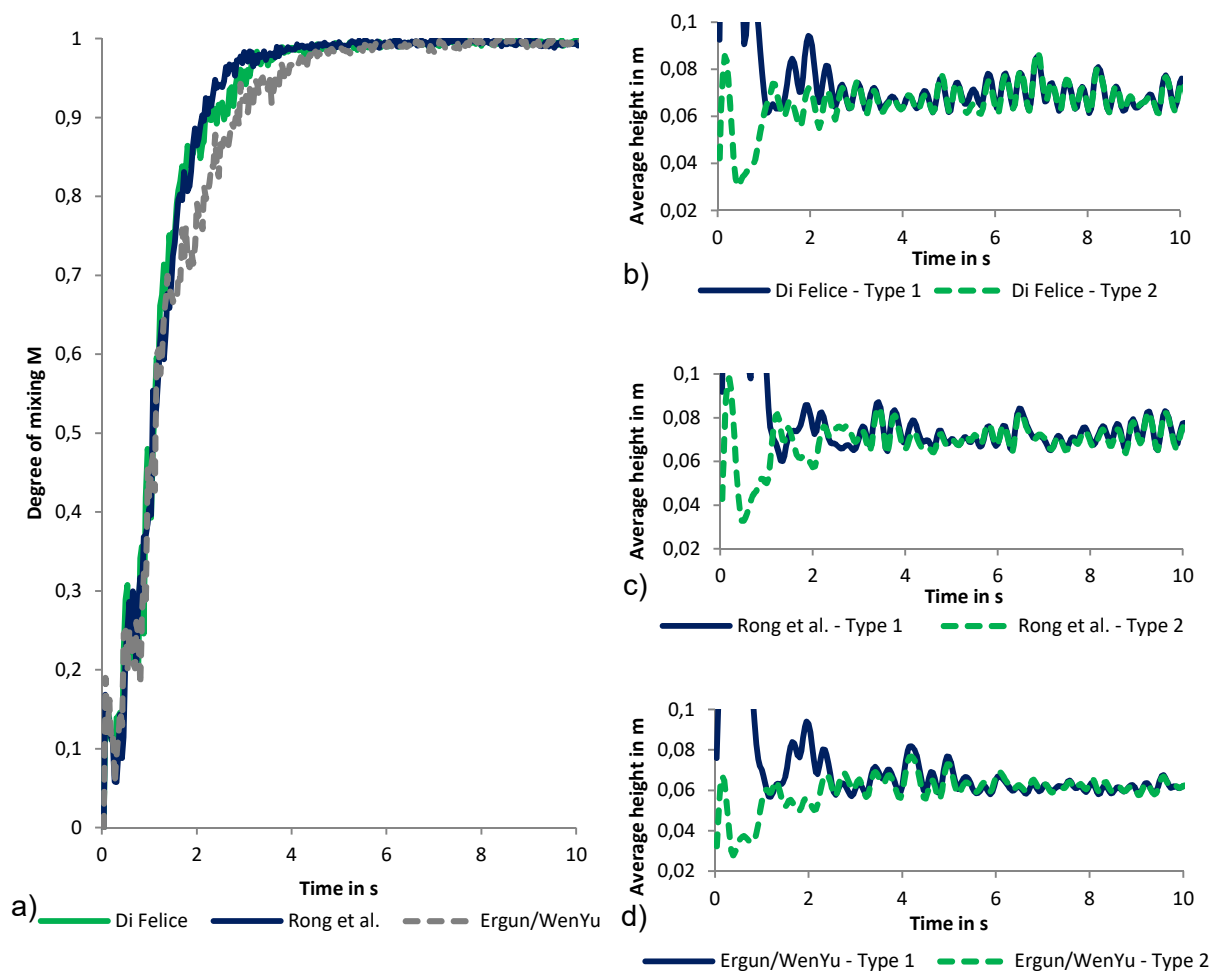


Fig. 16: (a): Degree of mixing M plotted against time and averaged heights for the drag force model by: (b) Di Felice [42] and (c) Rong et al. [44] and (d) Ergun [38] / Wen and Yu [182].

4.9 Variation of the grid accuracy

In a further investigation a grid study was performed to investigate the influence of the grid solution on the mixing in the base-case configuration. As a comparison, the base-case with 11x11x41 cells referred to as fine grid, with 7x7x26 cells referred to as medium grid and with 4x4x15 cells referred to as rough grid are considered. The degree of mixing M and the average heights are plotted in fig. 17. It is noticeable that all cases have different mixing behaviors (fig. 17a). With 8 seconds it takes twice as long until the particles are completely mixed using the rough grid compared to the fine grid. The mixing behavior obtained on the medium grid is bounded by both coarse and fine grid. When examining the average heights, it is remarkable that the rough grid induces very strong height fluctuations at low frequency compared to the medium and the fine grid. Furthermore, the particle height in average is enlarged by using a rough grid.

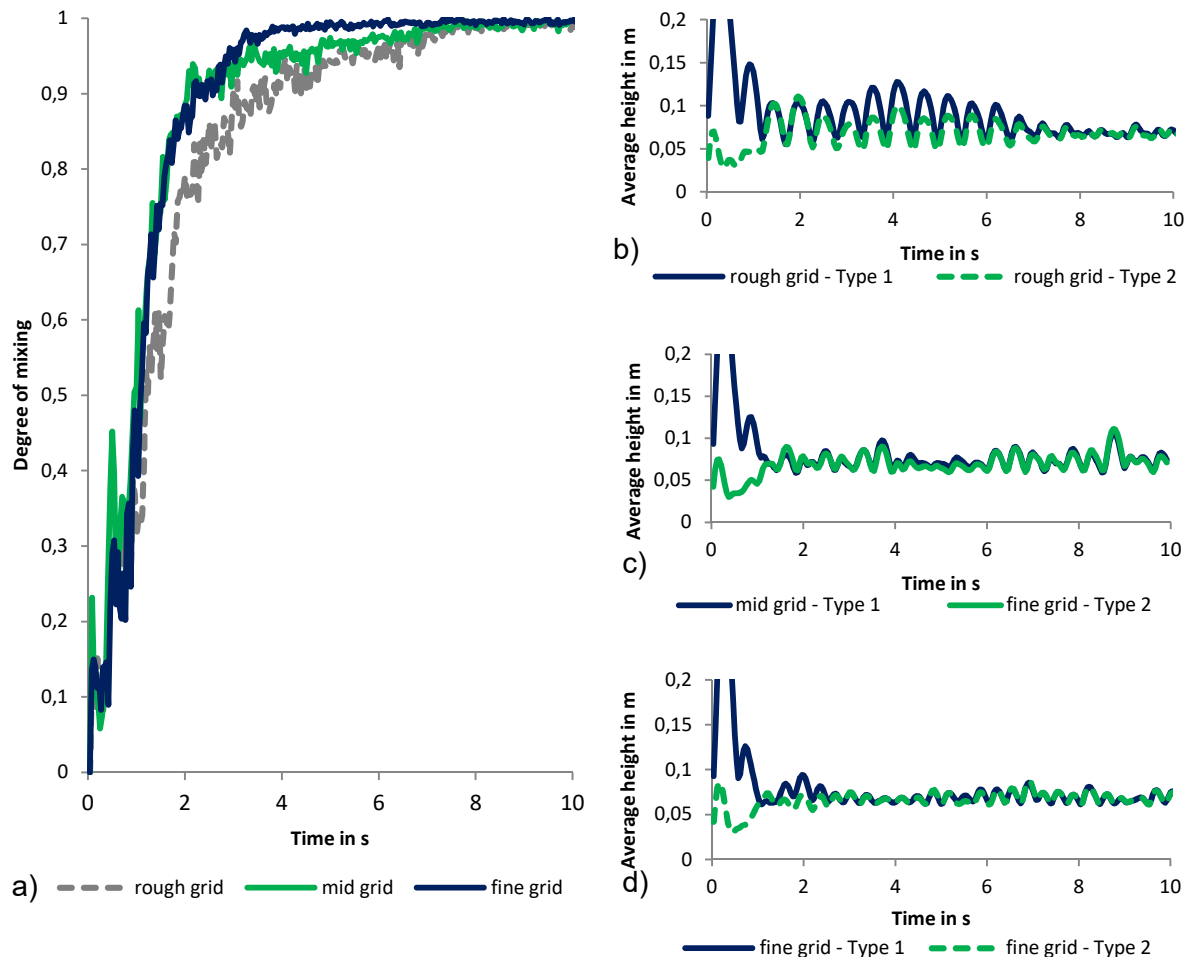


Fig. 17: (a): Degree of mixing M plotted against time and averaged heights for: (b) Rough grid approximation (4x4x15 cells) and (c) fine grid approximation (11x11x41 cells).

4.10 Variation of shape

In the last investigation different particle shapes are considered. Here, parallelepipedal shapes with the sizes of $6 \times 6 \times 5 \text{ mm}^3$ and $10 \times 9 \times 2 \text{ mm}^3$ are treated instead of the volume equivalent cylindrical shape from the base-case. The volume is again equivalent to a 7mm diameter sphere. Rectangles are fully describable as polyhedrons, which favors the use of this approximation. Each polyhedron can be represented by only 8 points, 12 triangles and 18 edges. In contrast, the rough cylinder requires 26 points, 48 triangles and 72 edges. The results on mixing are shown in fig. 18. Due to their geometric differences the mixture curves of the cuboid and plate are different. The plate like particles reach values of $M=1$ where the cuboids obtain values of only $M=0.85$. The reason for the improved mixing behavior can be seen in the obtained particle heights which are in favor for the plate-like shape (figs. 18 b and 18c). The results regarding the orientation are shown in fig. 19.

In fact, only the angles 0° , 90° and 180° occur as peaks for all three simulations in the interior of the fluidized bed. This stands well in agreement to the coarse polyhedron case (figs. 15c – 15f). Both probabilities to be positioned on the side and on the front or back are equally given for both particle shapes (figs. 19a – 19d).

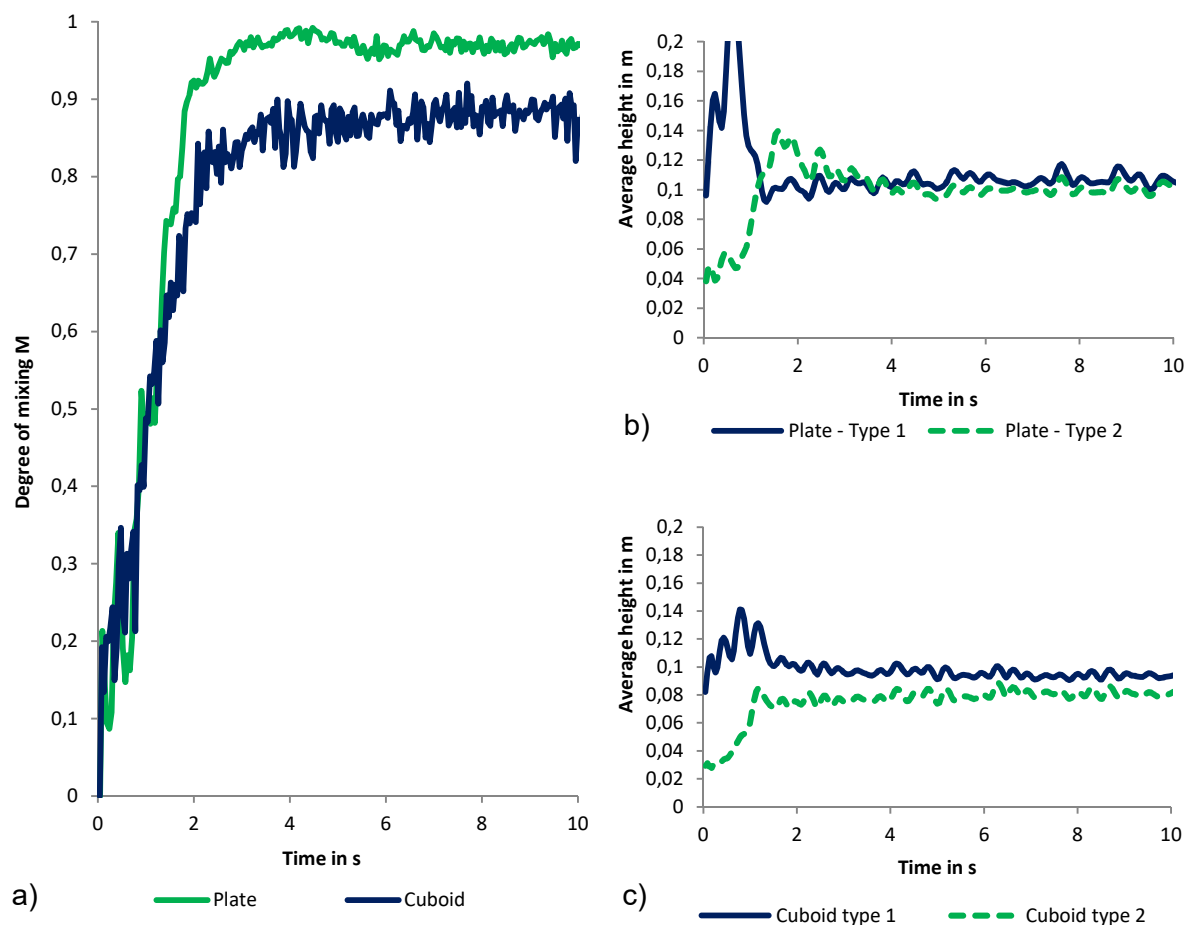


Fig. 18: a): Degree of mixing M plotted against time and averaged heights for: (b) plate shaped particle and (c) a cuboid.

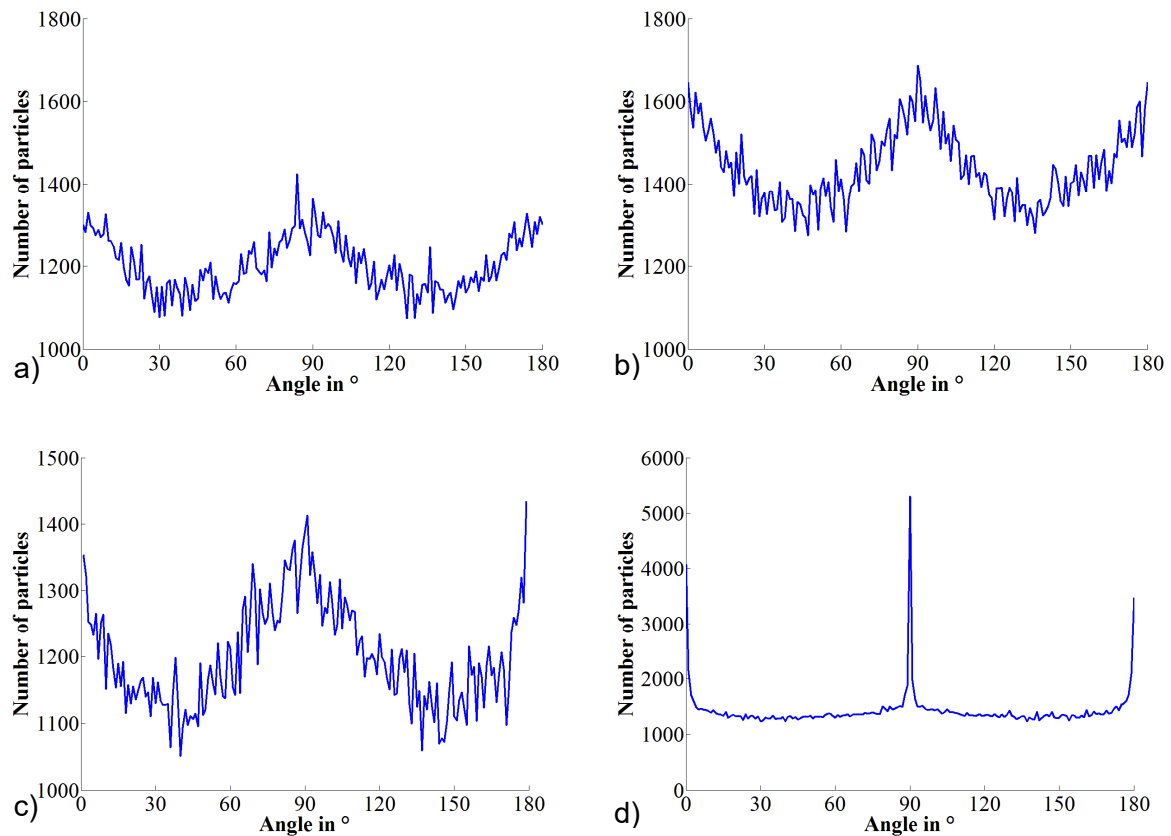


Fig. 19: Distribution of the particle orientation for a plate (a, c) and a cuboid (b, d): (a, b) Time summarized orientation in the inner region based on the projection on the x-y-plane and (c, d) time summarized orientation in the inner area based on a projection on the x-z-plane.

5. Conclusions

A numerical investigation of mixing in a model type fluidized bed is performed based on the three-dimensional discrete element method coupled with computational fluid dynamics (CFD). Therefore, a DEM/CFD-framework was extended allowing the consideration of clustered-spheres and polyhedrons as shape representation approaches. Results are very rich in details. The following conclusions can be drawn from this study with regard to mixing and orientations taken up by the particles:

- Gas velocity enhances mixing in case of complex shaped particles. Due to the influence of the cross-sectional area low gas velocities can lead to an incomplete mixing in comparison to spheres. It is confirmed that horizontal mixing is stronger than vertical mixing. Additionally, elongated particles (decreasing aspect ratios) tend to mix slower with increasing elongation. Smaller changes in density do have a weak influence on the progression of mixing. In case of strong variations of the particle density, bed expansion is reduced and mixing slowed down. Mixtures of spheres and complex shaped volume

equivalent particles reveal the tendency to segregate under certain operational parameters. Weakly elongated particles reveal the tendency to mix quicker than spheres due to larger variations of the cross-sectional area resulting out of rotational motion which induces differences in the particle/fluid-forces and thereby enhances mixing. The representation accuracy in both cases (clustered-spheres as well as polyhedrons) has strong influence on the particle mixing due to differences in the particle weight, the crosswise-surface area and sphericity as well as the differences in the inertia tensor. For clustered-spheres reduced approximation accuracies enhance mixing; in case of polyhedrons mixing is slowed down due to enlarged blockiness. Recently developed models [44] do not affect mixing significantly in contrast to models like [42], whereas the application of models which do not represent the change in crosswise particle area due to rotations do influence mixing results strongly. Different shapes are attributed to very different mixing behavior in case that the elongation is varied.

- In fluidized beds different regions can be identified which are either close to the walls or in the interior of the bed. Elongated particles tend to align parallel to the walls of the vessel where an overall preferred orientation is taken up by the particles. A smaller number of particles take up orientations perpendicular to the walls. Orientation in the outer region of the bed influence particles in the interior of the bed. At elevated gas velocity and with decreasing sharpness/increasing roundness particles tend to be equally distributed. Elongated particles seem to take up preferably upright positions.

The obtained results are numerical. The current state of the particle fluid coupling in DEM/CFD-frameworks requires further investigations and model advances [11],[143],[44],[184]. Especially, for elongated particles the effect of disregarding certain particle/fluid forces and moments as well as not resolving flow in detail is so far not fully understood. For the future experimental investigations have to be performed that provide a validation of the numerically observed phenomena. It has to be analyzed to which extent DEM/CFD-simulations can represent real particle/fluid systems involving complex shaped particles with the currently available models.

Acknowledgements

Financial support by the DFG - KR 3446/6-1 is greatly acknowledged.

III. Numerical Investigation of the Mixing of Non-Spherical Particles in Fluidized Beds and during Pneumatic Conveying

Tobias Oschmann^{a,*}, Kevin Vollmari^a, Harald Kruggel-Emden^a, Siegmar Wirtz^a

^aRuhr-University Bochum, Department of Energy Plant Technology, Bochum, Germany

The following accepted manuscript appeared as journal version in Oschmann T., Vollmari K., Kruggel-Emden H., Wirtz S., 2014, Numerical Investigation of Mixing of Non-Spherical Particles in Fluidized Beds and during Pneumatic Conveying, 7th World Congress on Particle Technology, Beijing, China. and may be found at <https://doi.org/10.1016/j.proeng.2015.01.220>.

Abstract

Fluidized beds as well as pneumatic conveying are of high relevance to many processes in chemical engineering and energy technology. A possible framework to describe these systems is to use a combined Computational Fluid Dynamics (CFD) - Discrete Element Method (DEM) approach. All particles in the system are addressed by solving the Newtonian and Eulerian equations of motion. The fluid flow is resolved through the Navier-Stokes equations using the finite-volume method. In recent years, simulations focused mainly on spherical particles, although real bulk solids consist of complex shaped particles. For these particles, contrary to spheres, an important factor that plays a fundamental role in describing their principal behavior is the orientation which can be accurately expressed by a number of rotation parameters. So far only few CFD-DEM studies have been performed in order to investigate particle-fluid systems of complex shaped particles. Especially mixing is not well understood for non-spherical particles in the context of a CFD-DEM coupling.

We performed CFD-DEM simulations of a model type fluidized bed as well as of a pipe bend being part of a pneumatic conveying system in order to investigate the influence of particle shape on mixing. Results indicate that mixing is strongly influenced. Hence, the coupled CFD-DEM framework using complex shaped particles captures the system behavior more detailed than by using spheres and gives a better understanding of mixing phenomena.

© 2014 The Authors. Published by Elsevier Ltd.

Selection and peer-review under responsibility of Chinese Society of Particuology, Institute of Process Engineering, Chinese Academy of Sciences (CAS).

Keywords: fluidized bed; pneumatic conveying; pipe bend; simulation; CFD-DEM-approach; complex shaped particles; mixing

* Corresponding author. Tel.: +49-234-32-26334 ; fax: +49-234-32-14227 .

E-mail address: oschmann@leat.rub.de

1. Introduction

Many investigations have addressed spherical particles in the context of the CFD-DEM-methodology [95,133,141,146,147,150,152,165]; so far only few particle/gas-systems were studied involving complex shaped bodies. The fluid/particle interaction of monodisperse particles in a fluidized bed was addressed by Zhong et al. [142] for cylindrical particles approximated by clustered spheres. Generally obtained flow features in the simulations matched those in corresponding experiments. As fluid/particle forces only drag forces derived from the model of Tran Cong et al. [168] were taken into account. Hilton et al. [40] analyzed systems of fluidized monodisperse superellipsoids within a CFD-DEM-framework. As drag force model, the approach of Hölzer and Sommerfeld [48] was coupled with a model for the representation of the void fraction by Di Felice [42]. Hilton et al. [40] were able to show that the pressure drop during the onset of fluidization calculated from the sphericity corrected Ergun equation [38] significantly differed from results where the drag force of particles was based on the cross sectional area of individual particles. In a further study Hilton and Cleary [11] investigated the pneumatic transport of monodisperse superellipsoids. In addition to the drag force, rotational drag and, Magnus and Saffman lift forces were considered based on models available for spherical particles [8]. The investigation revealed different flow modes and the dependencies for their transition. Hilton and Cleary also investigated raceway formation resulting from gas injected into a particle bed consisting of complex shaped objects [169]. A similar model framework to that of Hilton et al. [40] was applied by Zhou et al. [143] to investigate the behavior of prolate and oblate ellipsoids in a fluidized bed. A CFD-DEM-framework for modeling corn shaped particles represented by clustered spheres was proposed recently [144] and applied to a spouted bed and validated against experiments. In a further study it was successfully applied to mixing of non-spherical particles for the first time [145]. Simulation conditions and their influence on the mixing in fluidized beds of complex shaped particles were thoroughly addressed by Oschmann et al. [185].

Although mixing was widely investigated for fluidized beds [95,133,165] and in some cases for pneumatic conveying [186] involving spherical particles for a wide range of operational parameters within the CFD-DEM-method, it is considered for particle/gas systems with particles of complex shape only in singular cases. Even coupled modeling frameworks involving non-spherical shapes not focusing on mixing were applied only in few studies. The general applicability and sensitivity of these frameworks still has to be tested. To extend the knowledge on these important aspects of fluidized systems the current study is performed focusing on the mixing of volume equivalent particles in fluidized beds as well as pneumatic conveying.

2. Methodology

In the coupled CFD-DEM-method the particle motion is represented within a DEM-framework, while the fluid phase is represented by solving the volume averaged Navier-Stokes equations [8]. In the discrete element method the translational and rotational motion is obtained by integrating Newton's and Euler's equations for each particle given in general form for arbitrarily shaped particles by

$$m_i \frac{d^2 \vec{x}_i}{dt^2} = \vec{F}_i^c + \vec{F}_i^{pf} + \vec{F}_i^g \quad (1)$$

$$\hat{I}_i \frac{d\vec{W}_i}{dt} + \vec{W}_i \times (\hat{I}_i \vec{W}_i) = \Lambda_i^{-1} \vec{M}_i, \quad (2)$$

with particle mass m_i , particle acceleration $d^2 \vec{x}_i / dt^2$, contact force \vec{F}_i^c , particle/fluid force \vec{F}_i^{pf} , gravitational force \vec{F}_i^g , angular acceleration $d\vec{W}_i / dt$, angular velocity \vec{W}_i , external moment resulting from contact or particle/fluid forces \vec{M}_i , the inertia tensor along the principal axis \hat{I}_i and the rotation matrix converting a vector from the inertial into the body fixed frame Λ_i^{-1} . The equations for translational and rotational motion are solved by explicit integration schemes [12]. A flexible approach to model complex shaped particles in the discrete element method is the multi-sphere or polyhedron method. In the multi-sphere method arbitrary sized spheres are clustered to resemble the desired complex particle shape [54]. In the polyhedron method a triangular surface mesh is applied to represent the desired particle shape and a common plane algorithm is used for contact detection of the individual vertexes representing the particle surface [55]. In both methods contact force laws are applied similarly as used for spherical particles [23,187]. The normal component of the contact forces is obtained from a linear spring damper model

$$\vec{F}^n = k^n \delta \vec{n} + \gamma^n \vec{v}_{rel}^n, \quad (3)$$

where k^n is the spring stiffness, δ the virtual overlap, \vec{n} a normal vector, γ^n a damping coefficient and \vec{v}_{rel}^n the normal velocity in the contact point. Both k^n and γ^n determine the coefficient of normal restitution between particles e_{pp}^n as well as particles and walls e_{pw}^n . For the calculation of the tangential forces a linear spring limited by the Coulomb condition is used

$$\vec{F}^t = \min(k^t |\vec{\xi}^t|, \mu_C |\vec{F}^n|) \vec{t} \quad (4)$$

where k' is the stiffness of a linear spring, μ_c is the friction coefficient, $\vec{\xi}^t$ is the relative tangential displacement and \vec{t} is the tangential unit vector. Rotational friction is neglected in the investigation here.

The fluid phase is described with Computational Fluid Dynamics (CFD) in an Eulerian framework, in which the interior of the fluidized bed is meshed with equal cells. The fluid velocity is addressed as a spatially averaged quantity per cell. The CFD-framework passes the fluid properties and the velocity vector of the fluid to the discrete element method. The equation of continuity (5) and the equation of momentum (6) are solved

$$\frac{\partial(\varepsilon_f \rho_f)}{\partial t} + \nabla(\varepsilon_f \rho_f \vec{u}_f) = 0, \quad (5)$$

$$\frac{\partial(\varepsilon_f \rho_f \vec{u}_f)}{\partial t} + \nabla(\varepsilon_f \rho_f \vec{u}_f \vec{u}_f) = -\varepsilon_f \nabla p + \nabla(\varepsilon_f \bar{\tau}) + \varepsilon_f \rho_f \vec{g} + \vec{f}_{int}, \quad (6)$$

where \vec{u}_f , ρ_f , and p are the fluid velocity, density and pressure. \vec{f}_{int} is the volumetric particle/fluid interaction applied in each CFD cell, ε_f is the local fluid porosity and $\bar{\tau}$ is the fluid viscous stress tensor $\bar{\tau} = \mu \left[(\nabla \vec{u}_f) + (\nabla \vec{u}_f)^{-1} \right]$ with μ_e the effective viscosity determined from the standard k- ε turbulent model. The particle/fluid interaction \vec{f}_{int} is given component wise as $f_{int_i} = \bar{\beta}_i (u_i - \bar{v}_i)$, where \bar{v}_i is the fluid cell averaged particle velocity and $\bar{\beta}_i$ is the fluid cell averaged particle/fluid drag coefficient with $i=x, y, z$.

The particle/fluid force \vec{F}_i^{pf} consists of all individual particle/fluid forces such as drag force \vec{F}_i^d , pressure gradient force $\vec{F}_i^{\nabla p}$ and forces due to fluid shear stress or the deviatoric stress tensor $\vec{F}_i^{\nabla \tau}$ acting on a particle i written as

$$\vec{F}_i^{pf} = \vec{F}_i^d + \vec{F}_i^{\nabla p} + \vec{F}_i^{\nabla \tau}. \quad (7)$$

Under the assumption of parallel flow the rotational motion of particles as well as the particle/fluid stress term can be neglected leading to $\vec{F}_i^{\nabla \tau} = 0$. The drag force \vec{F}_i^d and the pressure gradient force $\vec{F}_i^{\nabla p} = \bar{\beta}_i (\vec{u}_F - \vec{v}_i) / \varepsilon_F$ can be combined to $\vec{F}_i^d + \vec{F}_i^{\nabla p} = \bar{\beta}_i V_i (\vec{u}_F - \vec{v}_i) / (\varepsilon_F (1 - \varepsilon_F))$ after some transformation, where V_i is the particle volume. For the calculation of the drag force \vec{F}_i^d and the combined drag and pressure gradient force $\vec{F}_i^d + \vec{F}_i^{\nabla p}$ various models are available. Very popular and widely used for spherical particles and also applicable for non-spherical particles is the approach by Di Felice [42], where the force for an isolated spherical particle is calculated and altered by the influence of surrounding particles. The respective force reads

$$\vec{F}_i^{pf} = \vec{F}_i^d + \vec{F}_i^{vp} = \frac{1}{2} \rho_F |\vec{u}_F - \vec{v}_i| C_D A_\perp \varepsilon_F^{1-\chi} (\vec{u}_F - \vec{v}_i) \quad (8)$$

where C_D is the drag coefficient, A_\perp is the cross-sectional area perpendicular to the flow and χ a correction factor. Equation (8) can be rewritten in terms of the particle/fluid drag coefficient as

$$\vec{\beta}_i = \frac{1}{2} \rho_F C_D A_\perp \varepsilon_F |\vec{u}_F - \vec{v}_i| (1 - \varepsilon_F) \frac{1}{V_i} \varepsilon_F^{(1-\chi)}. \quad (9)$$

where V_i is the particle volume. χ is calculated as a function of the particle Reynolds-number $Re = \varepsilon_F \rho_F d_p |\vec{u}_F - \vec{v}_i| / \mu_F$ as

$$\chi = 3.7 - 0.65 \exp(-(1.5 - \log(Re))^2 / 2) \quad (10)$$

with d_p the diameter of a volume equivalent spherical particle and μ_F the fluid viscosity. The drag coefficient C_D of a single particle (spherical or non-spherical) can be derived from correlations such as Hölzer und Sommerfeld [48] which can be written as

$$C_D = \frac{8}{Re} \frac{1}{\sqrt{\phi_\perp}} + \frac{16}{Re} \frac{1}{\sqrt{\phi}} + \frac{3}{\sqrt{Re}} \frac{1}{\phi^{3/4}} + 0.42 \times 10^{0.4(-\log(\phi))^{0.2}} \frac{1}{\phi_\perp} \quad (11)$$

where ϕ_\perp is the crosswise sphericity which is the ratio between the cross-sectional area of the volume equivalent sphere and the projected cross-sectional area of the considered particle perpendicular to the flow. The sphericity ϕ is the ratio between the surface area of the volume equivalent sphere and the surface area of the considered particle.

For spherical particles the cross-sectional area A_\perp perpendicular to the flow required for equations (8 and 9) or the crosswise sphericity ϕ_\perp needed for equation (11) can be readily calculated. For clustered overlapping spherical particles or polyhedra which are used to represent the complex shaped particles in the investigation here iterative procedures are applicable. Due to computational reasons the cross-sectional area A_\perp of each particle is calculated in advance and is tabulated in dependence on three symmetric Euler parameters and the sign of the fourth parameter.

The porosity is calculated each time step. Based on a subgrid and its subgrid cell centers it is checked if a particular center lies within part of a particle. If this is the case the respective subcell is considered as fully filled with solid. Based on the ratio of the overall CFD-cell volume

V_{CFD} minus the solid volume V_{sol} of the respective subcells to the overall CFD-cell volume the fluid porosity is calculated as $\varepsilon_F = (V_{CFD} - V_{sol})/V_{CFD}$.

3. Simulation setups and simulation parameters

The considered simulation setups are a fluidized bed with a quadratic base area as shown in fig. 1a and a 90° pipe bend shown in fig. 1b. In the fluidized bed a gaseous fluidizing agent is passed into the vessel from the bottom. The base area of the fluidized bed is 0.11 m x 0.11 m - its total height is 0.41 m. 4500 particles are placed within the vessel and settle under gravity to form a 0.11 m thick layer. As particles shapes, spheres (d=7 mm), cylinders (d=6 mm, l=6 mm), cuboids (l=6 mm, w=6 mm, h=5 mm) and plates (l=2 mm, w=9 mm, h=10 mm) are applied which are all of equivalent volume. The particles have a density of 1380 kg/m³. The coefficients of restitution are given as $e_{pp}^n = 0.913$ and $e_{pw}^n = 0.88$. The friction coefficients are determined as $\mu_{pp}^C = 0.12$ and $\mu_{pw}^C = 0.19$. The gas velocity at the inlet of the fluidized bed is 3 m/s. The fluid density is constant with $\rho_f = 1.225 \text{ kg/m}^3$ and the dynamic viscosity is 1.79E-5 N/sm². The simulations are performed for t=10 s.

In pneumatic conveying a 90° pipe bend is considered. The particles are charged equally distributed with an initial velocity of v=7 m/s at a mass flow rate of 31.1 kg/m²s in the horizontal section of the pipe. The considered particle shapes are spheres (d=2.8 mm), cylinders (d=2 mm, l=3.76 mm), plates with a quadratic base (l=3.39 mm, w=3.39 mm, h=1 mm) and cubes (l=w=h=2.26 mm). Again, all shapes are volume equivalent. The fluid velocity at the inlet is 11.9 m/s. Particles and fluid exit the pipe after the bend in the vertical section. The pipe has a diameter of d=0.05 m. The horizontal section has a length of $l_h = 0.5 \text{ m}$; the vertical section has a length of $l_v = 1 \text{ m}$. The radius of the bend is set to r=0.05 m. The particles have a density of 1123 kg/m³. The coefficients of restitution are given as $e_{pp}^n = 0.3$ and $e_{pw}^n = 0.3$. The friction coefficients are determined as $\mu_{pp}^C = 0.3$ and $\mu_{pw}^C = 0.3$. The fluid density is calculated through the ideal-gas law and the dynamic viscosity is set to 1.79E-05 N/sm². The simulations are performed for t=3 s.

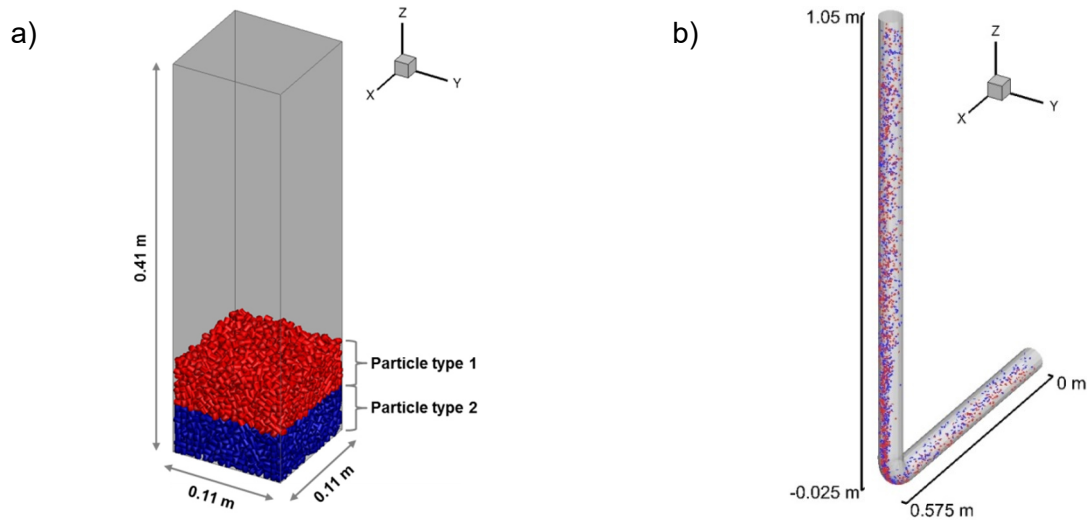


Fig. 1: Schematic diagram of the simulation setup: a) fluidized bed and b) pipe bend

The degree of mixing is evaluated based on the local state of homogeneity of a number of samples in which particles are colored by two distinct colors. Initially 50% of the particles are of the first color; 50 % of the second color. Particles are charged in two layers with particles of type 2 (colored in blue) placed atop particles of type 1 (colored in red) for the fluidized bed (comp. fig. 1a). For pneumatic conveying particles are colored at the inlet. Particles placed above the pipe midpoint are of type 2 (colored in blue) and below the pipe midpoint of type 1 (colored in red). The normalized variance is used to classify the mixing quality known as the Lacey mixing index

$$M = 1 - \frac{s^2 - s_r^2}{s_0^2 - s_r^2}, \quad (12)$$

where s_0^2 represents the completely unmixed and s_r^2 the stochastically mixed state.

4. Results and discussion

4.1 Fluidized Bed

The influence of the particle shape on mixing in the fluidized bed setup is considered in the first investigation for spheres, cylinders, plates and cuboids which are all volume equivalent. Snapshots of the mixing process over time are shown in fig. 2. It can be seen, that in all cases particles are separated into two vertical layers at $t=0$ s. Depending on the particle shape the initial bed height varies; spheres lead to the smallest initial bed height. During fluidization the bed expansion varies depending on the particle shape; particles with a larger cross-sectional area (cylinders, cubes and plates) exhibit larger bed expansions. The mixing progresses continuously over time for spheres and cylinders. Opposite to that cuboids and plates exhibit un-

mixed areas in the vicinity close to the walls. Therefore, visually no progress in mixing is observed between $t=5$ s and $t=10$ s for both particle shapes. From these visual impressions it can be concluded that the blockiness of particles can have a strong impact on the ability to mix due to structure formation processes in the particle system.

Quantitative results on the mixing are outlined in fig. 3 based on the mixing index (fig. 3a) and based on the averaged heights of the particles by color (fig. 3b). Results indicate that up to a time of $t=2$ s, the most intense mixing occurs for plates followed by cylinders, cuboids and spheres. After a time of $t=2$ s only cylinders and spheres continue to mix significantly. The plate like particles obtain final values of $M=0.95-0.99$ where the cuboids obtain values of only $M=0.85$. The mixing of spheres is slower compared to non-spherical shapes, but more complete as for cuboids and plates. Cylinders are the only shape which are fully mixed after $t=10$ s with a degree of mixing of $M=1$. The reason for the accelerated mixing of the non-spherical shapes in the first seconds of the mixing process is given through the averaged particle heights which are larger for the non-spherical shapes, see fig. 3b.

In the fluidized state the total bed heights of the cylinders are in average larger than the corresponding heights of cuboids and spheres. For a fully mixed system such as the cylinder case the averaged heights of both particle types are identical. Cuboids with the lowest degree of mixing have the largest deviation in height between the two differently colored particle types.

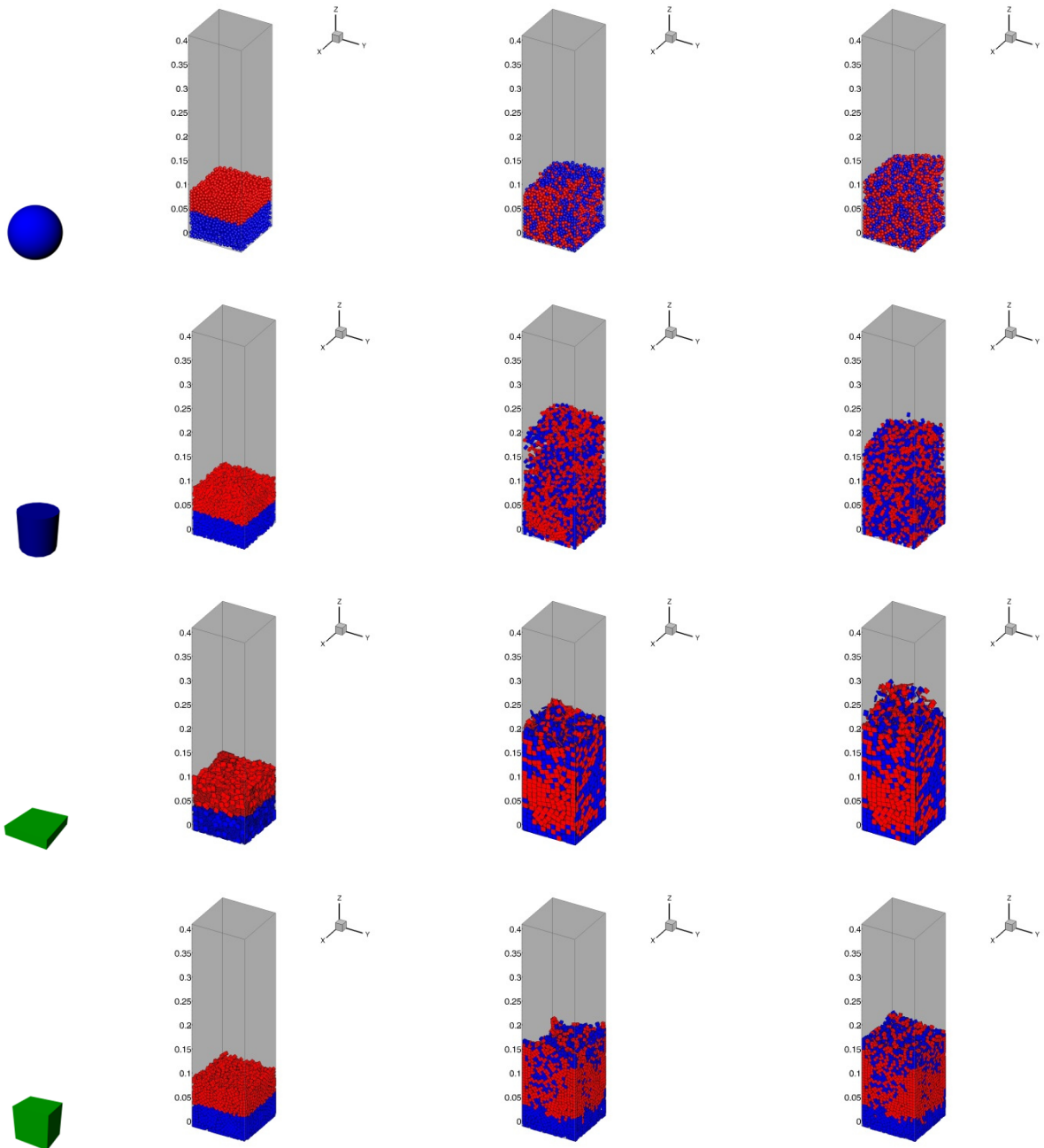


Fig. 2: Snapshots of the mixing process in the fluidized bed at $t=0$ s (left), $t=5$ s (middle) and $t=10$ s (right) for spheres, cylinders, plates and cuboids.

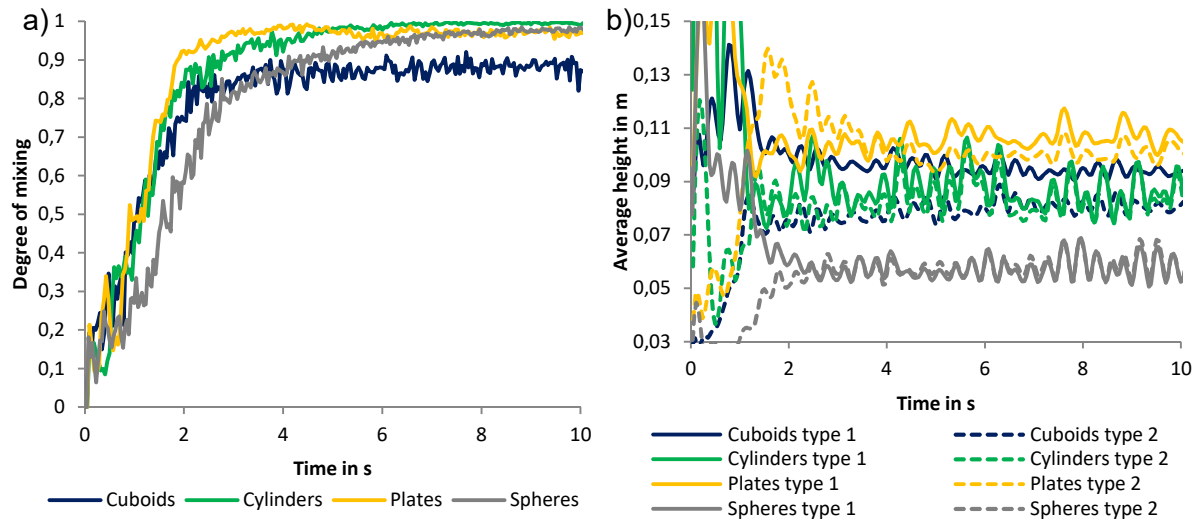


Fig. 3: (a) Degree of mixing M and (b) averaged heights by color plotted against time for spheres, cylinders, plates and cuboids.

4.2 Pipe bend

In the second investigation the mixing within a 90° pipe bend is investigated. All particle shapes obtain a quasi-stationary distribution in the bend after a simulation time of $t=1$ s, see fig. 4.

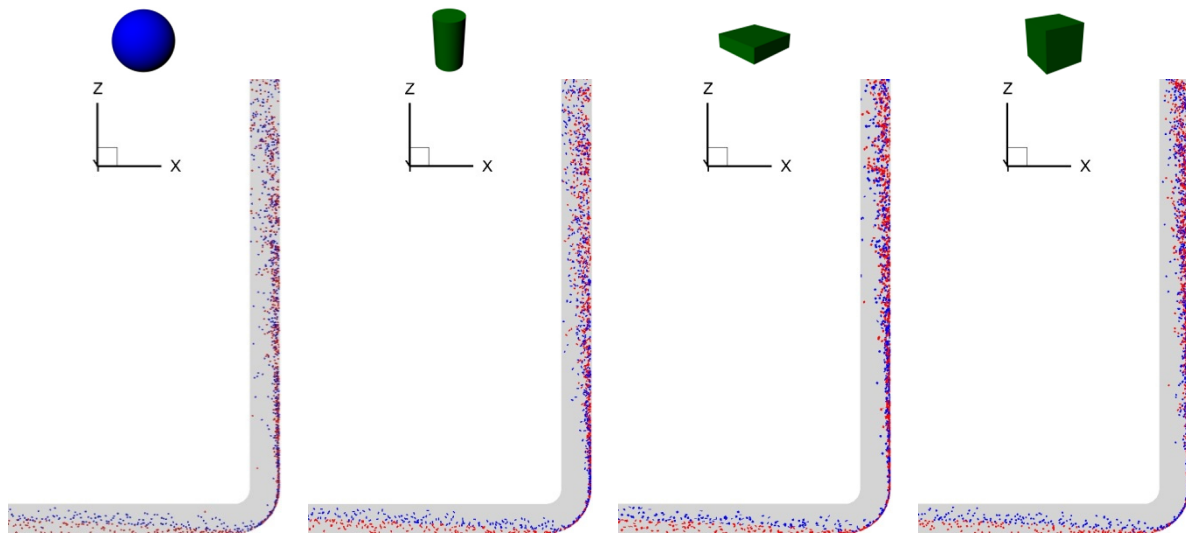


Fig. 4: Snapshots of the mixing process in the pipe bend at $t=1$ s for spheres, cylinders, plates and cubes.

Therefore, instead of quantifying the mixing over time the mixing is evaluated over the dimensionless pipe length (comp. fig. 5, with $l_{\text{total}}=1.61$ m). In the horizontal pipe section particles slowly settle to the ground due to gravity while being pneumatically conveyed resulting in overall parabolic particle trajectories. When particles pass the bend they get compacted due to inertia and a rope forms. Due to strong particle/particle and particle/wall interactions in the bend the initially unmixed blue and red colored particles get instantaneously mixed. Beginning with the bend exit the rope starts to disperse in the vertical pipe section and the particles leave the pipe in a mixed state (comp. fig. 4).

Depending on the particle shape, differences form out for the location where particles first contact the pipe walls in the horizontal pipe section and for the rate at which the rope disperses. As spheres have a smaller cross-sectional area compared to the non-spherical shapes, they are less accelerated by the surrounding fluid ($v_{\text{fluid}}=11.9$ m/s) and therefore impact the pipe walls earlier. On the other hand, a rope consisting of spheres or cylinders disperses at a faster rate than one consisting out of cuboidal shapes (see fig. 4). These characteristics influence the mixing as outlined in fig. 5; the bend is situated at $l/l_{\text{total}}=0.36$.

Initially the degree of mixing ranges between $M=0.78-0.8$ for all shapes in the horizontal pipe section. Spheres, the particle shape with the first particle/wall contacts, achieve the highest degree of mixing in the horizontal pipe section. After passing the bend, the simulation results for M of spheres, cuboids, cubes and cylinders increase up to $M=0.97-0.99$. Observable differences are a result of the varying dispersion rates in the vertical pipe section. Spheres which are already fully dispersed at the pipe outlet obtain the largest values for M close to 1.0.

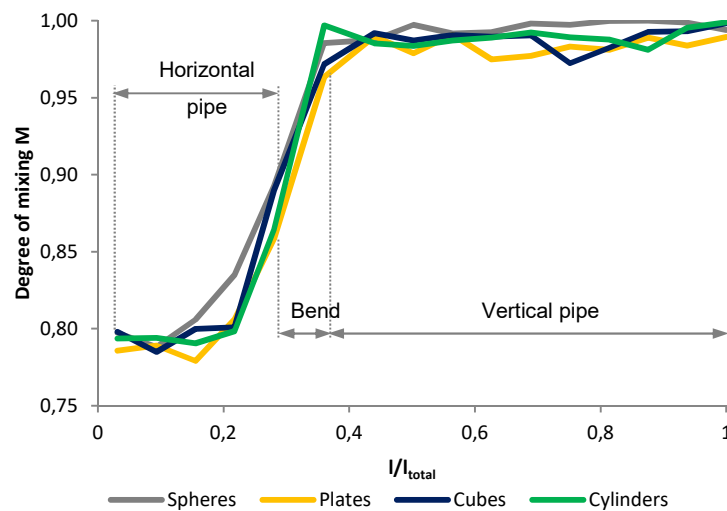


Fig. 5: Degree of mixing M plotted over the dimensionless pipe length for pneumatic conveying.

5. Conclusions

A numerical investigation of the influences of different shapes on mixing in a model type fluidized bed and during pneumatic conveying is performed based on the three dimensional Discrete Element Method (DEM) in combination with computational fluid dynamics (CFD). To quantify the mixing behavior, the degree of mixing is estimated over time for the fluidized bed and over the pipe length for the quasi-stationary pneumatic conveying system. Mixing is evaluated qualitatively through snapshots taken over time and quantitatively through the degree of mixing based on the Lacey-index.

In case of the fluidized bed the following conclusions can be drawn:

- Spheres show the slowest mixing over time but obtain higher final values for the degree of mixing than cuboids and plates.
- After 10 s only cylinders are fully mixed ($M=1.0$) and their average heights by color are equal.
- For cuboids and plates regions can be identified in which particles close to the walls are hindered in their motion. This behavior influences the progression of the degree of mixing M .
- Particle heights and deviations in the heights by color also affect the degree of mixing.

For the pipe bend the most important aspects are:

- Mixing over the pipe length is influenced by initial particle/wall contacts, rope formation and dispersion.
- Due to the fastest formation of particle/pipe contacts, spheres hold the highest value for the degree of mixing before the bend.
- Mixing of cubes and plates with delayed rope dispersion stagnates in the vertical pipe section, initially.

In both setups considered, particle shape strongly influences the mixing behavior. Therefore complex shaped particles should be always considered in the context of mixing and particle-fluid coupling in case that the investigated system comprises of such particles.

Acknowledgements

Financial support by the DFG-KR 3446/6-1 is greatly acknowledged.

IV. Numerical study of rope formation and dispersion of non-spherical particles during pneumatic conveying in a pipe bend

H. Kruggel-Emden*, T. Oschmann

Ruhr-Universitaet Bochum, Universitaetsstrasse 150, D-44780 Bochum, Germany

The following accepted manuscript appeared as journal version in Kruggel-Emden, H., Oschmann, T.: Numerical study of rope formation and dispersion of non-spherical particles during pneumatic conveying in a pipe bend. Powder Technol. 268, 219–236 (2014) and may be found at <https://doi.org/10.1016/j.powtec.2014.08.033>

Abstract

In pneumatic conveying bends are used to interconnect vertical and horizontal pipe sections. During conveying bends are known to be related to several characteristic flow phenomena. Experimentally, their investigation turns out to be difficult which favors the use of numerical approaches instead. Detailed investigations become possible by relying on Euler-Lagrange methods. Here, particularly combined Discrete Element Method and Computational Fluid Dynamics (DEM-CFD) approaches allow the transient description of the particle/fluid interaction. So far, only spherical particles have been considered by the DEM-CFD during pneumatic conveying with very few exceptions, e.g. [11], as DEM-CFD frameworks capable of representing non-spherical particles are not yet widely established. There is an ongoing discussion on proposed frameworks regarding applicable particle/fluid force models and the way of the particle shape representation. Due to these unresolved questions conveying of non-spherical particles through pipe bends involving phenomena like rope formation and dispersion has not been considered with numerical approaches such as the DEM-CFD, yet. Therefore, as many bulk solids involve complex shaped particles, rope formation and dispersion are investigated for non-spherical particles by a DEM-CFD approach for the first time. Exemplarily, cubes, octahedrons, pyramids, plates and icosahedrons are addressed. A DEM-CFD framework is developed which allows the modelling of arbitrary shaped particles. To underline the validity of the approach, results are benchmarked against established correlations which are available for certain particle shapes. Obtained results indicate differences in the pressure drop, particle velocity distribution, rope dispersion and the particle/particle, particle/wall and particle/fluid forces which are strongly dependent on particle shape.

Keywords: pneumatic conveying; pipe bend; simulation; DEM-CFD-approach; non-spherical particles; rope formation

1. Introduction

Pneumatic conveying of bulk solids is important to industries varying from agricultural, chemical, energy conversion, plastics, food, pharmaceutical to minerals processing [188]. Advantages of pneumatic conveying are a high level of safety, low operation costs, flexibility in terms of layout, simple installation / automation and low maintenance. Of disadvantage are equipment and bulk solids wear and a large energy demand. Pneumatic conveying is often performed in horizontally or vertically aligned pipe sections which are linked by bends. Among all of the equipment pipe bends are least investigated and are not well understood despite their simplicity [189]. Typical problems related to bends appear in a strong contribution to the overall pressure drop, possible product degradation, erosive wear and a not well understood and strongly product dependent rope formation and dispersion especially in industrial applications.

In order to increase the overall bend design as well as to understand the complex flow patterns, mathematical modelling is a powerful tool which relies on different modelling frameworks. In Euler-Euler approaches [135] both fluid and particle phase are modelled as two interpenetrating continua based on the kinetic theory of granular flow. Alternatively, approaches are established by an Euler-Lagrange description where the fluid phase is modelled as a continuum and the particles as discrete entities. Depending on the required level of detail, the particle sizes and concentrations, collisions among particles as well as a two way coupling between particles and fluid phase are neglected in the most simplified frameworks. More advanced models include a two way coupling between particles and fluid phase and represent particle/particle collisions based on stochastic models [190] or by deterministically tracking individual particles including their collisions over time. The latter approach is known as the combined Discrete Element Method and Computational Fluid dynamics (DEM-CFD) approach [8] and allows a transient description of both fluid and solid phases. Details on the state of the art of the outlined methods and to which extent they are capable of modelling particle/fluid systems comprising of non-spherical particles is discussed in the following.

Generally, Euler-Euler models are preferred in applied research or for process modelling, as their computational load is lower than that of Euler-Lagrange models. However, for detailed investigations they are not applicable because they do not correctly represent segregation phenomena [140]. Particles have to be small with regard to the system size to fulfill the continuum assumption and shape cannot be correctly represented (limitation to spheres), although progress has been recently made for the modelling of polydisperse particle systems [136,137]. Even for spherical particles a large drawback of Euler-Euler methods is their limited capability

to represent the rotational degree of freedom influenced by possible tangential particle interactions. Additionally, multi-particle interactions are not modelled for [140] which is a weakness especially in dense systems.

Despite the known drawbacks, Euler-Euler frameworks built on the kinetic theory of granular flow [135] were considered firstly by Eskin [191] for the modelling of pneumatic conveying within a 1D model. Despite its simplicity comparisons with experimental data and results obtained from Lagrangian simulations proved its general applicability. Dense pneumatic conveying in vertical [192] and horizontal directions [193] were simulated by a 3D Euler-Euler framework for coal dust by Pu et al. at elevated pressure. Results indicate a reasonable representation of pressure drop and solids concentrations. Plug flow in a pipeline enlargement was addressed by an Euler-Euler model by McGlinchey et al. [194]. Just recently Behera et al. proposed a 1D model for dense phase [195] and for dilute conveying of very fine particles [196].

Euler-Lagrange frameworks allow for a more precise modelling of particle fluid systems compared to Euler-Euler models as particles are tracked as discrete entities. The fluid phase is often only considered in steady-state. Proposed modelling frameworks usually focus on spherical particles e.g. [197–201], with the exception of [202] (details are given below). Often particle/particle collisions are neglected which limits the applicability of the frameworks to dilute flow situations. In case that particle/particle collisions are modelled for, stochastic approaches are often used which are accurate [190] but limited in their application to spherical particle shapes. Euler-Lagrange frameworks therefore generally disqualify for setups involving non-spherical dense particle flow such as targeted in the investigation here.

Examples for Euler-Lagrange frameworks include works by Lain and Sommerfeld [202] who investigated steady-state pneumatic conveying of non-spherical particles in a horizontal channel. Due to dilute conditions particle/particle collisions were neglected and particle/wall collisions were modeled by a stochastic approach. For the drag force the particle asphericity was considered. Rotational motion which strongly influences drag forces (comp. [180]) as well as lift forces were not modelled for. Probably due to the dilute conditions, obtained velocity profiles were in reasonable agreement with experimental investigations. Based on an extended framework Lain and Sommerfeld [197] later investigated spherical particles within horizontal flow for different wall roughnesses. The extended framework [197] additionally considered particle/particle collisions, lift forces and the rotational particle motion and was also used for the investigation of horizontal flow in circular pipes [198] and ducts [199]. A detailed comparison of channel and pipe flow was performed by Lain and Sommerfeld [200] more recently. A detailed model similar to that of Lain and Sommerfeld [200] was developed and applied by Aletto and Breuer [201] for the investigation of secondary flow characteristics forming during horizontal conveying.

The combination of the Discrete Element Method coupled to Computational Fluid dynamics (CFD) is a special, refined form of Euler-Lagrangian frameworks and always relies on a two-way coupling as well as a deterministic collision description [8]. The coupled DEM-CFD usually resolves both fluid and particle flow transiently and allows for the inclusion of arbitrarily shaped particles [185] and therefore perfectly qualifies for the simulation setup considered in this investigation. A large drawback of the DEM-CFD method currently is that frameworks capable of representing non-spherical particles reliably are not yet established. Only a handful of studies have been performed involving the DEM-CFD in the context of complex particle shapes e.g. [40,143–145,185] and only one investigation addressed pneumatic conveying (channel flow) so far [11].

In the context of pneumatic conveying the DEM-CFD was firstly applied by Tsuji et al. [15]. Horizontal plug flow of spherical particles was investigated and results were compared to experimental investigations. The particle phase was considered in 3D; the fluid phase was modeled in steady-state by a 1D-formulation. The obtained numerical results were identified as reasonable with regard to the wave-like motion of the flow boundary. Stationary layer thickness and plug flow velocity matched experimental results. More than 10 years after the pioneering work by Tsuji et al. [15], Han et al. [203] used a 2D transient DEM-CFD model to address attrition during transport of spherical particles in a conveying system consisting of horizontal and vertical pipe elements. Ouyang et al. [204] applied a 2D hard sphere model and coupled it to CFD for the simulation of gas/solid flow in a vertical pipe. Axial as well as radial pressure drops in dense phase plugs were investigated experimentally and numerically by Mc Glinchey et al. [205] based on a 2D DEM-CFD model. Based on a 3D DEM-CFD-model involving spheres Lim et al. [206] reproduced different flow patterns such as dispersed and plug flow for vertical conveying and homogenous, stratified, moving dunes and plug flow for horizontal conveying as reported from experimental investigations. Lim focused on voidage waves in hydraulic conveying for narrow pipes [207]. Similar to the approach of Tsuji et al. [15], Fraige and Langston [208] investigated horizontal conveying of spherical particles employing a 3D DEM model coupled to a steady-state 1D CFD approach. Flow patterns reported experimentally were quantitatively reproduced. Plug flow in vertical conveying and slug flow in horizontal conveying were investigated by Strauss et al. [209,210]. Inclined pneumatic conveying was investigated numerically and experimentally by Zhang et al. [211]. Experimental matched numerical results obtained from DEM-CFD simulations. Kuang et al. investigated horizontal pneumatic conveying in slug flow [212] as well as flow regimes during vertical pneumatic conveying [213]. In both contributions a 3D DEM model involving spherical particles was applied and coupled to a 2D CFD model for horizontal conveying and to a 3D CFD model for vertical pneumatic conveying. For horizontal conveying results indicated that slug velocity is linearly dependent

on gas velocity only and slug length is affected by both gas and solid flow rates. For vertical pneumatic conveying a new phase diagram was proposed in terms of key forces.

Especially in the last four years the interest in modelling of pneumatic conveying strongly increased. Recently, a review on DEM-CFD coupling schemes for spherical particles was performed by Zhou et al. [214]. Some of the schemes widely used in literature were identified to be valid for steady and uniform flow conditions only. Recommendations for the use of the schemes for horizontal pneumatic conveying were made. Vertical pneumatic conveying was also modeled by Sturm et al. [215] and showed a good match compared to experimental results. Xian et al. [186] addressed segregation during horizontal conveying of spheres. Results indicated an influence of gas velocity as well as density differences of the involved particle fractions. A comparison of hard- and soft-sphere approaches within a DEM-CFD framework of pneumatic conveying was performed by Mezherichter et al. [216].

Most recent DEM-CFD models rely on a fully 3D description of both fluid and particle phases, where the particle phase still comprises of only spheres. Based on the model derived for vertical conveying [213] a full 3D model was also applied to horizontal conveying [217] and a general phase diagram in terms of particle/particle, particle/fluid and particle/wall forces was proposed. Very recently Hilton and Cleary considered the influence of particle shape on horizontal conveying for the first time [11] by conducting DEM-CFD investigations. In contrast to spherical particles, non-spherical particles show tendencies not to transition to slug flow for increasing gas flow rates. Similarly to the investigation by Zhang et al. [211], Kuang et al. [218] considered inclined pneumatic conveying at different inclination angles focusing on spheres. Different interaction forces were analyzed and results indicate that they are strongly influenced by the inclination angle. The influence of simulation parameters was already considered earlier by, e.g., Fraige and Langston [208] - Li et al. [219] extend this study by focusing on friction and restitution coefficients. They clearly outlined that the transition of flow modes is strongly affected by friction as well as restitution coefficients in case of spherical particles.

Similarly to pneumatic conveying in horizontal and vertical pipe sections, bends were investigated with the previously outlined modelling approaches, where the same limitations apply as discussed. To our knowledge particularly for pipe bends, complex shaped particles have not yet been considered in any type of simulation approach such as Euler-Euler, Euler-Lagrange or DEM-CFD frameworks.

The earliest works addressing the numerical modelling of pipe bends date back to Levy and Mason [220] and Schallert and Levy [221]. Referring to an Euler-Euler model [220] and a simple Euler-Lagrange approach [221] segregation of differently sized spherical particles was investigated. The same approach was also used to model and experimentally investigate rope formation and dispersion during pneumatic conveying [222] and for the flow analysis after a

pipe bend when switching from a vertical to a horizontal section [223]. Pipe bends at low gas velocities were investigated by Akilli et al. [224]. Bernert et al. [225] used an Euler-Lagrange approach accounting for stochastic particle/particle and particle/wall collisions which was applied to duct flow involving bends and flow splitters. Quek et al. [226] investigated particle fluid flow in horizontal and vertical bends based on an Euler-Lagrange approach neglecting particle/particle collisions. The influence of particle size, as well as bend radius, on the concentration profiles was investigated in detail. Kuan et al. [227] experimentally and numerically investigated dilute gas-solid flow based on a one way coupled Euler-Lagrange framework where the fluid flow was not influenced by the particle motion. Chu and Yu [228] were the first to apply the coupled DEM-CFD approach to pneumatic conveying in a pipe bend addressing a variety of parameters. U-bends were addressed by El-Beheri et al. [229] with a two way coupled model neglecting particle/particle collisions. El-Beheri et al. [229] tested among other parameters the influence of turbulence models on the simulation outcome. A Euler-Lagrange model neglecting particle/particle collisions was applied by Vashisth and Grace [230] recently to investigate the behavior of different Geldart group particles in a pipe bend. Very recently the Euler-Lagrange approach proposed by Lain and Sommerfeld applied earlier to pneumatic conveying in horizontal and vertical channels and pipe sections [197,198,202] was used for the investigation of a combination of vertical and horizontal pipes with bends in between [231]. The model accounted for rough walls and inter-particle collisions in an Euler-Lagrange framework. Available experimental data on velocities and pressure drop for spherical particles was matched well by the proposed model.

Extending the outlined DEM-CFD frameworks involving only spherical particles, a pipe bend is addressed in this study within a framework accounting for complex shaped particles for the first time. The influence of particle shape on the flow is investigated. To ensure the validity of the framework numerical results are validated against correlations predicting the rope dispersion as well as the pressure drop within the bend for both spherical and some non-spherical particles [232,233]. Fluid and particle flow properties as well as particle/fluid, particle/particle and particle/wall interactions are investigated. Thereby details on the microstructural phenomena behind the rope formation and dispersion are gained.

2. Methodology

In the coupled DEM-CFD method the particle motion is represented within a DEM-framework, while the fluid phase is represented by solving the volume averaged Navier-Stokes equations [8]. For the DEM an in-house code and for the CFD Ansys FLUENT 15 is used. In the DEM the translational and rotational motion is obtained by integrating Newton's and Euler's equations of each particle given by

$$m_i \frac{d^2 \vec{x}_i}{dt^2} = \vec{F}_i^c + \vec{F}_i^{pf} + \vec{F}_i^g \quad (1)$$

$$\hat{I}_i \frac{d\vec{W}_i}{dt} + \vec{W}_i \times (\hat{I}_i \vec{W}_i) = \Lambda_i^{-1} \vec{M}_i \quad (2)$$

with particle mass m_i , particle acceleration $d^2 \vec{x}_i / dt^2$, contact force \vec{F}_i^c , particle/fluid force \vec{F}_i^{pf} , gravitational force \vec{F}_i^g , angular acceleration $d\vec{W}_i / dt$, angular velocity \vec{W}_i , external moment resulting out of contact or particle/fluid forces \vec{M}_i , the inertia tensor along the principal axis \hat{I}_i and the rotation matrix converting a vector from the inertial into the body fixed frame Λ_i^{-1} . The equations for translational and rotational motion are solved by explicit integration schemes [171]. A flexible approach to model complex shaped particles in the discrete element method is the polyhedron method. In this method a triangular surface mesh is applied to represent the desired particle shape and a common plane algorithm is used for contact detection of the individual vertexes representing the particle surface [55]. Mainly due to the more complex contact detection the overall simulation time increases in case of complex shaped particles by a factor of 2-3 depending on the particle shape considered compared to spheres. In case of complex shaped particles contact force laws are applied similarly as used for spherical particles [23,187]. The normal component of the contact forces is obtained from a linear spring damper model

$$\vec{F}^n = k^n \delta \vec{n} + \gamma^n \vec{v}_{rel}^n \quad (3)$$

where k^n is the spring stiffness, δ the virtual overlap, \vec{n} a normal vector, γ^n a damping coefficient and \vec{v}_{rel}^n the normal velocity in the contact point. Both k^n and γ^n determine the coefficient of normal restitution between particles e_{pp}^n as well as particles and walls e_{pw}^n . For the calculation of the tangential forces a linear spring limited by the Coulomb condition is used

$$\vec{F}^t = \min(k^t |\vec{\xi}^t|, \mu_C |\vec{F}^n|) \vec{t} \quad (4)$$

where k^t is the stiffness of a linear spring, μ_C is the friction coefficient, $\vec{\xi}^t$ is the relative tangential displacement and \vec{t} is the tangential unit vector. Rotational friction is neglected.

The fluid phase is described with Computational Fluid Dynamics (CFD) in an Eulerian framework, in which the interior of the pipe bend is meshed by hexagonal cells. The fluid velocity is

addressed as a spatially averaged quantity per cell. The CFD-framework passes the fluid properties and the velocity vector of the fluid to the DEM. The equation of continuity (5) and the equation of momentum (6) are solved

$$\frac{\partial(\varepsilon_f \rho_f)}{\partial t} + \nabla(\varepsilon_f \rho_f \vec{u}_f) = 0, \quad (5)$$

$$\frac{\partial(\varepsilon_f \rho_f \vec{u}_f)}{\partial t} + \nabla(\varepsilon_f \rho_f \vec{u}_f \vec{u}_f) = -\varepsilon_f \nabla p + \nabla(\overline{\varepsilon_f \vec{\tau}}) + \varepsilon_f \rho_f \vec{g} + \vec{f}_{int}, \quad (6)$$

where \vec{u}_f , ρ_f and p are the fluid velocity, density and pressure. \vec{f}_{int} is the volumetric momentum source term for the particle/fluid interaction applied in each CFD cell, ε_f is the local fluid porosity and $\vec{\tau}$ is the fluid viscous stress tensor $\vec{\tau} = \mu \left[(\nabla \vec{u}_f) + (\nabla \vec{u}_f)^{-1} \right]$ with μ_e the effective viscosity. It is determined from a k- ε turbulent model which has been used widely in other DEM-CFD or Euler-Lagrangian studies [228,231,234]. The particle/fluid interaction \vec{f}_{int} is given component wise as $f_{int_i} = \bar{\beta}_i (u_i - \bar{v}_i)$, where \bar{v}_i is the fluid cell averaged particle velocity and $\bar{\beta}_i$ is the fluid cell averaged particle/fluid friction coefficient with $i=x, y, z$.

The particle/fluid force \vec{F}_i^{pf} consists of all individual particle/fluid forces such as drag force \vec{F}_i^d , pressure gradient force $\vec{F}_i^{\nabla p}$ and forces due to fluid shear stress or the deviatoric stress tensor $\vec{F}_i^{\nabla \tau}$ acting on a particle i written as

$$\vec{F}_i^{pf} = \vec{F}_i^d + \vec{F}_i^{\nabla p} + \vec{F}_i^{\nabla \tau}. \quad (7)$$

Under the assumption of parallel flow the rotational motion of particles as well as the particle/fluid stress term can be neglected leading to $\vec{F}_i^{\nabla \tau} = 0$. The drag force \vec{F}_i^d and the pressure gradient force $\vec{F}_i^{\nabla p} = \vec{\beta}_i (\vec{u}_F - \vec{v}_i) / \varepsilon_F$ can be combined to $\vec{F}_i^d + \vec{F}_i^{\nabla p} = \vec{\beta}_i V_i (\vec{u}_F - \vec{v}_i) / (\varepsilon_F (1 - \varepsilon_F))$ after some transformation, where V_i is the particle volume. For the calculation of the drag force \vec{F}_i^d and the combined drag and pressure gradient force $\vec{F}_i^d + \vec{F}_i^{\nabla p}$ various models are available. Very popular and widely used for spherical particles and also applicable for non-spherical particles is the approach by Di Felice [42], where the force for an isolated spherical particle is calculated and altered by the influence of surrounding particles. The respective force reads

$$\vec{F}_i^{pf} = \vec{F}_i^d + \vec{F}_i^{\nabla p} = \frac{1}{2} \rho_F |\vec{u}_F - \vec{v}_i| C_D A_{\perp} \varepsilon_F^{1-\chi} (\vec{u}_F - \vec{v}_i) \quad (8)$$

where C_D is the drag coefficient, A_\perp is the cross-sectional area perpendicular to the flow and χ a correction factor. Equation (8) can be rewritten in terms of the particle/fluid friction coefficient as

$$\vec{\beta}_i = \frac{1}{2} \rho_F C_D A_\perp \varepsilon_F |\vec{u}_F - \vec{v}_i| (1 - \varepsilon_F) \frac{1}{V_i} \varepsilon_F^{(1-\chi)}. \quad (9)$$

where V_i is the particle volume. χ is calculated as a function of the particle Reynolds-number

$$Re = \varepsilon_F \rho_F d_p |\vec{u}_F - \vec{v}_i| / \mu_F \quad (10)$$

as

$$\chi = 3.7 - 0.65 \exp(-(1.5 - \log(Re))^2 / 2) \quad (11)$$

with d_p the diameter of a volume equivalent spherical particle and μ_F the fluid viscosity.

The drag coefficient C_D of a single particle (spherical or non-spherical) can be derived from correlations such as Hölzer und Sommerfeld [48] which can be written as

$$C_D = \frac{8}{Re} \frac{1}{\sqrt{\phi_\perp}} + \frac{16}{Re} \frac{1}{\sqrt{\phi}} + \frac{3}{\sqrt{Re}} \frac{1}{\phi^{3/4}} + 0.42 \times 10^{0.4(-\log(\phi))^{0.2}} \frac{1}{\phi_\perp} \quad (12)$$

where ϕ_\perp is the crosswise sphericity which is the ratio between the cross-sectional area of the volume equivalent sphere and the projected cross-sectional area of the considered particle perpendicular to the flow. The sphericity ϕ is the ratio between the surface area of the volume equivalent sphere and the surface area of the considered particle.

For spherical particles the cross-sectional area A_\perp perpendicular to the flow required for equations (8 and 9) or the crosswise sphericity ϕ_\perp needed for equation (12) can be readily calculated. For polyhedra which are used to represent the complex shaped particles in the investigation here iterative procedures are applicable. Due to computational reasons the cross-sectional area A_\perp of each particle is calculated in advance and is tabulated in dependence on three symmetric Euler parameters and the sign of the fourth parameter [185].

The porosity is calculated each time step. Based on the subgrid cell centers it is checked if a particular center lies within a part of a particle. If this is the case the respective subcell is

considered as fully filled with solid. Based on the obtained ratio the fluid porosity is calculated. Detailed information on this procedure are given in [185].

3. Simulation conditions

3.1 Simulation setup and parameters

A pipe bend as investigated by Chu and Yu [228] is considered in the investigation here. A sketch of the setup is shown in Fig. 1. The setup consists of a horizontal and vertical pipe section interconnected by a 90° bend. Air is entering into the horizontal pipe section at $X = 0$ m, $Y = 0$ m, $Z = 0$ m and exits at $X = 0.55$ m, $Y = 0$ m, $Z = 1.05$ m in the vertical pipe section. The pipe has a diameter of $D = 0.05$ m. The horizontal pipe section is of 0.5 m, the vertical pipe section of 1 m length. The bend has a radius of $R = D$ and its boundaries are given by $0.5 \text{ m} < X < 0.575 \text{ m}$, $-0.025 \text{ m} < Y < 0.025 \text{ m}$ and $-0.025 \text{ m} < Z < 0.05 \text{ m}$.

An overview of the applied particle shapes consisting of spheres, cubes, pyramids, plates and icosahedrons is given in table 1. The particles are charged equally distributed over the cross-section of the pipe at $X = 0.02$ m at random orientations. The whole bend was meshed with 39,875 hexagonal cells. The no-slip condition was applied to the walls in the simulations.

All particles colored in green are approximated as polyhedrons of equivalent volume to a 2.8 mm diameter sphere as this is a widely accepted approach for comparing the influence of particle shape on fluid flow on different system scales in both numerical and experimental investigations [40,180,235]. Thereby, particles have an equivalent mass but a varying surface area. Based on the definition of the Reynolds-number according to equation (10) equality of the Re-number as well as of the Archimedes-number is ensured within the performed comparison which is essential to guarantee the same fluidization characteristics (comp. [233]).

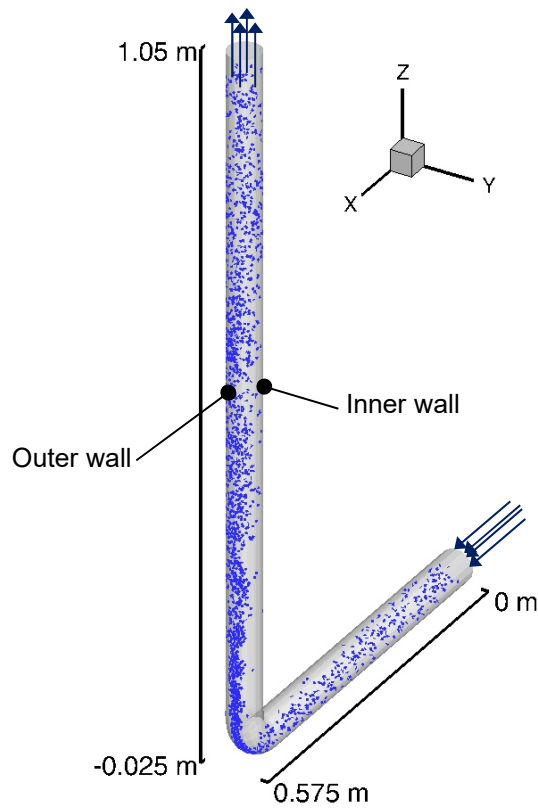
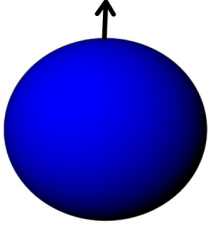
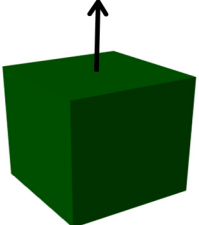
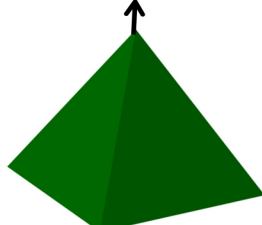
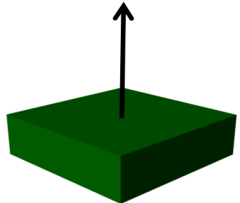
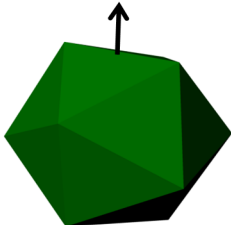


Fig. 1: Schematic diagram of the simulation setup

Table 1: Particle shapes, sizes and sphericities applied. The letters a, b, c, refer to particle edge dimensions, h to the height and d to the particle diameter. The arrow represents the orientation vector rotating with a particle.

Shape	Sphere	Cubes	Pyramids
			
Size	d 2.8 mm	a 2.26 mm	a 3.26 mm b 3.26 mm h 3.26 mm
Sphericity	1	0.8060	0.7184
Shape	Plates	Icosahedrons	
			
Size	a 3.39 mm b 3.39 mm c 1 mm	a 1.74 mm	
Sphericity	0.6739	0.9393	

All simulations are initialized with the parameters in table 2 and are performed for $t=3$ s. The Reynolds-number based on the volume equivalent diameter according to equation (10) for $\varepsilon_F = 1$ and $\vec{v}_i = 0$ m/s is calculated with $Re=1860$.

Table 2: Particle and fluid properties applied in the simulations

Particle properties	
Mass flow rate	31.1 kg/(m ² s)
Density	1123 kg/m ³
Friction coefficient	0.3
Coefficient of restitution	0.3
Velocity at inlet	7 m/s
Time step	1×10^{-6} s
Fluid properties	
Density	Ideal gas law
Dynamic viscosity	1.79E-05 Ns/m ²
Velocity	11.9 m/s
Temperature	300 K
Time step	1×10^{-4} s

All simulation parameters except fluid time step, temperature and fluid density are aligned to the numerical investigation of Chu and Yu [228] who focused on spherical particles in a DEM-CFD framework. Chu and Yu based their investigation on the experimental work of Lee et al. [236] who studied conveying of spherical glass and polypropylene particles in a pipe bend. Instead of relying on a non-linear force model [228] a linear model is used for simplicity here where k^n and γ^n are derived based on the predefined time step and coefficient of restitution given in Table 2. The related k^n and γ^n for a DEM time step of $t = 1 \times 10^{-6}$ s leads to particle/particle overlaps smaller than 1 % of the particle diameter which is in accordance with the suggestions by Kruggel-Emden et al. [31] and prevents unwanted alterations of the simulations. Particle/particle and particle/wall contacts are treated with the same contact parameters.

3.2 Assessment of particle-particle, particle-wall and particle-gas forces

To assess the particle-particle, particle-wall and particle-gas interaction, the respective interaction forces are averaged in the time period of $t=1 - 3$ s while a stationary system behavior occurs in all simulations. For calculating the fluid cell based averaged particle-particle (PTACI) and the surface based particle-wall forces (WTACI) the time-averaged collision intensity (TACI) as proposed in [228] is used. The PTACI is derived as

$$PTACI = \frac{\sum_{iter=1}^{iter=N} \sum_{i=1}^{i=k_m} \|\vec{F}_{PC}\|}{V \cdot N}, \quad (13)$$

where V is the volume of the respective fluid cell, N is the total number of iterations in dependence on the considered simulation duration, k_m is the number of particles which are in contact and \vec{F}_{pc} is the particle-particle contact force. For particle-wall contacts the respective wall surface area A and the particle-wall contact force \vec{F}_{WC} is used to calculate the WTACI as

$$WTACI = \frac{\sum_{iter=1}^{iter=N} \sum_{i=1}^{k_m} \|\vec{F}_{WC}\|}{A \cdot N}. \quad (14)$$

In addition to that, the cell-based momentum source averaged over time / iterations \bar{f}_{int} estimates the particle-gas interaction per fluid cell

$$\bar{f}_{int} = \frac{\sum_{iter=1}^{iter=N} \|\vec{f}_{int}\|}{N}. \quad (15)$$

4. Validation of the rope dispersion and of the pressure drop

To classify and validate the numerically obtained data on the rope formation in the pipe bend from the DEM-CFD an analytical comparison of the calculated particle velocities is performed, based on the empirical model by Muschelknautz and Wojahn [232,237]. Three exemplarily selected shapes such as spheres, cubes and icosahedrons are considered. Note that only for a limited number of shapes empirical models are available so far [232,237]. As velocities, the bend exit velocity, the pipe exit velocity as well as the theoretical maximal velocity in an infinite vertical pipe section are calculated. Additionally, pressure drops in the pipe bend are derived analytically based on empirical models outlined in [232,233] – here only spherical particles are considered. Note that it would have been preferable to use experimental data on non-spherical particles for the validation of the investigation. However, suitable experimental investigations of rope formation and dispersion of coarse well specified non-spherical Geldart group D particles are, to our knowledge, not available in literature for pipe bends. Performed experimental investigations either involve spherical particles, e.g. [236,238–241], or very fine bulk materials such as coal [222–224,227,242–245]. The use of the latter would result in too large particle numbers for the DEM-CFD simulations – moreover, information on the detailed particle shape necessary for a validation study is usually not provided.

In the analytical model by Muschelknautz and Wojahn [232,237] the bend inlet velocity is used as an input which is taken as averaged particle velocity from the DEM-CFD. The bend exit velocity c_2 is calculated in dependence on the inlet velocity c_1 , the wall friction f_{gl} and the reflection angle ε as

$$c_2 = c_1 \exp(-f_{gl} \varepsilon). \quad (16)$$

At the vertical pipe section outlet, at $l= 1\text{m}$ after the bend, the velocity $c_{l=1m}$ is given through the following equation

$$c_{l=1m} = 1 - \exp -(1.4L)^{0.52} \quad (17)$$

with the dimensionless length

$$L = \frac{gl}{v^k w_s^{2-k}}, \quad (18)$$

where g is the gravitational constant, v is the gas velocity, l the length after the bend exit, w_s the sedimentation velocity and k a constant dependent on the particle Reynolds number Re_s and the shape-parameters A , B and C given as

$$k = \frac{A+0.5B\sqrt{Re_s}}{A+B\sqrt{Re_s}+CRe_s}. \quad (19)$$

The values for A , B and C can be obtained from tables given in [232]. The maximal reachable particle velocity can be derived from a dimensionless equation of motion such as

$$\frac{dc}{dL} = \pm(1 - C) \frac{(1-c)^{2-k}}{c} - \frac{B\beta}{c} - CBa \frac{\lambda_s^*}{2}, \quad (20)$$

where $dC/dL=0$ with $C = c/v$ being the particle to gas velocity ratio and Ba the Barth-Number

$$Ba = \frac{v^k w_s^{2-k}}{Dg}. \quad (21)$$

The parameters β and B are given as

$$\beta = \sin(\alpha) + f_{gl} \cos(\alpha), \quad (22)$$

$$B = \left(\frac{w_s}{v}\right)^{2-k}, \quad (23)$$

where α characterizes the slope angle between the vertical pipe section and the horizontal.

The velocities obtained through equations (16) – (23) and the DEM-CFD are shown in table 3.

Table 3: Analytically and DEM-CFD derived velocities at the bend exit, at $l=1$ m and the maximum possible in an infinite vertical pipe.

Shape	Velocity [m/s]					
	Empirical results [232,237]				DEM-CFD	
	Bend inlet	Bend Exit	Pipe Exit	Max	Bend Exit	Pipe Exit
Spheres	5.70	3.56	3.68	4.17	3.58	3.72
Cubes	5.38	3.36	4.05	6.07	3.28	3.83
Icosahedrons	5.42	3.38	3.93	5.95	3.42	4.39

The analytical results indicate a good agreement with the DEM-CFD results. Spheres followed by cubes and icosahedrons have the largest velocities at the bend exit. The simulations match the analytical results for spheres by 100.74 % (101.18 %), for cubes and icosahedrons by 97.68 % (105.74 %) and 98.74 % (89.52 %). Values not given in brackets indicate deviations at the bend exit; deviations in brackets are obtained at the vertical pipe section outlet. It can be noticed that cubes have the largest possible outlet velocity followed by icosahedrons and spheres in an infinite vertical pipe section.

In addition to the velocities the pressure drop over the pipe bend is compared between DEM-CFD results and analytical models. For the analytical pressure drop the models [233] and [232] are used. In both models the overall pressure drop consists of the sum of pressure drops Δp due to gas transport Δp_L and particle transport Δp_S

$$\Delta p = \Delta p_L + \Delta p_S. \quad (24)$$

The particle transport pressure drop Δp_S can be divided into the acceleration pressure drop Δp_a , the bend pressure drop due to deceleration and reacceleration of the particles in the bend Δp_{bend} , work by gravity pressure drop Δp_g and friction pressure drop Δp_{fr} [233]

$$\Delta p_S = \Delta p_a + \Delta p_{bend} + \Delta p_g + \Delta p_{fr}. \quad (25)$$

In contrast to the definition in [233], in [232] work by gravity Δp_g and friction pressure drop Δp_{fr} are combined to one parameter $\Delta p_{g,fr}$ and acceleration pressure drop Δp_a and bend pressure drop Δp_{bend} are combined to $\Delta p_{a,bend}$ which is considered as a second parameter determining Δp_S

$$\Delta p_S = \Delta p_{g,fr} + \Delta p_{a,bend}. \quad (26)$$

In [232], in opposition to [233], the pressure loss coefficient ξ of the bend is considered for the calculation of Δp_L . For a 90° circular pipe with $R/D = 1$ as in our setup the pressure loss coefficient ξ obtains a value of 0.21 [246].

The total pressure drop of both models and the DEM-CFD simulations for spheres are shown in table 4. It can be seen that both models agree well with the simulation results. The maximum error is 4.8% reported by the model in [233] in comparison to the average pressure drop of the simulations.

Table 4: Total pressure drop of the analytical models and of the DEM-CFD including its standard deviation due to pressure fluctuations for spheres.

Δp [232]	Δp [233]	Δp DEM-CFD
245.58 Pa	233.84 Pa	(245.66 \pm 15.82) Pa

Results obtained in this section from empirical models [232,233,237] for both particle velocities after the bend and pipe outlet as well as pressure drops indicate the validity of the applied DEM-CFD simulation framework for spherical and non-spherical particles. As outlined, for the future own experimental investigations are planned to allow for a more thorough comparison exceeding the considered spheres, cubes and icosahedrons.

5. Results and discussion

Initially, the key flow features are analysed with regard to the considered particle shape. Thereafter, the distributions of rotational and translational velocities are derived and later total averaged forces and pressure drops are evaluated.

5.1 Key flow features by particle shape

Spheres: In the first simulation spheres with a diameter of 2.8 mm are investigated. Results are shown for the particle velocities in Fig. a, for the porosities in Fig. b, for the gas velocities in Fig. c and for the particle-gas, particle-particle and particle-wall forces in Fig. d - Fig. f, respectively. The particle velocities in the horizontal pipe section (Fig. a) are constant while the particles have not yet contacted the pipe bottom due to gravity. Within the bend a rope forms as particles are concentrating to regions close to the outer wall due to inertia and inelastic collisions. The particle velocity reduces from initially 7 m/s to \sim 3.5 m/s at the bend exit. These results agree well with the observations of Chu and Yu [228]. In the vertical pipe section the rope disperses as particles shift from the outer to the inner wall with increasing height. Throughout the vertical pipe section particles are rarely accelerated as the particle velocity at the outlet is insignificantly larger in comparison to the bend exit.

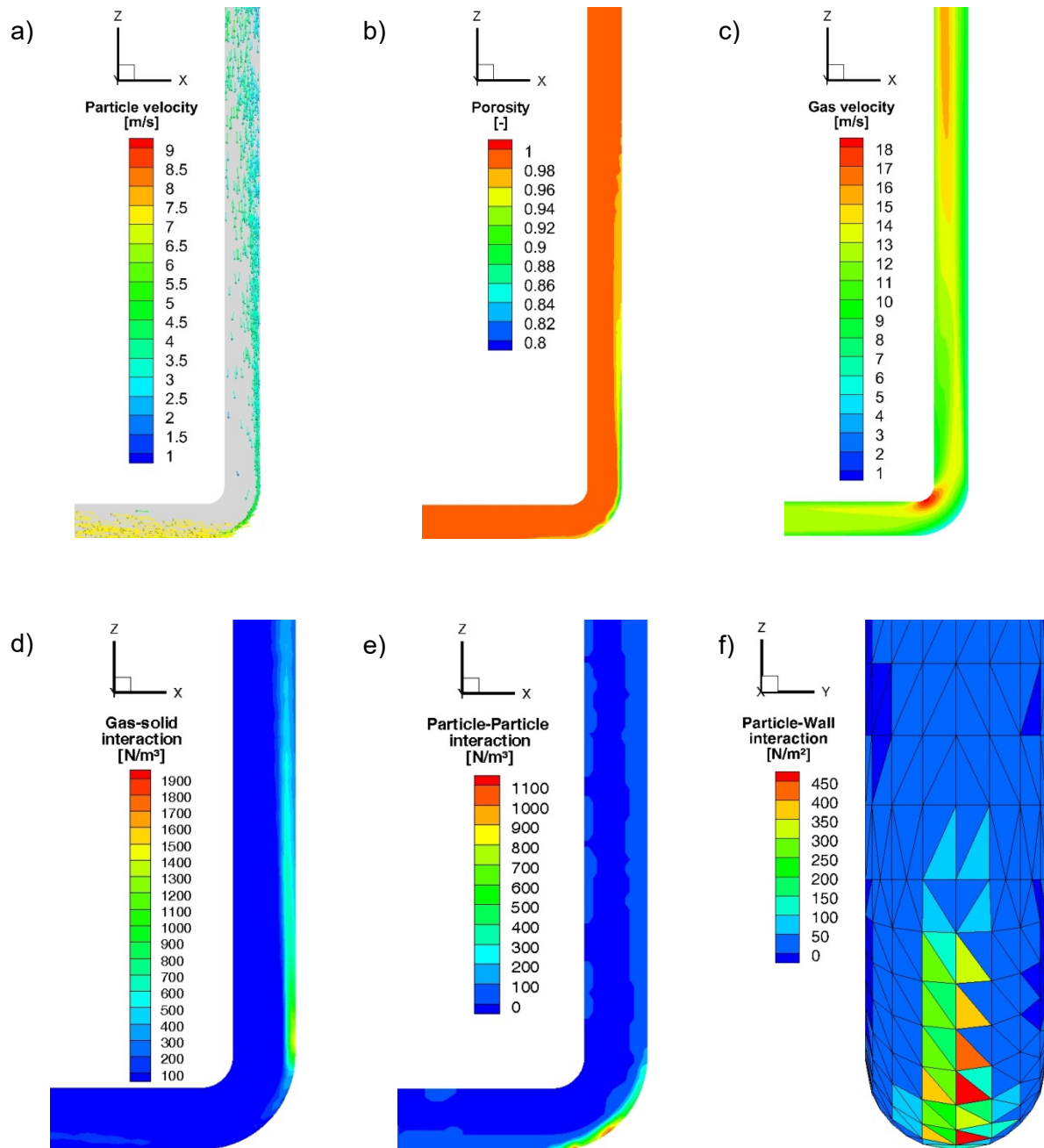


Fig. 2: Cross-sectional view of the pipe bend for spheres: a) Particle velocity at a random time step, b) averaged porosity, c) averaged gas velocity, d) averaged gas-solid interaction e) averaged particle-wall interaction and f) averaged particle-wall interaction; averaged in the time period 1-3 seconds.

In the regions where the rope forms and slowly disperses downstream, porosities do show declined values (Fig. 2b). Gas velocities are increased towards the inner wall region of the bend where no particles are present and further up in the vertical section of the pipe close to the inner wall. Maximum gas velocities of 17 m/s in the bend and porosities below 0.94 at the bend exit are well in alignment with results obtained by Chu and Yu [228], although differences exist in the way particles are charged in both investigations and due to differently chosen simulation parameters (linear contact model, ideal gas law). Values obtained for the gas-solid, particle-particle and particle-wall interaction deviate from results obtained by Chu and Yu [228] as the interaction parameters are defined differently – yet, general tendencies do agree. Zones

of large gas solid interaction are located upwards from the bend exit as the difference between the particle and gas velocity is largest in this area. Areas of most intense particle-particle and particle-wall interactions are situated within the pipe bend mainly, with most intense particle-particle and particle-wall interaction located throughout the first 2/3 of the bend length. In its width the particle-wall interaction zone is narrowing towards the second half of the bend; it is well centered in the pipe. Qualitatively, these results match those obtained by Chu and Yu [228].

Snapshots of the orientation of spheres at the bend entry and within the bend are outlined in Fig. 3a and Fig. 3b with their related orientations. The particle orientations are calculated based on the orientation angle α calculated between the particle orientation vector shown in table 1 which is projected into the x-y-plane and the x-axis vector (comp. Fig. 3a). No preferred orientation is taken up by the spherical particles during their movement through the pipe bend. The particles are colored by their velocity according to the legend shown in Fig. 2a.

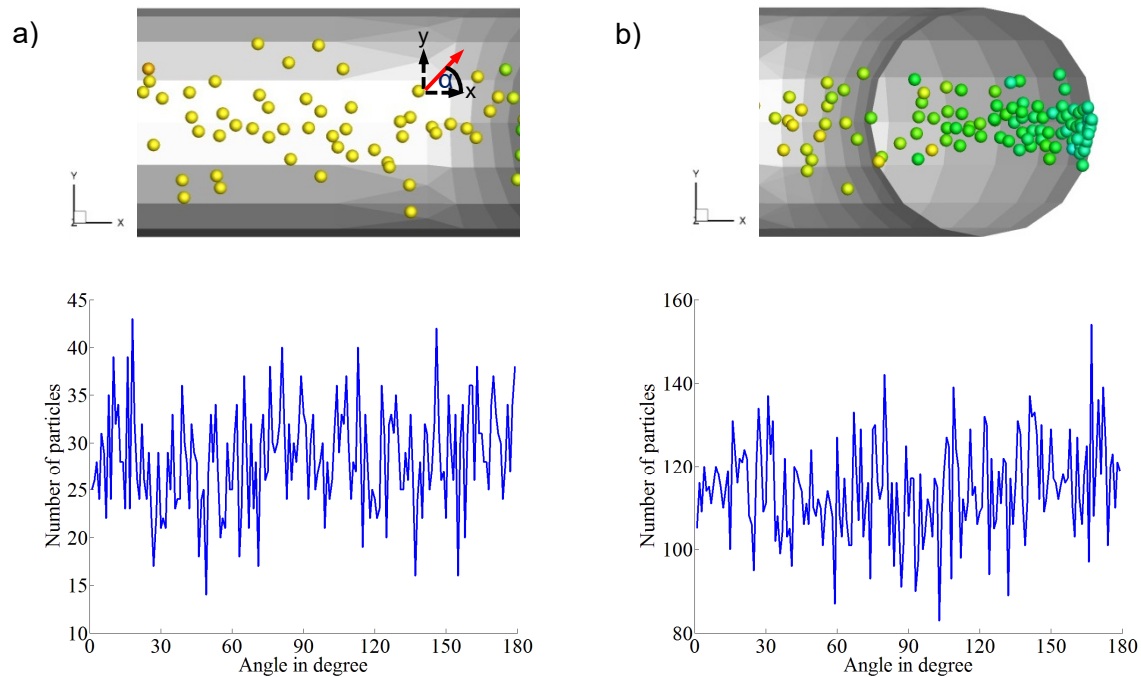


Fig. 3: Time summarized distribution of the particle orientations based on the projection on the x-y-plane for spheres with the corresponding zone used for the summation: (a) Bend entry and (b) throughout the bend.

Cubes: Results for cubes while being pneumatically conveyed through the pipe bend are shown in Fig. 4. Due to the possibly larger cross-sectional area of cubes ($A_{\perp\max} = 8.82 \text{ mm}^2$, $A_{\perp\min} = 5.09 \text{ mm}^2$) compared to spheres ($A_{\perp\max} = A_{\perp\min} = 6.16 \text{ mm}^2$) the cubes are initially accelerated during the horizontal section of the pipe. In average particles reach velocities of $\sim 7.3 \text{ m/s}$ (Fig. 4a) with minimum velocities of 5.5 m/s and maximum velocities of 8 m/s when entering the pipe bend. Cuboidal particles exit the pipe bend with smaller velocities than spheres ($v = 3.28 \text{ m/s}$). Exit velocities at the outlet of the vertical section are obtained with 3.83 m/s in average (minimum: 3 m/s , maximum 6.3 m/s). It is obvious that the rope disperses slower

compared to spheres with most particles concentrated to the outer wall region even at the exit of the vertical pipe section. This is also confirmed by the porosity distribution in the pipe bend. Porosities with values below 0.98 can be encountered nearly up to the pipe section outlet (Fig. 4b). Due to the strong particle concentration in the vertical pipe section close to the outer wall a gas velocity maximum can be encountered nearly all along the inner wall of the vertical pipe section with fluid velocities exceeding 18 m/s (Fig. 4c).

Due to the strong particle velocity reduction in the pipe bend as well as a larger possible cross-sectional area a maximum of the gas solid interaction is detectable at the bend exit. Although the downstream zone of intensive gas-solid interaction widens more strongly, the dispersion of a rope consisting of cubes occurs slower compared to spheres as the particle velocity is more reduced for cubes at the bend exit (Fig. 4d). The particle-particle interaction is more intense for cubes and extends to a larger zone due to a more random collision behavior affecting the trajectories after collisions (Fig. 4e). The particle-wall interaction zone is centered on the outer bend wall. Due to the overall velocity reduction of the particles it extends less upwards around the bend into the vertical pipe section than for spheres. The particle wall interaction is more intense and spreads over a larger region (Fig. 4f).

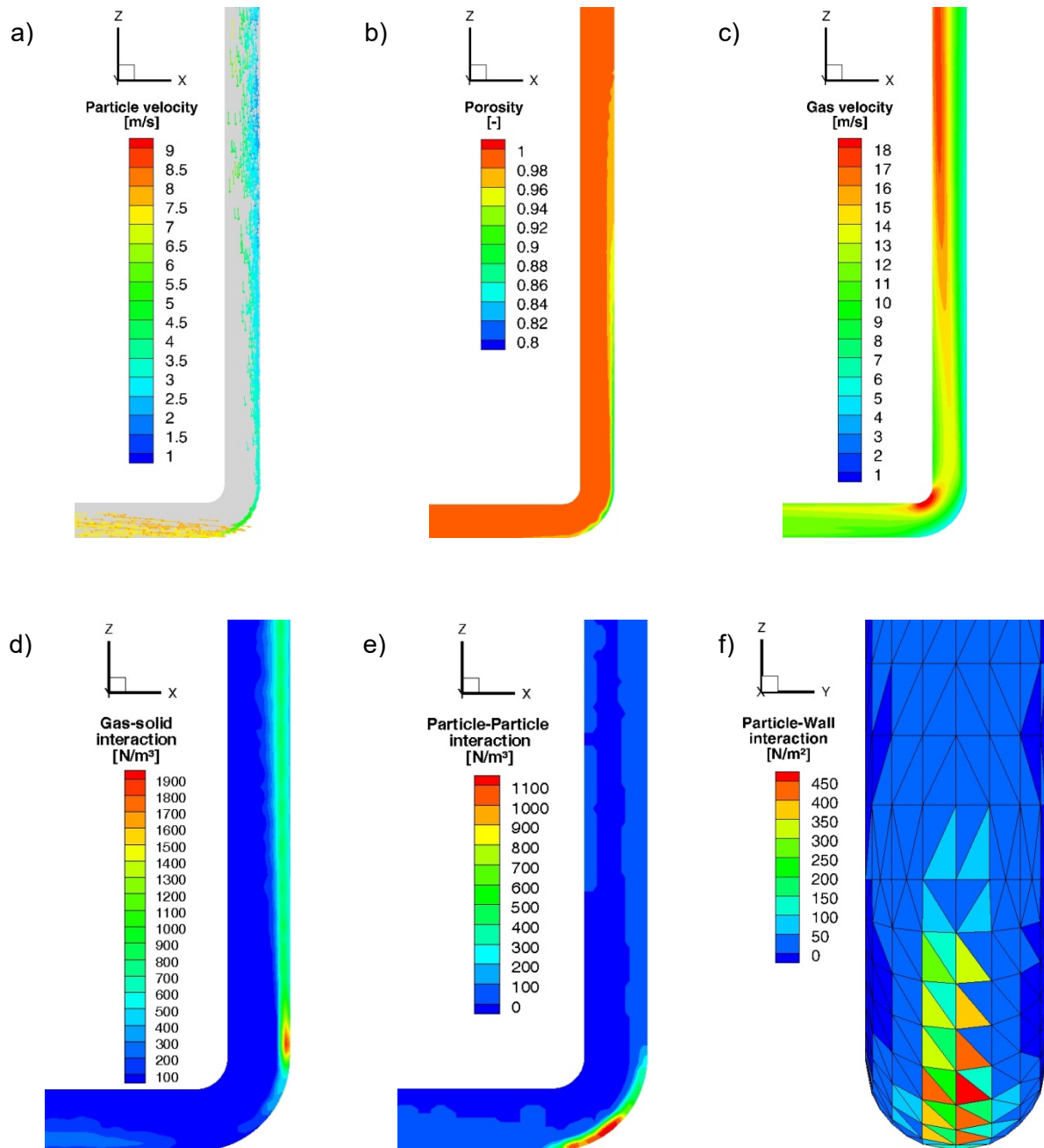


Fig. 4: Cross-sectional view of the pipe bend for cubes: a) Particle velocity at a random time step, b) averaged porosity, c) averaged gas velocity, d) averaged gas-solid interaction e) averaged particle-wall interaction and f) averaged particle-wall interaction; averaged in the time period 1-3 seconds.

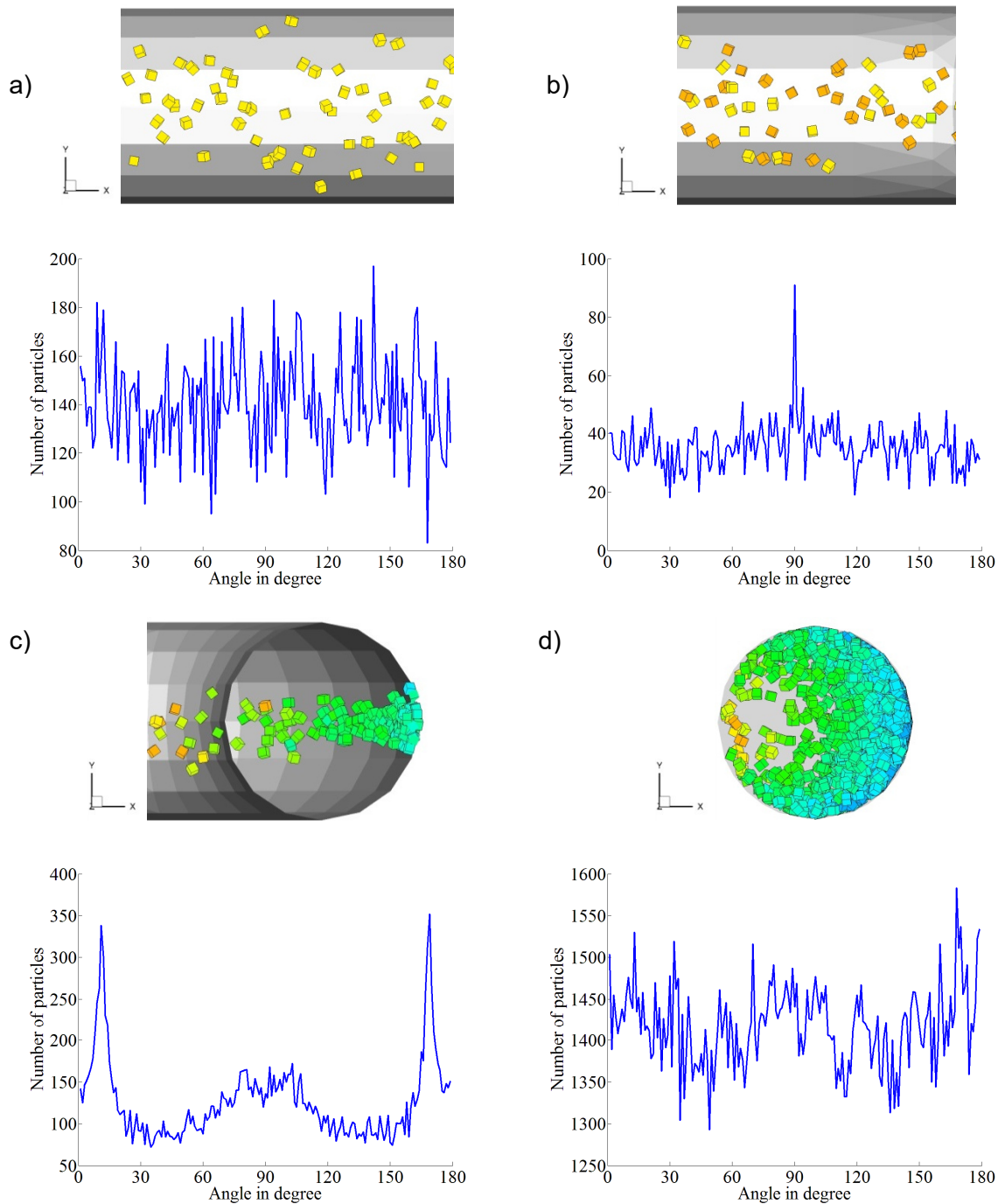


Fig. 5: Time summarized distribution of the particle orientations based on the projection on the x-y-plane for cubes with the corresponding zone used for the summation: (a) Pipe inlet, (b) bend entry, (c) throughout the bend and (d) at the pipe outlet.

Results for the orientation of cubes are outlined in Fig. 5. Particles in the charging zone at the inlet of the horizontal section are outlined in Fig. 5a. Particles are placed with equally distributed orientations in the x-y-plane with constant particle velocities. At the inlet of the bend the cuboidal particles are still equally distributed, with a slight peak at 90° . The mainly equal distribution results from particles that are not yet in contact with the walls. Particles that are in contact with a wall are contacting with one of the six cube sides. In case that the orientation vector is orientated normal to the pipe wall they contribute to the 90° peak when being projected into the x-y-plane (Fig. 5b). As particle orientation is shifted by 90° in the pipe bend,

peaks form out at roughly 0° and 180° as shown in Fig. 5c, originating from the particles previously contributing to the peak at 90° in Fig. 5b. The peaks at 0° and 180° are not precisely centered at 0° and 180° due to the fact that particles are never fully centered in the pipe.

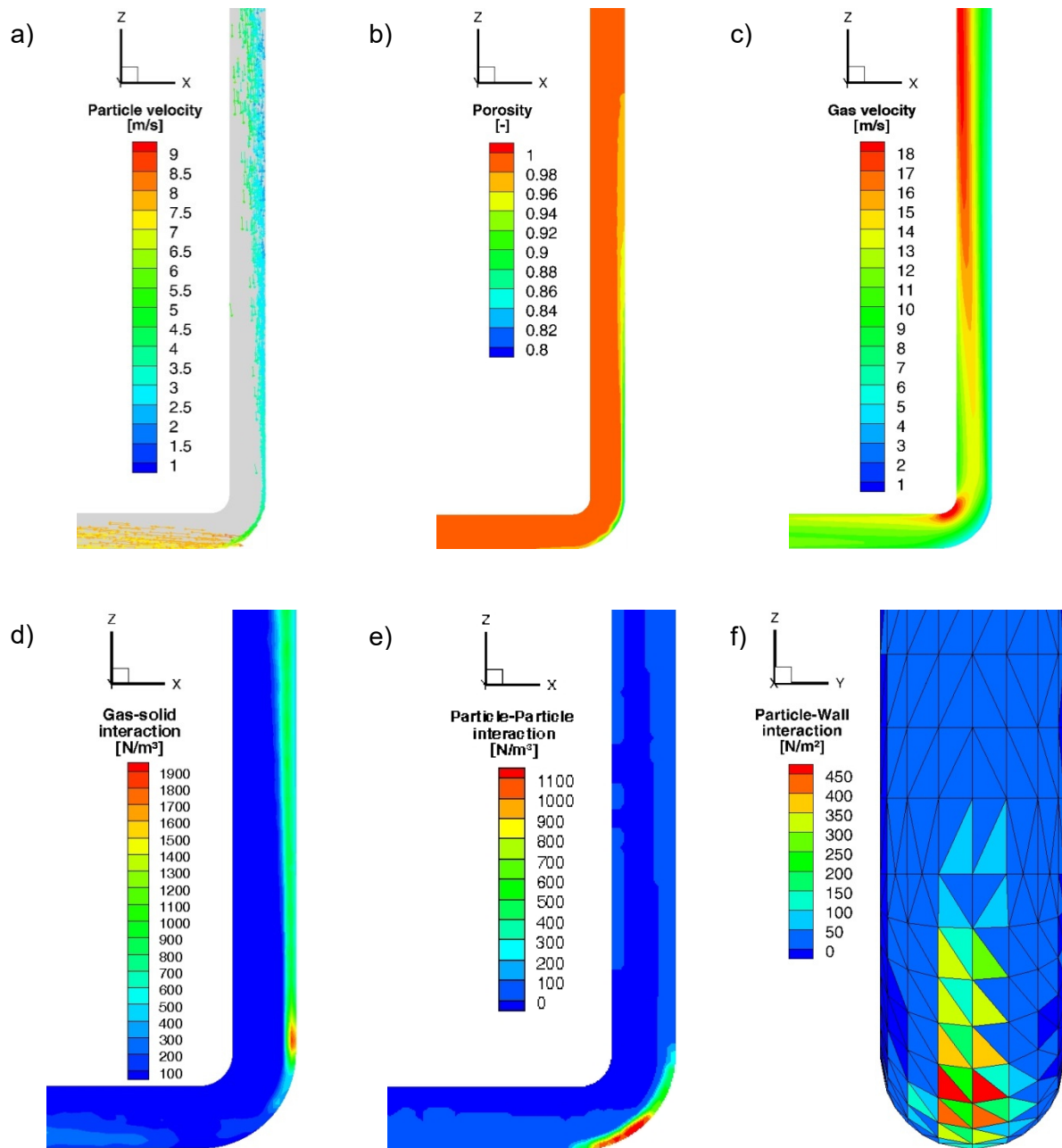


Fig. 6: Cross-sectional view of the pipe bend for pyramids: a) Particle velocity at a random time step, b) averaged porosity, c) averaged gas velocity, d) averaged gas-solid interaction e) averaged particle-wall interaction and f) averaged particle-wall interaction; averaged in the time period 1-3 seconds.

Additionally, particles yet not in contact with walls and particles still being in the horizontal section of the pipe contribute to the weak peak at around 90° and the equally distributed values for different orientation angles. Particle velocities are slowly decreasing while particles are being transported through the bend. In the section after the bend particles are equally distributed again (Fig. 5d). Particles close to the outer walls have a significantly smaller velocity. Towards the center and especially close to the inner wall particle velocities are larger.

Pyramids: Results for pyramid shaped particles are outlined in Fig. 6. Due to the enlarged cross-sectional area of $A_{\perp\max} = 10.60 \text{ mm}^2$ which exceeds the area of cubes, pyramids are accelerated while placed in the horizontal pipe section from initially 7 m/s to 7.4 m/s in average (Fig. 6a). In the pipe bend pyramids decelerate to $\sim 3.27 \text{ m/s}$. In the vertical section pyramids accelerate again leading to a velocity distributed in the range of 3.45 m/s – 6.75 m/s at the outlet of the vertical pipe section. In comparison to cubes and spheres, pyramids obtain larger velocities. The porosity distribution shown in Fig. 6b indicates a very similar dispersion behavior for pyramids as for cubes which is also supported by the results for the gas velocity distribution in Fig. 6c.

The particle fluid interaction shown in Fig. 6d indicates a smaller maximum as encountered for cubes. As pyramids align with the wall, their cross-sectional area becomes smaller leading to a smaller particle fluid velocity difference which results in the less intense peak visible. The zone of large particle-fluid interaction downstream from the peak zone forms out similarly to cubes. Intense zones of particle-particle interaction are situated within 2/3 of the bend (Fig. 6e). Compared to cubes, the zone of most intense particle-wall interactions shifts towards the entry of the pipe bend (Fig. 6f).

Results on the orientation of the pyramid shaped particles are given in Fig. 7. At the inlet particles are equally distributed as shown in Fig. 7a. Close to the bend inlet (Fig. 7b) some particles are still in free flight (colored in yellow/orange); others (colored in green) already contacted the pipe walls. As particles contact with one of their lateral plains aligned to the wall surface an orientation distribution as outlined in Fig. 7b is obtained. The peak at 90° results from particles whose orientation vector is aligned normal to the pipe walls. In the bend these particles are shifted by 90° leading to one peak at roughly 180° shown in Fig. 7c. Further downstream an equal distribution begins to develop while particles are distributing over the whole cross-section of the pipe (Fig. 7d).

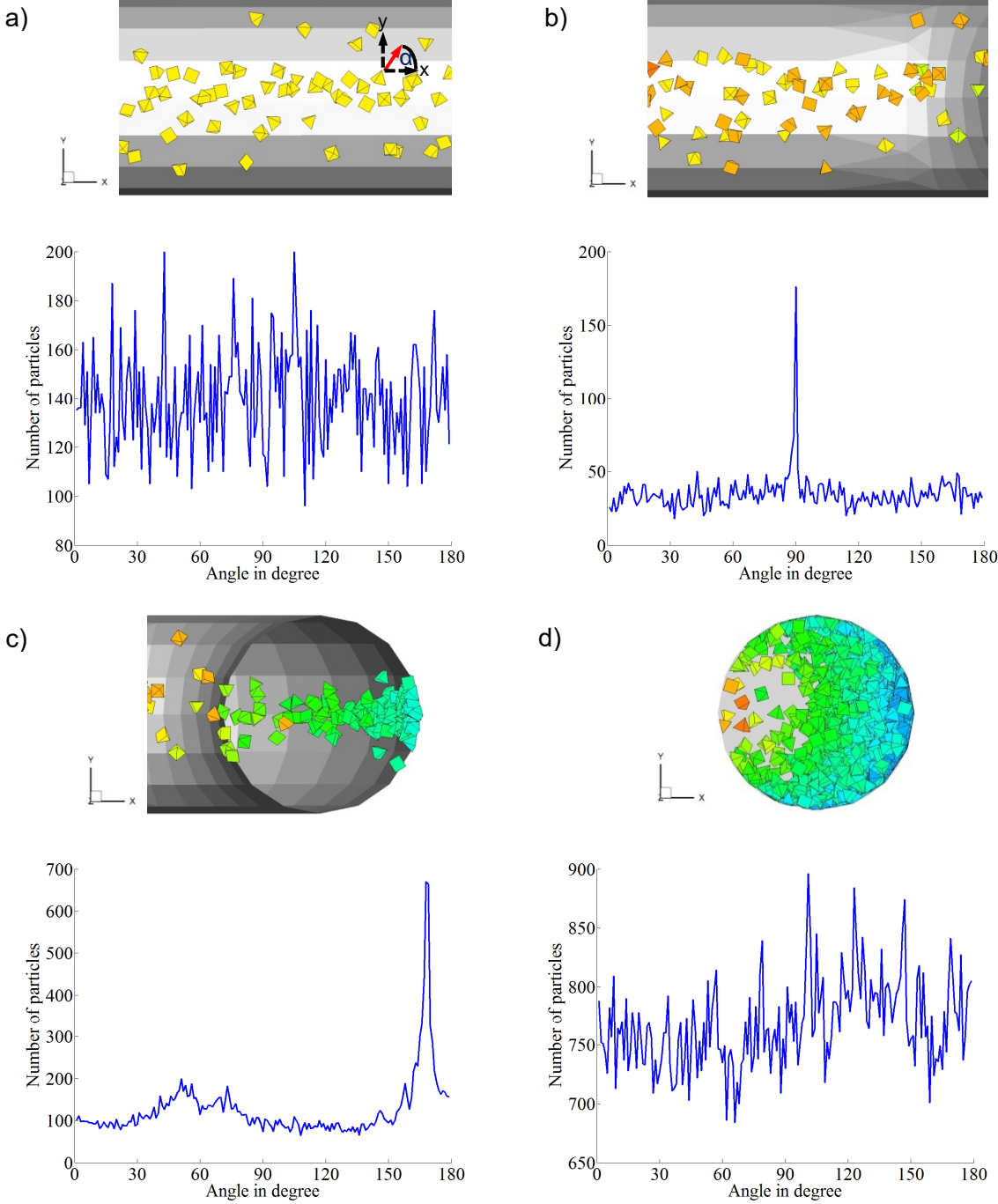


Fig. 7: Time summarized distribution of the particle orientations based on the projection on the x-y-plane for pyramids with the corresponding zone used for the summation: (a) Pipe inlet, (b) bend entry, (c) throughout the bend and (d) at the pipe outlet.

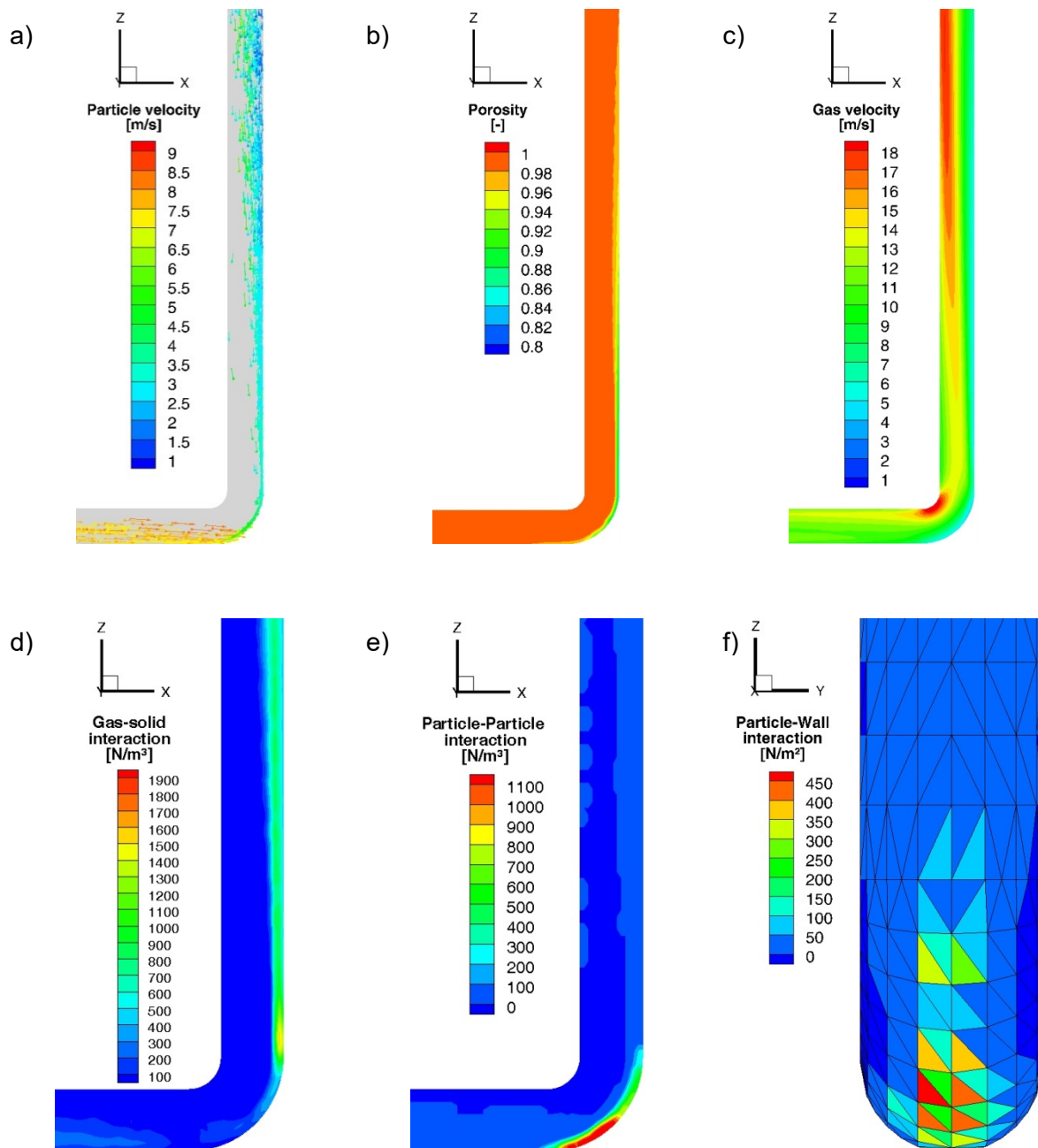


Fig. 8: Cross-sectional view of the pipe bend for plates: a) Particle velocity at a random time step, b) averaged porosity, c) averaged gas velocity, d) averaged gas-solid interaction e) averaged particle-wall interaction and f) averaged particle-wall interaction; averaged in the time period 1-3 seconds.

Plates: Results for plates in the pipe bend are shown in Fig. 8. Plates with a large cross-sectional area due to their orientation are accelerated and impact the pipe bend at a position of $z = -0.018$ m. Plates with a small cross-sectional area in contrast drop quickly and impact the bottom of the horizontal pipe section. Average velocities can be estimated with 7.36 m/s (minimum velocities: 5.89 m/s; maximum velocities: 8.29 m/s). When getting in contact with the bend wall, plates align themselves with the pipe walls resulting in a thin, compact rope. Plates are leaving the bend with a mean velocity of 3.28 m/s. In the vertical pipe section plates are slowly accelerated as the side surface is oriented perpendicularly to the flow. Accelerated particles spread up leading to a wide velocity distribution at the outlet of the vertical pipe section

(Fig. 8a). Due to the in average small cross-sectional area of the plates the zone with a porosity of below 0.98 extends far up the vertical pipe section to $z=0.73$ m (Fig. 8b). This also affects the gas velocities with flow concentrating towards the inner wall in the vertical pipe section (Fig. 8c).

The particle-fluid interaction is not strongly pronounced. This is not because of the particle velocities but because of the comparably small particle surfaces involved. From the pipe bend a clearly visible zone of strong particle- fluid interaction extends downstream (Fig. 8d). Particle-particle interactions behaves similarly to other particle shapes (Fig. 8e). In contrast particle-wall interaction is concentrated to the lower part of the bend up to $z= 0.07$ m (Fig. 8f).

Details on the orientation of plates are outlined in Fig. 9. At the inlet plates are equally distributed (Fig. 9a); close to the entry to the bend particle start to get in contact with the pipe walls leading to a maximum at 90° in the respective orientation plot (Fig. 9b). As the plates turn by 90° in the bend, peaks with 10° and 170° form at the bend exit (Fig. 9c). At the outlet of the vertical pipe section the particles are oriented equally distributed with regular peaks every 22.5° (Fig. 9d). These peaks result from the pipe wall discretization in the simulations.

Icosahedrons: Icosahedrons are very sphere like with a sphericity of 0.94. Therefore, flow features of icosahedrons in the pipe bend develop similarly to spheres (Fig. 10a). Icosahedrons accelerate in the horizontal pipe section to velocities of 7.2 m/s (spheres: 7.08 m/s). In the bend they are decelerated to 3.42 m/s (spheres: 3.58 m/s) and accelerated to 4.39 m/s in the vertical pipe section (spheres: 3.72 m/s). So far, all complex shaped particles studied, except icosahedrons, reveal strong variations in their cross-sectional area especially in the vertical pipe section. velocity differences at the outer and inner wall are less pronounced for particles with orientation independent projection areas like icosahedrons or spheres. Nevertheless a deviation up to 12 % exists between the projection areas of icosahedrons ($A_{\perp\max}= 6.87$ mm², $A_{\perp\min}= 6.27$ mm²) and spheres ($A_{\perp} = 6.16$ mm²). Hence, particle-fluid interaction forces and as a consequence particle-particle interactions increase in comparison to spheres. Influenced by this, in case of icosahedrons the rope leaving the bend quickly disperses with the first particles reaching the inner pipe wall after 0.2 m (Fig. 10a). Minimal velocities close to the outer wall are obtained with 3.76 m/s, maximal velocities at the inner wall with 5.58 m/s for icosahedrons (minimal/maximal sphere velocity: 2.31 m/s / 4.66 m/s). The quick dispersion of the rope in case of icosahedrons gets visible in the porosity plot shown in Fig. 10b. A homogenous porosity of at least 0.98 is reached at $z= 0.37$ m which is a result of a constant large particle-fluid force. The gas velocity profile reveals a maximum close to the inner bend wall and further downstream in the vertical pipe section at $z=0.47$ m. At the outlet of the pipe the gas velocity is already decreasing for icosahedronic shaped particles again (Fig. 10c).

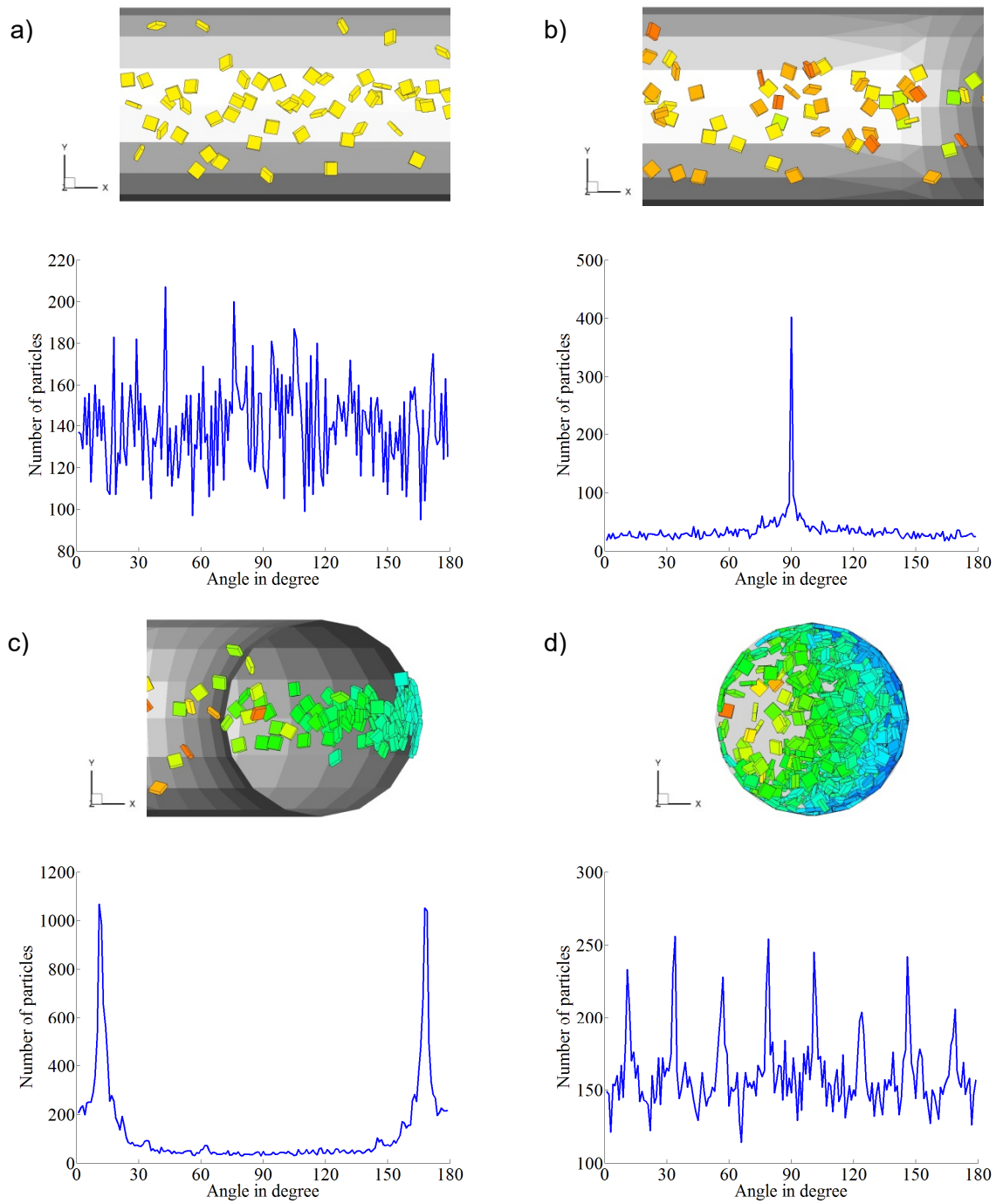


Fig. 9: Time summarized distribution of the particle orientations based on the projection on the x-y-plane for plates with the corresponding zone used for the summation: (a) Pipe inlet, (b) bend entry, (c) throughout the bend and (d) at the pipe outlet.

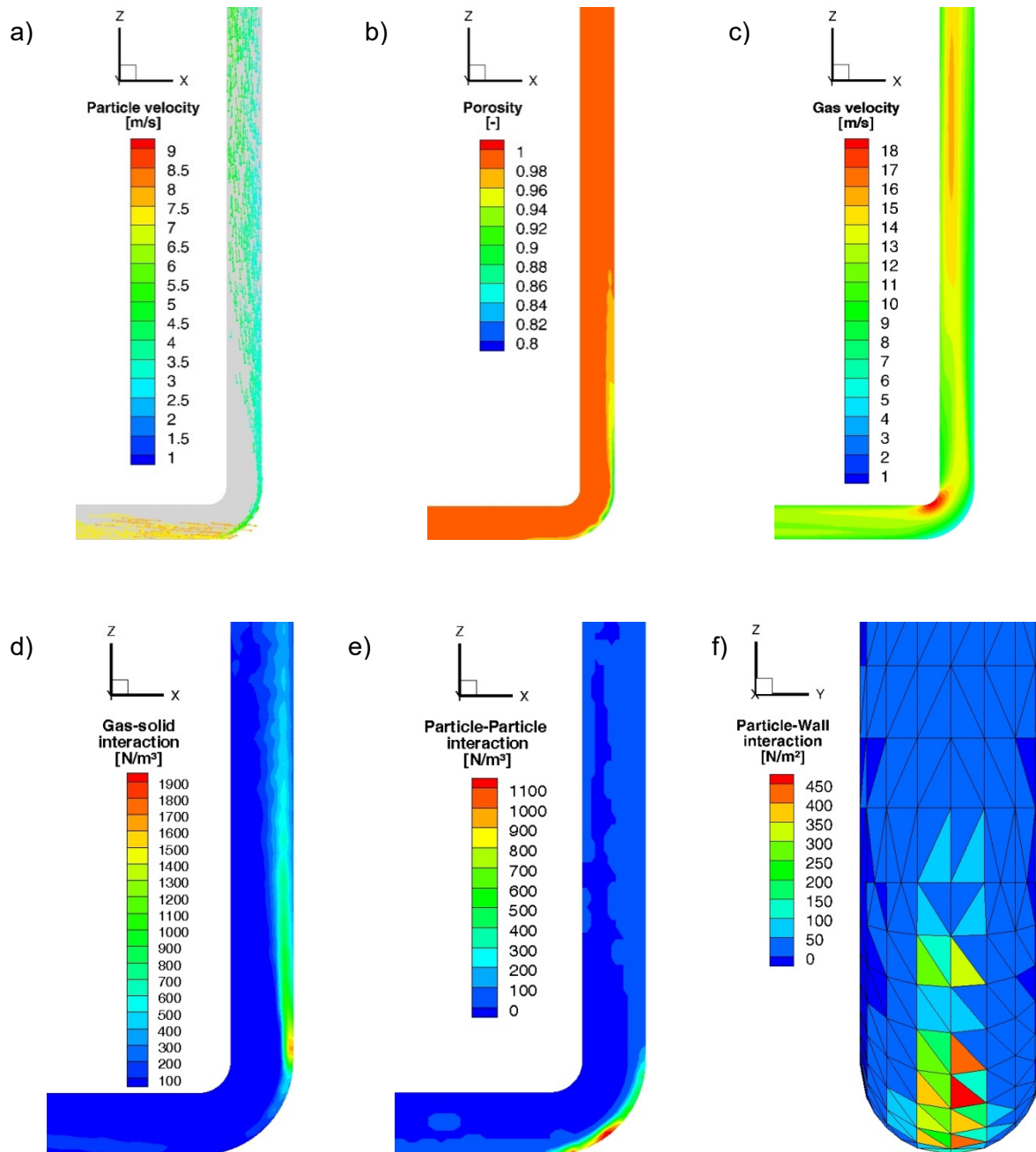


Fig. 10: Cross-sectional view of the pipe bend for icosahedrons: a) Particle velocity at a random time step, b) averaged porosity, c) averaged gas velocity, d) averaged gas-solid interaction e) averaged particle-wall interaction and f) averaged particle-wall interaction; averaged in the time period 1-3 seconds.

In the rope close to the outer wall particles obtain preferred orientations which result in low projection areas. When particles disperse towards the inner wall no preferred orientations with inherently low projection areas are taken up, see Figs. 6, 8, 10 and 12. As a consequence the Details on the particle-fluid, particle-particle and particle-wall interaction of icosahedrons are given in Fig. 10d – Fig. 10f. In contrast to spheres, the maximum in the particle-fluid interaction after the bend exit is more pronounced. Downstream from here the zone of significant gas-fluid interaction is more widened than for spheres and continuously narrowing towards the pipe outlet (Fig. 10d). For the particle-particle interaction two separated areas are distinguishable

within the pipe bend as noticeable for spheres (Fig. 10e). The overall particle-particle contact intensity is slightly larger as for spheres. The distribution of the particle-wall interaction is alike to what is reported for spheres (Fig. 10f).

Orientations of icosahedrons in the horizontal pipe section close to the bend inlet (Fig. 11a) and within the bend (Fig. 11b) indicate an equal distribution in both zones. This result is in alignment with results acquired for spheres.

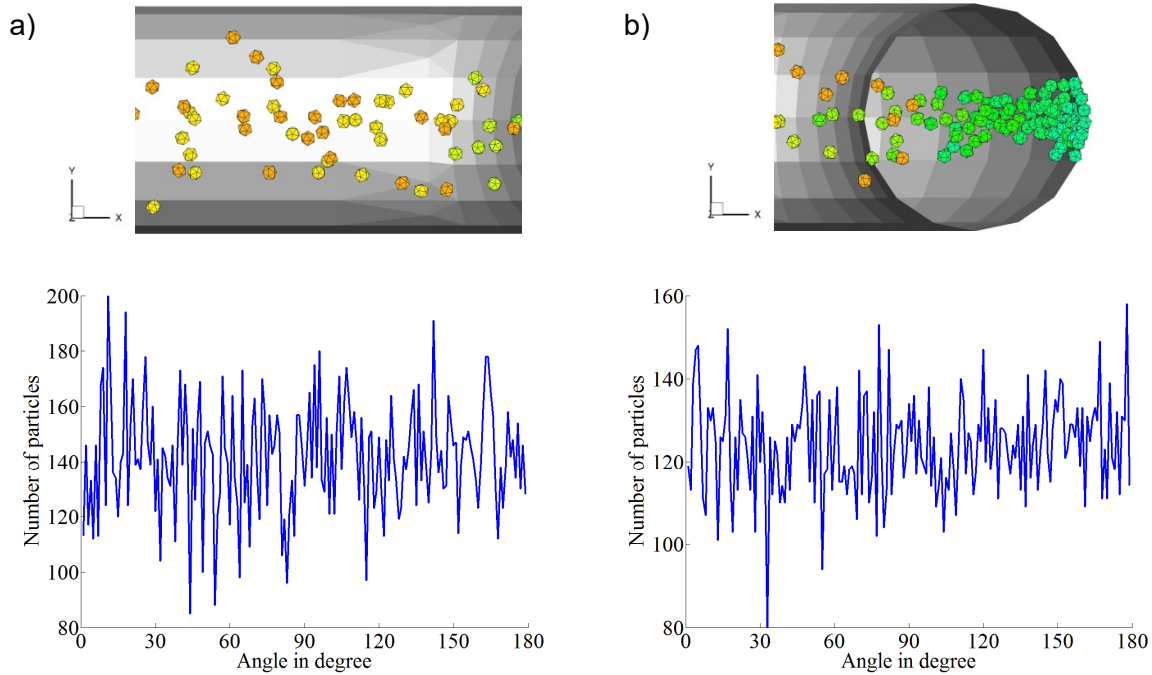


Fig. 11: Time summarized distribution of the particle orientations based on the projection on the x-y-plane for icosahedrons with the corresponding zone used for the summation: (a) Bend entry and (b) throughout the bend.

5.2 Distribution of the translational and rotational particle velocities

To determine the differences in particle velocity reduction after the bend in dependence on shape as well as the particle acceleration in the horizontal pipe section and possible particle rotations, distribution functions of the overall translational velocities v and rotational velocities ω are calculated. Again the regarded time period is 1 – 3 s. The results are shown in Fig. 12.

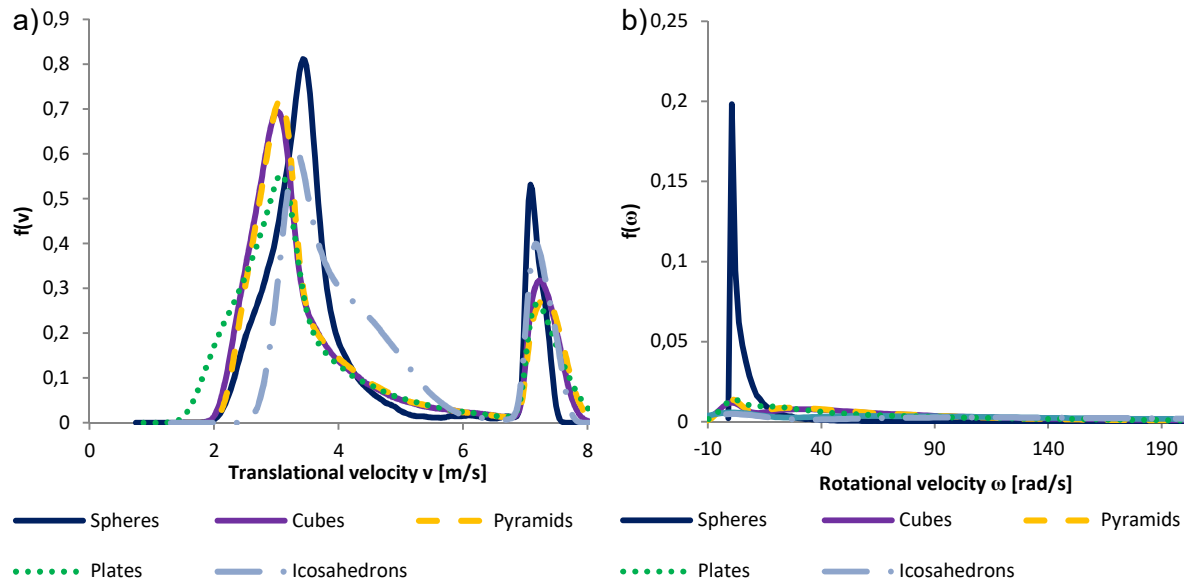


Fig. 12: Calculated distribution functions of: a) Overall translational velocities v and b) overall rotational velocities ω .

In the distribution function of the overall translational particle velocities v two peaks can be seen (Fig. 12a). The first represents the reduced particle velocity after the bend and the second the nearly uniform velocity in the horizontal pipe section after charging the particles into the system. Spheres obtain the largest reduced velocity after the bend. Complex shaped particles accelerate to larger velocities in the horizontal pipe as a consequence of larger drag forces resulting out of in average larger cross-sectional areas. Independent of particle shape the velocity distribution is uniform at the inlet of the horizontal pipe. The lower velocities for complex shaped particles after the bend are caused by increased velocities in the horizontal pipe. This implies a stronger wall impact in the bend dissipating eventually more energy. Additionally, the motion of non-spherical particles as a bulk is more chaotic and leads to a stronger dissipation of kinetic energy and therefore reduced velocities. Icosahedrons, the non-spherical particles with the largest sphericity in this investigation, are behaving most similar to spheres.

In addition to the overall translational velocities v the distribution of the overall rotational velocities ω is represented in Fig. 12b. Only for spheres a clear peak is distinguishable for lower rotational velocities. All other non-spherical particles do not show a preference for a certain rotational velocity. The rotation velocity attributed to spheres results from their ability to take up a rolling motion while passing through the pipe bend. All other particle shapes slide through the bend preferably. Even icosahedrons although very sphere-like show this behavior of a sliding/jumping motion which is a result of the edges generally attributed to the shape description by polyhedra.

5.3 Summarized averaged forces in the bend and total pressure drop

To investigate the influence of the particle shape on possible erosive wear in the bend as well as on possible product degradation the particle-wall and particle-particle forces are averaged in the bend region. Furthermore, the total pressure drop throughout the whole pipe is calculated for the different particle shapes. Again, the considered time period is 1 – 3 s. Fig. 13 shows the averaged forces for all DEM-CFD simulations performed.

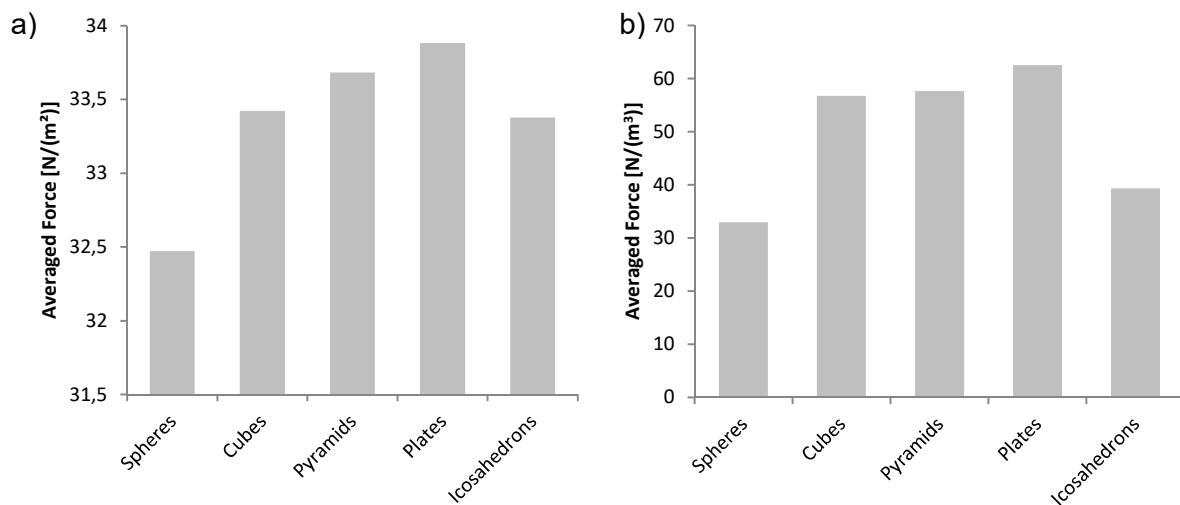


Fig. 13: Averaged forces in the bend region: a) Particle-wall forces and b) particle-particle forces.

It is noticeable that the particle shape influences the particle-particle more than the particle-wall interactions. For all shapes particles drop to the pipe bottom in the horizontal pipe section due to gravity thereby contributing equally intense to the particle-wall interaction before entering the bend. Complex shaped particles experience larger particle-wall forces as they usually accelerate within the horizontal pipe section more strongly and therefore enter the pipe bend with larger velocities than spheres.

Significant differences, however, are observable for the averaged particle-particle interactions for the differently shaped particles. The averaged forces for the complex shaped particles are up to twice as large as those of spherical particles – this would equally affect possible particle degradation. During the transport through the bend the velocity is reduced stronger for non-spherical particles (comp. Fig. 12a) resulting in more particles being present within the bend. This effect is less distinct for icosahedrons as the shape is most similar to spheres. Therefore, icosahedrons exhibit averaged particle-particle forces close to values obtained for spheres. Values are however a bit larger as the icosahedrons can take up slightly larger circumscribed spheres.

The averaged total pressure drop including its standard deviation due to pressure fluctuations is illustrated for all particle shapes in Fig. 14. Pressure drop fluctuations are below 20 Pa for all shapes. However, deviations are apparent for the mean pressure drop. The pressure drop in a system with in- and outflow is mainly influenced by the amount of particles in the system affecting the porosity and the momentum each particle exchanges with the fluid. The amount of particles in the system is dependent on the particle velocities within the bend in our setup as the inlet mass flow is constant for all simulations. Thus, the pressure drop decreases for cases with larger particle velocities as the porosity increases as a consequence. In the case of a lower momentum exchange of particles with the surrounding fluid the pressure drop also forms out lower. The exchange of momentum per particle mainly depends on the crosswise particle area and the relative velocity between particles and the fluid.

The most strongly varying parameter affecting the drag force and thereby the momentum exchange and pressure drop is the crosswise area of particles depending on the specific orientation and of course on the relative velocity between the particle and the fluid. As a consequence of a similar crosswise area and comparable velocities throughout the simulations, the values for the pressure drop of icosahedrons are close to the pressure drop of spheres. Note that the obtained pressure drop for spheres is in good agreement with results gained by Lee et al. [236] experimentally. In case of cubes, pyramids and plates a large momentum exchange occurs due to acceleration of particles in the horizontal bend, large relative velocities through the lower reduced velocity after the bend or an increased source of momentum through a larger crosswise area. In addition to that, the amount of particles grows in the system as the average velocities are lower than for spheres, see Fig. 12.

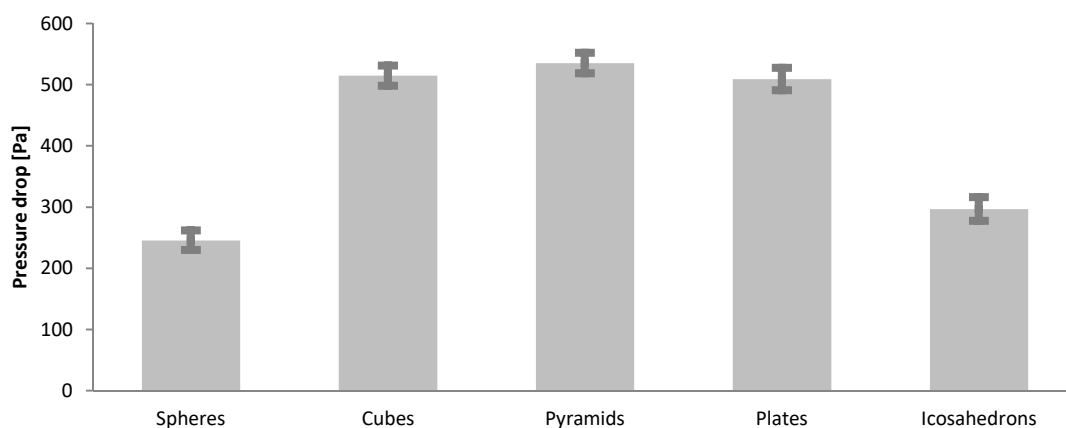


Fig. 14: Pressure drop with standard deviation due to pressure fluctuations averaged over the time period $t = 1-3$ s.

6. Conclusions

The coupled DEM-CFD approach has been extended to include complex shaped particles and has been applied to the simulation of a 90° pipe bend connecting a horizontal and vertical pipe section. As particle shapes a selection of volume equivalent spheres, cubes, pyramids, plates and icosahedrons are considered. DEM-CFD results have been validated against empirical models for the bend exit velocities for spherical and non-spherical shapes as well as for overall pressure drops for spheres revealing a good agreement. Results for spheres also match results from an earlier study by Chu and Yu [228]. Regarding the rope formation, dispersion and general flow features, the following results have been obtained.

- Rope formation in the pipe bend is initiated with the first particle-wall contact. The point of initial contact depends on the particle velocity which is affected by the particle shape. Spheres obtain the lowest maximal velocity before entering the bend and the largest bend exit velocity. It is observed that non-spherical particles with larger projection areas are accelerated stronger in the horizontal pipe section. Pyramids with the largest average cross-sectional area obtain the largest velocities. Accordingly, the point where the rope starts to form differs as particles with lower velocities impact the wall earlier.
- Particle-wall interaction in the bend increases for larger particle entry velocities. The bend exit velocities differ for the investigated particle shapes due to varying particle-particle and particle-wall interactions. Differences in the particle-particle interactions are more noticeable than for the particle-wall interactions due to particle shape. The highest particle-particle interactions in the bend region and lowest velocities are attributed to plates followed by pyramids and cubes. The particle-particle interactions and particle velocities of icosahedrons are close to those of spheres due to their geometric similarity.
- Particle shape strongly affects the rope dispersion. Icosahedrons are the particle shape with the fastest rope dispersion followed by spheres, pyramids, cubes and plates. In general, a strong particle-fluid interaction, particle-particle collisions and large bend exit velocities lead to accelerated rope dispersion.
- Icosahedrons and spheres are geometric similar but reveal differences regarding their particle-particle and particle-fluid interactions. This can be explained due to a larger circumscribed sphere attributed to icosahedrons compared to the investigated spheres which results in a 12 % larger projection area and therefore a larger collision probability. Cubes, pyramids and plates have a low bend exit velocity and obtain a low particle-particle interaction slowing down rope dispersion.

- The gas velocity which increases towards the inner bend wall where no particles are present and further up in the vertical section of the pipe close to the inner wall influences the particle velocity distribution at the outlet. Cubes, plates and pyramids with large maximum gas velocities reveal large differences in particle velocities between outer and inner wall at the outlet.

The obtained results are based on a numerical investigation and its analysis. Although, the particle bend exit and pipe exit velocities as well as pressure drops have been validated against empirical correlations for spherical and selected non-spherical shapes, the whole simulation framework should be validated more thoroughly against experimental investigations including a broader selection of particle shapes in the future. Experimental data from literature where complex shaped particles have been addressed within a pipe bend is not readily available to the authors' knowledge. Own experimental investigations with the particle shapes addressed in this investigation are therefore currently in preparation.

For the future the derived simulation framework could be used to gain more general correlations for the rope formation and dispersion behavior including a broader variety of shapes [232,237]. These correlations could be helpful for solving practical engineering design problems related to pneumatic conveying involving bulk solids comprising of complex shaped particles. Additionally, the framework would be helpful to investigate rope formation and dispersion under larger solids loadings. In this case particle and fluid flow could become fluctuating with temporally varying solids volume fractions [236] – here the DEM-CFD which inherently models fluid and particle phase transiently would be ideally suited to represent occurring phenomena.

Acknowledgements

Financial support by the DFG - KR 3446/6-1 is greatly acknowledged. Collaboration with the chair of energy technology (LEAT) is appreciated.

V. Development and verification of a resolved 3D inner particle heat transfer model for the Discrete Element Method (DEM)

T. Oschmann*, M. Schiemann, H. Kruggel-Emden

Ruhr-Universitaet Bochum, Universitaetsstrasse 150, D-44780 Bochum, Germany

*Corresponding author. Tel.:+49 234 32 26334; fax: +49 234 32 14227; E-mail address: Oschmann@leat.rub.de

The following accepted manuscript appeared as journal version in Oschmann T., Schiemann M., Kruggel-Emden H.: Development and verification of a resolved 3D inner particle heat transfer model for the Discrete Element Method (DEM), Powder Technology 291, 392-407 (2016) and may be found at <https://doi.org/10.1016/j.powtec.2015.12.008>.

Abstract

An implicit 3D heat transfer model is derived to represent resolved heat conduction within spherical and non-spherical particles in the presence of a surrounding fluid. The proposed method, based on a finite difference solution, is integrated into the Discrete Element Method (DEM) applicable to multi-particle systems accounting for the following heat transfer mechanisms: particle-particle, particle-wall, particle-fluid-particle heat conduction, particle-particle radiation and particle-fluid convection. For this purpose, boundary conditions of the second and third kind are formulated. Based on various verifications performed, the underlying sub-approaches of the heat transfer model are validated against resolved FVM simulations performed with the commercial CFD-package ANSYS Fluent. This firstly includes cases with constant heat flux and heat transfer coefficient prescribed for a single particle which allows a basic systematic verification of the implemented model. Secondly particle-particle radiation and particle-particle heat conduction are investigated. These cases are of greater complexity as the resolution of the used heat transfer model and the local heat transfer itself become important. In addition to the thorough model validation on the small scale, heat transfer within packed beds is addressed as large scale cases. To compare the implemented resolved inner particle heat transfer model with literature data, the effective thermal conductivity (ETC) is calculated for packings of thermally thin particles with various particle thermal conductivities. To underline the importance of a resolved 3D heat transfer model in the context of the DEM, material parameters are considered which are attributed to thermally thick particles, thereafter. Here the resolved heat transfer model is compared against the more commonly used unresolved model approach with one constant temperature value associated to a particle. Noticeable differences occur when evaluating heat fluxes within the packing, the time to reach the steady state and

for ETC-values obtained. The performed investigations lay the foundation to include the derived resolved DEM inner particle heat transfer model as part of a coupled DEM-CFD framework.

Keywords: 3D heat transfer; DEM; Convection; Contact heat conduction; Radiation; Resolved intra-particle heat conduction

1. Introduction

In the field of energy technology and thermal process engineering, particulate heat transfer in the presence of a surrounding fluid is an important phenomenon relevant to numerous industrial applications. Among these, drying is a prominent example which is performed in vessels such as moving beds, rotating drums, fluidized beds or in entrained flow. Depending on the process variant applied, differently dense particle systems form out, which are passed through by a fluid. The heat transfer is thereby attributed to the mechanisms conduction, convection and radiation. With varying magnitude all three mechanisms influence the local mass transfer and thereby govern the progression of the drying [247–249]. Besides drying, a detailed understanding of the dominant particulate heat transfer mechanisms is relevant in packed bed heat exchangers, catalyst packings, blast furnaces, calciners, fluidized beds and many more [95,250–256]. In this context simulation approaches such as the Discrete Element Method (DEM) or the coupled DEM-Computational Fluid Dynamics (DEM-CFD) become versatile assets if heat transfer is modelled for in detail resolving the particles as discrete entities.

Good progress has been made up to today to realize the varying heat transfer mechanisms within the DEM and DEM-CFD. Under the assumption of a flat circular contact, Batchelor and O'Brien [257] derived an approach for the particle-particle heat conduction which is often used in the context of the DEM [70,258–261]. Cheng et al. [259] modified the approach and additionally considered the conduction through the stagnant fluid allowing particles to exchange heat in point and surface contact or even when being spatially separated. In case of short contact times Sun and Chen [262] proposed a model which was refined by Zhou et al. [263] who proposed a more accurate model to determine the particle-particle heat transfer due to short collisions. Zhou et al. [4, 13] reviewed relevant heat transfer mechanisms and combined them with the convective heat transfer and a simple radiation model into a CFD-DEM framework and applied it to packed and fluidized beds. To consider the radiation between particles more detailed than in [70] view factors need to be considered. Cheng et al. [264] did so for spheres and implemented the radiation network method [265] into the DEM. Note that in DEM and DEM-CFD studies investigators usually assumed a homogeneous temperature distribution within particles also referred to as lumped capacity approach (comp. e.g. [70]). The evolution of the particle temperature T_p is then calculated by solving the energy balance

$$\frac{dT_p}{dt} = \frac{\sum Q}{m_p c_p}, \quad (1)$$

where Q is the heat flux comprising of conduction, convection and radiation, m_p the particle mass and c_p the specific heat capacity. It has to be kept in mind that such a simplification is valid for small particles with a good thermal conductivity only; accordingly such particles are usually addressed in DEM and DEM-CFD studies involving heat transfer in literature or it is at least assumed that particles behave this way (see below).

The Discrete Element Method (DEM) in combination with heat transfer in gas-solid flows was firstly applied by Li et al. [266] to model particulate heat transfer during pneumatic transport. A comparison of gas pressure drop and wall temperatures indicated a good agreement between DEM-CFD and experimental results. Later Li et al. [267] demonstrated the key role of transversal motion of rebounding particles in altering the fluid temperature and additionally showed the influence of the particle transverse motion on the fluid thermal boundary layer characteristics [268]. Besides convective heat transfer the investigations [266–268] mainly addressed particle-particle heat conduction due to short contacts. In opposite to that Vargas et al. [260] presented a methodology based on the Hertz's elastic contact theory to calculate the contact radius for the heat conduction due to long lasting contacts which are relevant in packed and slowly moving beds. With this model integrated into the DEM they were able to show that the conductivity of particulate material becomes highly anisotropic at low compressive loads [269]. Additionally interstitial gas was modelled for [270]. Also for packed beds Zhang et al. [271] investigated the effect of the external compression force, particle size, solid volume fraction and coordination number on the effective thermal conductivity (ETC) in a granular bed. They were able to firstly validate DEM with detailed FEM results and finally compare obtained data to experiments from literature. The ETC increased with the enlargement of external compression force, particle size, volume fraction and coordination number. In the context of a packed bed Tsory et al. [261] developed a contact conduction model for long lasting contacts of rough particles. With that model as part of the DEM-CFD they highlighted that the heat conduction through the packed bed pores cannot be neglected especially when the particle surface is rough.

Besides packed beds and pneumatic transport, special attention was given to fluidized beds in terms of heat transfer where usually particle-gas heat transfer dominates. For a spouted bed Swasdisevi et al. [272] identified by DEM-CFD that particle-gas heat transfer is most active in the central spout region of the bed. Other investigators focused on the heat transfer behavior of liquid-particle flows [273]. Malone and Xu found out that both overall heat transfer coefficient and normalized mean particle velocity correlate strongly with the bed voidage. In addition to fluid-particle convection Di Maio et al. [274] investigated the influence of various heat transfer

mechanisms such as particle-particle, fluid-surface and particle-surface heat transfer in a DEM-CFD study involving small fluidized particles of $715 \mu\text{m}$ diameter surrounding an immersed object. Similar sized small particles with a maximum size of 1 mm were also investigated in a fluidized bed with an immersed tube by Zhao et al. [275] to show the effect of superficial gas velocity and particle diameter on the tube heat transfer coefficient. In a further study dealing with heat transfer in fluidized beds Sae-Heng et al. compared CFD-DEM simulations with experiments [276]. They achieved acceptable results for predicted gas temperature profiles and heat transfer coefficients, but their model was unable to reproduce the particle temperatures accurately. Noticeable particle temperature differences between experiments and numerical results were also reported in the work by Nguyen et al. [277]. Here the evolution of the particle temperature was overestimated in the simulations. Patil et al. [278] evaluated bubble diameters and temperatures by a DEM-CFD approach where hot gas was inserted into a cold particle bed in order to estimate the bubble heat transfer coefficient. Obtained deviations with available correlations thereby grew with increasing particle size.

Further attention in the context of discrete modelling of particulate heat transfer gained rotating drums in literature while usually also assuming a homogenous temperature distribution within the particles. Chaudhuri et al. [279] performed DEM simulations for particles with high thermal conductivities of $192.5 - 385 \text{ W/mK}$ and small sizes of $1 - 1.5 \text{ mm}$ to simulate flow, mixing and heat transport in rotary calciners and impregnators. Kwapinska et al. [280] highlighted the advantages of the DEM in comparison to simpler continuum theory motivated penetration models. For their considered setup the DEM was able to assess influences that were not accessible by the penetration model as particle motion is not modelled for. As follow-up research they suggested that three dimensional effects regarding the temperature distribution should be considered. Shi et al. [281] used a coupled CFD-DEM model to simulate simultaneous conductive and convective heat transfer in a rotary kiln. Their chosen particulate materials all yield Biot numbers $\text{Bi} = h \cdot L / k \ll 1$ which allows the use of the constant particle temperature assumption. In the Biot number, h is the convective heat transfer coefficient, L is the characteristic particle length and k is the thermal conductivity. In more recent investigations the influence of the mixing on the heat-transfer characteristics were analyzed [282,283] in drums.

Although the assumption of a homogenous particle temperature is widespread in DEM and DEM-CFD investigations Zhou et al. [70] intensively discussed the limitations of this lumped-capacity model. The latter approach is only valid for thermally thin particles with small Biot numbers; these Biot numbers are usually a consequence of large thermal conductivities in combination with small particle diameters and low convective heat transfer. To overcome this limitation and to model technical relevant particle systems where particles are often thermally thick (drying, calciners, granular heat exchangers, blast furnaces, etc.), spatially resolved inner particle heat conduction has to be modelled for. This also requires an adaption of the heat

transfer models which in their current outline assume a constant particle temperature. Steps in this direction were made by Laguerre et al. [284] who used a dispersed particle approach with a 1D radial conduction model for the calculation of transient heat transfer by free convection to avoid the use of a resolved CFD model of both fluid pores and particle interior with high computational costs. To consider the temperature distribution on the particle scale in pneumatic conveying Brosh et al. [285] implemented a 1D radial temperature model into the DEM-CFD. A comparison of obtained results with experimental values showed a better agreement compared to the application of a uniform temperature model. Later Sadhukhan et al. [286] also applied the 1D radial temperature approach in combination with the finite volume method to predict the pyrolysis behavior of single large coal particles. In addition to that, a comparison between a detailed 2D model resolving the gas phase and the uniform temperature model was performed by Schmidt et al. [287] who investigated the heating of coal particles in a rotating kiln. They indicated an over-prediction of the heating rate in the simulations that assumed a homogeneous particle temperature. In a recent work a 1D radial temperature model was applied by Rickelt et al. [183]. They extended the coupled CFD-DEM approach through a 1D radial temperature model to investigate heat transfer on a generic grate system. In the context of drying a 1D radial temperature model was successfully applied by Mahmoudi et al. [288] for a packed bed.

Up to now 3D resolved inner particle heat transfer modelling is often limited to the single particle scale [289–293]. In the context of the DEM Hahn et al. [294] presented a 2D DEM model to describe the thermal field within a solid body in a resolved way. To determine the temperature distribution in shells, a rectangular DEM-mesh provided acceptable results for 1D heat fluxes, whereas a hexagonal DEM-mesh was required for 2D heat fluxes. Terreros et al. [295] firstly integrated 3D resolved heat transfer in a Cartesian formulation into the DEM and validated results against FEM-investigations. Just recently Sudbrock et al. [249] proposed a 3D heat transfer model as part of the DEM-CFD for convective drying where fluid flow around individual particles is not resolved for convective drying of silica gel and beech wood spheres in mechanically agitated beds. Additionally, a constant temperature model was considered and the results were compared to experimental findings. For the drying rate only the multidimensional temperature model was able to match the experiments well in all cases.

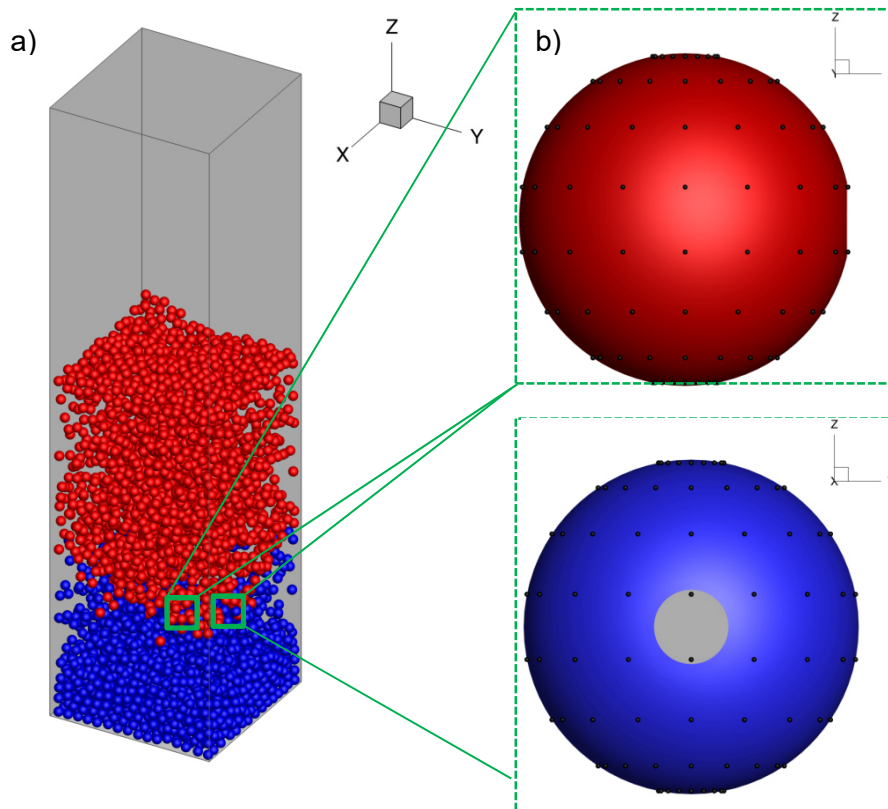


Fig. 1: (a): Application for resolved heat transfer modelling; (b): Hot (red) and cold (blue) particle with resolved 3D heat transfer nodes in spherical notation. The grey marked area is the contact zone forming out as a consequence of a particle-particle contact in the bed.

In conclusion it can be summarized that resolved 3D heat transfer models are considered only in singular cases for the DEM or DEM-CFD. To close this gap a new implicit 3D heat transfer model in spherical and Cartesian coordinates is derived and validated in representative cases against simulations performed with the resolved Finite Volume Method (FVM) as part of the commercial CFD-code ANSYS Fluent. The derived framework can be of use in many applications such as for the investigation of heat transfer in a fluidized bed, see Fig. 1. Here (Fig. 1a) a model type fluidized bed is shown with hot (red) and cold (blue) particles passed through by a fluid from the bottom. Besides the heat convection which is considered individually for each particle, particle-particle heat conduction mechanisms as well as radiation have to be modelled for in the contact area (shown in grey) as well as for the whole surface areas of the two colliding hot and cold particles (Fig. 1b). In the shown example the particle surface is resolved with 128 temperature nodes. Note that the setup shown in Fig. 1 only represents a possible application; focus of the study here is to derive and validate the required sub-models of a heat transfer framework – a final framework (including fluid flow as well as the handling of possible non-spherical particles) yet has to be obtained; nonetheless the required governing equations should be already outlined in the next section.

2. Methodology

The heat transfer model resolving temperature within individual particles in 3D is derived as part of an in-house DEM-framework. In the Discrete Element Method the translational and rotational motion are obtained by integrating Newton's and Euler's equations for each particle given in general form for arbitrarily shaped particles by

$$m_i \frac{d^2 \vec{x}_i}{dt^2} = \vec{F}_i^c + \vec{F}_i^{pf} + \vec{F}_i^g, \quad (2)$$

$$\hat{I}_i \frac{d\vec{W}_i}{dt} + \vec{W}_i \times (\hat{I}_i \vec{W}_i) = \Lambda_i^{-1} \vec{M}_i, \quad (3)$$

with particle mass m_i , particle acceleration $d^2 \vec{x}_i / dt^2$, contact force \vec{F}_i , possible particle/fluid force \vec{F}_i^{pf} , gravitational force \vec{F}_i^g , angular acceleration $d\vec{W}_i / dt$, angular velocity \vec{W}_i , external moment \vec{M}_i resulting out of contact or particle/fluid forces, the inertia tensor \hat{I}_i along the principal axis and the rotation matrix converting a vector from the inertial into the body fixed frame Λ_i^{-1} [12]. In the DEM contact force laws comprising of a normal and tangential component are utilized. The normal component of the contact force is obtained from the Hertz theory [18,22,151]

$$\vec{F}_i^n = \frac{4}{3} E^* \sqrt{R^*} \delta_n^{3/2} \vec{n} + \gamma^n (8m_{ij} E^* \sqrt{R^*} \delta_n)^{1/2} \vec{v}_{rel}^n, \quad (4)$$

where $E^* = 1/((1 - \nu_1^2)/E_1 + (1 - \nu_2^2)/E_2)$ is the effective Young's modulus, $R^* = R_1 R_2 / (R_1 + R_2)$ the effective radius, $m_{ij} = m_1 m_2 / (m_1 + m_2)$ the effective particle mass, $k^n = 4/3 E^* \sqrt{R^*}$ the resulting spring stiffness, δ_n the virtual overlap, \vec{n} a normal vector, γ^n a damping coefficient and \vec{v}_{rel}^n the normal velocity in the contact point. Even for curved particles deviating from a sphere (eq. (4)) can still be applied reasonably [57].

For the calculation of the tangential forces a linear spring limited by the Coulomb condition is used

$$\vec{F}_i^t = -\min(k^t |\vec{\xi}|, \mu_c |\vec{F}_i^n|) \cdot \vec{t}, \quad (5)$$

where $k^t = \chi m_{ij} \pi^2 / (t^n)^2$ is the stiffness of a linear spring dependent on the ratio of tangential and normal stiffness χ and t^n the particle collision time [25], μ_c the friction coefficient, $\vec{\xi}$ the relative tangential displacement and \vec{t} the tangential unit vector. The polyhedron approach can be used to represent non-spherical particles if required. Details on the contact detection and displacement calculation are described in [55,172,175,297,298]. Note, that although heat transfer and temperature distribution for non-spherical single particles are evaluated, packings in the last section only consist of spheres. For them eq. 3 characterizing the rotational motion simplifies to $I_i (d\vec{W}_i / dt) = \vec{M}_i$. Additionally, particle-fluid interaction is not considered in this

study rendering $\vec{F}_i^{pf}=0$ in eq. 2. Without fluid flow also convective heat transfer is yet not modelled for on the particle system level. Both would be required for a setup as outlined in Fig. 1 and is the focus of currently ongoing research. For further information regarding a possible calculation of the particle/fluid interaction for non-spherical particles, see [185,299].

For the latter non-spherical particles the temperature field within a particle is solved through the 3D heat conduction equation with constant properties and no internal heat generation [76] given as

$$\frac{1}{\alpha} \frac{\partial T}{\partial t} = \frac{\partial^2 T}{\partial x^2} + \frac{\partial^2 T}{\partial y^2} + \frac{\partial^2 T}{\partial z^2}, \quad (6)$$

where $\alpha = k/(\rho c_p)$ is the thermal diffusivity (quotient of the particle thermal conductivity k , density ρ and particle specific heat capacity c_p), T is the particle temperature, t is the solution time and x, y, z are the coordinates in Cartesian form. For the special case of representing a spherical particle a Cartesian formulation leads to a staircase shaped representation of the particle surface; a correction of the surface area might be required. Hence, in case of spherical particles the heat equation is conveniently rewritten in spherical coordinates [68] circumventing this problem

$$\frac{1}{\alpha} \frac{\partial T}{\partial t} = \frac{\partial^2 T}{\partial r^2} + \frac{1}{r} \frac{\partial T}{\partial r} + \frac{1}{r^2 \sin \theta} \frac{\partial}{\partial \theta} \left(\sin \theta \frac{\partial T}{\partial \theta} \right) + \frac{1}{r^2 \sin^2 \theta} \frac{\partial^2 T}{\partial \phi^2}, \quad (7)$$

with the spherical coordinates r, θ and ϕ in radial, polar and azimuthal direction. Both equations (eq. (6) and eq. (7)) are solved through an implicit finite difference scheme to calculate the temperatures at the next time step.

To consider the different heat transfer mechanisms acting on a particle, boundary conditions of the second and third kind are used. For the consideration of convection the boundary condition of third kind is realized as

$$k \frac{\partial T}{\partial i} + h T_B = h T_{\infty, B} = \text{Known} \quad i = x, y, z, r, \quad (8)$$

where i is the specific Cartesian or spherical coordinate, T_B the boundary node temperature, $T_{\infty, B}$ the ambient temperature of the fluid and h is the local heat transfer coefficient between particle and fluid, respectively. The integral heat transfer coefficient can be provided through widely available Nusselt-correlations (comp. [249]). Distribution functions (local Nusselt or Sherwood numbers) [300,301] can be used to account for non-uniform convective heat transfer h at the particle surface. Note that up to now only for simple geometric particles distribution functions are available. Note again that fluid flow is not yet considered here on the multi-particle

level therefore convective heat transfer is prescribed directly by applying a heat transfer coefficient h if required.

When the heat flux per unit area q_B acting on the particle is known e.g. for heat transfer through radiation or through contact conduction a prescribed flux boundary condition (second kind) can be used

$$k \frac{\partial T}{\partial i} = q_B = \text{Known} \quad i = x, y, z, r. \quad (9)$$

For the investigation of particle-particle radiation the heat flux per surface area $q_{i,j}$ between particles i and j is calculated through the view factor $F_{i,j}$:

$$q = \sigma F_{ij} (T_i^4 - T_j^4), \quad (10)$$

$$A_i F_{ij} = \int_{A_i} \int_{A_j} \frac{\cos \phi_i \cos \phi_j dA_i dA_j}{\pi L^2}, \quad (11)$$

with σ the Stefan-Boltzmann constant, T_i and T_j the respective mean particle surface temperatures averaged over the part of the surface of each particle which is in visual contact with the other and $A_i = 4\pi R_i^2$ the total particle surface area. The diffuse radiation view factor between two spheres is calculated through the approach by Jones [302] which allows a simplified view factor calculation applicable to sphere couples of varying diameters. If applied to a dense packing of monodisperse spheres a view factor is only calculated for particles up to being R apart. In case of non-spherical particles instead of the approach by Jones [302] (eq. (11)) needs to be evaluated explicitly to calculate view factors. Here dA_i and dA_j represent surface elements of the two bodies, L is the distance between the two surface elements and ϕ_i and ϕ_j are the angles between the respective normal of the surface elements and line L . Note that the heat flux (eq. (10)) is differently calculated as in [258]; the calculation of view factors according to Jones [302] does not allow to directly reduce areas being in visual contact to those derived from the Voronoi-polyhedra approach [13, 15].

The latter approach [70,259] is widely used to calculate particle-particle heat conduction (comp. Fig. 2).

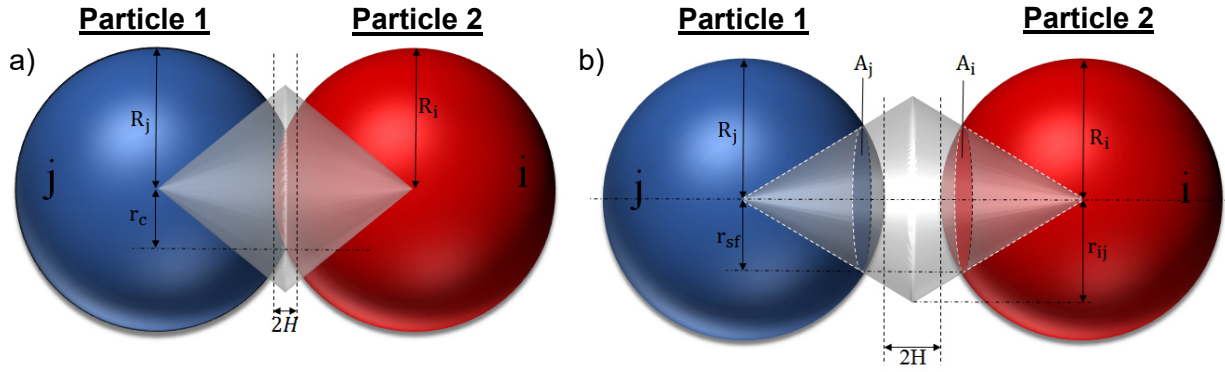


Fig. 2: Two spheres i and j in contact (a) and in near contact (b). Given parameters illustrate the used particle-particle contact heat transfer model according to [70,259]. Here R is the particle radius, $\delta=2H$ the overlap/separation distance (comp. (eq. (14)), r_c the contact radius, r_{ij} is a lens of fluid between the contacting or near contacting spheres (comp. eq. (16)) and r_{sf} is defined by (eq. (15)).

For the conduction due to static particle-particle contact of spheres the equation of Batchelor and O'Brien [257] is modified following [250] leading to

$$Q_{i,j} = \frac{4r_c c (T_j - T_i)}{\left(\frac{1}{k_{pi}} + \frac{1}{k_{pj}}\right)} \quad \text{with } c = \left(\frac{E_{Sim}}{E_{Real}}\right)^{1/5}, \quad (12)$$

where $Q_{i,j}$ is the heat exchange rate from particle i to j , r_c the contact radius and k_{pi} , k_{pj} are the thermal conductivities of both particles. For a constant particle temperature model (comp. (eq. (1))) T_i and T_j are the respective undisturbed constant particle temperatures. To save computational effort the simulation Young's modulus E_{Sim} is normally a few times lower than the real Young's modulus E_{Real} . To compensate an overestimated contact radius the calculated heat flux is corrected with the real Young's modulus through a correction factor c [250]. To model for particle-fluid-particle heat conduction the approach of Cheng et al. [259] is taken into account

$$Q_{i,j} = (T_j - T_i) \cdot \int_{r_{sij}}^{r_{sf}} \frac{2\pi \cdot r dr}{\left[\sqrt{R^2 - r^2} - r(R + H)/r_{ij}\right] \cdot (1/k_{pi} + 1/k_{pj}) + 2[(R + H) - \sqrt{R^2 - r^2}]/k_f} \quad (13)$$

$$\text{with } H = \frac{s - 2R}{2} \quad (14)$$

$$r_{sf} = \frac{R \cdot r_{ij}}{\sqrt{r_{ij}^2 + (R + H)^2}} \quad (15)$$

$$r_{ij} = 0.560R(1 - \varepsilon_i)^{-\frac{1}{3}}, \quad (16)$$

where R is the particle radius, s is the distance between both particles and ε_i is the porosity. In (eq. (13)) r_{sij} is 0 when particles are not in contact and r_c when particles are in contact.

According to Zhou et al. [70] the heat flux is ignored for ratios of $H/R > 0.5$. Note that (eqs. (12-16)) for contact heat conduction are strictly applicable for spheres only (with (eq. (16)) the approach is further restricted to monodisperse packings of spheres); for arbitrarily shaped particles even of simple geometry currently no heat conduction models are available as the shape/size of the contact zone cannot yet be predicted.

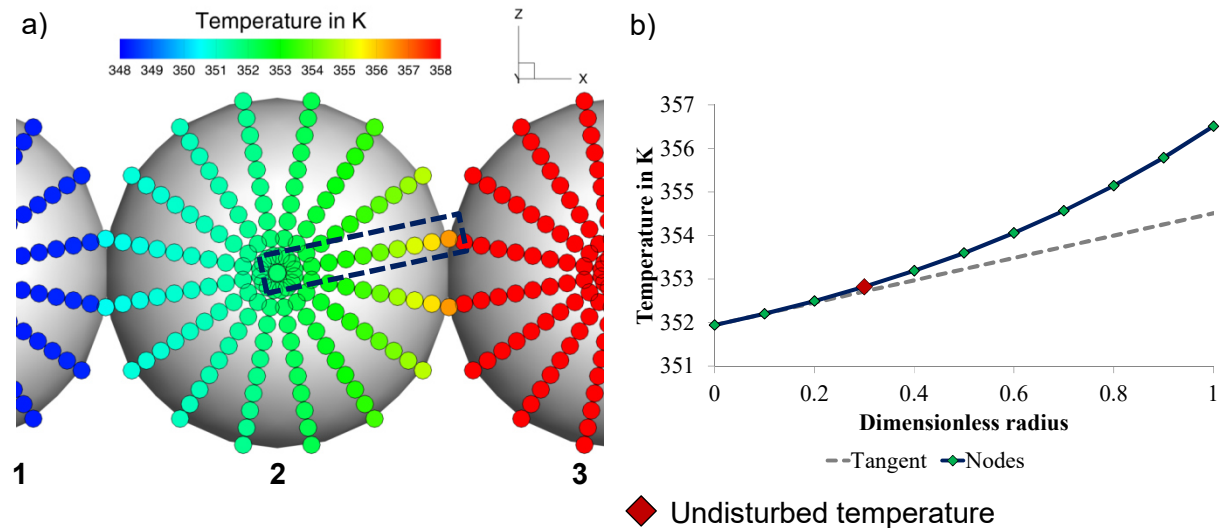


Fig. 3: Undisturbed temperature determination [303]: (a) Temperature distribution in a cut plane ($y=0$ m) for three particles in contact with different mean temperatures - node values are shown as scatter plot; (b) node temperature values from nodes between particle center and contact area, exemplary shown for one row (see marked area in Fig. 3a). The most outer undisturbed temperature is marked as red scatter point.

In the context of a resolved inner particle heat transfer model as proposed here one can argue if it is required to calculate heat transfer due to contact according to (eqs. (12-16)). As can be seen in Fig. 3 the contact area in the DEM is small compared to the particle size and the used resolution. Therefore, a resolved representation of the temperature distribution in the contact area becomes infeasible. Using (eqs. (12-16)) requires the determination of the undisturbed temperature close to the contact for each particle [303], see Fig. 3b, as they enter e.g. (eq. (12)) and (eq. (13)).

Exemplarily the procedure is shown for spherical particles being in contact, where the temperature field is represented in spherical coordinates. As can be seen each row of nodes with the same polar and azimuthal coordinate that is part of the contact area is processed. For every row a tangent is calculated between the core node and the node on the first shell. Then the temperature values for all remaining nodes on the row are checked against the tangent, beginning with the second shell. The last node temperature value which corresponds with the tangent is treated as the undisturbed temperature value of this row. Finally all undisturbed temperature values of all rows are averaged to one value as required by e.g. (eq. (12)) and (eq. (13)).

3. Numerical procedure and simulation parameters

In the following various verifications are performed to underline the validity of the derived 3D heat transfer model integrated into the DEM. Firstly 2nd (prescribed heat flux) and 3rd kind (prescribed heat transfer coefficient) boundary conditions are investigated, followed by a simple case involving radiation heat transfer. After that particle-particle heat conduction is considered. Obtained results are validated against the commercial CFD-package ANSYS Fluent relying on the Finite Volume Method (FVM). The use of a commercial CFD-package in combination with a fine mesh allows to critically assess requirements for the grid resolution when addressing 2nd and 3rd kind boundary conditions in the DEM. Additionally note that in the latter two heat transfer examples (heat transfer through radiation and particle contact) the view factors are calculated explicitly solving (eq. (11)) and the contact zone for conduction is also resolved in detail thereby having no need to rely on the set of equations (eqs. (12-16)). Both the radiation heat exchange model as used for the constant particle temperature model in [264] and the model for heat conduction [70,258,259] are validated against a detailed resolved simulation approach for the first time. Additionally, the temperature resolution in the particles is thereby considered in full 3D within the DEM. Finally heat transfer simulations in a packed bed with thermally thin and thick particles are performed which clearly underline the necessity to model particles that are thermally thick resolved in 3D.

In the simulations different materials are addressed in the investigation as outlined in table 1.

Table 1: Materials and their respective physical/thermal properties used in the simulations [250,265]

Material	Density ρ [kg/m ³]	Specific heat capacity c_p [J/(kgK)]	Thermal conductivity k [W/(mK)]	Thermal diffusivity α [m ² /s]
Glass	2225	835	1.4	7.54E-07
Steel	7900	477	14.9	3.95E-06
Aluminum	2702	903	237	9.71E-05
Model materials	1000	573	1 - 75	1.75E-06 - 1.31E-04

All materials have varying thermal characteristics as they differ strongly in density, specific heat capacity and thermal conductivity. In this context thermally thin and thick particles are characterized through the thermal diffusivity $\alpha = k/(\rho c_p)$ as in most simulations the heat transfer coefficient is zero (convection is neglected) not allowing to use the Biot number $Bi=h \cdot L_d/k$ for characterization. Glass the material with the lowest thermal diffusivity is defined as thermally thick whereas all remaining materials are defined as thermally thin. For the heat transfers simulation within a packed bed, model materials with a wide range of thermal conductivities are considered (comp. table 1). As the used implicit numerical scheme is unconditionally stable

there are no specific restrictions regarding the size of the time step in the context of stability. After a thorough evaluation of the simulation accuracy the thermal time step is set to $\Delta t = 0.1$ s for the cases involving boundary conditions of 2nd and 3rd kind, heat exchange by radiation and heat conduction in contact. A time step of $\Delta t = 0.1$ s is several orders larger than a typical DEM time step¹. Further details on the simulation conditions and parameters are given in the results and discussion section in the following.

For the simulation of the particle packings the parameters as outlined in table 2 are used. Case A involves simulations with thermally thin particles utilizing varying model materials; Case B involves thermally thick particles with the thermal properties of glass. To generate the packing 2500 spherical particles with a diameter of $d_p=2$ mm are randomly distributed which then settle due to gravity. The resulting packing is of size $13d_p \times 13d_p \times 13d_p$ and has a porosity of $\epsilon=0.4$. To introduce a heat flux through the packing the particles which intersect the bottom plane are set to a constant temperature of 398.15 K. The same number of particles on the top of the bed is set to a constant temperature with 100 K difference (298.15 K). The initial temperature of all remaining particles is the arithmetic mean of both temperatures. In case of a resolved heat transfer model all nodes of a particle obtain the same initial temperature value.

Table 2: DEM parameters of the particle packing simulations in alignment with [250]. Case A: Thermally thin particles, Case B: Thermally thick particles.

Parameter	Abbreviation	Value
Number of particles	n	2500
Material	–	Case A: Model materials Case B: Glass
Particle diameter	d_p	Case A: 0.002 m Case B: 0.02 m
Friction coefficient	μ	0.4
Damping coefficient	γ	0.3
Young's modulus	E_{Sim}	10 MPa
Correction coefficient	c	0.182
Poisson ratio	ν	0.3
Tangential to normal stiffness ratio	χ	0.88
Temperature of bottom plane	T_B	398.15 K
Temperature of top plane	T_T	298.15 K
Fluid thermal conductivity	k_f	0.02818 W/(mK)
Mechanical time step	Δt_m	1.43×10^{-5} s

¹ Typical DEM time steps are in the range of $\Delta t_m = 10^{-5} - 10^{-6}$ s [228,299,331]

4. Results and discussion

4.1 Convective boundary condition (boundary condition of 3rd kind)

In the first verification a constant convective heat transfer coefficient of $h = 10^4 \text{ W}/(\text{m}^2\text{K})$ is imposed on a cubical particle (comp. Fig. 4a (top)).

The initial particle temperature is set to 300 K, the fluid temperature to 600 K and the edge length of the cube is 0.1 m. The mesh resolution equals for both methods (FVM: Ansys Fluent, FD: DEM) with 68921 Cartesian cells/nodes. Although the number of cells (FVM) and nodes (DEM) is chosen identical the node positions between the FVM and the DEM differ minimally. The DEM boundary nodes (finite difference method) coincide with the particle surface, the FVM nodes which are the cell midpoints (finite volume method) are placed in contrary half-cell spacing away from the surface. In Fig. 4a the volume averaged temperature over all nodes is plotted over time for the materials aluminum, steel and glass and exemplarily both mesh topologies are shown.

The results indicate that aluminum the material with the highest thermal conductivity holds the most intensive increase in temperature. Glass with the lowest thermal conductivity heats up slower than aluminum and steel. The fine mesh cases match the FVM results well, only small deviations occur at the beginning of the simulation for the material glass. A finer FVM mesh reduces the deviation between DEM and FVM which is not shown in this figure.

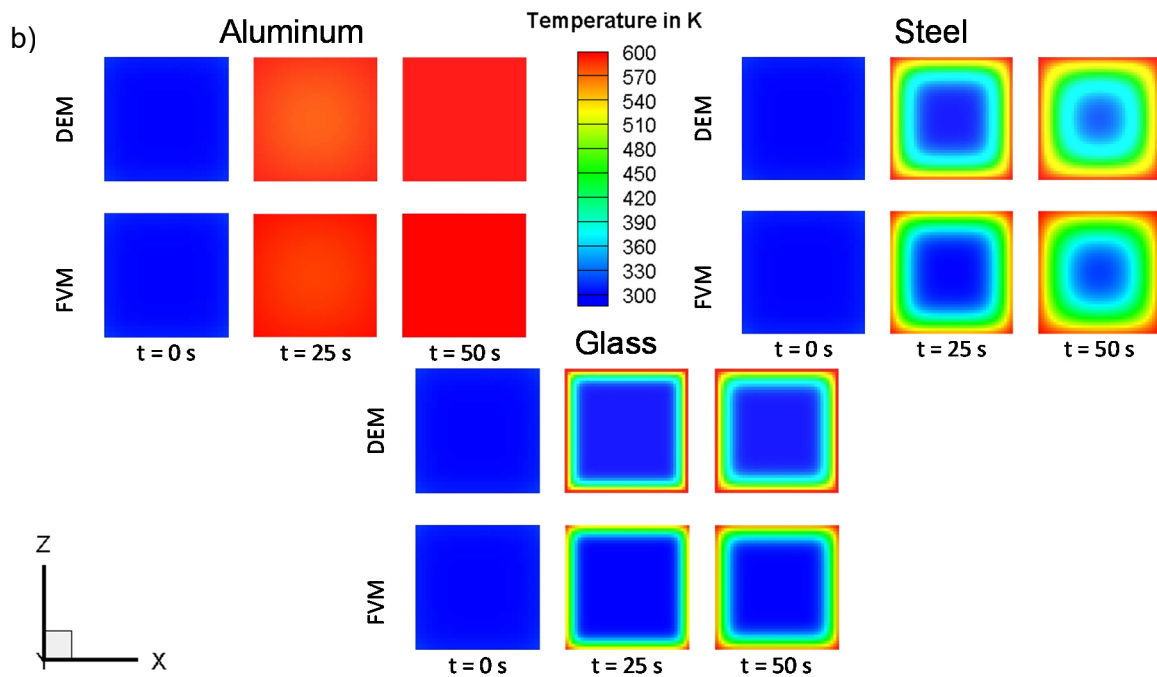
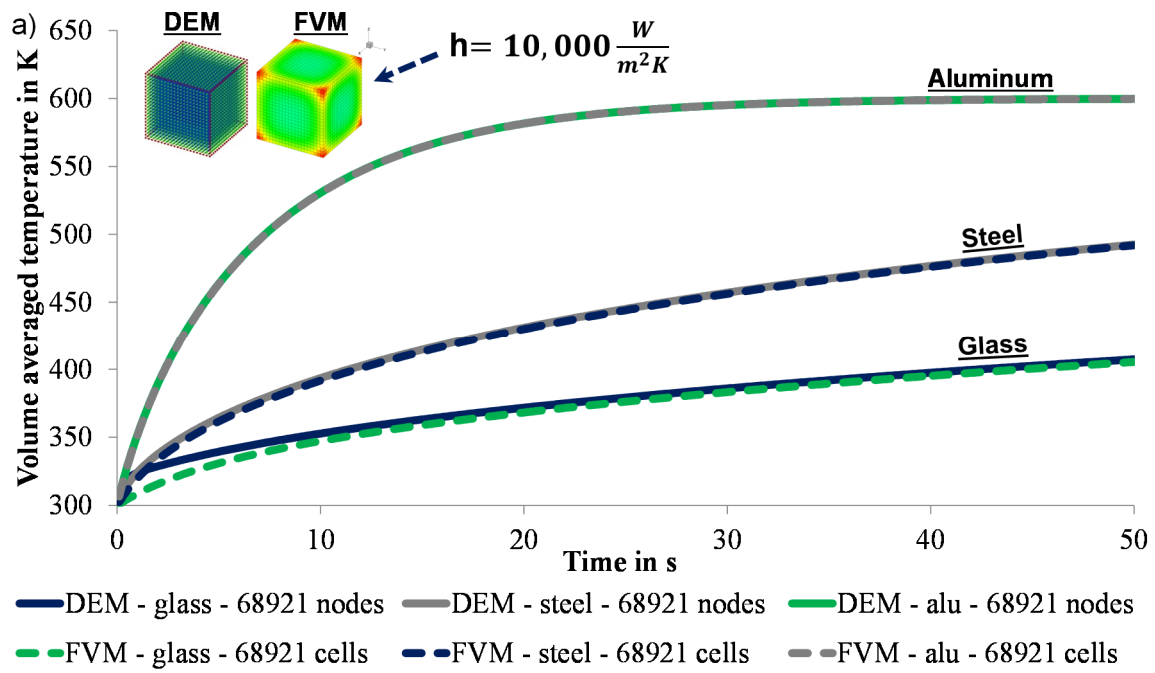


Fig. 4: (a): Temperature distribution over time for a cube with a constant heat transfer coefficient of $h = 10,000 \text{ W/(m}^2\text{K)}$ applied, an ambient temperature $T_a = 600 \text{ K}$ and initial particle temperature $T_i = 300 \text{ K}$. Considered materials are glass, steel and aluminum. Grid resolution is identical for the DEM (left) and the FVM (right). (b): Evolution of the inner particle temperature in the DEM and the FVM (grid resolution: 68921 cells/nodes) for cubes of different materials with constant convective boundary conditions.

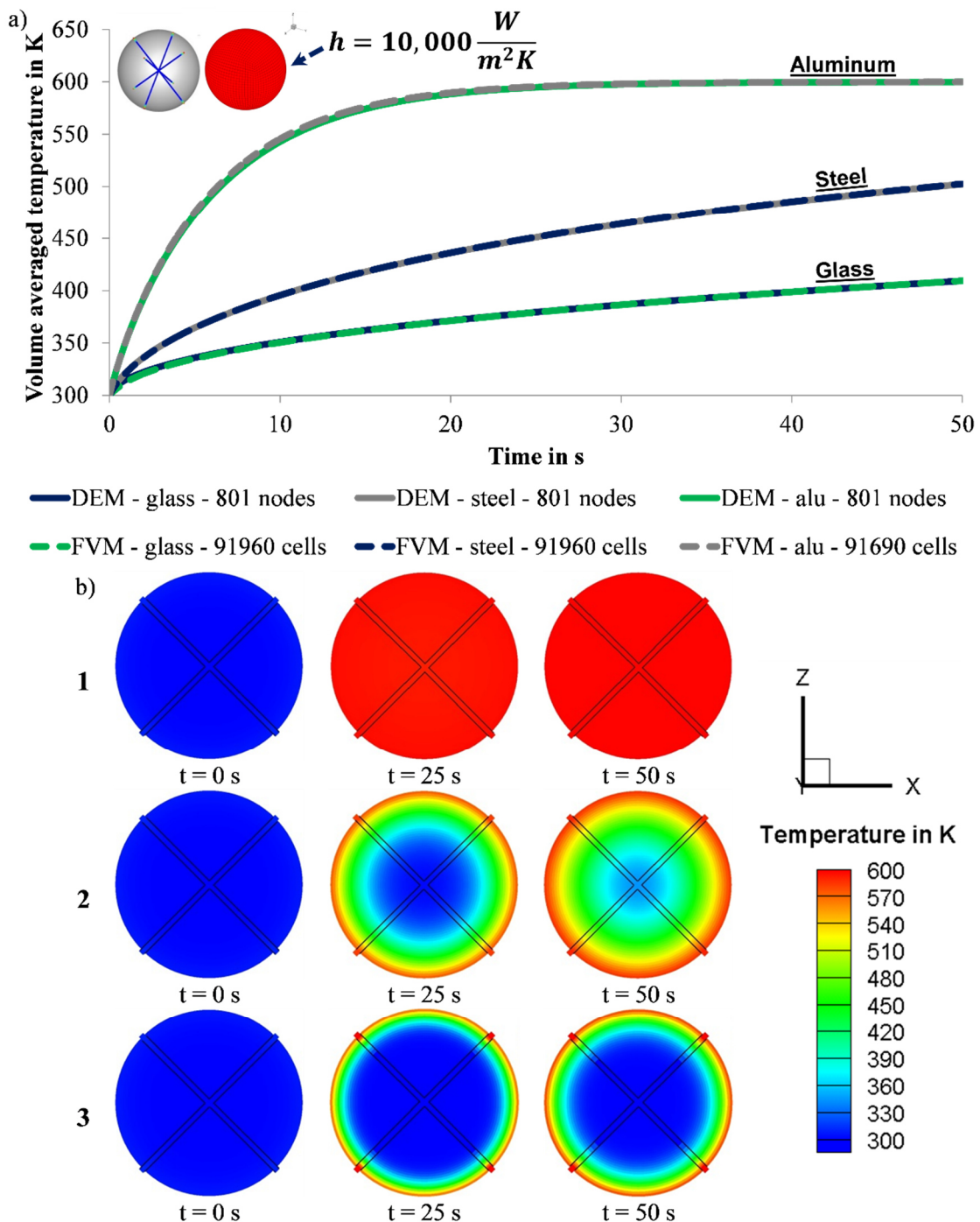


Fig. 5: (a): Temperature distribution over time for a sphere with a constant heat transfer coefficient of $h = 10,000 \text{ W}/(\text{m}^2\text{K})$ and an ambient temperature of $T_a = 600 \text{ K}$ and initial particle temperature $T_i = 300 \text{ K}$. Considered materials are glass, steel and aluminum. In total 801 nodes are used within the DEM and 91,960 cells for the FVM. (b): Comparison of the evolution of the inner particle temperatures between DEM (801 nodes) and FVM (91,960 cells) for spheres with the constant convective boundary condition applied made out of different materials such as aluminum (1), steel (2) and glass (3). Shown as cross are the node mid-points of the finite difference approach integrated in the DEM.

To compare the material dependent temperature evolution within a particle in more detail and to outline the suitability of the FD-method within the DEM in Cartesian notation (eq. (6)), the

temperature in a cut plane ($y=0$ m) is shown at $t= 0$ s, $t= 25$ s, $t= 50$ s in Fig 4b. Again differences are only noticeable between the considered materials. Glass shows in opposite to aluminum a non-uniform temperature distribution as the thermal conductivity is more than 150 times smaller.

To validate the boundary conditions of 3rd kind for the spherical notation of the heat conduction equation (eq. (7)) the same heat coefficient is imposed on a sphere with a diameter of 0.1 m. The mesh topology is differing between FVM and DEM as the node position for the DEM is in spherical coordinates and for the FVM an O-Grid is used. Therefore, the cell resolutions differ strongly (DEM: 801 nodes, FVM: 91200 cells). The remaining simulation parameters are identical with the previous simulation case. Results are shown in Fig. 5a. The same observations can be drawn as for the cubical particle except the differences at the beginning for the material glass. The temperature distribution within the particle in a cut plane ($y = 0$ m) is shown in Fig 5b. To compare the temperature values of both methods the DEM nodes are depicted as squares which are plotted atop the FVM results shown as contour plot. The temperature distribution within the particle is more uniform for aluminum as for glass and steel. No observable differences occur between DEM and FVM.

4.2 Prescribed heat flux boundary condition (boundary condition of 2nd kind)

In addition to the investigation of a constant heat transfer coefficient, the boundary condition of 2nd kind resulting in a constant heat flux is analyzed for a cubical and a spherical particle. For both particle shapes a constant heat flux of $q = 10^4$ W/m² is imposed on the particle with edge length/diameter of 0.1 m at an initial temperature of 300 K.

The temperature field for the cuboidal particles is represented by 9261 cells in the FVM and by the equivalent number of nodes in the DEM. Obtained results on the volume averaged temperature are shown for the three materials glass, steel and aluminum in Fig 6a. Exemplarily the DEM and FVM meshes are shown in this figure on the top. The results indicate that for all materials the average temperature increases linearly with no deviation between the DEM and the FVM. Glass, the material with the lowest mass and relatively high specific heat capacity, holds the largest final temperature ($T \approx 460$ K after 50 s); steel with the largest mass and lowest heat capacity the lowest final temperature ($T \approx 380$ K after 50 s).

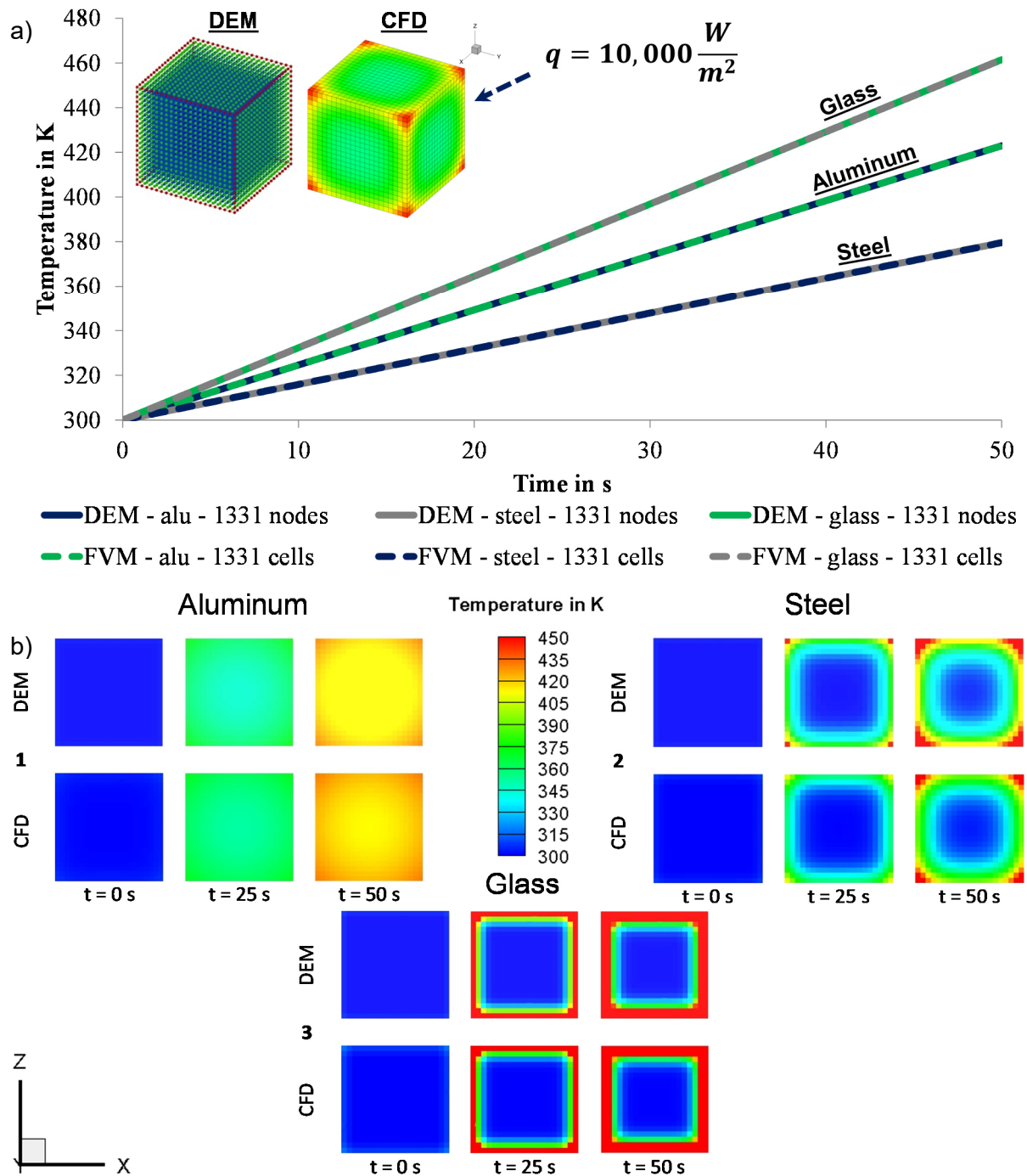


Fig. 6: (a): Volume averaged temperature distribution over time for a constant heat flux of $q = 10,000 \text{ W/m}^2$. The mesh with 9261 nodes is shown exemplary for the DEM (left) and the FVM (right). (b): Comparative evolution of the inner particle temperatures in the DEM and the FVM (grid resolution: 9261 cells) for a cube with the constant heat flux boundary condition applied made out of aluminum (1), steel (2) and glass (3).

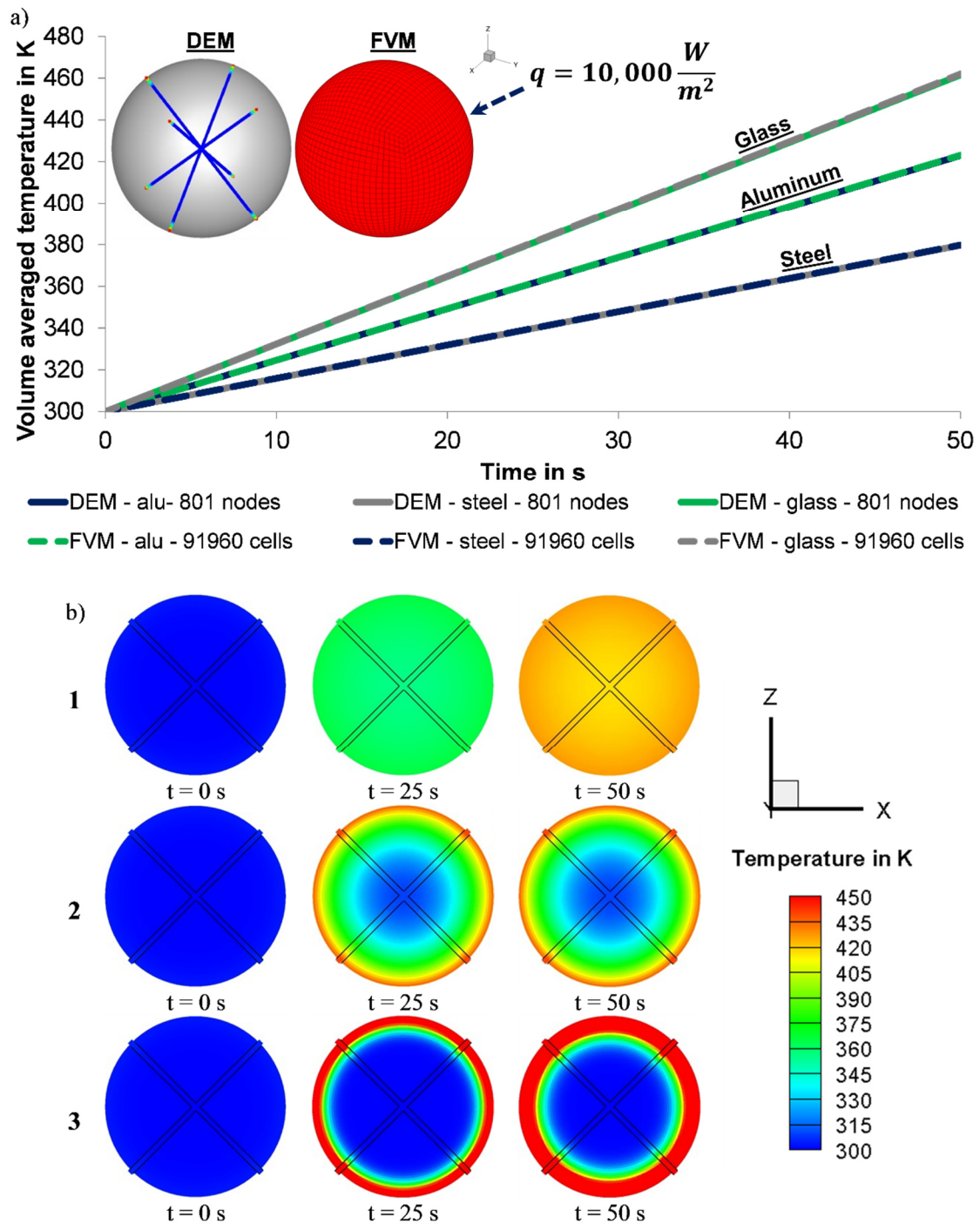


Fig. 7: (a): Temperature distribution over time for a constant heat flux of $q = 10,000 \text{ W/m}^2$ imposed on a sphere. Considered materials comprise of glass, steel and aluminum. Grid resolution is 801 nodes for the DEM and 91960 cells for the FVM solver. Meshes with 801 nodes (DEM) and 91960 cells (FVM) are shown exemplary. (b): Evolution of the inner particle temperature calculated within the DEM (801 nodes) and by the FVM (91960 cells) for a sphere with constant heat flux boundary condition and comprising of aluminum (1), steel (2) and glass (3). Shown as cross are the node midpoints of the finite difference approach integrated into the DEM.

Results outlining the temperature evolution within the particles are shown for three representative time steps in Fig. 6b. Similar to the simulations with a constant heat transfer coefficient,

aluminum obtains a more uniform temperature distribution than glass and steel. Agreement between DEM and FVM is good.

A linear increase in temperature with no deviation between DEM and FVM is also observable for the constant heat flux imposed on a sphere, see Fig 7a. Here the same mesh topologies are applied as for the investigation of the constant heat transfer coefficient. Again, glass is the material with the highest final temperature, followed by aluminum and then steel.

For the sake of completeness, the temperature evolution over time within a cross section of the spheres is presented in Fig 7b. The DEM results are in a good agreement with results obtained from the FVM for all three materials. In this and all previously outlined simulations a simpler 1D radial temperature model would provide the same results as the boundary conditions applied so far are not varying in circumferential direction. Therefore, the investigation presented up to now are a systematic validation of the boundary conditions and the inner particle conduction model. The upcoming investigations such as particle-particle radiation and heat conduction of contacting particles involve boundary conditions varying in circumferential direction and therefore reflect the advantages of the derived 3D heat transfer model in contrast to 1D or constant temperature models.

Particle-particle radiation heat transfer is considered to validate the implemented 3D heat transfer model in the setup shown below (Fig. 8).

In the setup two spheres with a diameter of 0.1 m and different initial temperatures are placed apart in a distance of $s = 0.105$ m. Both spheres are treated as black bodies and only the radiation between them is considered. The initial temperature of the colder particle is set to 300 K. The temperature of the second particle is constant with $T=1500$ K. For the FVM-solver the S2S model is used which solves (eq. (11)). In the DEM the heat flux is obtained from view factors calculated according to Jones [302] as presented previously. Each particle in the DEM is resolved by 801 nodes for the calculation of the heat transfer. In contrast, the FVM mesh consists of 32,000 cells for the particle which is heated up. The exterior around the spheres is approximated by 77,600 cells in the FVM. Fig 8a shows exemplary a cut plane of the FVM-model and the evolution of the volume averaged temperatures over time for the colder particle. The results obtained by the DEM are in good agreement with the FVM, although the view factors are calculated differently in both methods. Results on the temperature distribution over time are shown in Fig. 8b.

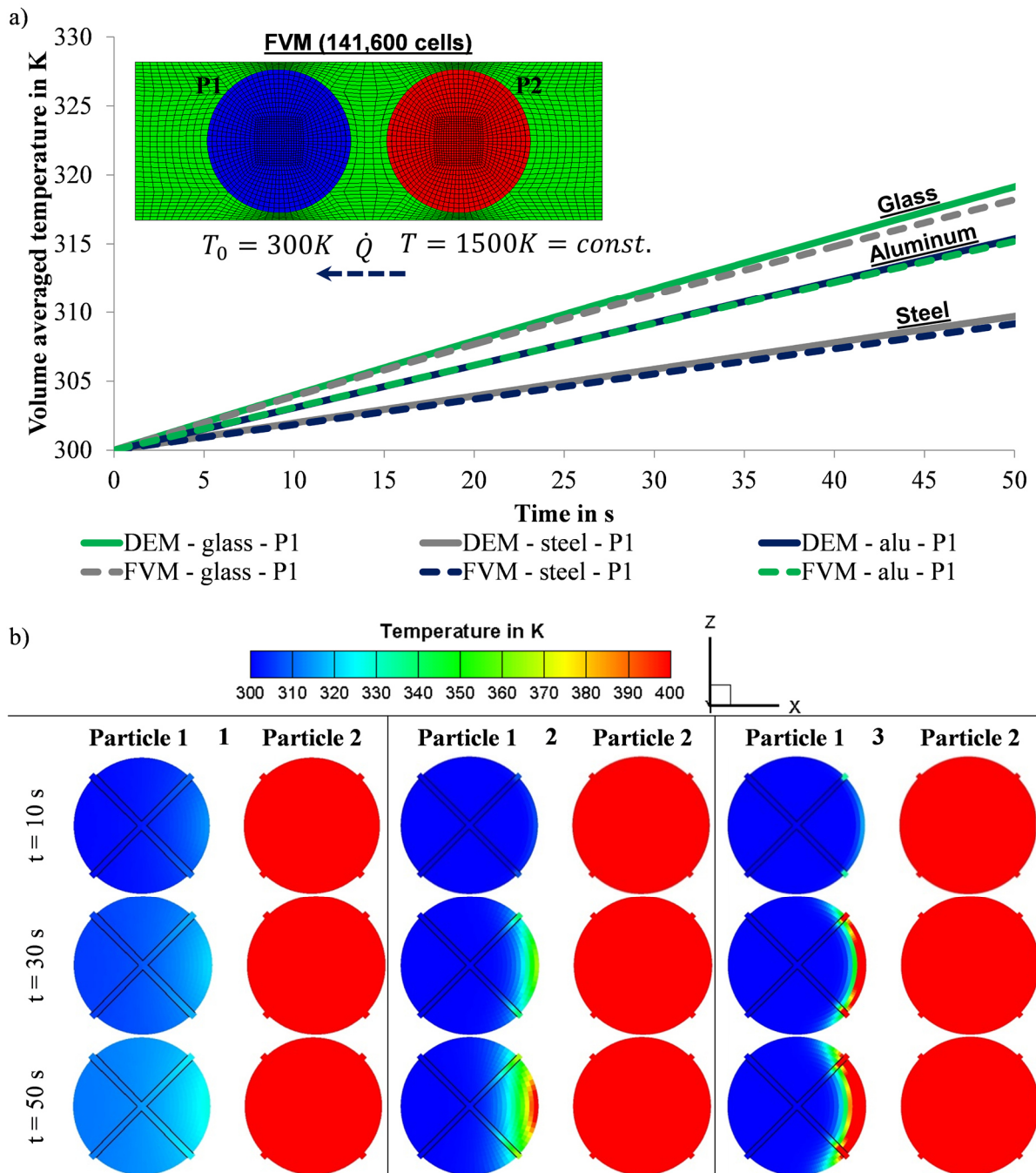


Fig. 8: (a): Temperature evolution for particle 1 (left particle) over time. Considered materials are glass, steel and aluminum. The temperature field in the particle is represented by 801 nodes in the DEM and 32000 cells in the FVM. The surrounding volume around the particles and the volume within both particles are represented by 141,600 cells as shown exemplary. (b): Evolution of the inner particle temperature distribution over time for a cut plane involving the materials aluminum (1) steel (2) and glass (3) under the previously outlined simulation conditions.

As DEM simulations with heat transfer often involve a large number of particles a coarse approximation in azimuthal and polar in combination with a detailed approximation in radial direction is used. The results indicate that even in this case the DEM provides acceptable agreement with the FVM. The considered setup is leading to an asymmetric temperature distribution due to the locally imposed heat flux. A 1D radial temperature model which is currently state of

the art in DEM simulations [183,288] in contrast to the derived 3D model would have predicted the particle surface heated up slower which would have resulted in an overestimated heat flux. Therefore, a radial or even less detailed unresolved model is not able to precisely reproduce the observed transient heat exchange.

4.3 Particle-Particle heat conduction

In addition to the investigation of particle-particle radiative heat transfer, the heat conduction through a static contact of two spheres with the same diameter ($d = 0.1$ m) is analyzed. For this investigation one particle is set to an initial temperature of 300 K and the other to 600 K. The spheres are placed in distance so that the overlap is $\delta = 2.5E - 03$ m and the contact radius is $r_c = 1.11E - 02$ m. For the FVM solver an O-Grid mesh is created with 192,000 cells. Two mesh qualities are used within the DEM. The coarser grid (162 nodes) has only 2 nodes per particle within the contact area (8 nodes on the particle surface) and the finer (20482 nodes) has 64 nodes per particle in the contact area (512 nodes on the particle surface). The solution time is 1000 s as the imposed heat flux is smaller than the heat flux in the previous simulations. The results for the volume averaged temperature over time for the three materials are shown in Fig. 9.

In contrast to the previous simulations, aluminum is the material with the largest change in temperature. In fact, only the aluminum spheres reach the same mean temperature within the simulation time. The DEM results match the FVM results well for all materials. Especially the aluminum spheres, with the largest change in temperature, are experiencing no noticeable deviations between DEM and FVM even for a resolution of just $2 \times 4 \times 10$ nodes + 1 center node, where particularly the polar and azimuthal resolution is low. However, the accuracy of the representation of the average temperature increases with the number of nodes on the particle surface inclining and an enhanced polar and azimuthal resolution. Temperatures are nearly identical for the fine DEM mesh and the FVM, even for aluminum. For longer simulation times the deviations of the coarse DEM mesh and the FVM diminish for aluminum as temperatures of both spheres equalize. The reason for the quicker temperature equalization of aluminum is a larger imposed heat flux due to larger thermal conductivities. For the same temperature difference the heat flux between aluminum spheres is 169 times larger than for glass and still 16 times larger than for steel, see (eq. (12)). Snapshots of the temperature distribution within the particle are outlined in Fig. 10.

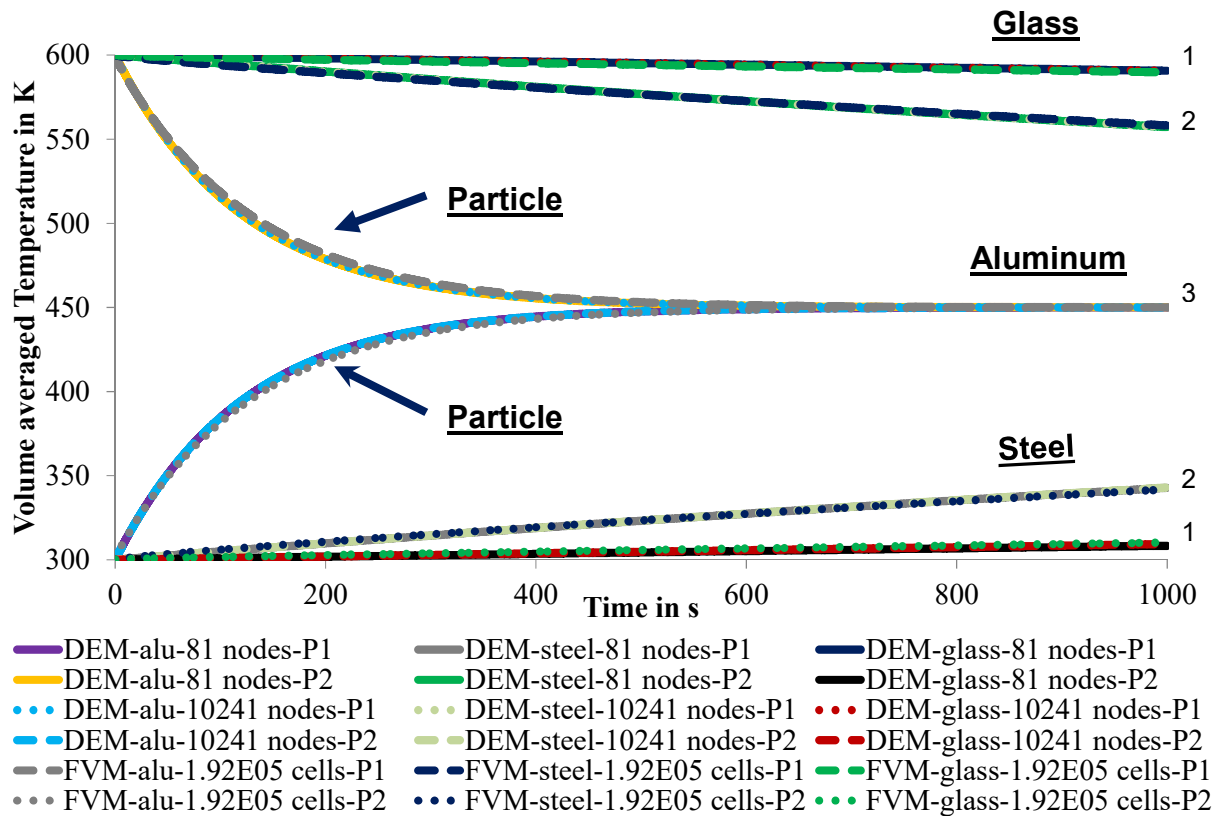


Fig. 9: Temperature evolution over time for two contacting spheres P1 and P2 with different initial temperatures ($T_{S1} = 600$ K and $T_{S2} = 300$ K). Considered materials are glass (1), steel (2) and aluminum (3). Total number of grid points for both spheres are 162 / 20482 nodes for the DEM and 192000 cells for the FVM. The contact radius is $r_c = 1.11E-02$ m and the static overlap $\delta = 2.5E-03$ m.

In Fig. 10 the DEM nodes are depicted as squares which are plotted atop the FVM results. Only temperatures for the colder particle are shown; the others are blanked to prevent the overlap of boundary nodes in the contact area of both particles. For aluminum the considered simulation time is reduced to 100 seconds as the temperature of both particles is nearly uniform after 500 seconds. In opposite to the unresolved temperature models the DEM in connection with a 3D resolved heat transfer model is able to describe the temperature distribution within the contact area as good as the FVM reference case. Only at the beginning ($t = 1$ s) the DEM slightly underpredicts the temperature in the contact area.

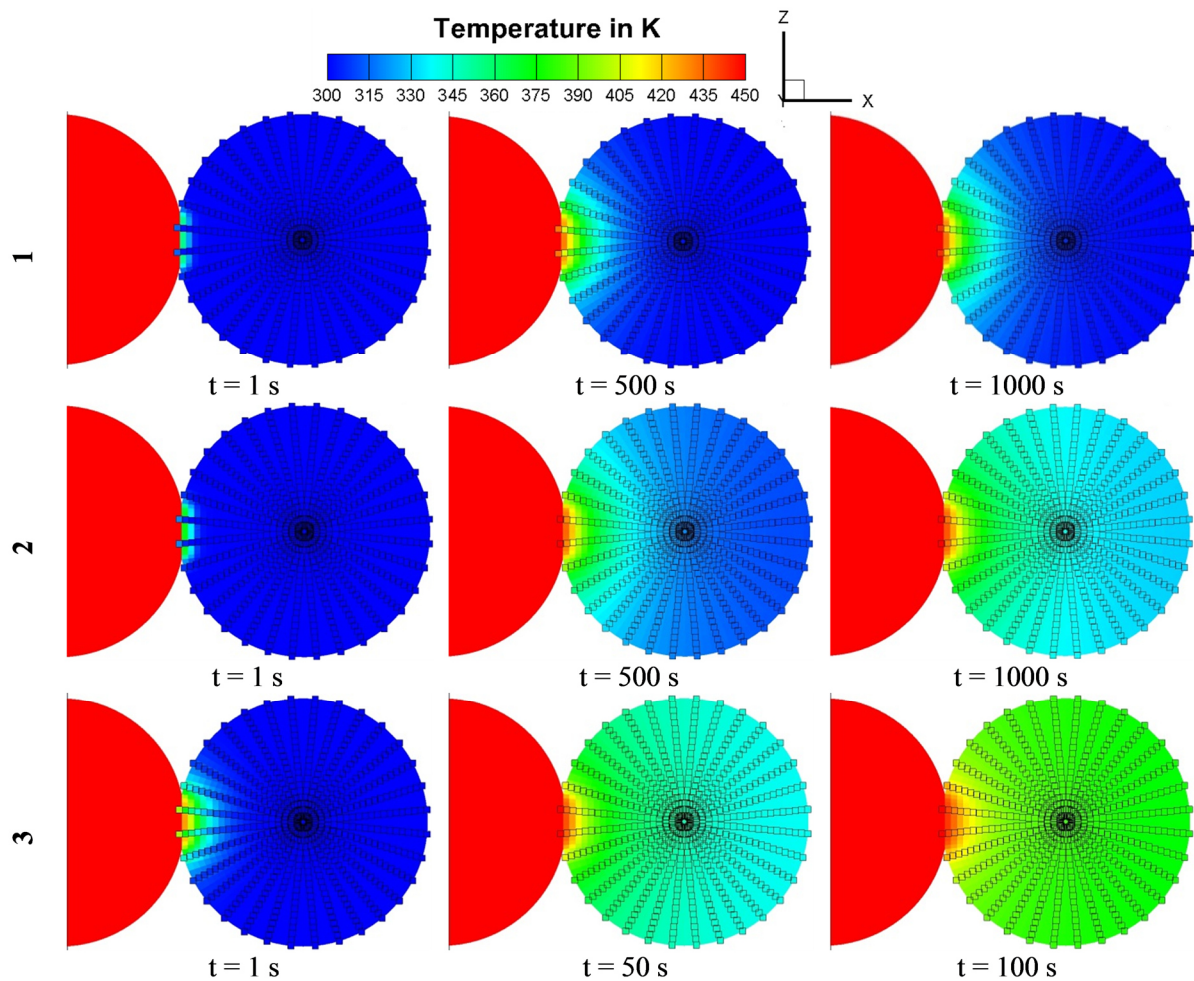


Fig. 10: Temperature evolution based on a fine DEM mesh (20482 nodes) and by the FVM (192000 cells) for two spheres in contact. Values of particle 1 are blanked to shift the focus on particle 2. DEM nodes are represented through scattered squares; FVM results are shown as contour plot. Used materials are glass (1), steel (2) and aluminum (3).

To underline the differences between a resolved and unresolved heat transfer model in case of thermally thick particles a further study is performed. Additionally, the validity of the derivation of the undisturbed temperature as required for the calculation of the particle-particle heat flow (eq. (12)) is demonstrated. Therefore, one simulation with the resolved model and undisturbed temperature referred to as “resolved - $T_c = T_{undist}$ ” and another with the resolved model where the contact temperature is calculated as the mean particle temperature referred to as “resolved - $T_c = T_{mean}$ ” is performed. In this investigation a uniform heat flux \dot{Q} is passed through the contact areas of three lined-up particles.

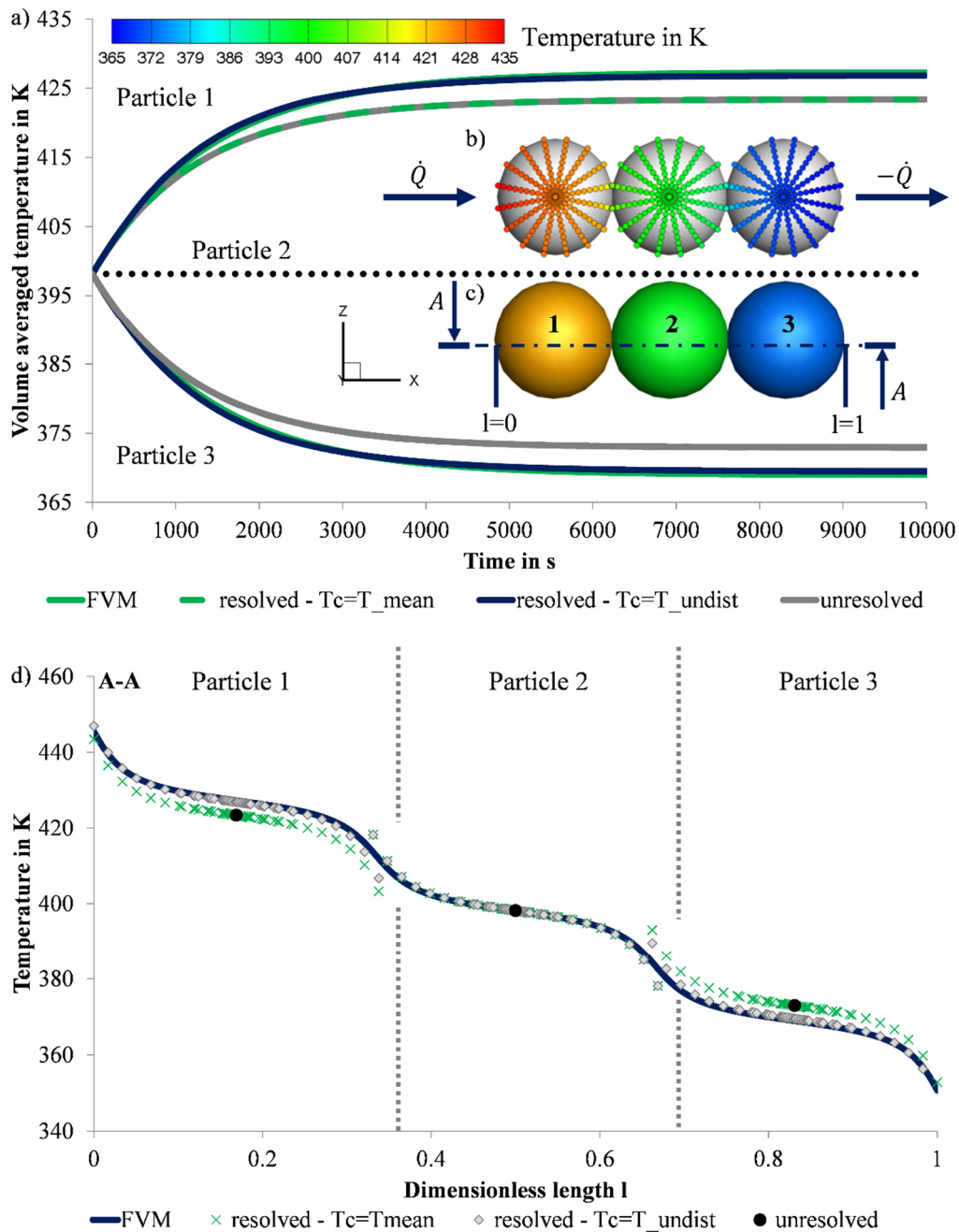


Fig. 11: (a): Evolution of particle temperature for the FVM and different DEM heat transfer models when a constant heat flux ($\dot{Q} = 0.1569 \text{ W}$) is imposed on particles 1 and 3 of a chain of 3 contacting particles ($T_i = 398.15 \text{ K}$, $\delta = 2.5 \text{ E} - 03 \text{ m}$, material: Glass). Additionally the temperature distribution in a cut plane ($y=0\text{m}$) is shown for the resolved (b) and the unresolved model (c) when the steady state is reached; (d): Temperature evolution over dimensionless length l in steady state for the DEM and the FVM.

As for the previously considered binary contact the overlap is $\delta = 2.5 \text{ E} - 03 \text{ m}$ and the contact radius $r_c = 1.11 \text{ E} - 02 \text{ m}$. 10241 nodes are used per particle to resolve the temperature field in the DEM. As a reference, a FVM case with a total of 288,000 cells is also considered. All spheres hold an initial temperature of 398.15 K. The results regarding the evolution of the volume averaged temperatures are shown in Fig. 11a.

After a certain time all simulations reach a steady state as can be seen by the constant particle temperature values being obtained. Snapshots of the temperature distribution within the particle in steady state for the resolved $T_c=T_{undist}$ and the unresolved model are shown in Fig. 11b and Fig. 11c. Particles modeled for in the unresolved model (Fig. 11c) obtain one mean temperature whereas particles represented by the resolved model reveal internally varying temperatures which are decreasing in the direction of the heat flux (Fig. 11b). Due to the constant heat flux on particle 1 and 3 and the initial temperature of particle 2, the volume averaged temperature of particle 2 remains constant over time for DEM and FVM. Differences form out for the temperature progression of particles 1 and 3 between resolved $T_c=T_{undist}$, resolved $T_c=T_{mean}$ and unresolved model as well as FVM. Both FVM and resolved $T_c=T_{undist}$ models hold a higher final temperature value (≈ 427 K after 6000 s) for particle 1 and a lower final temperature value (≈ 377 K after 6000 s) for particle 3 than the resolved $T_c=T_{mean}$ model and the unresolved model. The latter two models reach steady state earlier after approximately 4000 s. Results of the resolved model with mean temperature and the unresolved model reveal no significant differences in terms of the volume averaged temperatures. It can be clearly seen that only the resolved model which relies on the undisturbed particle temperatures matches the FVM solution well.

In addition to the volume averaged temperatures over time the node temperature in dependence on the dimensionless length l introduced in Figs. 11b, c in steady state is presented in Fig. 11d. Results for the unresolved model are plotted as scattered values at the respective l values of the sphere midpoints. The results indicate that the unresolved, resolved model relying on the mean temperatures noticeably deviate in every node of particle 1 and 3, whereas the resolved model relying on the undisturbed particle temperature only deviates minimally in the contact region compared to the FVM. The minor deviation in the contact region can be explained by two aspects. Firstly the FD mesh in the DEM is coarser than the mesh used for the FVM. Secondly the DEM boundary nodes are overlapping and penetrating into the other contact partner. This volume which is an artefact of the DEM is not considered in the FVM.

4.4 Heat transfer simulation in a packed bed

In the last part of this investigation the applicability of the derived 3D resolved heat transfer model is demonstrated for multi particle systems. As heat transfer mechanisms it is limited to particle-particle and particle-fluid-particle (contact and non-contact) heat conduction in the following. Firstly, the validity of the implemented model is tested on larger scale by comparing effective thermal conductivities of particle packings consisting of particles with different solid thermal conductivities with literature data involving thermally thin particles. Secondly, a setup where 10 thermally thick particles are positioned in a row is addressed to calculate the effective

thermal conductivity as a prequel to the last investigation where a larger packing of thermally thick particles is considered.

For the first investigation material parameters as well as the simulation setup are chosen in accordance to the investigation of Zhou et al. [250]. These parameters are outlined in section 3. A packing is formed and the particles which intersect the bottom plane are set to a constant temperature of $T_b=398.15$ K. The same number of particles on the top of the bed is set to a constant temperature of $T_t=298.15$ K. The initial temperature of all other particles is the arithmetic mean of both temperatures. For the investigation thermal conductivities are varied as outlined in table 1. A method often used to validate heat transfer in a packed bed is the determination of the effective thermal conductivity (ETC). The ETC k_e is calculated by

$$k_e = \frac{q}{(T_b - T_t)/H}, \quad (17)$$

where q and H are the heat flux and the distance between top and bottom plane that intersect the particles with constant temperature, T_b the temperature of the bottom and T_t of the top plane, respectively. To compare the simulation results with experimental and numerical results from literature the ratio of effective to fluid thermal conductivity k_e/k_f is plotted over the ratio of solid to fluid thermal conductivity k_s/k_f in Fig. 12.

9 simulations with varying solid thermal conductivities for the constant temperature approach and the 3D resolved heat transfer model were performed. Simulations A [70] and B [250] are both performed on the basis of the real Young's modulus involving glass beads. The various measurements are taken from the investigation of Cheng et al. [259] who performed a literature review. The results indicate that k_e is equal for the resolved and the unresolved model and in good agreement with data from literature. This fact underlines that the unresolved temperature approach is valid for this simulation case where particles are thermally thin. No improvement is gained through the resolved model here; nonetheless the agreement with experimental data verifies the correctness of the model approach in the context of a multi particle system.

The necessity to use a resolved heat transfer model for the meaningful simulation of thermally thick particles is shown in the last two investigations. Thermal conductivity, specific heat capacity and density are chosen according to the material glass, see table 1. The particle diameter is enlarged ten times to 20 mm. The first simulation configuration is shown in Fig. 13b.

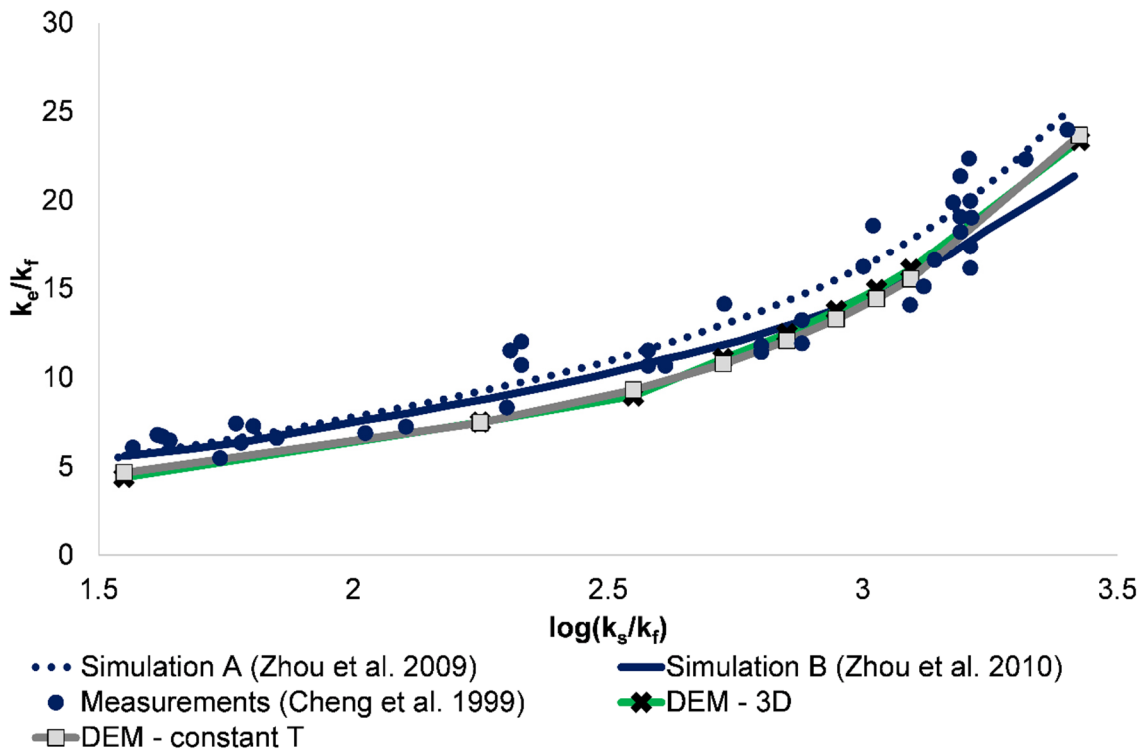


Fig. 12: Comparison between own DEM simulations involving materials with varying thermal conductivities and experimental/numerical results from literature.

10 particles in a row are placed in distance so that the overlap is 5 % of the particle radius. Particle 1 holds a constant temperature of 398.15 K. All remaining particles are set to an initial temperature of 298.15 K. The heat flow over time for three selected particles is shown in Fig. 13a.

The results indicate that the deviations between resolved and unresolved model increase with the distance to particle 1. No significant differences are observable for the progression of the heat flux of particle 2. In contrast significant differences are visible for particle 5 and 10. In case of the unresolved model the heat flux increases more rapidly during the first seconds. After a certain period of time the deviations decrease and the results start to converge. This behavior is more pronounced for particle 10 than particle 5. In general the heat flux is faster transported through the particle row in case of the unresolved model than for the resolved model. The presented heat fluxes correspond to particle temperatures not shown in Fig. 13 which would be also deviating.

Phenomena observed for a row of particles also affect heat conduction in larger particle packings and influence properties like the ETC when thermally thick particles are considered. To show the influence on the ETC various simulations with a different particle numbers are performed. The calculated ETCs of resolved and unresolved model are shown in Fig. 14a including their respective deviations.

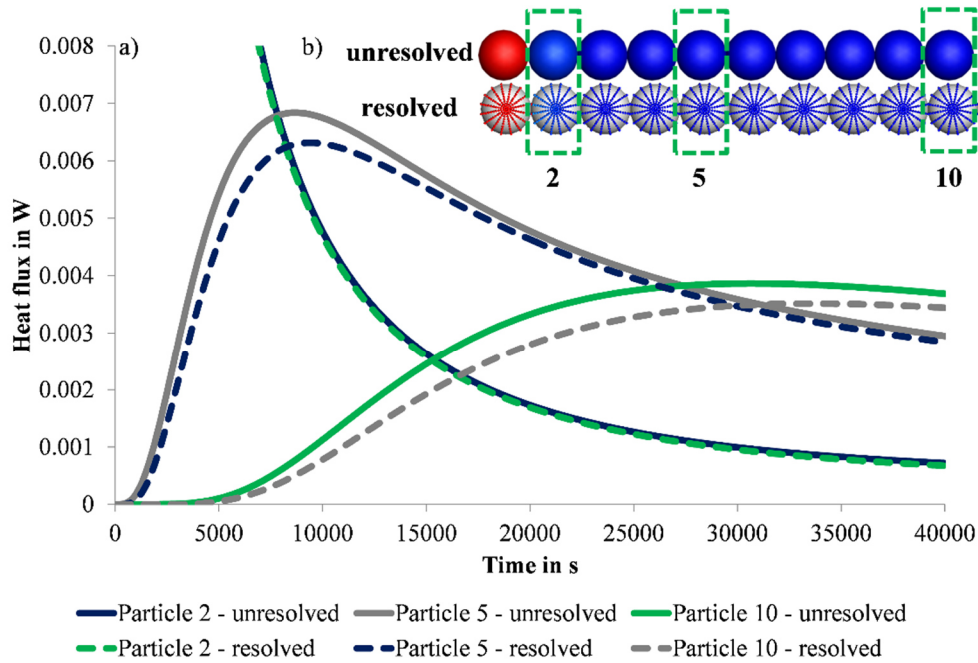


Fig. 13: a) Heat flux over time for particle 2, 5 and 10 for the resolved and the unresolved heat transfer model; b) Principle simulation setup with one particle being kept at constant temperature (particle 1).

In the base case the bed consists of 2500 particles and is of similar structure as in the thermally thin case (Fig. 14b left). For the second setup (Fig. 14b middle left) the ETC is calculated upon the particles in a cube of a length of 8 particle diameters, obtained by removing the outside particles. In the next case (Fig. 14b middle right) the width of the cube is further reduced until only one particle persists in contact with the bottom and top wall. Finally (Fig. 14b right) one independent case with 5 particles in a row and an overlap of 5% of particle radius is considered. Here the heat flux persists only in axial direction. The highest calculated ETC with the highest deviations between resolved and unresolved model occurs for the 2500 particle case. For cases 2 and 3 deviations and the absolute value for the ETC decrease. Cheng et. al. [259] investigated also the effect of the number of particles on k_e by varying the cube size with the result that below a certain value the ETC decreases. They summarized if the number of particles (cube size) is too small it may not fully represent the packing structure which leads to a different ETC. The same can be observed in this study for the first three cases. Case 4 obtains a higher value for the ETC due to an overlap of 5% of the particle radius which is large compared to overlaps calculated through the Hertz model in the three previous cases.

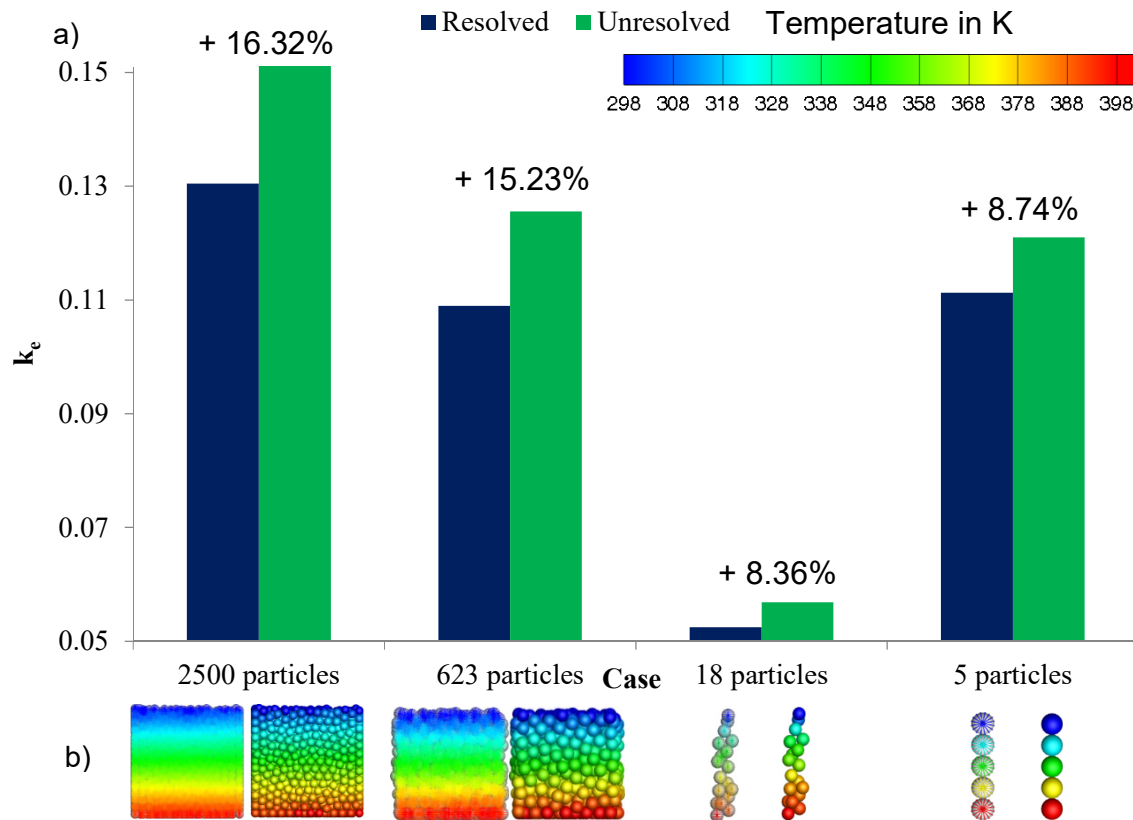


Fig. 14: (a): Calculated ETCs for various packing configurations and particle numbers. Deviations between resolved and unresolved model are shown above the bars. (b): Temperature distribution within the bed when the steady state is reached, left: resolved model; right: unresolved model.

Therefore, the ratio of the particle-particle heat flux to the total heat flux (particle-particle & particle-fluid-particle) is with nearly 0.29 significantly higher than the ratios of the first three simulation cases (0.17, 0.16 and 0.12). Cheng et al. [259] also demonstrated that k_e is not affected by the cube size as long as the number of particles is larger than 500. Their results based on one packing structure provided by Finney [304]. Beside that Zhou et al. [250] showed in a further study which was validated with the experimental data summarized in Cheng et al. that the ETC of a packed bed is influenced by particle size, their results indicate that an increase of the particle size leads to a higher ETC. As a consequence of this, their calculated ETC differed strongly for varying particle sizes. Based on these two arguments it is questionable if a lower bound of 500 particles and the resulting cube size is sufficient in general.

5. Conclusions

The DEM approach has been extended to include an implicit resolved 3D heat transfer model derived in spherical coordinates for spheres and in Cartesian coordinates for arbitrary shaped particles. Through the realization of boundary conditions of second and third kind the following heat transfer mechanisms can be accounted for: particle-particle, particle-wall, particle-fluid-

particle heat conduction, particle-particle radiation and particle-fluid convection. To partly validate the implemented heat equations, various test cases with three materials (glass, steel, aluminum) are formulated and compared against detailed FVM-simulations and later literature data. In the first test cases a constant heat transfer coefficient and heat flux are applied uniformly on a particle of cubical and spherical shape.

The DEM matches the FVM results well as the volume averaged temperature varies only in dependency on the used material. To show the advantages of the resolved 3D heat transfer model particle-particle radiation and particle-particle heat conduction are considered and results calculated within the DEM are compared against the FVM. Both heat transfer problems are attributed to heat fluxes varying in circumferential direction around the particle; heat fluxes therefore have to be imposed locally on the particle surface. This is impossible for radial or unresolved heat transfer models. For the investigation of the particle-particle heat conduction two cases are considered. Firstly, two contacting spheres with different initial temperatures are investigated. Secondly, a row of three particles with a constant heat flux imposed is investigated. In this context the most important aspects are:

For the particle row with an imposed heat flux a steady state is reached; the best agreement with the FVM is achieved by the resolved model which relies on the undisturbed inner temperature applied as contact temperature.

Unresolved and resolved model utilizing the mean temperature as contact temperature achieve similar results and reach the steady state earlier than predicted by the FVM.

To demonstrate the applicability of the derived 3D resolved heat transfer model for multi particle systems three cases are considered in the last part of the investigation. Here the heat transfer mechanisms particle-particle and particle-fluid-particle heat conduction are accounted for. Thereby the model is validated with literature data and the relevance of the implemented model for thermally thick particles is outlined. In this context the major issues are:

Numerical and experimental results from literature on the ETC [70,250,259] are matched well for thermally thin particles with the resolved heat transfer model; equal results would however result from an unresolved model.

For the row of contacting thermally thick spheres it was possible to show deviations in the transient heat fluxes between unresolved and resolved heat transfer model.

For the calculation of the ETC of thermally thick particles four cases are considered. Again differences between resolved and unresolved model are analyzed. The absolute ETC value and deviations between resolved and unresolved model increase with the number of particles. In all considered setups, the implemented 3D heat transfer model is able to describe the thermal behavior similarly well as the FVM. The resolved model allows to impose heat fluxes locally which is impossible for radial or lower detailed models. Especially the investigation of heat

transfer in a packed bed underlines the importance of multidimensional heat transfer as noticeable deviations occur between resolved and unresolved model for the ETC. For the future the derived 3D heat transfer model is extended to account for particle-particle heat conduction of arbitrarily shaped particles. Additionally, the DEM with the resolved heat transfer model is coupled with the CFD. This would allow to solve heat transfer problems involving bulk solids comprising of complex shaped particles passed through by a fluid in high detail for the first time.

Acknowledgements

Financial support by the DFG - KR 3446/6-1 is greatly acknowledged.

VI. Numerical and Experimental Investigation of the Heat Transfer of Spherical Particles in a Packed Bed with an Implicit 3D Finite Difference Approach

Tobias Oschmann^{1*}, Harald Kruggel-Emden¹

¹Mechanical Process Engineering and Solids Processing, TU Berlin, Ernst-Reuter-Platz 1, D-10587 Berlin, Germany

*Corresponding author. Tel.: +49-030-314-26321; Fax: +49-030-314-26432

E-mail address: tobias.oschmann@tu-berlin.de

The following accepted manuscript appeared as journal version in Oschmann T., Kruggel-Emden H.: Numerical and Experimental Investigation of the Heat Transfer of Spherical Particles in a Packed Bed with an Implicit 3D Finite Difference Approach, Granular Matter 19: 47 (2017) and may be found at <https://doi.org/10.1007/s10035-017-0711-z>

Abstract

Heat transfer in packed or fluidized beds in the presence of a surrounding fluid is an important phenomenon which is relevant to numerous industrial applications. Here we extend an earlier derived 3D heat transfer model [305] to take into account particle-fluid heat convection in the case of Biot numbers $Bi \gg 1$. The Discrete Element Method (DEM) which is coupled with the commercial Computational Fluid Dynamics (CFD) package ANSYS Fluent is used as the modelling framework. As a first approximation of the flow induced inhomogeneity of the local heat transfer on the particle surface a distribution function is employed. To validate the resolved heat transfer model, we compare DEM/CFD simulations of three different materials (wood, Polyoxymethylene (POM) and aluminum) with performed experiments. This firstly includes cases where particle surface temperatures are compared with measurements of an infrared camera. Secondly, a numerical study of the average bed temperatures of particle core and surface is conducted to show the differences of the used materials. Thirdly, the core temperatures of three selected particles are compared against experiments. The DEM/CFD framework provides an accurate description of the temperature evolution where the wall effects are negligible. Close to the walls a qualitative agreement can only be achieved for materials with low thermal conductivities. As a consequence of this, in the second part of our investigation we provide various CFD simulations for the heating of an aluminum oxide wall which is required for the evaluation of the particle surface temperatures measured by an infrared camera. The simulation results show the same tendencies as the experiments, underline the complexity of the heat transfer at the walls and are a first step for the formulation of a complex particle-wall heat transfer model in the context of a DEM/CFD framework.

Keywords: 3D heat transfer; DEM/CFD; Convection; Contact heat conduction; Resolved intra-particle heat conduction; packed bed; experiments

1. Introduction

In the field of energy technology and thermal process engineering heat transfer in the context of particulate solids is an important process relevant to many industrial applications e.g. drying which is performed in vessels such as rotating drums, fluidized beds or in entrained flow. In the listed vessels, differently dense particle systems form out which are passed through by a fluid. The heat transfer in these particle systems can be attributed to the heat transfer mechanisms conduction, convection and radiation.

A lot of investigators [272,279,281–283,306–309] mainly focused on a homogeneous temperature distribution within the particle which is only valid for thermally thin particles with small Biot numbers. Note that small Biot numbers are usually accompanied by large thermal conductivities. To overcome this limitation, spatially resolved heat transfer models are required. Only a few investigators have considered simple 1D radial [183,234,286] or more accurate 3D heat transfer models [294,295] for the DEM. To close this gap, we formulated a new implicit 3D heat transfer model in spherical and Cartesian coordinates and validated the method in parts against resolved CFD in a previous study [305]. Besides heat conduction, heat transfer in packed or fluidized beds in the presence of a surrounding fluid is an important phenomenon which is relevant to numerous industrial applications. In this investigation we extend the derived 3D heat transfer model to take into account particle-fluid heat convection in the case of Biot numbers $Bi \gg 1$. As a modelling framework the DEM is used, coupled with the commercial CFD-package ANSYS Fluent and compared against performed experiments. Furthermore, we show that wall effects have to be considered to describe the heat transfer precisely. As a first step we investigate various CFD simulations without DEM and compare them with experiments to analyze the temperature of the employed aluminum oxide wall.

2. Methodology

The heat transfer model resolving temperature within individual particles in 3D is implemented in an in-house DEM/CFD framework. In the DEM, the translational and rotational motion are obtained by integrating Newton's and Euler's equations for each particle given in general form for arbitrarily shaped particles by

$$m_i \frac{d^2 \vec{x}_i}{dt^2} = \vec{F}_i^c + \vec{F}_i^{pf} + \vec{F}_i^g, \quad (1)$$

$$\hat{I}_i \frac{d\vec{W}_i}{dt} + \vec{W}_i \times (\hat{I}_i \vec{W}_i) = \Lambda_i^{-1} \vec{M}_i, \quad (2)$$

with particle mass m_i , particle acceleration $d^2 \vec{x}_i / dt^2$, contact force \vec{F}_i^c , particle/fluid force \vec{F}_i^{pf} , gravitational force \vec{F}_i^g , angular acceleration $d\vec{W}_i / dt$, angular velocity \vec{W}_i , external moment \vec{M}_i resulting out of contact or particle/fluid forces, the inertia tensor \hat{I}_i along the principal axis and the rotation matrix converting a vector from the inertial into the body fixed frame Λ_i^{-1} [12]. For further information regarding the calculation of the particle/fluid force \vec{F}_i^{pf} , previous investigations are recommended [185,299]. In the DEM contact force laws comprising of a normal and tangential component are utilized. The normal component of the contact force is obtained from a non-linear contact model according to Tsuji [15] which is based on the Hertz theory [13]

$$\vec{F}_i^n = \frac{4}{3} E^* \sqrt{R} \delta_n^{3/2} \vec{n} + \gamma^n \delta_n^{1/4} \vec{v}_{rel}^n. \quad (3)$$

$E^* = 1/((1 - \nu_1^2)/E_1 + (1 - \nu_2^2)/E_2)$ is the effective Young's modulus, $R^* = R_1 R_2 / (R_1 + R_2)$ the effective radius, $m_{ij} = m_1 m_2 / (m_1 + m_2)$ the effective particle mass, $k^n = 4/3 E^* \sqrt{R^*}$ the resulting spring stiffness, δ_n the virtual overlap, \vec{n} a normal vector, γ^n a damping coefficient and \vec{v}_{rel}^n the normal velocity in the contact point. For the calculation of the tangential forces the non-linear contact model of Di Renzo [14] is used

$$\vec{F}_i^t = \min\left(\frac{2}{3} k^t |\vec{\xi}^t|, \mu_c |\vec{F}_i^n\right) \vec{t} \quad \text{with } k^t = 8G^* \sqrt{R \delta_n} \text{ and } \vec{\xi}^t \leq (1/k^t) F^n \quad (4)$$

where k^t is the stiffness of a spring, μ_c the friction coefficient, $\vec{\xi}^t$ the relative tangential displacement, $G^* = 1/((2 - \nu_1^2)/G_1 + (2 - \nu_2^2)/G_2)$ the effective shear modulus and \vec{t} the tangential unit vector.

For arbitrary shaped particles the temperature field within a particle is solved through the three-dimensional heat equation with constant properties and no internal heat generation [76] given as

$$\frac{1}{\alpha} \frac{\partial T}{\partial t} = \frac{\partial^2 T}{\partial x^2} + \frac{\partial^2 T}{\partial y^2} + \frac{\partial^2 T}{\partial z^2}, \quad (5)$$

where $\alpha = k/(\rho c_p)$ is the thermal diffusivity (quotient of the particle thermal conductivity k , density ρ and particle specific heat capacity c_p), T is the node temperature, t is the solution time and x, y, z are the coordinates in Cartesian form. For the special case of representing a spherical particle a Cartesian formulation leads to a staircase shaped representation of the

particle surface. Therefore, a correction of the surface area is required. Hence, in case of spherical particles the heat equation is rewritten in spherical coordinates [68] circumventing these problems

$$\frac{1}{\alpha} \frac{\partial T}{\partial t} = \frac{\partial^2 T}{\partial r^2} + \frac{1}{r} \frac{\partial T}{\partial r} + \frac{1}{r^2 \sin \theta} \frac{\partial}{\partial \theta} \left(\sin \theta \frac{\partial T}{\partial \theta} \right) + \frac{1}{r^2 \sin^2 \theta} \frac{\partial^2 T}{\partial \phi^2}, \quad (6)$$

with the spherical coordinates r , θ and ϕ in radial, polar and azimuthal direction. Both equations are solved through an implicit finite difference scheme to calculate the temperatures at the next time step.

To consider the different heat transfer mechanisms acting on a particle, boundary conditions of the second and third kind are used. Both are applied at the external surface at the outer nodes of a particle. For the consideration of convection (when particles are surrounded by a fluid) the Robin boundary condition (third kind) is implemented as

$$k \frac{\partial T}{\partial r} + hT_B = hT_{\infty,B} = \text{Known}, \quad (7)$$

with T_B the boundary node temperature, $T_{\infty,B}$ the ambient temperature of the fluid and h the local heat transfer coefficient between particle and fluid, respectively. For the determination of the local heat transfer coefficient a distribution function $f(\vartheta)$ is used which is dependent on the angle to the point of stagnation ϑ [249]

$$f(\vartheta) = 2.1098 + 0.208\vartheta - 1.018\vartheta^2 + 0.2552\vartheta^3, \quad \vartheta \in [0, \pi] \quad (8)$$

$$h = f(\vartheta)\bar{h}. \quad (9)$$

The point of stagnation is the point where the local velocity is zero. An illustration of this is outlined in Fig. 1.

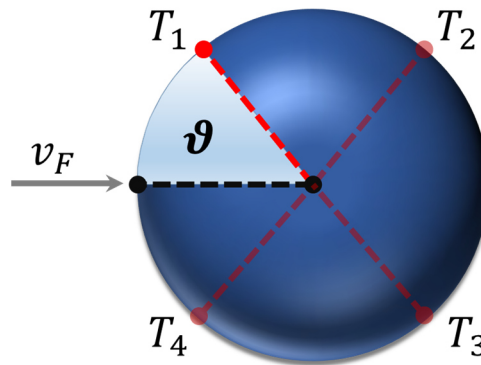


Figure 1: One sphere passed by a fluid. v_F is the fluid velocity, T_{1-4} are the surface node temperatures and ϑ is the angle of the point of stagnation.

The average heat transfer coefficient \bar{h} related to Nu can be obtained through e.g. [310] by

$$Nu_p = 2 + \sqrt{Nu_{lam}^2 + Nu_{turb}^2}, \quad (10)$$

$$Nu_{lam} = 0.664Re^{1/2}Pr^{1/3}, \quad (11)$$

$$Nu_{turb} = (0.037Re^{0.8}Pr)/(1 + 2.443Re^{-0.1}(Pr^{2/3} - 1)), \quad (12)$$

$$Nu = f_\varepsilon Nu_p, \quad (13)$$

$$f_\varepsilon = 1 + 1.5(1 - \varepsilon). \quad (14)$$

When the heat flux q_B acting on the particle is known (particle-particle conduction or radiation) a prescribed flux boundary condition (second kind) can be used

$$k \frac{\partial T}{\partial i} = q_B = \text{Known} \quad i = x, y, z, r. \quad (15)$$

Particle-particle conduction is solved through the Voronoi-polyhedra approach [259]. A detailed explanation of this approach is given in our previous study [305]. The fluid phase is described with Computational Fluid Dynamics (CFD) in an Eulerian framework. Further information about this approach can be found in our previous studies [185,299].

3. Numerical/experimental setup and parameters

In this investigation two simulation cases are performed. Firstly, the integrated 3D heat transfer model is compared against experiments in the context of the DEM/CFD to validate the heat transfer due to convection (convection dominated system). Secondly, the temperature evolution of the aluminum oxide wall is investigated due to the higher heat loss compared to the polycarbonate wall. Here, only a CFD simulation without DEM in an empty chamber is considered. The experimental and numerical setups are shown in Fig. 2a, b and Fig. 2c respectively. A laboratory scale fluidized bed is used to perform the experiments. The vessel consists of antistatic polycarbonate on three sides with a height of 0.41 m, a width of 0.11 m and a depth of 0.01 m. To measure the particle surface temperatures with an infrared camera, two 1 mm depth aluminum oxide glasses with an air gap of 8 mm depth are installed on one side with a height of 0.21 m. A 0.11 x 0.11 m square based porous plate is placed at the bottom to assure an even fluid inflow. Cold air is heated up to a temperature of 373.15 K through a heating

cartridge with a total power of 11 KW and then passed into the vessel from the bottom. Thermocouples of type T with a total measurement error of 0.5 K are installed to measure the fluid temperature, wall temperature and particle core temperature. A more detailed view of the experimental chamber is shown in Fig. 3b. A porous plate and multiple flow straighteners are placed below the orifice to assure an even fluid flow. More details regarding the experimental setup can be found in previous investigations [311–313]. For both numerical setups (DEM/CFD and single CFD) only the green marked area of Fig. 3a is considered. A snapshot of the packed bed simulation with the 3D resolved heat transfer method is shown exemplarily in Fig. 3c. For these heat transfer calculations one particle is represented by 1 node in the core region, 10 nodes in radial, 8 in polar and 16 in azimuthal direction. In the simulations different materials are addressed as outlined in table 1.

All materials have varying mechanic and thermal characteristics as they differ strongly in material parameters like damping, friction coefficient or coefficient of restitution, density, specific heat capacity and thermal conductivity. In this context, the three materials wood, aluminum and POM can be characterized through the Biot number $Bi = h \cdot \frac{d_p}{k}$ as the system is dominated by convection. Wood and POM with $Bi = 23.5$ are defined as thermally thick ($Bi \gg 1$) whereas aluminum with $Bi = 3.21E - 03$ is defined as thermally thin ($Bi \ll 1$). To generate the packing, 1461 spheres with a diameter of $d_p = 10 \text{ mm}$ are randomly distributed and then settle due to gravity. The resulting packing has a bed height of 0.11 m.

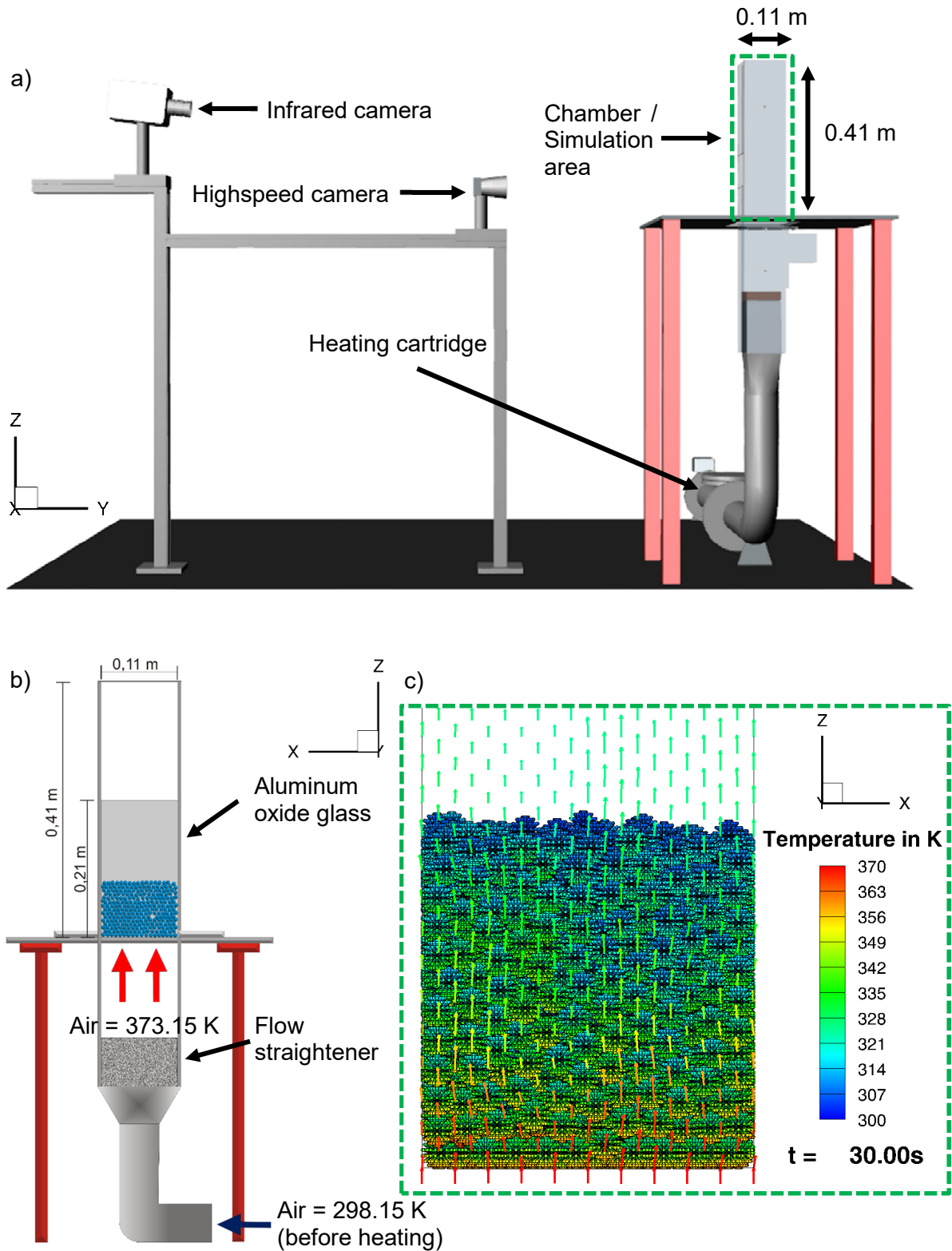


Figure 2: Schematic experimental (a, b) and DEM/CFD numerical setup (c). Small DEM temperature nodes in the numerical setup are plotted as circles and the velocity of the flow field as vectors. Velocity and particle nodes are colored by the temperature.

Table 1: All simulation and experimental parameters are in alignment with [249,250,265]. The Biot number is calculated with a porosity of $\varepsilon = 0.4$ and thermal properties of air at 373.15 K and 1 bar [314]

Setup and particle properties			
Geometry	0.11mx0.11mx0.44m		
DEM mesh	10x10x40 cells		
Particle diameter	0.01 m		
Number of particles	1461		
Material	Wood	Aluminum	POM
Young's modulus	1.60E+10 N/m ²	7.00E+10 N/m ²	3.00E+09 N/m ²
Shear modulus	8.00E+09 N/m ²	2.55E+10 N/m ²	1.05E+09 N/m ²
Poission ratio	0.00	0.33	0.35
Damping coefficient	37.00	86.00	20.41
Friction coefficient	0.50	0.28	0.28
Coefficient of restitution	0.76	0.36	0.87
Density	7.00E+02 Kg/m ³	2.71E+03 Kg/m ³	1.37E+03 Kg/m ³
Specific heat capacity	1.50E+03 J/(KgK)	8.75E+02 J/(KgK)	1.50E+03 J/(KgK)
Thermal conductivity	3.00E-01 W/(mK)	2.20E+02 W/(mK)	3.00E-01 W/(mK)
Thermal diffusivity	2.86E-07 m ² /s	9.28E-05 m ² /s	1.46E-07 m ² /s
Biot-Number	3.40E+00	4.63E-03	3.40E+00
Minimum fluidization velocity	1.58 m/s	3.14 m/s	2.24 m/s
Initial particle temperature	301.25 K		
Reynolds Number	553.84		
Nusselt-Number	32.23		
Heat transfer coefficient	101.90 W/(m ² K)		
Thermal time step	1 x 10 ⁻³ s		
Mechanical time step	8 x 10 ⁻⁷ s		
Wall properties			
Material	polycarbonate	aluminum oxide	
Density	1.20E+03 Kg/m ³	3.97E+03 Kg/m ³	
Specific heat capacity	1.17E+03 J/(KgK)	7.58E+02 J/(KgK)	
Thermal conductivity	2.00E-01 W/(mK)	4.00E+01 W/(mK)	
Young's modulus	2.40E+09 N/m ²	4.35E+11 N/m ²	
Shear modulus	2.30E+09 N/m ²	1.75E+11 N/m ²	
Poission ratio	0.4	0.3	
Material	Wood	Aluminum	POM
Friction coefficient	0.40	0.20	0.21
Coefficient of restitution	0.74	0.81	0.88
Damping coefficient	62.69	38.75	29.78
Fluid properties			
CFD mesh	coarse	mid	fine
	10x10x40 cells	1E+06 cells	5E+06 cells
Density	Ideal gas law		
Dynamic viscosity	2.19E-05 N/m ²		
Velocity	1.3 m/s		
Specific heat capacity	1.01E+03 J/(KgK)		
Thermal conductivity	3.16E-02 W/(mK)		
Temperature	373.15 K		
Time step	1 x 10 ⁻⁴ s		

For the investigation of the temperature evolution of the aluminum oxide wall 12 thermocouples on 4 levels are installed at the inner and the same amount at the outer aluminum oxide wall, comp. Fig. 3.

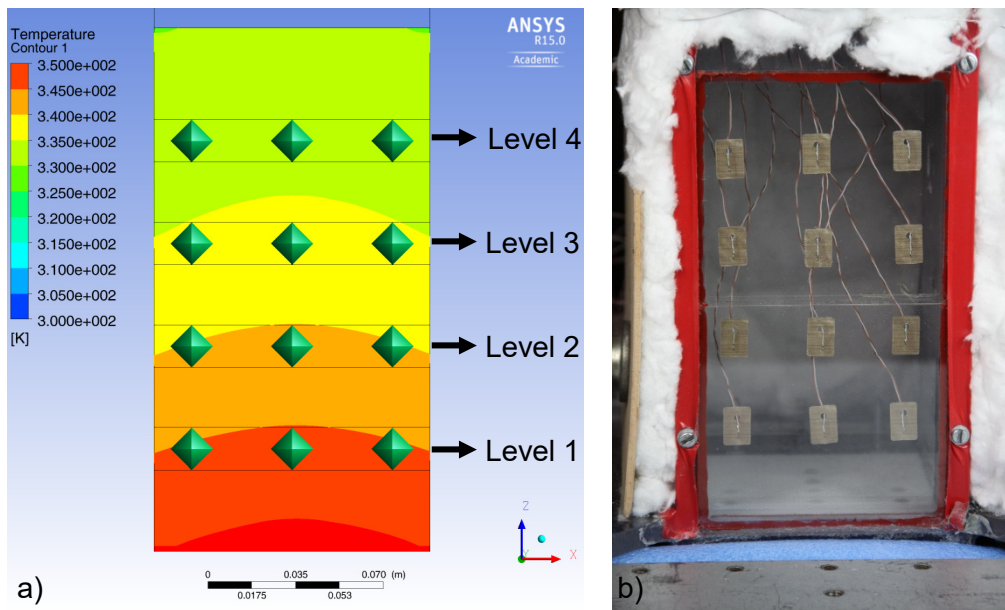


Figure 3: a): Temperature distribution after 350 s in the simulation and schematic positions of the thermocouples of the experiments (green octahedrons). Positions of the levels are level 1 = 0.041 m, level 2 = 0.082 m, level 3 = 0.123 m and level 4 = 0.164 m. b): Positions of the thermocouples in the experiments. The polycarbonate walls are isolated.

In the experiments the thermocouples are placed on the heights level 1 = 0.041 m, level 2 = 0.082 m, level 3 = 0.123 m and level 4 = 0.164 m. As turbulence model the SST k-omega model is used.

4. Results and discussion

4.1 DEM/CFD

In the first verification, the surface temperatures of all three materials are compared between DEM/CFD simulations and experiments measured by an infrared camera. For all simulations in this part, the equations 10 – 14 are used for the calculation of the heat transfer coefficient. In this case, the CFD provides the flow field velocities as input parameters. To quantify the temperature distribution over the particle surface the temperature evolution over time for the materials aluminum, wood and POM are shown in Fig. 4.

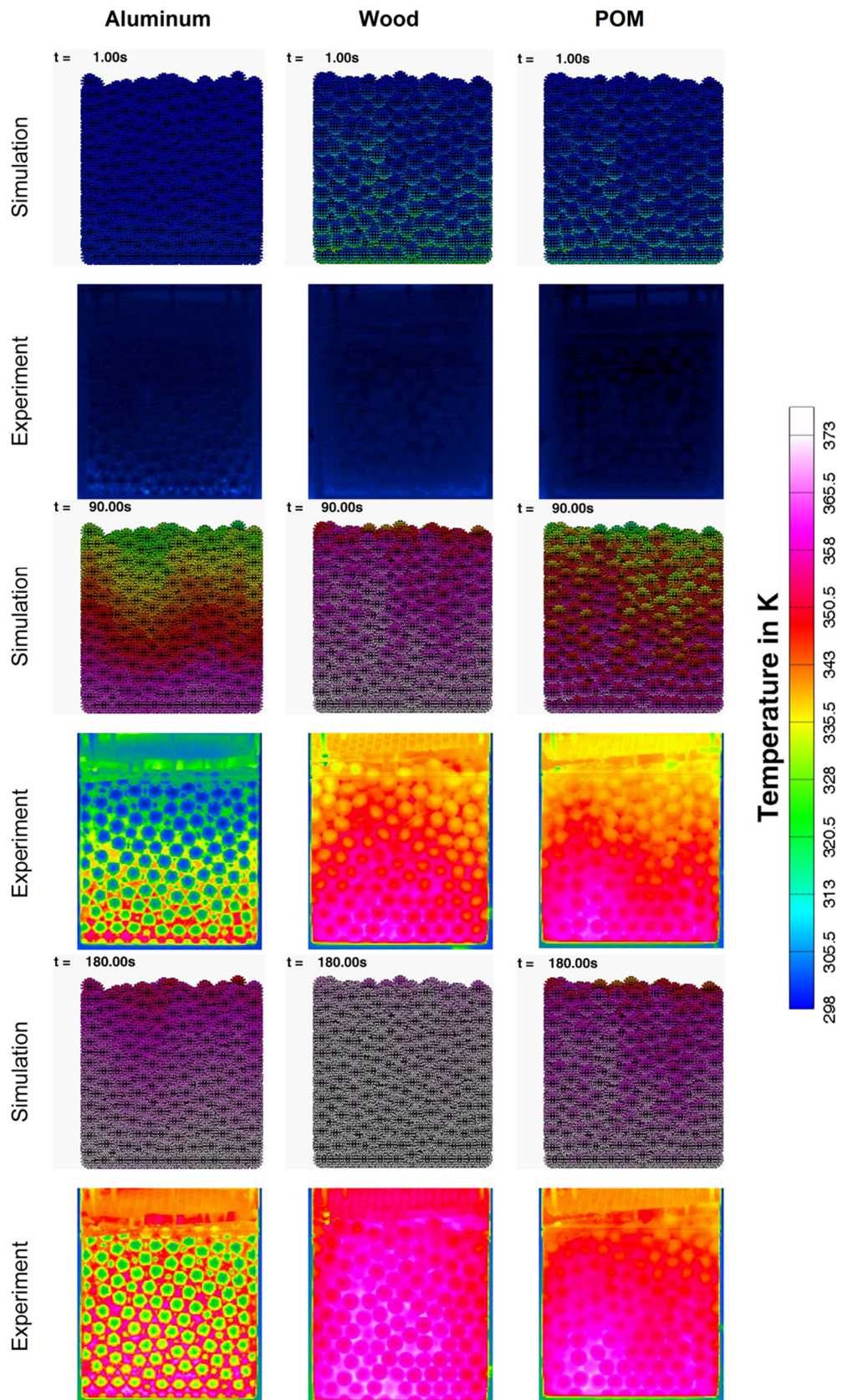


Figure 4: Comparison of the surface temperatures between DEM/CFD and experiments (visible surface temperatures are measured by an infrared camera) at three different time steps.

Here the local visible surface temperatures (without any averaging of the whole system) are compared. For the materials wood and POM the same tendencies are achieved. Wood which

is the material with the lowest mass heats up faster than POM. Strong deviations occur for the material aluminum where the experiment shows a stronger cooling in the contact area. Here, the simplification to neglect particle-wall heat conduction is not valid. As a consequence of this, we investigate the heating of the aluminum oxide wall in the last part of our study.

To show the differences between the used materials the surface and core temperatures of all particles in the bed at one-time step are averaged to one representative averaged bed temperature for the core and surface, respectively. Here, only DEM/CFD results are considered. The results are plotted over time in Fig. 5.

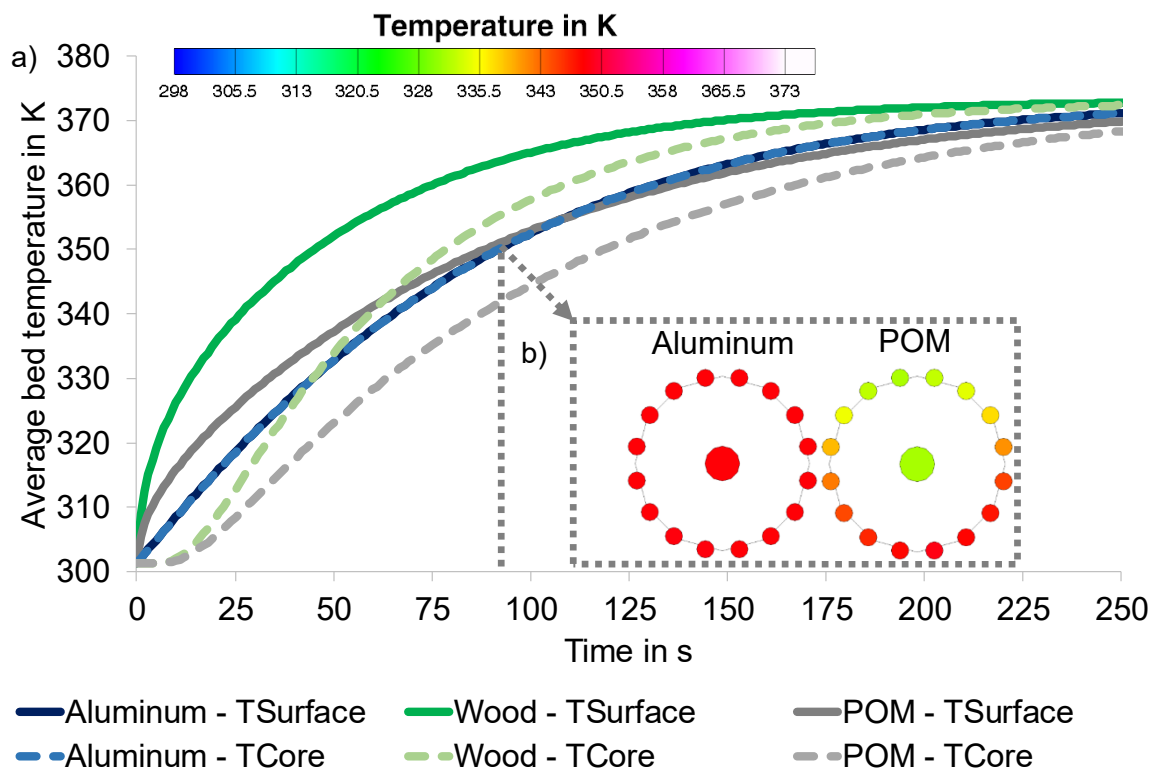


Figure 5: a): Averaged bed temperature evolution over time of core nodes and the surface nodes for the three materials aluminum, wood and POM. b): Comparison of core temperature and surface temperatures at $t = 90$ s for one representative aluminum and POM particle. Nodes are represented through scattered circles.

The initial temperature is set to $T_0 = 301.25$ K as measured in the laboratory. The results indicate that wood which is the material with the lowest mass and high specific heat capacity holds the largest final temperature value, whereas POM with a low thermal conductivity and a higher mass holds the lowest. The increase in temperature is lower for aluminum than for the POM surface at the beginning. After a certain time, the heating rate of POM decreases so that the final temperature value of the surface is slightly higher in case of aluminum. The largest differences occur for the material POM. Due to the high thermal conductivity the surface and core temperature are equal for the material aluminum. A more detailed view is given in Fig. 5b where the surface and core temperature nodes of one aluminum and one POM particle are shown at $t = 90$ s. Here it can be seen, that the surface temperatures are different for POM

and equal for aluminum. Finally, the results indicate that materials with low thermal conductivities hold large differences between core and surface temperatures whereas the curves of aluminum with a high thermal conductivity are similar.

To minimize the wall effects, the temperature evolution in the particle core is investigated in the center of the packing ($y=0.055$ m=depth). Therefore, three representative particles on different heights in z -direction are chosen, comp. Fig. 6b. The used materials are POM and aluminum as the differences in core temperature are more pronounced (comp. Fig. 5). For the experiments the thermocouples are placed into holes with a diameter of 1 mm in the center of the three particles. The results are plotted in Fig. 6a for the material aluminum.

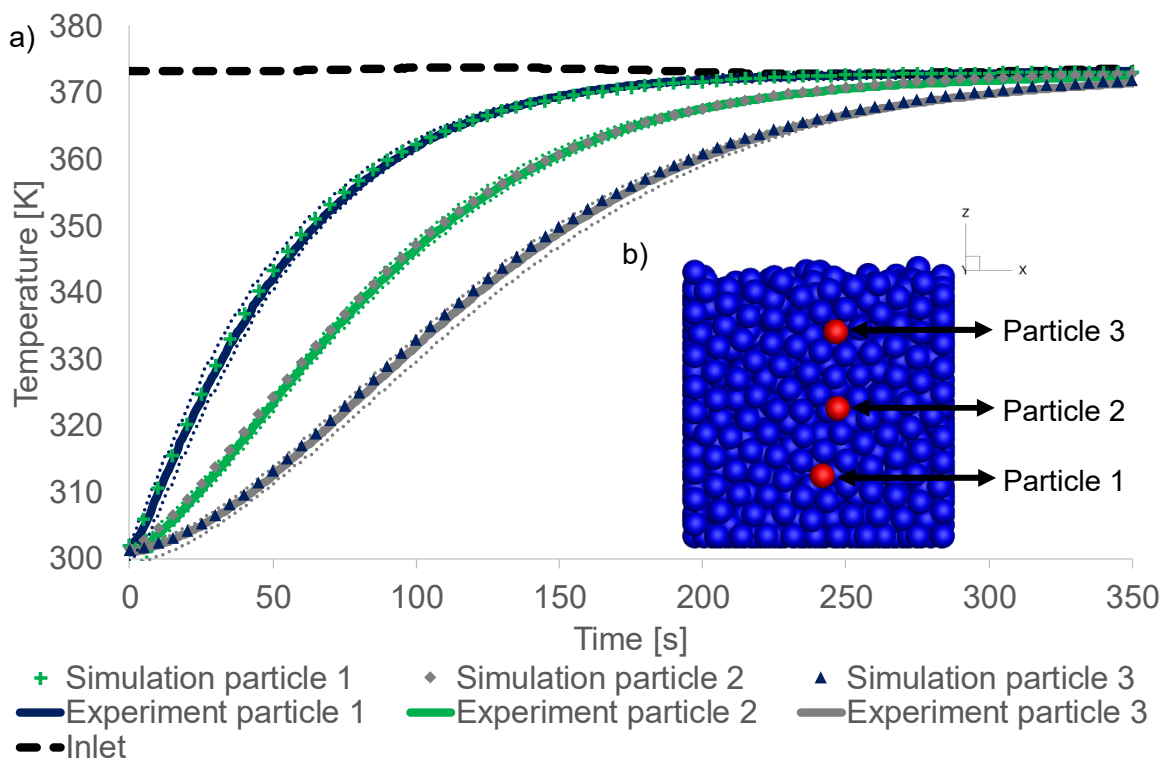


Figure 6: a): Comparison of the core temperature over time between simulations and experiments of three particles for the material aluminum. Average temperatures (curves) consist of 10 experiments to be representative with maximum and minimum experimental values plotted as dotted curves. b): Packing with investigated particles (colored red) on three different levels in z -direction (particle 1 = 0.0275 m; particle 2 = 0.055 m; particle 3 = 0.0825 m). All three particles lie in the midplane ($y=0.055$ m=depth).

The average curves of the three experiments consists of 10 measurements to be representative with the maximum and minimum measurements plotted as dotted curves. The black dashed curve describes the fluid temperature measured under the porous plate. The numerical results match the experimental results well. Differences are only noticeable between the considered particle heights. Particle 1 reaches the fluid temperature earlier than particles 2 and 3. To compare the material dependent temperature evolution within a particle for the material POM, the temperatures of three particles in a cut plane ($y = 0.055$ m) are shown in Fig. 7a.

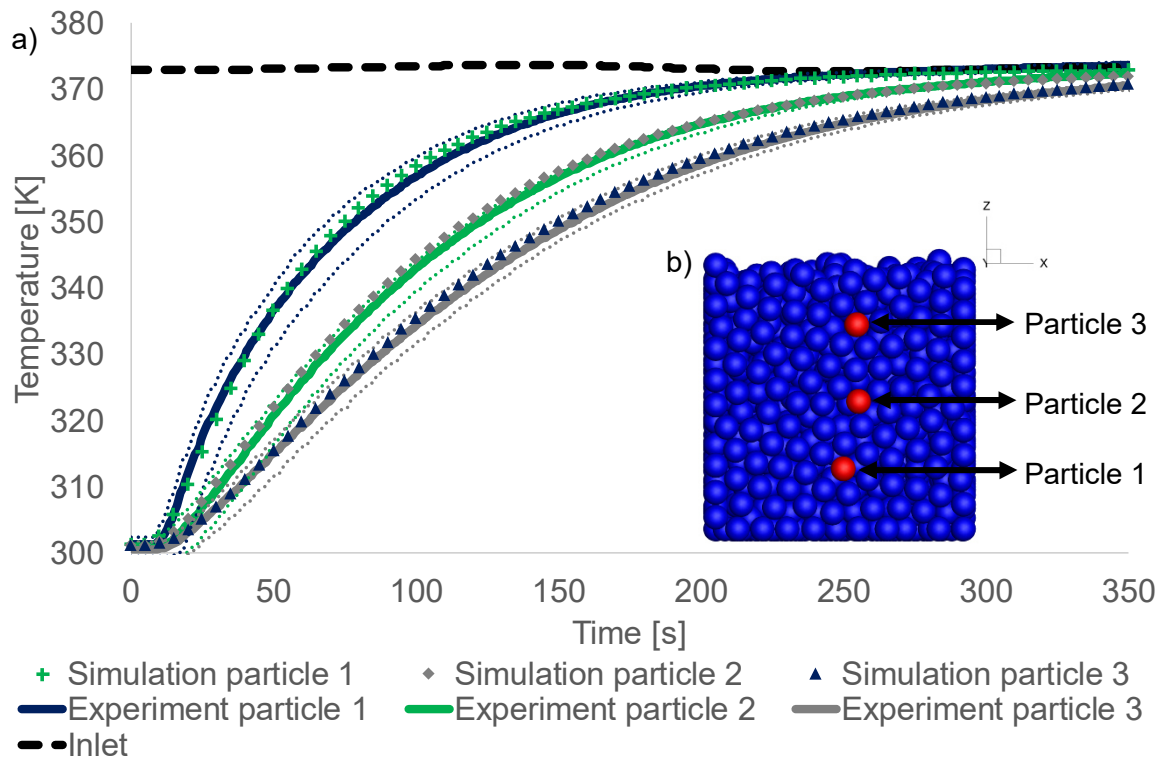


Figure 7: a): Comparison of the core temperature over time between simulations and experiments of three particles for the material POM. Average temperatures (curves) consist of 10 experiments to be representative with maximum and minimum experimental values plotted as dotted curves. b): Packing with investigated particles (colored red) on three different levels (particle 1 = 0.0275 m; particle 2 = 0.055 m; particle 3 = 0.0825 m).

Again, the experimental values are averaged over 10 measurements with the maximum and minimum value as dotted curve. Similar to the results of the material aluminum, simulation data is in a good agreement to the experiments. In opposite to the material aluminum, the temperature of the POM particle is constant for the first seconds due to the low thermal conductivity. The increase in temperature is also higher for aluminum. As a consequence of this, aluminum particles reach the steady state earlier.

4.2 CFD without DEM

In addition to the comparisons between DEM/CFD and experiments, the heating of the aluminum oxide wall is analyzed to provide first results for a future complex particle-wall heat transfer model. In such a model the heating of the wall has to be considered to obtain the correct wall temperature. In this investigation single CFD simulations of an empty chamber should be performed to assess if the CFD is able to calculate the wall temperature accurately. To save computational effort, we use the shell conduction model to simulate the heat transfer within the wall. With this approach it is possible to define different layers with different thermal conductivities to calculate the heat transfer through the wall instead of meshing the thickness of the wall. For this investigation 12 thermocouples in 4 levels are placed at the inner and the same amount at the outer wall. The results for the inner temperature evolution averaged from all

thermocouples on all levels are shown in Fig. 8. For this investigation three mesh qualities are used (compare table 1). Again the experiments are averaged over 10 measurements. The mesh quality has no significant influence as all three simulations are similar. The simulation data slightly underpredicts the experiments with decreasing deviations over time at the beginning. After nearly 250 seconds, the deviations increase and the simulations overpredict the temperature values of the experiments.

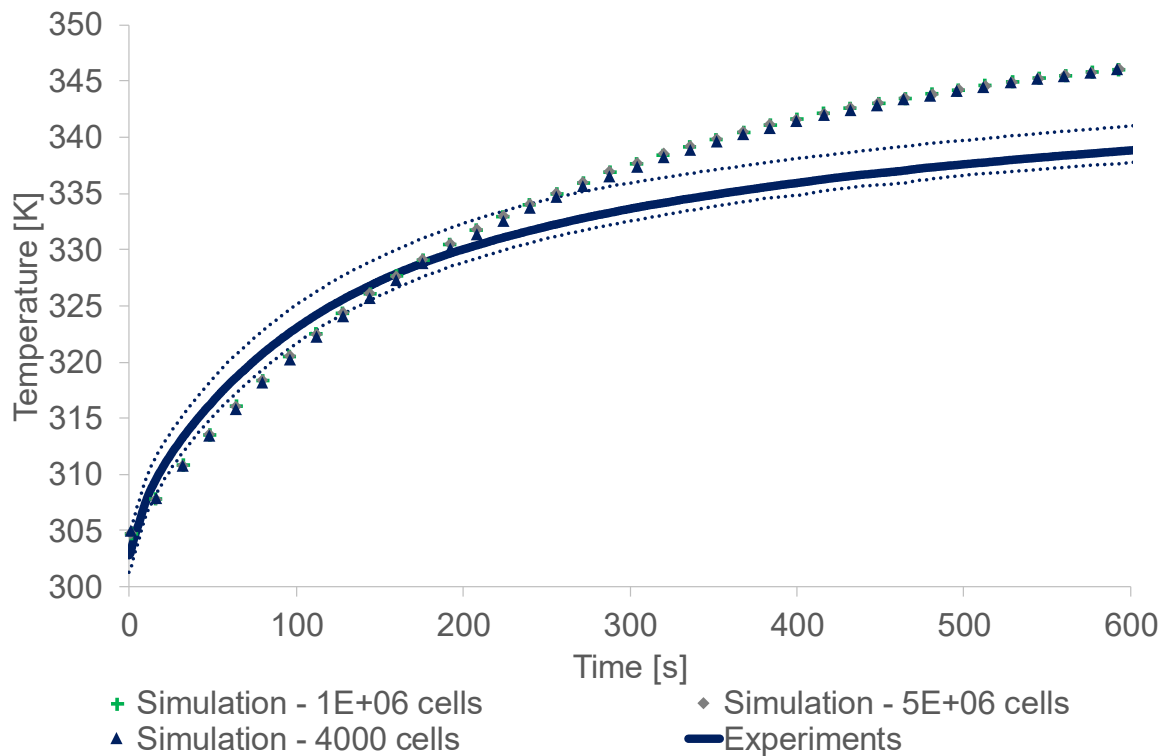


Figure 8: a): Temperature evolution of the inner aluminum oxide glass over time for three simulation cases with different mesh resolutions and experiments.

To analyze this behavior in a detailed manner, the average temperatures on each level are outlined in Fig. 9a. For clarity, the positions of the 4 level are shown in Fig. 9b. The deviations between simulation and experiment decrease over particle height.

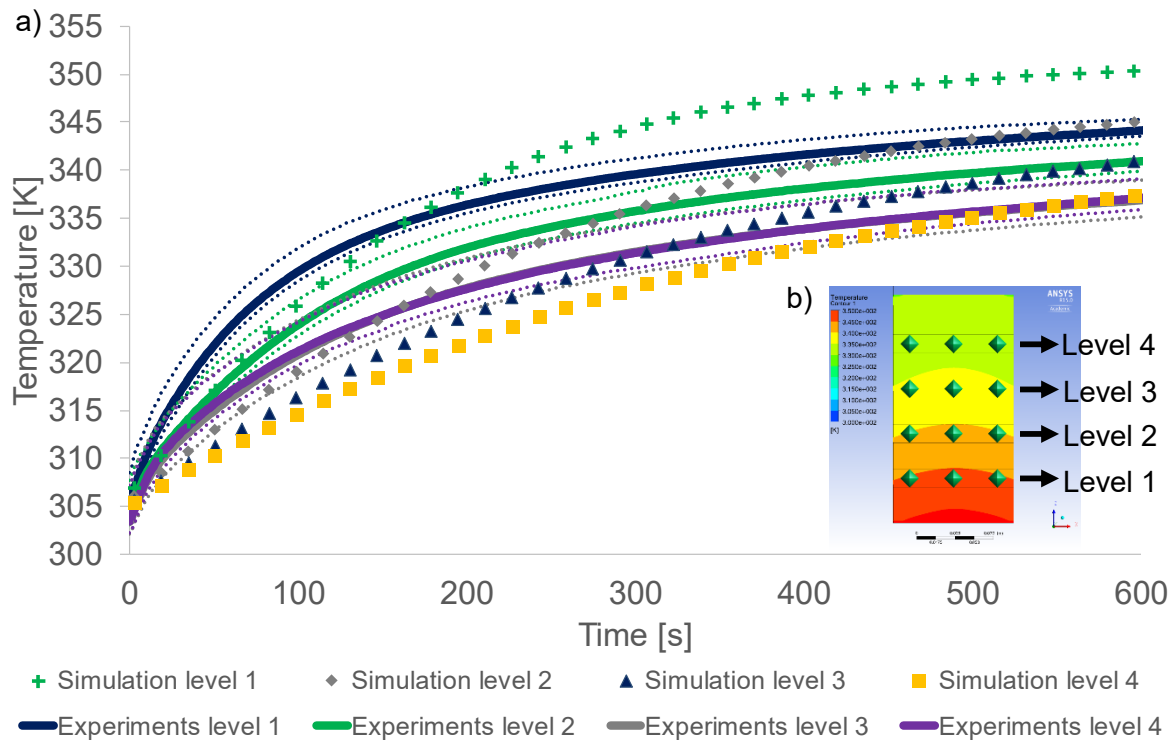


Figure 9: a): Comparison of the averaged temperatures on each level of the inner aluminum oxide wall between CFD simulation and experiments. Experiments are averaged over 10 measurements with the minimum and maximum measurement as dotted curves. b): Positions of the 4 different levels.

In the last part of this investigation the heating of the outer aluminum oxide wall is performed. Again a setup is considered where 12 thermocouples are positioned in 4 rows at the outer wall to determine the average temperature. Here, it is elaborated that the heat conduction through the wall is considered correctly. The average wall temperatures of experiment and simulation are shown in Fig. 10.

The heating of the wall starts earlier for the experiments but reveals the same increase in temperature after 200 s. One reason for the deviations between simulation and experiment is the boundary condition at the inlet. For the simulations, a velocity of 1.3 m/s is set as inlet boundary condition. In case of the experiments, the velocity distribution is exemplary shown in Fig 11.

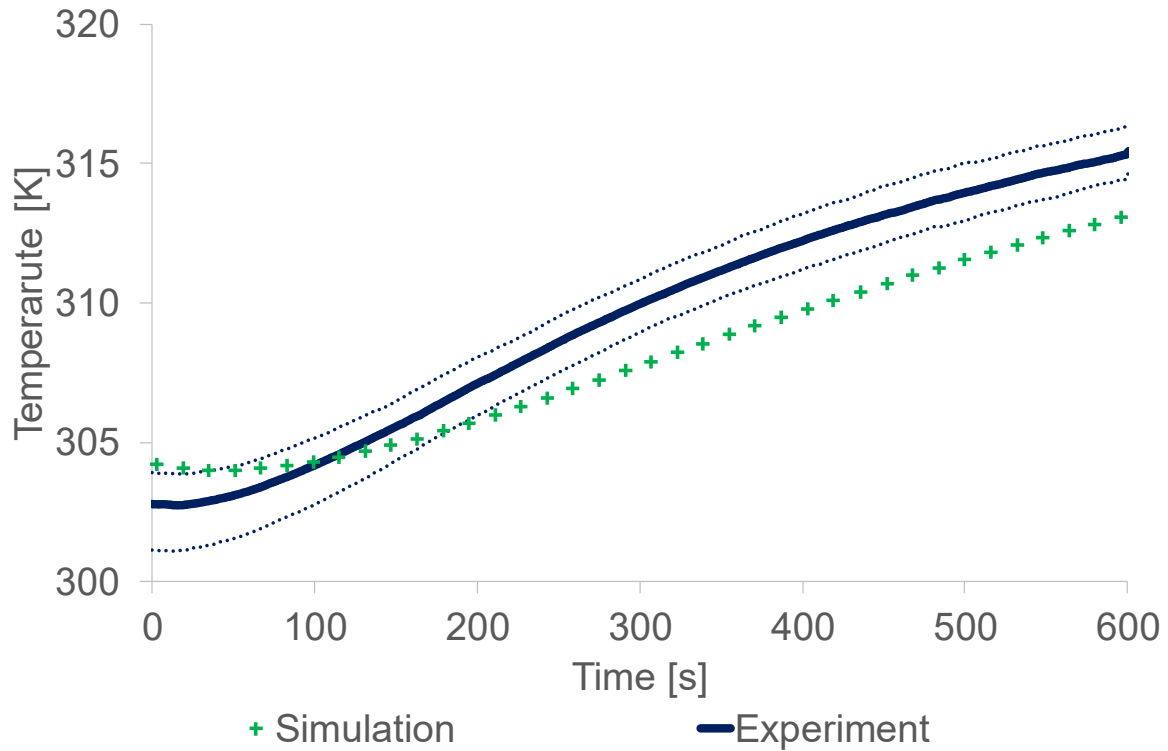


Figure 10: Comparison of the average temperature evolution between CFD simulation and experiment. Experimental values are averaged over 10 measurements. Dotted curves are the minimum and maximum experimental values.

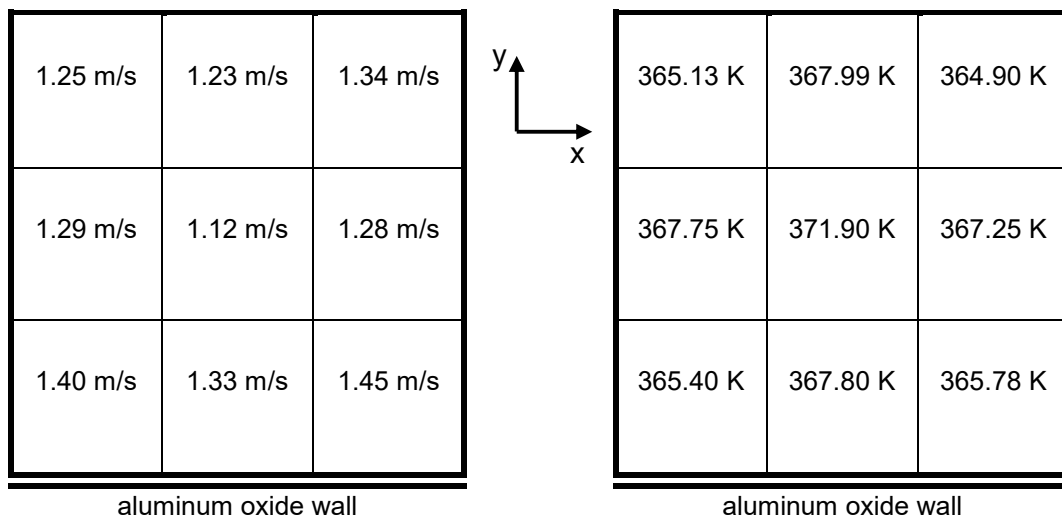


Figure 11: Velocity (a) and temperature distribution (b) at the inlet (z=0m).

Here the velocity is measured at 9 discrete points at the inlet with a tolerance of 5 %. Large wall effects are noticeable at the corners for the velocity as well as for the temperature. The standard deviation is 9.1 % around the mean value of 1.3 m/s. A higher increase in temperature of the wall could be explained due to a higher velocity at the corners. A detailed view on the temperature values shows lower values at the corners. Overall, the experimental setup must be improved to generate a more equal velocity and temperature distribution.

To summarize both CFD cases (inner and outer wall), the CFD is not suitable to describe this behavior exactly. Nevertheless, it is possible to forecast the same tendencies. Particularly, the region close to the porous plate shows the most deviations. In further investigations the results should be used to consider particle-wall heat conduction within the DEM/CFD framework. Here a time dependent wall temperature is necessary to match the experimental results of the infrared camera, especially for materials like aluminum where heat conduction through the wall becomes more important.

5. Conclusions

A spatially resolved 3D heat conduction model integrated into the DEM/CFD approach has been extended to account for surface variations of the particle-fluid convection. The following heat transfer mechanisms can be accounted for: particle-particle- and particle-fluid-particle heat conduction as well as particle-fluid convection. To validate the convective heat transfer, simulation results have been compared against performed experiments in a packed bed. Here the three materials wood, aluminum and POM with different thermal properties are used. Beside the DEM/CFD investigation a CFD simulation (without DEM) of the temperature evolution of the installed aluminum oxide wall is analyzed and compared against measurements of the outer and inner wall temperature. For the DEM/CFD simulations the following conclusions can be drawn from this study:

- A comparison between DEM/CFD and measurements with an infrared camera of the particle surface temperatures shows a qualitative good agreement for the material wood and POM.
- Noticeable differences occur for the material aluminum due to a stronger cooling of the particles in the contact area of the experiments. Here particle-wall heat transfer has to be taken into account.
- The results for the average bed temperatures indicate that materials with low thermal conductivities hold large differences between core and surface temperatures whereas no differences occur for aluminum, a material with a high thermal conductivity.
- The best agreement with the experiments is achieved in the simulation where three particles in the bed are investigated as the wall effects are minimal. Here the core temperatures of the simulations match the experimental results well.

As a first step for the integration of a complex particle-wall heat transfer model into the DEM/CFD framework with respect to the heating of the wall on the CFD side, several CFD simulations at the inner and outer wall are performed. In this context the major issues are:

- The coarse CFD mesh resolution, which is the same as in the DEM/CFD case, shows similar results as the finer meshes with 1 m and 4 m cells.

- Deviations are observable between simulations and experiments which decrease over height. Nevertheless, simulations are able to show the same tendencies as the measurements.

Especially the CFD case shows the complexity of the heat transfer modeling. There are many factors which can influence the heating of a wall like the porous plate, flow field, thermocouples in a flow field, et cetera which are currently not modelled in detail. The CFD simulation results have also shown that a resolved wall is necessary for the calculation of the heat transfer to get acceptable results for the aluminum oxide wall. In contrast, an assumption of an adiabatic wall is valid for the material polycarbonate due to the possibility to isolate it. In further studies the ability of the CFD to describe such systems in general should be investigated. Also important is the integration into the DEM/CFD, as this approach has more restrictions regarding the cell resolution. If the DEM/CFD is suitable, the CFD framework should be extended to consider a particle-wall heat transfer coupling algorithm. Here the heating of the wall can be described by the CFD and coupled back to the DEM. This would allow to consider the cooling of the particles at their contact areas. Additionally, the DEM/CFD framework needs to be extended to dynamic systems like fluidized beds where short contact times become more important.

Acknowledgements

Financial support by the DFG - KR 3446/6-1 is greatly acknowledged. The support of Saint Gobain Crystals for providing us the aluminum oxide samples is gratefully appreciated. The original form of the DEM-code "DEM-Calc" applied is based on a development of LEAT, Ruhr-Universität Bochum, Germany. The code "DEM-Calc" has then been continuously extended both at Ruhr-Universität Bochum and Technische Universität Berlin, Germany. We thank all who have contributed.

Conflict of Interest

The authors declare that they have no conflict of interest.

VII. A novel method for the calculation of particle heat conduction and resolved 3D wall heat transfer for the CFD/DEM approach

Tobias Oschmann^{1*}, Harald Kruggel-Emden¹

¹Mechanical Process Engineering and Solids Processing, TU Berlin, Ernst-Reuter-Platz 1, D-10587 Berlin, Germany

*Corresponding author. Tel.: +49-030-314-26321; Fax: +49-030-314-26432

E-mail address: tobias.oschmann@tu-berlin.de

The following accepted manuscript appeared as journal version in Oschmann T., Kruggel-Emden H.: A novel method for the calculation of particle heat conduction and resolved 3D wall heat transfer for the CFD/DEM approach, Powder Technology 338, 289-303 (2018) and may be found at <https://doi.org/10.1016/j.powtec.2018.07.017>

Abstract

A novel particle-wall heat transfer coupling algorithm is derived to resolve the heat transfer due to particle-wall contact and inner wall heat conduction. The proposed method is integrated in an existing Computational Fluid Dynamics / Discrete Element Method (CFD/DEM) framework where the particle-wall contact heat conduction is solved through the DEM and set as a source term to the CFD. The 3D temperature profile within the wall is solved in time and space in the CFD. The newly calculated wall temperatures are coupled back to the DEM to elaborate the new particle-wall heat fluxes. Two simulation cases are considered. Firstly, a simple rotating drum is simulated to underline the relevance of the realized wall heat transfer model. The focus is set on the calculation of the temperature evolution of the wall. Therefore, only particle-particle and particle-wall heat transfer mechanisms are considered. We use the material aluminum for both, particles and walls and choose the wall dimensions so that the wall mass is approximately one third of the total particle mass. In addition to that, the particle diameter is set to 8 mm which allows the usage of the lumped capacity approach (spatially constant particle temperature) for solving the particle temperature over time. To validate the particle-wall heat transfer, we compare CFD/DEM simulations involving the materials aluminum and polyoxymethylene (POM) with performed experiments in the second part of our investigation. The following heat transfer mechanisms are accounted for: particle-particle, particle-wall heat conduction, resolved particle and wall inner heat conduction and convection. For the determination of the local heat transfer coefficient of a particle, a distribution function is used. The convective heat transfer between fluid and walls is calculated in the CFD. Particle surface temperatures are compared with measurements of an infrared camera. To show the influence of the particle-wall heat transfer two simulation cases with and without particle-wall heat transfer are performed. The numerical results are in a good agreement with the experiments in case of POM. For the

material aluminum where the influence of the particle-wall heat transfer is more pronounced due to a higher thermal conductivity only the model with wall heat transfer fits the experimental results well.

Keywords: CFD/DEM-simulation, experiments, particle-wall contact heat conduction, resolved intra-wall heat conduction, rotating drum, packed bed

1. Introduction

The understanding of the transfer of thermal energy in the context of particulate systems is crucial for many industrial applications in the field of energy and thermal process engineering. Typical industrial examples are fluidized beds, entrained particulate flows, heat exchangers involving particulate solids or drying. For drying of particulate solids often rotating drums are utilized where the drying progress is influenced by many parameters like the mechanical mixing or the heat exchange between particles and walls. For all process examples given the Discrete Element Method (DEM) is a popular and powerful approach for their numerical description.

As one of the first authors, Kwapinska et al. [280,309] highlighted the advantages of the DEM for describing heat transfer in contrast to simple continuum theory referred to as penetration model. They summarized that the DEM was able to assess influences that were not accessible by the penetration model due to a missing modeling of the particle motion. Further attention in the context of modeling heat transfer gained rotating drums by Chaudhuri et al. [279] who performed DEM simulations for particles with high thermal conductivities (192.5 – 385 W/mK) and sizes (1 – 1.5 mm) to simulate flow, mixing and heat transfer in rotary calciners and impregnators. In their simulation setup a decreasing rotational speed and a lower number of baffles (depending on size) had a positive effect on the heat transfer and the temperature uniformity. To simulate simultaneous conductive and convective heat transfer in a 2D rotary kiln setup, Shi et al. [309] extended the DEM approach and calculated the fluid flow through Computational Fluid Dynamics (CFD). They chose different materials, rotational speeds and particle sizes to track the transition from convection dominated to conduction dominated heat transfer. To allow the use of a spatially constant temperature approach their chosen particulate materials all yield Biot numbers $Bi = hL/k \ll 1$. The Biot number is defined by the convective heat transfer h , the particle characteristic length L and the thermal conductivity k of the particle. Besides that, some authors investigated the interplay between mechanical mixing and heat transfer in case of drums by changing the cross-sectional shape, rotation rate or filling level [282,283]. Gui et al. [315] studied the heat transfer in wavy rotating drums which is in general enhanced compared to circular shaped drums. To quantify the heat transfer in an in-

direct heated rotating drum, Komossa et al. [316] carried out DEM simulations and corresponding experiments which showed a good agreement regarding the particle movement and heat transfer resulting from the simulations. Further attention has been drawn to the comparison with experiments by Liu et al. [317] who found out that the initial gas temperature mainly affects the heat transfer in their simulation environment. In dependency on the ratio of a thermal time constant and contact time between particle and walls, Emady et al. [318] identified three different heating time scales/regions for particle conduction where conduction (called first region) or convection (named second region) can be the dominating heat transfer mechanism. In the intermediate region (third region), the system obtained a cool core with warmer outer layers. To study the effect of the lifter geometry on the heat transfer within rotating drums, Xie et al. [319] varied the rotational speed and used different shaped lifters. Lifters generally increase the heat transfer, but decrease the heat transfer with the number and height of the lifters. Beside this they figured out that straight shaped lifters were more efficient than arc shape lifters. In a recent study, Nafsun et al. [320] investigated the mixing of hot and cold particles with different rotational speeds and filling degrees in an experimental rotating drum environment. The thermal mixing time decreased with higher rotational speed and lower filling degree. For high rotational speeds, the filling degree had no significant influence on the thermal mixing time.

In general, the heat transfer in rotating drums can be attributed to the heat transfer mechanisms conduction, convection and radiation. Radiation in the context of the DEM, which is not part of this investigation, can be considered through simple models like [70] or by calculation of the view factor between spheres [321]. In addition to that, view factors can be also determined by using the Ray tracing method [322]. The latter method is flexible in its application, but can be highly time consuming as part of a DEM framework. Beside radiation, heat transfer in a rotation drum in the presence of a surrounding moving fluid where convection has to be accounted for is an important phenomenon which can be relevant to numerous industrial application. Simple convection models only calculate the average heat transfer coefficient [70,183] whereas more complex models determine the local heat transfer coefficient at the particle surface over distribution functions [249,323]. The heat transfer mechanism due to conduction can be separated in contact and inner particle heat transfer. During the past, investigators [272,279,281–283,306–309,324] mainly focused on the so called lumped capacity approach where the particle temperature T_p is calculated by solving the energy balance

$$\frac{dT_p}{dt} = \frac{\sum Q}{m_p c_p}, \quad (1)$$

where $\sum Q$ represents the sum of heat fluxes comprising of conduction, convection and radiation, m_p the particle mass and c_p the specific heat capacity. This simplification of a homogeneous temperature distribution is only valid for thermally thin particles with small Biot numbers. Small Biot numbers are usually achieved by choosing materials with large thermal conductivities and/or small diameters. To overcome this limitation in recent literature more detailed resolved heat transfer models are derived. Here both, simple 1D radial heat transfer models [183,234,286,316,325] or more detailed 3D heat transfer models [249,294,295] are considered. Especially in the group of B. Peters the latter models are widely applied to reacting and/or phase changing particle systems [326,327]. Krause et al. [328] presented CFD/DEM simulations of transient processes occurring in an industrial scale vertical parallel flow regenerative lime shaft kiln (PFR-kiln) and showed the applicability of a 1D heat transfer model to industrial applications. In one of our previous studies we formulated an implicit 3D heat transfer model [305] in spherical coordinates and validated this method in parts against resolved CFD. Beside the intra particle heat transfer, energy can be transferred due to particle-particle or particle-wall contacts. For particle-particle heat conduction, Batchelor and O'Brien [257] derived an approach where the contact region is assumed as circular flat. This approach, also known as heat transfer due to static contact, is often used in the context of the DEM [70,258–261]. Cheng et al [259] extended this approach to consider the conduction through the stagnant fluid allowing particles to exchange heat in point and surface contact or even when they are being apart by a certain distance. For the conduction due to short particle-particle collisions Sun and Chen [262] proposed a more accurate model which was refined by Zhou et al. [263]. All models can be transferred to particle-wall contact where the wall is treated as a particle with an infinite diameter. Although investigations considered a particle-wall heat conduction treatment, detailed models of the description of the heat transfer within a wall are rarely used. In a newer study Lattanzi et al. [329] presented a simulation environment which allowed the determination of the wall temperature profile in space and time. Here they extended the CFD-DEM framework to provide a boundary condition for the total heat flux which can vary in space and in time for the solid and fluid phase. This new simulation framework was used to simulate the heat flux between a gas-solid flow and a heated wall for four different falling-particle heat exchangers with different baffle configurations and one bubbling bed heat exchanger. Beside this, Li et al. [330] additionally considered a gas-to-wall heat transfer coefficient for the heat loss through the wall in their CFD-DEM framework as the grid size typically exceeds the thickness of the thermal boundary layer. In one of our previous studies [323] larger deviations between simulations and experiments were observed regarding the heat transfer for materials with high thermal conductivities. We summarized that the CFD-DEM framework must be extended to consider a particle-wall heat transfer coupling algorithm. To close this gap, we implement a particle-wall heat transfer approach in our CFD-DEM framework where the temperature within the

wall is solved in space and time. In this investigation we firstly present a simple rotating drum simulation case which underlines the importance of considering multidimensional heat transfer within walls as local temperature differences occur. In the second part, we present a comparison between simulations and experiments to validate our newly derived model. In opposite to the first investigation, the 3D heat transfer model for solving the inner particle temperature is used to consider thermally thick particles. Thermally thick particles are defined as particles with a high Biot number ($Bi = h \cdot d_p/k$). The derived framework for a single particle-wall contact with resolved heat transfer within a particle and a wall is exemplary shown in fig. 1.

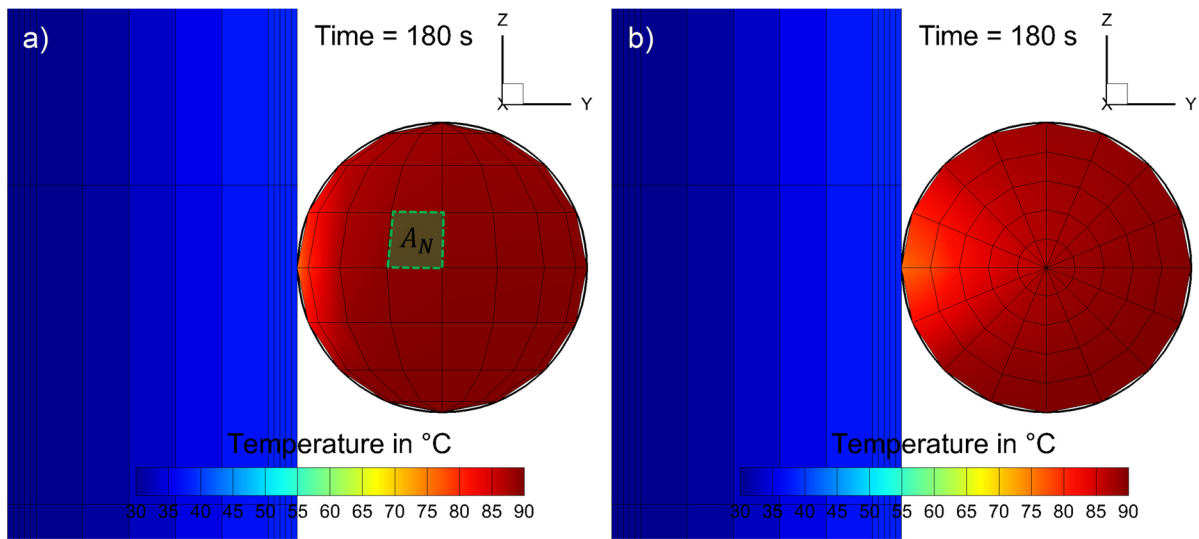


Figure 1: Single particle-wall contact requiring the solution of the temperature profile within each body in space and time. The used particle heat transfer grid is exemplary shown in two different views. (a): view on the particle surface, green marked area exemplarily shows a node surface; (b): cross-sectional view of the particle revealing the node structure.

In this example the respective cell temperature value of a particle corresponds to the calculated node temperature which lies in the cell center. One particle consists of 640 cells ($i = 5$ cells, $j = 8$ cells, $k = 16$ cells). The used wall mesh is coarse compared to the resolution of the particle as the imposed heat flux based on the particle-wall heat transfer appears mostly in one dimensional direction (here y-direction). However, for the firstly addressed rotating drum system and for general applicability the presented modelling approach is derived for multidimensional heat transfer. The required governing equations are outlined in the next section.

2. Methodology

The heat transfer model resolving particle-wall heat conduction is implemented in an in-house CFD/DEM framework. The Discrete Element Method solves the translational and rotational motion by integrating Newton's and Euler's equations for each particle given in general form for arbitrarily shaped particles by

$$m_i \frac{d^2 \vec{x}_i}{dt^2} = \vec{F}_i^c + \vec{F}_i^{pf} + \vec{F}_i^g, \quad (2)$$

$$\hat{I}_i \frac{d\vec{W}_i}{dt} + \vec{W}_i \times (\hat{I}_i \vec{W}_i) = \Lambda_i^{-1} \vec{M}_i, \quad (3)$$

where m_i is the particle mass, $d^2 \vec{x}_i / dt^2$ is the particle acceleration, \vec{F}_i^c is the contact force, \vec{F}_i^{pf} is the particle/fluid force, \vec{F}_i^g is the gravitational force, $d\vec{W}_i / dt$ is the angular acceleration, \vec{W}_i represents the angular velocity, \vec{M}_i is an external moment resulting out of contact or particle/fluid forces, \hat{I}_i is the inertia tensor along the principal axis and Λ_i^{-1} is the rotation matrix converting a vector from the inertial into the body fixed frame [12]. In the DEM the contact force laws can be subdivided in a normal and tangential component. In case of our heat transfer approach we use a non-linear contact model according to Tsuji [15] which is based on the Hertz theory [13] for the calculation of the normal component of the contact force

$$\vec{F}_i^n = \frac{4}{3} E^* \sqrt{R} \delta_n^{3/2} \vec{n} + \gamma^n \delta_n^{1/4} \vec{v}_{rel}^n, \quad (4)$$

with the effective Young's modulus $E^* = 1 / ((1 - \nu_1^2) / E_1 + (1 - \nu_2^2) / E_2)$, the effective radius $R^* = R_1 R_2 / (R_1 + R_2)$, the effective particle mass $m_{ij} = m_1 m_2 / (m_1 + m_2)$, the resulting spring stiffness $k^n = 4/3 E^* \sqrt{R^*}$, the virtual overlap δ_n , a normal vector \vec{n} , a damping coefficient γ^n and the normal velocity in the contact point \vec{v}_{rel}^n . In contrast to that the tangential force is determined through the non-linear contact model of Di Renzo [14] which is defined as

$$\vec{F}_i^t = \min \left(\frac{2}{3} k^t |\vec{\xi}^t|, \mu_c |\vec{F}_i^n| \right) \vec{t} \quad \text{with } k^t = 8G^* \sqrt{R \delta_n} \text{ and } \vec{\xi}^t \leq (1/k^t) F^n, \quad (5)$$

where k^t is the stiffness of a spring, μ_c the friction coefficient, $\vec{\xi}^t$ the relative tangential displacement, the effective shear modulus $G^* = 1 / ((2 - \nu_1^2) / G_1 + (2 - \nu_2^2) / G_2)$ and \vec{t} the tangential unit vector. As we only consider a rotating drum where convection and particle/fluid forces are intentionally neglected and a packed bed without moving particles the particle-fluid interaction force \vec{F}_i^{pf} plays a subordinate role and is not considered. For further information regarding this force in cases where it has to be considered, we refer to our previous studies like [299,331] where available models are addressed and discussed in detail.

For spherical particles the temperature field within a particle is solved through the three-dimensional heat equation in spherical coordinates [76] given as

$$\frac{1}{\alpha} \frac{\partial T}{\partial t} = \frac{\partial^2 T}{\partial r^2} + \frac{1}{r} \frac{\partial T}{\partial r} + \frac{1}{r^2 \sin \theta} \frac{\partial}{\partial \theta} \left(\sin \theta \frac{\partial T}{\partial \theta} \right) + \frac{1}{r^2 \sin^2 \theta} \frac{\partial^2 T}{\partial \phi^2}, \quad (6)$$

where $\alpha = k/(\rho c_p)$ is the thermal diffusivity (quotient of the particle thermal conductivity k , density ρ and particle specific heat capacity c_p), T is the node temperature, t is the solution time and r , θ and ϕ are the spherical coordinates in radial, polar and azimuthal directions. For spherical particles this formulation of the heat conduction equation circumvents the problem of a staircase shaped representation of the particle surface whereas such a Cartesian formulation requires a correction of the particle surface to be of enhanced accuracy. The differential equation (eq. 6) is preferably solved implicitly to be always stable. To consider the different heat transfer mechanisms acting on a particle, the Robin and Neumann boundary conditions are used. In case of the particle-fluid convection, the Robin boundary condition (third kind) is given as

$$k \frac{\partial T}{\partial r} + hT_N = hT_{\infty,B} = \text{Known}, \quad (7)$$

with T_B the boundary node temperature, $T_{\infty,B}$ the ambient temperature of the fluid and h the local heat transfer coefficient between particle and fluid, respectively. The average heat transfer coefficient \bar{h} related to the Nusselt number $Nu = \bar{h}d/k$ can be obtained through e.g. [310] by

$$Nu_p = 2 + \sqrt{Nu_{lam}^2 + Nu_{turb}^2}, \quad (8)$$

$$Nu_{lam} = 0.664 Re^{1/2} Pr^{1/3}, \quad (9)$$

$$Nu_{turb} = (0.037 Re^{0.8} Pr) / (1 + 2.443 Re^{-0.1} (Pr^{2/3} - 1)), \quad (10)$$

$$Nu = f_\varepsilon Nu_p, \quad (11)$$

$$f_\varepsilon = 1 + 1.5(1 - \varepsilon), \quad (12)$$

where $Pr = \nu/\alpha$ is the Prandtl number (ratio of momentum diffusivity to thermal diffusivity) and $Re = u \cdot d/\nu$ is the particle Reynolds number. To obtain information on the variation of the local heat transfer on the particle surface, a correlated distribution function $f(\vartheta)$ can be used, derived by either Direct numerical simulations (DNS) or from experimental results, which is dependent on the angle ϑ between the connecting line of the point of stagnation and the centroid

of the particle and the point on the surface for which the local heat transfer coefficient needs to be obtained for and again the centroid of the particle [249]

$$f(\vartheta) = 2.1098 + 0.208\vartheta - 1.018\vartheta^2 + 0.2552\vartheta^3 \quad (13)$$

$$h = f(\vartheta)\bar{h}. \quad (14)$$

The point of stagnation is the point where the local relative velocity between particle and fluid is zero. Within the coupled CFD/DEM, particles are placed in cells which are normally larger than the largest particle. The flow field in these cells is described by one averaged fluid velocity vector. To determine the point of stagnation the fluid velocity vector of the corresponding cell is extended towards the center of mass. An illustration of this is outlined for a static sphere in fig. 2.

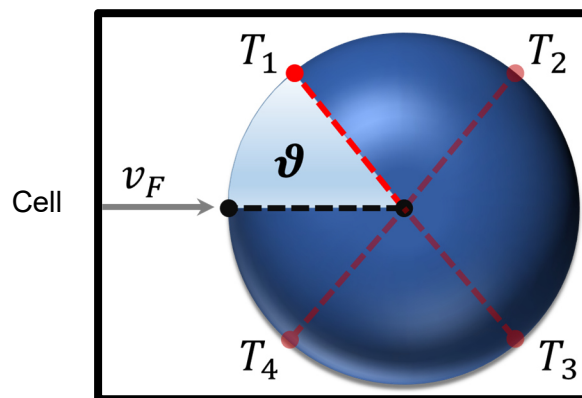


Figure 2: Static sphere considered in the CFD/DEM. The fluid passing the CFD cell (cell is larger than the particle) is represented by one fluid velocity vector v_F , T_{1-4} are the surface node temperatures and ϑ is the angle between a point on the surface towards the point of stagnation.

Besides convection, we take the particle-particle and particle-wall heat conduction into account. Here the quotient of heat flux $Q_{i,j}$ (calculated by eq. 16, 17 or 23) and node surface A_N (see fig. 1) acting on the particle node is known, so the Neumann boundary condition (second kind) can be used

$$k \frac{\partial T}{\partial r} = \frac{Q_{i,j}}{A_N} = \text{Known}. \quad (15)$$

A widely used method to calculate particle-particle or particle-wall conduction is the Voronoi-polyhedra approach [259]. In our previous studies [305,323], we have concentrated our investigation on the interaction of particles and analyzed it very detailed. Now we extend our CFD/DEM framework to consider particle-wall heat transfer and concentrate on its description. A sketch of a single particle-wall contact with all important geometric values for the particle-wall heat transfer is shown in fig. 3.

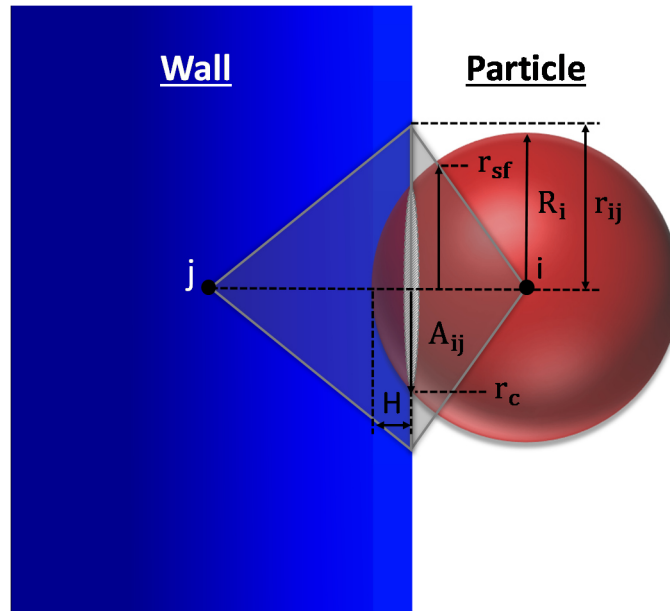


Figure 3: Particle i and wall j in contact. Given parameters illustrate the used particle-wall contact heat transfer model analog to the particle-particle contact heat transfer [70,259]. Here R is the particle radius, H the overlap/separation distance (comp. (eq. 17)), r_c the contact radius, r_{ij} is a lens of fluid between the contacting or near contacting sphere and wall (comp. eq. 26) and r_{sf} is defined by eq. 25

The particle-wall heat transfer can be subdivided into particle-wall heat transfer through static contact, collision contact and particle-fluid-particle heat transfer. For the conduction due to static particle-particle contact (long lasting contacts) the equation of Batchelor and O'Brien [257] is modified following [250] leading to

$$Q_{i,j} = \frac{4r_c c (T_j - T_i)}{\left(\frac{1}{k_{pi}} + \frac{1}{k_{pj}}\right)} \quad \text{with } c = \left(\frac{E_{Sim}}{E_{Real}}\right)^{1/5}, \quad (16)$$

where $Q_{i,j}$ is the heat exchange rate from particle i to wall j , r_c the contact radius and k_{pi} , k_{pj} are the thermal conductivities of particles and wall, respectively. T_i and T_j are the respective undisturbed temperatures of particle and wall. Further details regarding the determination of the particle temperature are given in a former study [305]. The undisturbed wall temperature is determined accordingly. The correction factor c compensates an overestimated contact radius due to a lower used simulation Young's modulus E_{Sim} than the real Young's modulus E_{Real}

(compare table 1). To consider the heat transfer during short contacts due to collisions Zhou et al. [263] presented a modified equation of Sun and Chen which can be easily adapted to the DEM [262] where

$$Q_{i,j} = c' \frac{(T_j - T_i) \pi r_c^2 t_c^{1/2}}{(\rho_{pi} c_{pi} k_{pi})^{-1/2} + (\rho_{pj} c_{pj} k_{pj})^{-1/2}}, \quad (17)$$

$$c' = 0.435 \left(\sqrt{c_2^2 - 4c_1(c_3 - F_0)} - c_2 \right) / c_1 \quad (18)$$

$$c_1 = -2.300 \left(\frac{\rho_{pi} c_{pi}}{\rho_{pj} c_{pj}} \right)^2 + 8.909 \left(\frac{\rho_{pi} c_{pi}}{\rho_{pj} c_{pj}} \right) - 4.235 \quad (19)$$

$$c_2 = 8.169 \left(\frac{\rho_{pi} c_{pi}}{\rho_{pj} c_{pj}} \right)^2 - 33.770 \left(\frac{\rho_{pi} c_{pi}}{\rho_{pj} c_{pj}} \right) + 24.885 \quad (20)$$

$$c_3 = -5.785 \left(\frac{\rho_{pi} c_{pi}}{\rho_{pj} c_{pj}} \right)^2 + 24.464 \left(\frac{\rho_{pi} c_{pi}}{\rho_{pj} c_{pj}} \right) - 20.511 \quad (21)$$

$$t_c = 2.94 \left(\frac{5m_{ij}}{4E_{ij}} \right)^{2/5} (R_{ij} v_{ij})^{-1/5}. \quad (22)$$

Here ρ , c_p are density and specific heat capacity of the wall and particle, t_c the collision time and $F_0 = \alpha t_c / (r_c)^2$ the thermal diffusivity. The wall is treated as particle with an infinite mass and radius which leads to $m_{ij} = m_i$ and $R_{ij} = R_i$. If the particle-wall collision time t_c according to eq. (22) is smaller than the particle-wall contact duration time t_d that particles are in contact and that is obtained in the simulation $t_c < t_d$, first contact heat transfer (during the time t_c) following eq. (17) and then heat transfer according to eq. (16) is considered successively (during $t_d - t_c$) for the contact. Otherwise only the heat transfer during collision according to eq. (17) is applied ($t_c \geq t_d$). To model the particle-fluid-particle heat conduction extending eq. (16) the approach of Cheng et al. [259] is used

$$Q_{i,j} = (T_j - T_i) \cdot \int_{r_{sij}}^{r_{sf}} \frac{2\pi \cdot r dr}{[\sqrt{R^2 - r^2} - r(R+H)/r_{ij}] \cdot (1/k_{pi} + 1/k_{pj}) + 2[(R+H) - \sqrt{R^2 - r^2}]/k_f} \quad (23)$$

$$\text{with } H = \frac{s-2R}{2}, \quad (24)$$

$$r_{sf} = \frac{R \cdot r_{ij}}{\sqrt{r_{ij}^2 + (R+H)^2}}, \quad (25)$$

$$r_{ij} = 0.560R(1 - \varepsilon_i)^{-1/3}, \quad (26)$$

with the particle radius R , the distance s between particle and wall and the porosity ε_i of the particle system in the surrounding as required in eq. 26. The lower bound of the integral r_{sij} in eq. (23) is zero when the particle and the wall are not in contact and $r_{sij} = r_c$ when they are in contact. According to Zhou et al. [70] the heat flux is neglected for ratios of $H/R > 0.5$. Note that eqs. 16-19 for contact heat conduction are strictly applicable for spheres only (with eq. 26) the approach is further restricted to monodisperse systems of spheres). For arbitrarily shaped particles (not considered in this study) applicable heat conduction models are currently not available (see conclusion) as the shape/size of the contact zone cannot be accurately predicted.

The fluid phase for the packed bed considered as second simulation case is represented with Computational Fluid Dynamics (CFD) in an Eulerian framework. Here all relevant properties for the calculation of the particle-fluid convection such as fluid density and fluid temperature (from CFD) or heat transfer coefficient (from DEM) are exchanged between DEM and CFD whereas the convection heat transfer between fluid and wall is only calculated on the CFD side. Further, more detailed information about this coupling for the calculation of the interaction forces can be found in our previous studies [299,331]. The convective heat flux Q_{conv} between particle and fluid is considered as a volumetric energy source term $S_h = Q_{conv}/V_{cell}$ in the energy transport equation given for fluid regions as

$$\frac{\partial}{\partial t}(\rho_f \varepsilon_f c_p T) + \nabla \cdot (\vec{u}_f (\rho_f \varepsilon_f c_p T)) = \nabla \cdot (k_{eff} \nabla T) + S_h, \quad (27)$$

$$Q_{conv} = A_N h (T_{\infty, B} - T_N), \quad (28)$$

with the fluid velocity \vec{u}_f , thermal conductivity k_{eff} , the fluid density ρ_f , fluid porosity ε_f , fluid heat capacity c_p and fluid temperature T . Additionally, the continuity and momentum exchange has to be considered as part of the Navier-Stokes equations not stated here. If details are required it is referred to [250].

The temperature distribution within the wall is solved through the CFD by the energy transport equation in solid regions

$$\frac{\partial}{\partial t}(\rho h) + \nabla \cdot (\vec{v}(\rho h)) = \nabla \cdot (k \nabla T) + S_h, \quad (29)$$

where ρ is the wall density, h is the enthalpy, k is the thermal conductivity, T is the wall temperature, \vec{v} is the velocity field vector computed from the solid body motion and $S_h = Q_{ij}/V_{cell}$ represents the volumetric energy source term by particle-wall contact applied in each CFD cell.

The heat flux $Q_{i,j}$ out of particle-wall heat contact is calculated after the undisturbed temperatures are determined [305] and set to all CFD cells which are lying in the respective contact region to distribute the heat flux in space.

3. Numerical/experimental setup and parameters

In this investigation two simulation cases are performed. Firstly, a simple rotating drum system is addressed to present a system where the particle-wall heat conduction plays a dominant role and where the wall is significantly affected by this phenomenon. Secondly, a packed bed of a previous study [323] where convection is the dominating heat transfer mechanism is considered. Here an existing 3D heat transfer model is used as one of the considered materials obtains a high Biot number $Bi = 34 \gg 1$ (thermally thick) and the lumped capacity approach is not valid to be used. For addressing the heat loss through the walls, this method is extended by particle-wall heat conduction and compared against experiments. The heat transfer through the wall can be reduced to a 1D heat transfer problem. Therefore, a coarse CFD solid grid perpendicular to the direction of the particle-wall heat flux (compared to the particle heat transfer grid) is used. The simulation setup for the rotating drum case with the used mesh is shown in fig. 4. In the first simulation case a rotating drum with a diameter of 0.11 m and a total length of 0.11 m is used. The wall in radial direction and the front/back walls have a thickness of 0.0015 m (see green marked area). The total mesh resolution is 46500 cells with 60 cells in radial direction, 10 cells for describing the wall thickness and 30 cells for the inner cylinder barrel along the x-coordinate. To adapt the mesh on the geometry an o-grid is used. To generate the packing, 1000 spheres with a diameter of $d_p = 8 \text{ mm}$ are randomly distributed within the rotating drum and then settle due to gravity. For the wall and the particles, the material aluminum is used. The particles hold a total mass of $m_{particles} = 0.7265 \text{ kg}$ which is nearly three times higher than the mass of the cylindrical encasing ($m_{wall} = 0.2369 \text{ kg}$). In this part of the investigation the focus is set on the influence of the particle-wall heat transfer on the walls, so following assumptions are taken. For clarity, all faces of the rotating drum geometry are defined as walls in the following. The heat transfer mechanisms convection and radiation are neglected. No fluid within the rotating drum is considered. For the calculation of the heat transfer within the particles, the constant temperature approach is used. This assumption is made as the aluminum particles hold a high thermal conductivity ($k = 220 \text{ W/(mK)}$) and are large in diameter ($d_p = 8 \text{ mm}$). In systems where convection is considered these two properties often result in small Biot numbers which allow the usage of the lumped capacity approach.

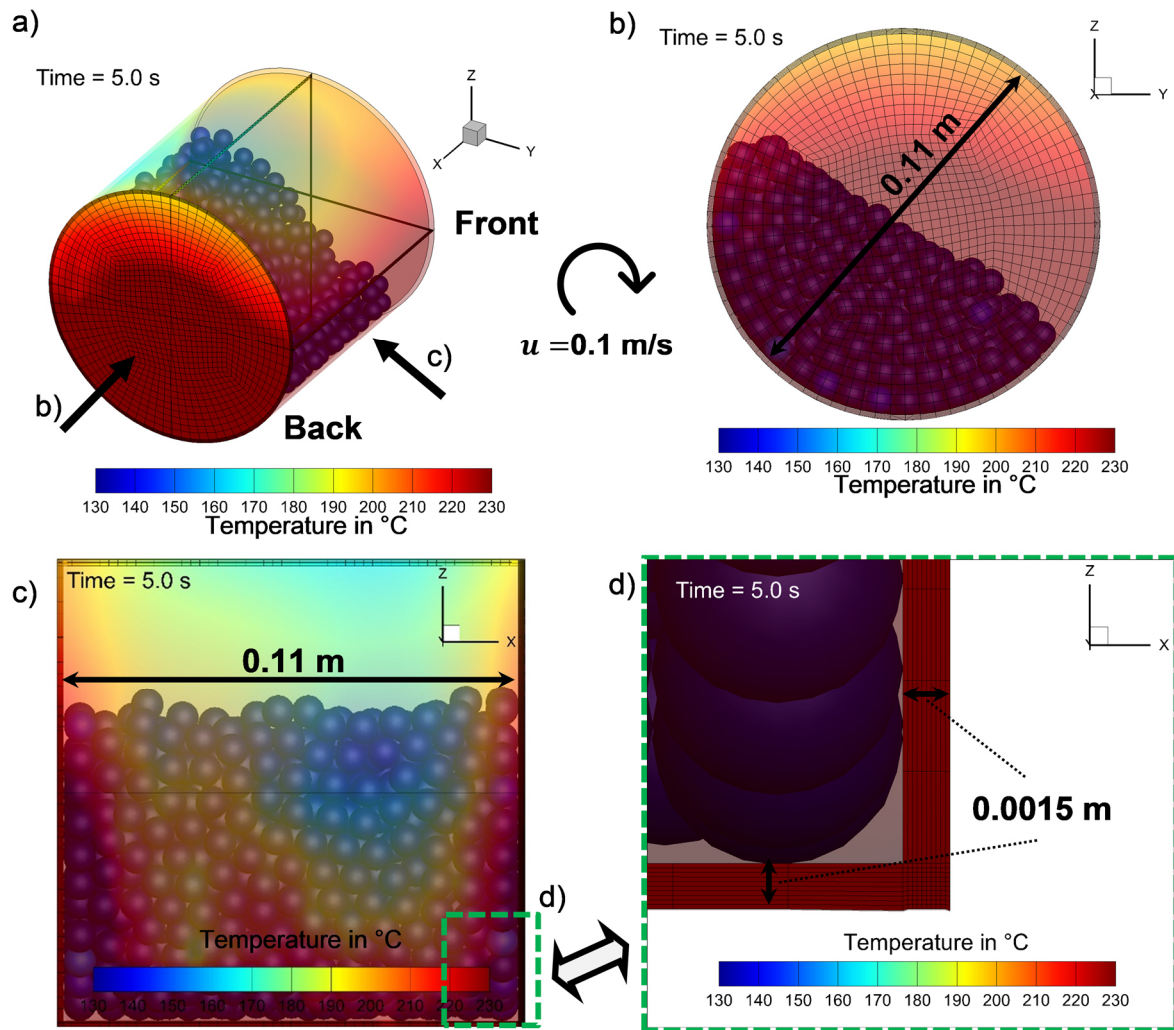


Figure 4: Different views of the rotating drum at $t = 5$ s (total simulation time 100s) with 1000 aluminum particles. The used mesh is shown in all four views.

For the second part of the investigation a laboratory scale setup is used to perform packed bed experiments and corresponding simulations with a total simulation time of 180 s, see fig. 5a.

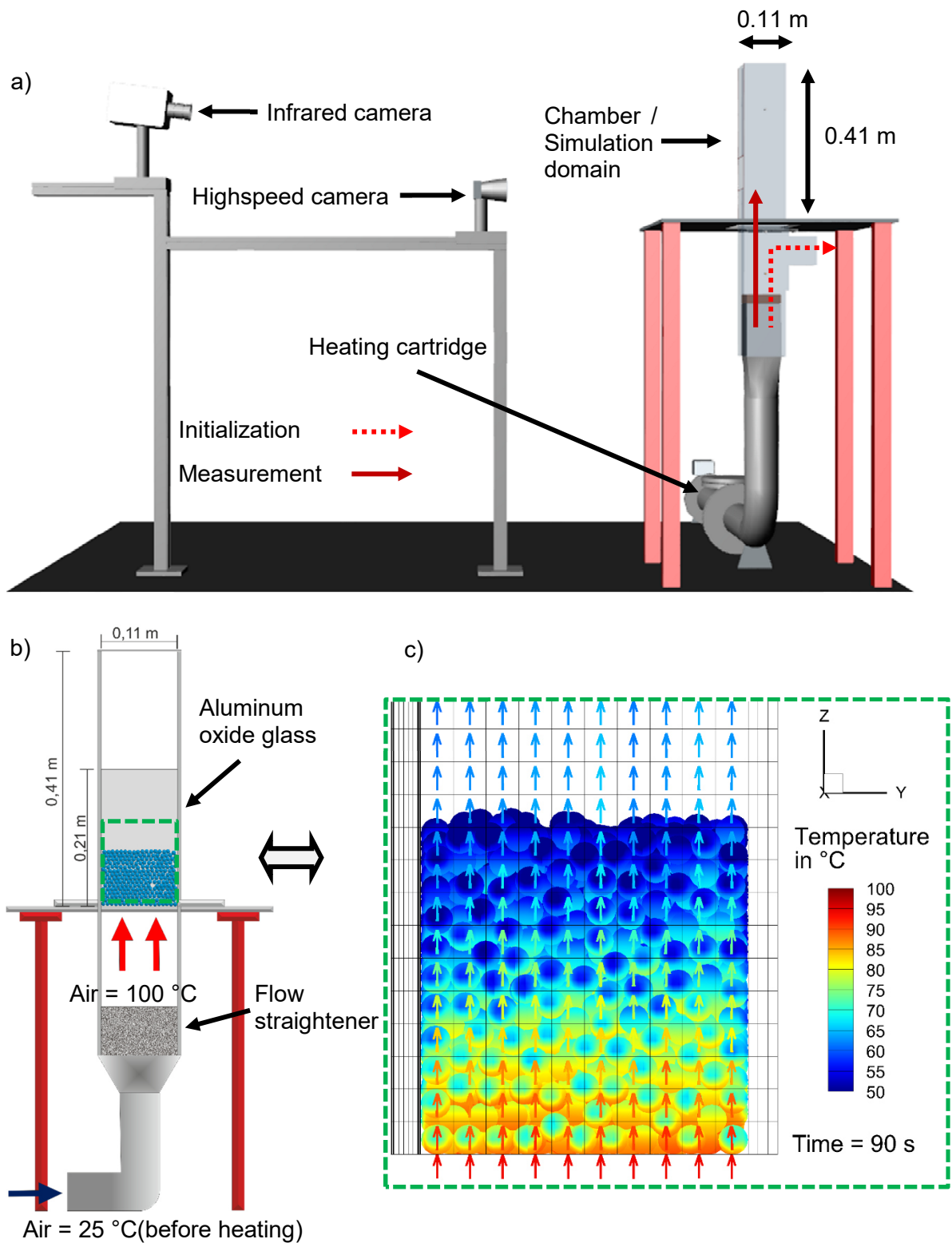


Figure 5: Schematic experimental (a, b) and CFD/DEM numerical setup (c). For clarity, part (b) is simplified. The fluid field is represented by vectors. Fluid velocity and particles are colored by their respective temperature at $t = 90\text{s}$ (total simulation time is 180 s).

The experimental system consists of antistatic polycarbonate on three sides with a height of 0.41 m, a width of 0.11 m and a depth of 0.01 m. The average inlet velocity is set to 1.3 m/s which is below the minimal fluidization velocity (2.24 m/s for POM) and therefore also below

that of aluminum. Therefore, the movement of the particles during the experiment and the simulation can be neglected and the particles have not to be fixed. The particle surface temperatures are measured by an infrared camera. As polycarbonate is an infrared impermeable material, two 1 mm depth aluminum oxide glasses with an air gap of 8 mm depth and a height of 0.21 m are installed on one side of the setup. Thermocouples of type T with a total measurement error of 0.5 °C are installed directly above the particle bed to measure the fluid temperature after passing the packing. A more detailed view of the experimental setup with all relevant items is shown in fig. 5b. To assure an even fluid flow a 0.11 x 0.11 m porous plate and multiple flow straighteners are placed below the orifice. A heating cartridge with a total power of 11 KW heats up cold air from a temperature of 25 °C to 100 °C which is then passed into the vessel from the bottom. To guarantee a constant temperature of 100°C of the air entering the flow chamber containing the packing directly from the beginning of the experiment onwards, the lower parts of the experimental setup must be brought to temperature in advance to performing the experiments. Therefore, the air is directed by a Teflon slider to the initialization outlet. During that initialization step no air is passed into the chamber, but the lower parts of the experimental setup are brought to temperature. When the air temperature has obtained 100 °C the slider is removed, and the initialization outlet is closed thereby. With this the air is passed into the chamber and the measurements are started. More details regarding the experimental setup can be found in previous investigations [311–313,323]. The respective simulation cases are limited to the green marked area of fig. 5a. A snapshot of the packed bed simulation with the 3D resolved heat transfer method and heat transfer through particle-wall conduction is shown exemplarily in fig. 5c. Again, the particles are randomly placed and settle down due to the gravitation force. Here the used materials are aluminum and POM which differ strongly in material parameters like damping, friction coefficient or coefficient of restitution, density, specific heat capacity and thermal conductivity. In opposite to the first simulation case, convective heat transfer is considered and the heat transfer within the particles is resolved through a 3D-approach. Both materials (aluminum and POM) can be characterized through the Biot number $Bi = h \cdot d_p / k$. POM with $Bi = 23.5$ is defined as thermally thick ($Bi \gg 1$) whereas aluminum with $Bi = 3.21E - 03$ is defined as thermally thin ($Bi \ll 1$). On the CFD side the SST k-omega model is used to consider turbulent flow. We outlined in a previous study [323] (comp. section 1) that our earlier simulation results deviate from experimental results due to a missing particle-wall heat transfer model. Therefore, the aim of the second part of the investigation is to validate this assumption. For the sake of completeness, all relevant simulation parameters of both simulation cases (drum and packed bed) are outlined in table 1. In opposite to the packed bed, the movement of the particles is considered in the rotating drum. To save computational effort, time step and damping coefficient are softened and a correction

factor $c = 0.182$ for eq. 16 is needed. No correction of this factor is necessary for the packed bed system as the real particle properties are used for the generation of the initial packing.

Table 1: All simulation and experimental parameters in alignment with [249,250,265]. The Biot number is calculated with thermal properties of air at 100 °C and 1 bar [314].

DEM setup and particle properties			
Case	Rotating drum	Packed bed	
Geometry	0.113x0.113x0.113 m	0.11mx0.11mx0.44m	
DEM mesh	12x12x12 cells	10x10x40 cells	
Particle diameter	0.008 m	0.01 m	
Number of particles	1000	1461	
Material	Aluminum	Aluminum	POM
Young's modulus	1.40E+07 N/m ²	7.00E+10 N/m ²	3.00E+09 N/m ²
Shear modulus	5.90E+06 N/m ²	2.55E+10 N/m ²	1.05E+09 N/m ²
Poission ratio	0.33	0.33	0.35
Damping coefficient	3.78 kg/(sm ^{1/4})	86.00 kg/(sm ^{1/4})	20.41 kg/(sm ^{1/4})
Friction coefficient	0.28	0.28	0.28
Coefficient of restitution	0.36	0.36	0.87
Density	2.71E+03 Kg/m ³	2.71E+03 Kg/m ³	1.37E+03 Kg/m ³
Specific heat capacity	8.75E+02 J/(KgK)	8.75E+02 J/(KgK)	1.50E+03 J/(KgK)
Thermal conductivity	2.20E+02 W/(mK)	2.20E+02 W/(mK)	3.00E-01 W/(mK)
Thermal diffusivity	9.28E-05 m ² /s	9.28E-05 m ² /s	1.46E-07 m ² /s
Biot-Number	-	4.63E-03	3.40E+00
Minimum fluidization velocity	-	3.14 m/s	2.24 m/s
Initial particle temperature	25 °C	25 °C	
Particle Reynolds Number	-	553.84	
Nusselt-Number	-	32.23	
Heat transfer coefficient	-	101.90 W/(m ² K)	
Mechanical time step	1 x 10 ⁻⁵ s	without particle movement	
Correction factor	0.182	1	
Simulation time	100 s	180 s	
Wall properties			
Material	Aluminum	Polycarbonate	Aluminum oxide
Density	2.71E+03 Kg/m ³	1.20E+03 Kg/m ³	3.97E+03 Kg/m ³
Specific heat capacity	8.75E+02 J/(KgK)	1.17E+03 J/(KgK)	7.58E+02 J/(KgK)
Thermal conductivity	2.20E+02 W/(mK)	2.00E-01 W/(mK)	4.00E+01 W/(mK)
Young's modulus	7.00E+10 N/m ²	2.40E+09 N/m ²	4.35E+11 N/m ²
Shear modulus	2.55E+10 N/m ²	2.30E+09 N/m ²	1.75E+11 N/m ²
Poission ratio	0.33	0.4	0.3
Contact partner	Aluminum	Aluminum	POM
Friction coefficient	0.28	0.20	0.21
Coefficient of restitution	0.36	0.81	0.88
Damping coefficient	6.64 kg/(sm ^{1/4})	38.75 kg/(sm ^{1/4})	29.78 kg/(sm ^{1/4})
CFD setup and fluid properties			
CFD mesh	46500 cells	17920 cells	
CFD time step	1 x 10 ⁻³ s	1 x 10 ⁻³ s	
Density	-	Ideal gas law	
Dynamic viscosity	-	2.19E-05 N/m ²	
Velocity	-	1.3 m/s	
Thermal conductivity	-	3.16E-02 W/(mK)	
Specific heat capacity	-	1.01E+03 J/(KgK)	
Initial wall temperature	326.85 °C	30 °C	
Ambient heat transfer coefficient	adiabatic	2.50E+01 W/(m ² K)	

In this study we fixed all physical properties for the calculation of eq. 6 as only small particle temperature differences occur (rotating drum: max 175 °C; packed bed: max 75 °C). Neverthe-

less, the node temperatures are calculated time depended and therefore it is possible to account for temperature dependent physical properties if needed. For the rotating drum both serial and parallel simulations (on four CPU cores) are conducted. To simulate 1s simulation time 120 min are needed for the serial simulation case and 30 minutes for the parallel case. As the packed bed study is simulated without particle movement and 1s simulation time only requires 2 min real time no parallel simulations are performed. Note that solving the heat equation per particle by the applied implicit scheme only requires 3 percent of the total simulation time. Therefore, the proposed novel method can be easily adapted to industrial-scale systems with higher amounts of particles.

4. Results and discussion

4.1 Rotating drum

In the first verification, a simple rotating drum is considered to show the relevance of the implemented model. Here all heat transfer mechanisms except the particle-wall and particle-particle heat transfer are neglected. The wall temperature evolution of the rotating drum is shown in fig. 6 for six specific moments in time (total simulation time is 100 s).

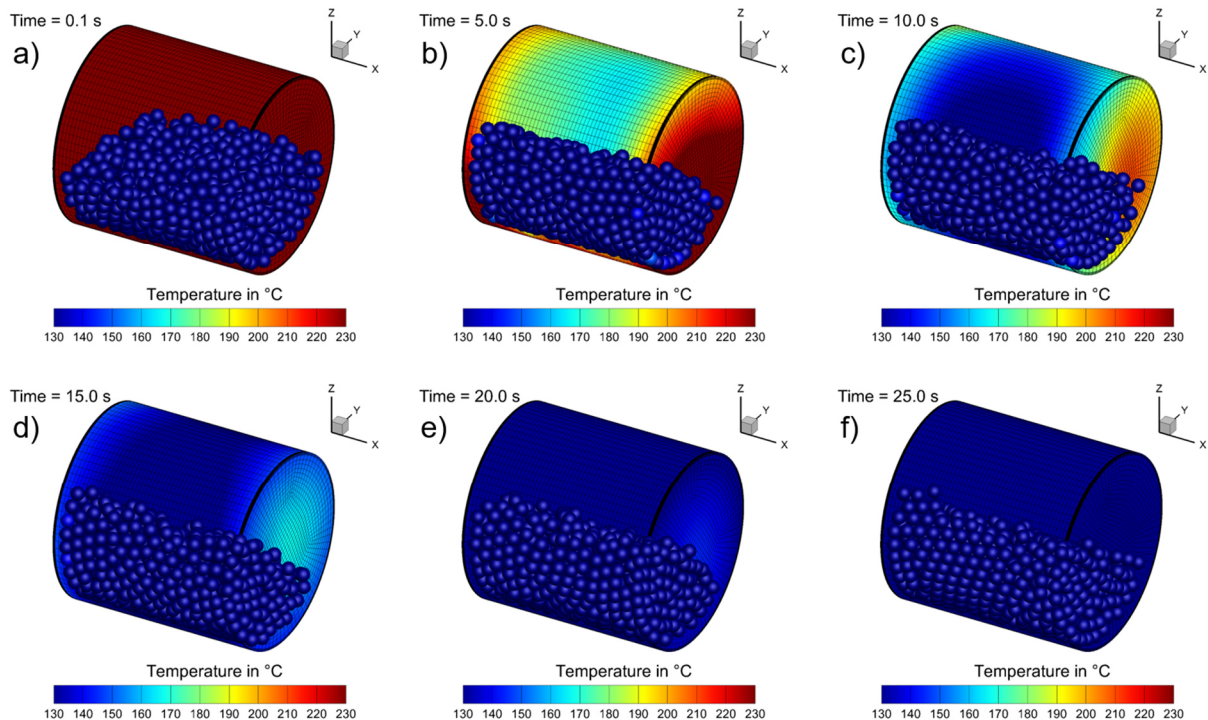


Figure 6: Temperature evolution of particle and wall over time in a rotating drum. The range of the temperature scale is given with 100 °C difference to highlight the temperature of the wall.

Here the focus is set on the qualitative visible evolution of the wall temperature. Therefore, the plotted temperature scale is reduced to 100 °C difference to see the evolution in time and

space on the outer surface of the rotating drum more clearly. For clarity, a more detailed analysis of the temperature evolution is given below by quantitative values. The boundary conditions are considered as described in section 3. The color of the particles representing their temperatures does not change within the shown 25 seconds as the particle temperature is always below 130 °C. At the beginning at $t = 0.1\text{s}$ (fig. 6a), no variation in temperature is seen over the wall surface. After 5 seconds (fig. 6b) noticeable local differences in the temperature profile can be observed in x-direction and at the front wall (back wall is not shown) in radial direction of the rotating drum. In x-direction the temperature distribution is asymmetric with lower temperature values in the middle of the geometry. The asymmetric distribution can be explained through different initial particle heights / solid concentrations along the x-axis. A higher solid concentration leads to a higher particle-wall overlap due to the influence of particles on higher levels. The highest temperature values can be observed at the side walls in radial direction. In general, the heat transfer through particle-wall contacts at the front / back walls is less pronounced as the gravitation force acts only to some parts of the side walls (only in normal direction). In addition, not all parts of the front and back wall (e.g. the center) intersect the particle bed due to a low bed height. A more symmetric temperature distribution in x-direction can be seen after 10 s (fig. 6c) where the minimum temperature is encountered in the center of the rotating drum. This phenomenon is the consequence of the restriction of side walls and a relocation of the particles over time. In the next two subsequent moments in time (figs. 6d and 6e)), the temperature becomes more uniform. Differences are only noticeable at the visible front wall. Finally, all temperature values are equal or below 130 °C after 25 seconds (fig. 6f)). To quantify the steady state, the time-dependent transmitted energy through particle wall heat transfer and the volume averaged wall and particle temperatures are plotted in fig. 7.

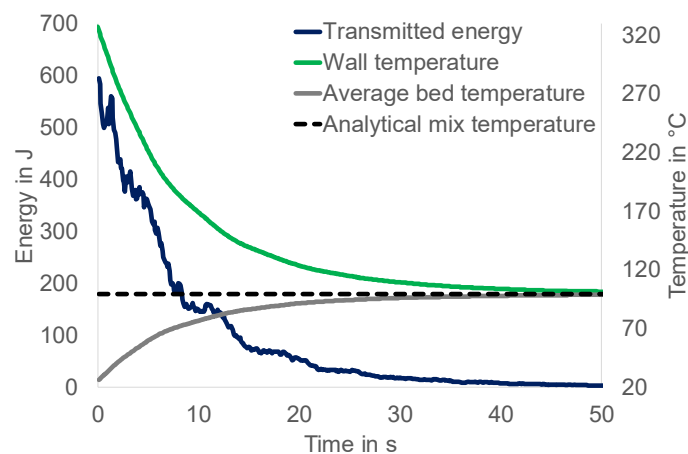


Figure 7: Transmitted energy and volume averaged temperatures of the particle bed and the walls over time.

To prove the validity of the implemented model and to fulfill the energy conservation (system as a whole is adiabatic) the analytical mixing temperature is plotted as a dotted line. The analytical mixing temperature T_m can be calculated as [332]

$$T_m = \frac{m_{Wall}T_{Wall} + m_{Particles}T_{Particles}}{m_{Wall} + m_{Particles}}, \quad \text{with } c_{p,wall} = c_{p,particles}, \quad (30)$$

where T_{Wall} , $T_{Particles}$ are the volume averaged temperature and m_{Wall} , $m_{Particles}$ are the total mass of the wall and the particles. The analytical mixing temperature has a value of $T_m = 99.23 \text{ }^\circ\text{C}$ which is reached by the simulation after 50 seconds. The results indicate that the wall temperature decreases more rapidly due to a lower mass. The transmitted energy shows some fluctuations at the beginning which can be explained though a more unequal temperature distribution in radial direction. In general, the transmitted energy is dependent on the temperature difference between particles and walls which decrease over time. After 50 seconds no difference can be seen so that the transmitted energy becomes zero. To quantify the explained and qualitative investigated local change in temperature on the rotating drum surface (compare fig. 6), all radial temperature values in z- and y-direction at one x-coordinate are averaged to one value and compared between seven different moments in time over the dimensionless length in fig. 8a.

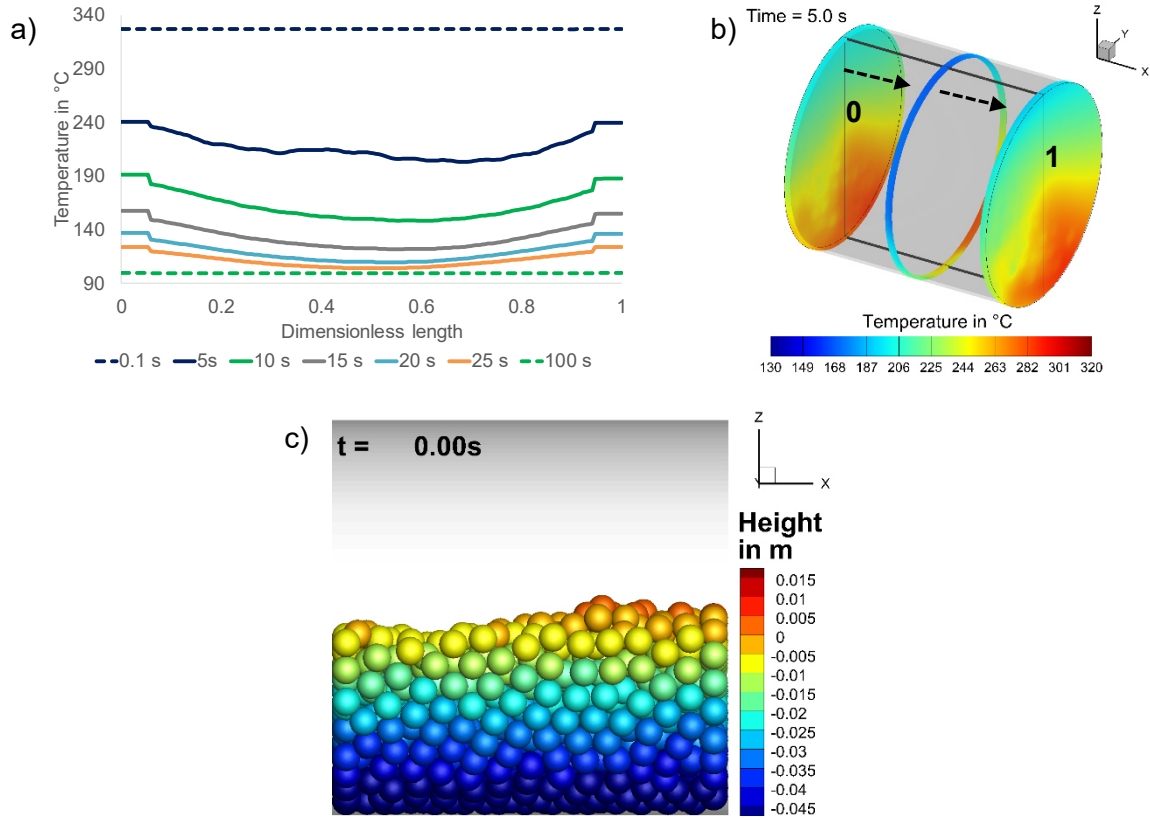


Figure 8: Averaged radial temperature over dimensionless height at seven specific instances in time a), which is exemplary shown for three slices in b) as well as the initial particle distribution in the drum with particles colored by their height in c).

The dimensionless length x_{dim} is the quotient of the local x-coordinate x_i and the maximum x-coordinate x_{max} .

$$x_{dim} = \frac{x_i}{x_{max}}, \quad (31)$$

The determination of the averaged wall temperature is exemplarily shown for three specific x-coordinates in fig. 8b. Here, each colored surface represents the temperatures which are averaged to one value. Similar observations can be drawn as in fig. 6. The dotted lines in fig. 8a represent the initial state ($t = 0.1$ s; $T = 326.85$ °C) and the thermal steady state ($t = 100$ s; $T = 99.23$ °C). After $t = 5$ seconds the front and back wall hold the highest values which vary between 239.5 °C – 240.46 °C. Within the rotating drum, starting from $x_{dim} = 0.059$, the temperature decreases to $T = 211$ °C up to a value of $x_{dim} = 0.31$. Afterwards, first the temperature slightly increases again and then decreases to a minimum value of $T = 202.95$ °C at $x_{dim} = 0.68$. As mentioned before, the temperature profile within the rotating drum is not symmetric due to a variation in particle bed height in the initial packing, see fig. 8c. Here the initial packing is colored in dependency on the particle height z . The minimal temperature after 5 seconds is a consequence of the higher packing height at this location. This effect can be minimized by generating an equal bed height or averaging the respective value over multiple

simulations. As no experimental comparison is done for this part, we limited ourselves to one simulation. Back to fig. 6b, the temperature increases close to the front wall. In general, the results indicate that the temperature difference between front-, backwall and the inner part decreases and the minimum temperature within the rotating drum shifts to the center for the remaining considered moments in time. The temperature difference between the maximum and minimum temperature value firstly increases from $\Delta T \approx 37.51\text{ }^{\circ}\text{C}$ ($t = 5\text{ s}$) to $\Delta T \approx 43.06\text{ }^{\circ}\text{C}$ ($t = 10\text{ s}$) and decreases thereafter to $\Delta T \approx 35.03\text{ }^{\circ}\text{C}$ ($t = 15\text{ s}$), $\Delta T \approx 27.54\text{ }^{\circ}\text{C}$ ($t = 20\text{ s}$) and $\Delta T \approx 20.09\text{ }^{\circ}\text{C}$ ($t = 25\text{ s}$). No significant temperature difference is observable at $t = 100\text{ s}$ ($\Delta T \approx 0.37\text{ }^{\circ}\text{C}$). The effect of the initial packing on the location of the minimum temperature is minimized over time as the temperature minimum shifts to the center of the rotating drum and the temperature profile becomes more symmetric.

4.2 Packed bed

In the second part of this investigation we perform a simulation of a packed bed and compare the results to experimental and numerical results (without particle-wall heat transfer) of our previous study [323]. To compare the temperature distribution over the particle surface the temperature evolution over time for the materials aluminum (fig. 9) and POM (fig. 10) are shown for three moments in time. Here the CFD provides the fluid velocities as input parameters and the experimental results are measured by an infrared camera. In both figures the local visible surface temperatures without any averaging of the whole system are compared. POM which is a material with a lower thermal conductivity and mass heats up faster than aluminum. By comparing both numerical simulations with the experiments for the material aluminum, higher deviations occur for the simulation case without wall heat transfer where the experiments show a stronger cooling in the contact area. The realization of a wall heat transfer through conduction decreases the discrepancies between simulation and experiment. However, deviations are still observable. Better visible agreements are achieved for the material POM. The influence of the particle-wall heat conduction is less pronounced due to the low thermal conductivity of the material POM, but deviations are still observable which are probably based on inaccuracies in the fluid-wall heat transfer due to convection. Here the influence of particles on the fluid-wall heat transfer due to convection is not explicitly considered. Nevertheless, as later shown, the realized particle-wall heat conduction is able to reduce the deviations between simulation and experiment when considering volume averaged temperatures. Furthermore, a good agreement is achieved for the temperature distribution over dimensionless height and for the averaged fluid temperature above the packed bed.

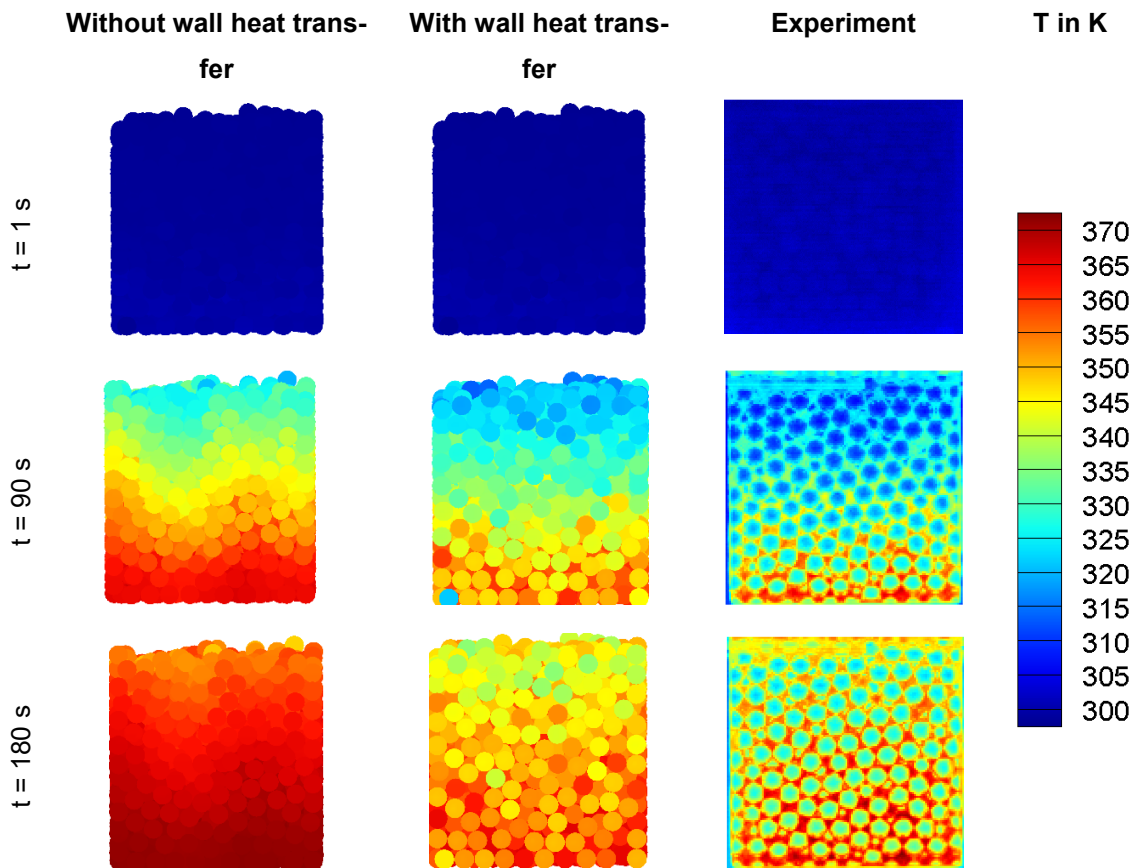


Figure 9: Comparison of the surface temperatures between DEM/CFD models and experiments (measured by an infrared camera) at three different instances in time for the material aluminum.

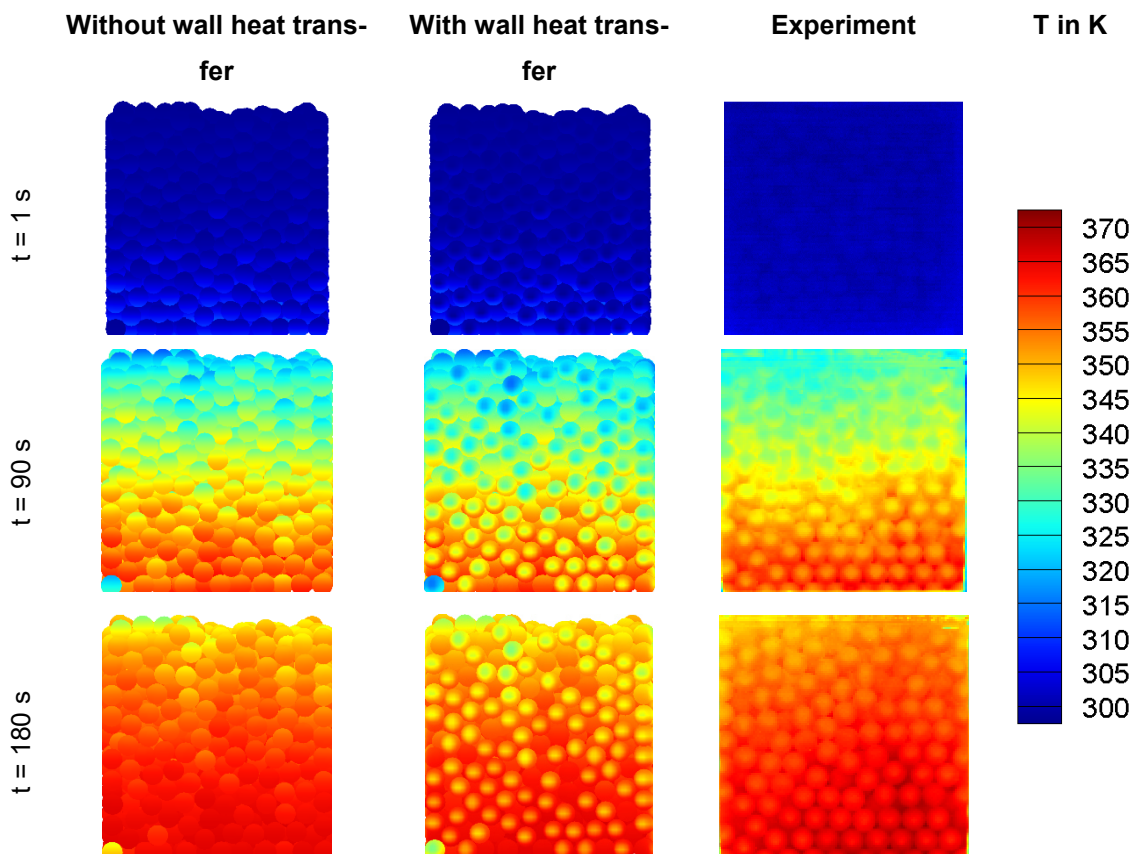


Figure 10: Comparison of the surface temperatures between CFD/DEM models and experiments (measured by an infrared camera) at three different instances in time for the material POM.

To quantify the differences between the simulations and the experiments the temperature values of all visible particles behind the aluminum oxide wall are averaged and plotted over time in fig. 11.

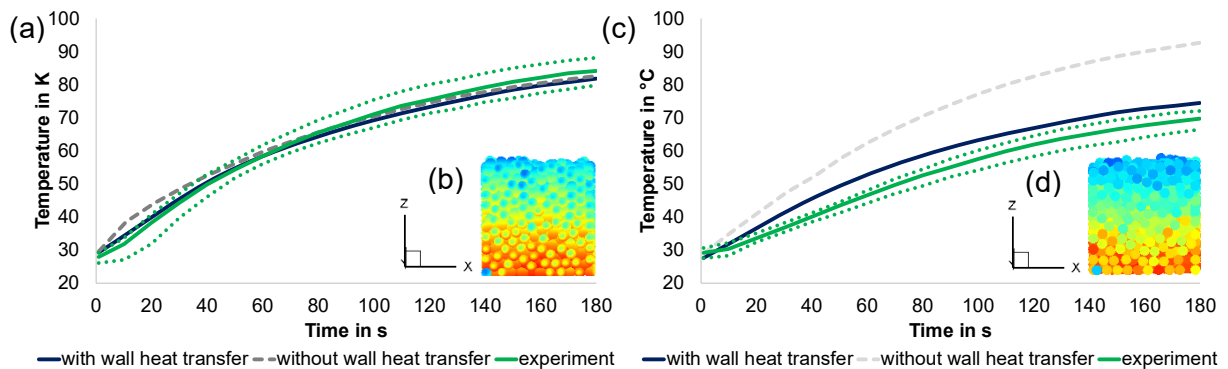


Figure 11: Comparison of the average temperature evolution of the visible particles behind the aluminum oxide glass (see (b) and (d)) between CFD/DEM simulations and experiments for the material POM (a) and aluminum (c). Experimental values are averaged over 10 measurements. Dotted curves represent the minimum and maximum experimental values.

The experimental curve is averaged over 10 measurements to be representative. In addition to that, the dotted curves represent the maximum and minimum temperature value out of these 10 measurements. For clarity, snapshots of the visible particles behind the aluminum oxide glass are shown in figs. 11b and 11d. The simulation results match the experiments well over time, differences are only noticeable for the simulation without wall heat contact model at the beginning. In contrast to that, strong deviations which increase over time occur for the simulation case without wall heat transfer model. The other simulations (with wall heat transfer model considered) slightly overpredict the experiments with increasing deviations over time until the first 60 seconds. After that time the deviations decrease, and the average temperature is close to the corresponding average experimental temperature after 180 seconds. To analyze this behavior in a detailed manner, the average temperature in dependency on the dimensionless particle height are determined in fig. 12.

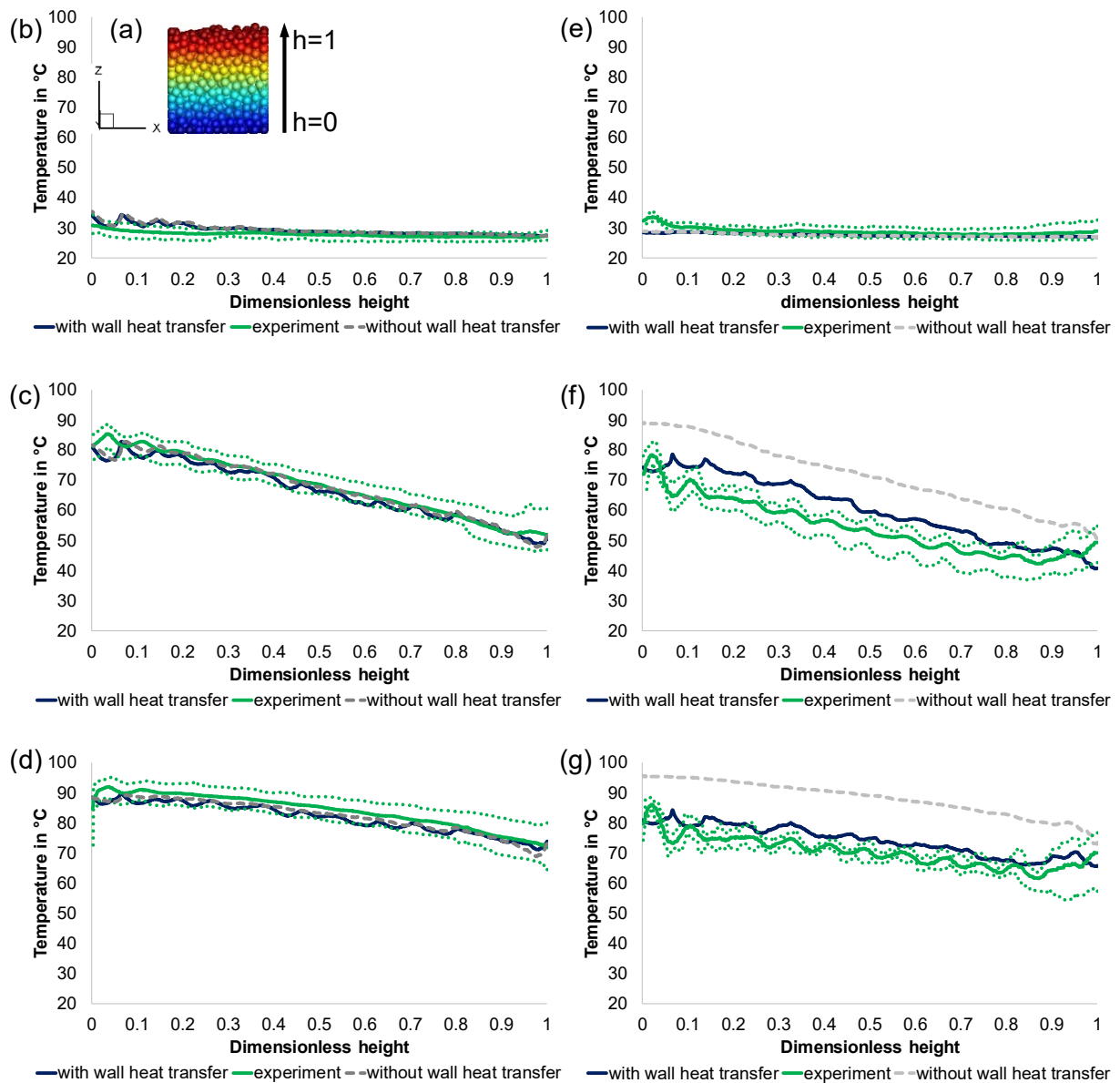


Figure 12: Temperature distribution over dimensionless height at three specific instances in time ($t = 1$ s, $t = 90$ s and $t = 180$ s) for the material POM (b-d) and aluminum (e-g). Average temperature is determined over the dimensionless height of the visible particles in z -direction (a).

The dimensionless particle height is calculated in the same way as the dimensionless length in fig. 8. For demonstration, a colored snapshot of the particle bed is shown in fig. 12a. Here the maximum z -coordinate represents a particle height of $h = 1$ whereas the minimum particle z -coordinate holds a value of $h = 0$. In this part of the investigation the three moments in time $t = 0.1$ s, $t = 90$ s and $t = 180$ s are considered, for POM in figs. 12b-d and for aluminum in figs. 12e-g. Again, differences are more pronounced for the material aluminum. At the beginning (fig. 12b) both simulation cases slightly overpredict the average temperature at the bottom of the vessel, which can be explained by simplifications with which the porous plate below the particle packing is realized in the DEM/CFD. This porous plate must be heated first (not depicted in the simulation environment) and because of this a lower fluid temperature reaches

the packing at the beginning of the investigation in the experiment. The realization of the porous plate thereby also explains the small differences in temperature of the experimental results in comparison to the simulations at the bottom of the vessel for the material aluminum. At $t = 0.1$ s the porous plate also influences the experimental results for the material aluminum where particle-wall heat transfer between the hot porous plate and particles slightly heat up the bed from the bottom. Although we reduced this influence to a minimum, the porous plate is heated up by small leakage losses and heat conduction with the side walls during the experimental initialization, see section 3. However, for later instances in time this effect is less pronounced as the temperature difference between simulation and experiment is smaller. In conclusion, no significant differences can be observed for POM whereas stronger deviations between simulation and experiments occur for the simulation without particle-wall heat conduction model when considering aluminum as material. To have a more detailed view on the whole system and not only on the visible particles behind the aluminum oxide wall, the fluid temperatures are plotted over time in fig. 13 for both simulations and experiments.

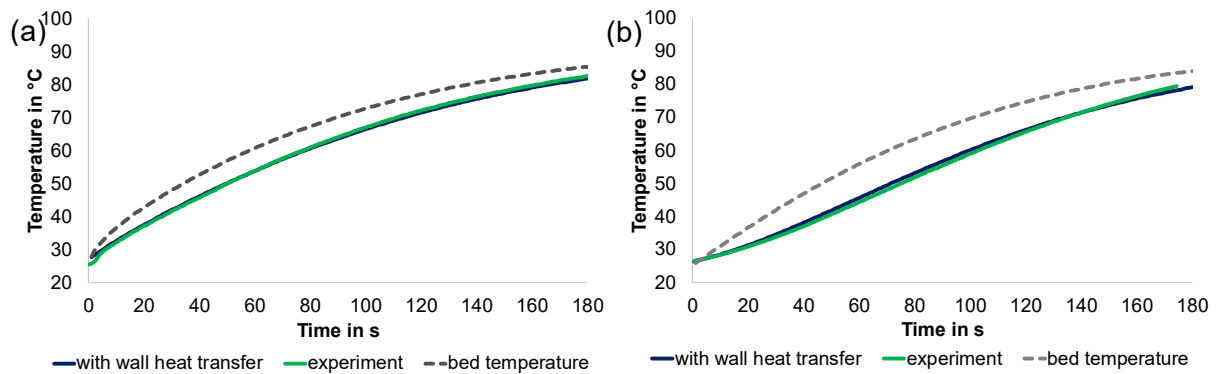


Figure 13: Evolution of the fluid temperatures above the packing for the material POM (a) and aluminum (b). Additionally, the volume averaged bed temperature over time as obtained from the simulations is plotted for both materials.

In case of the experiments a setup is considered where 9 thermocouples are positioned in one row 0.01 m above the packing to determine the average fluid temperature. For this part of our investigation only the simulation with particle-wall heat conduction model is considered. For both materials the simulation predicts the temperature development in the same manner as the experiments. Between the materials it can be summarized that the increase in fluid temperature is slower for aluminum due to a slower heating of the particle bed at the beginning of the investigation. Besides the temperature development within the chamber, the temperature distribution within the aluminum oxide wall is considered. Here only simulation results are shown due to the complexity of measuring the wall temperature in a resolved way. To compare the temperature development through the wall, all temperature values in one point along the

dimensionless length are averaged. The simulation results for three different moments in time are shown in fig. 14.

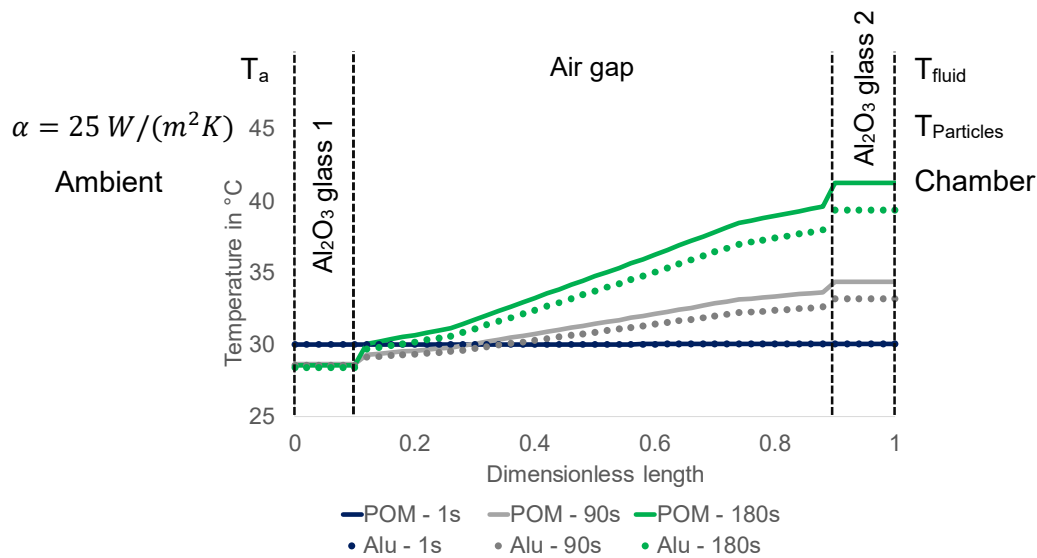


Figure 14: Temperature profile of the two aluminum glasses and the air gap in between them.

The aluminum oxide wall consists of two aluminum oxide glasses with a depth of 0.001 m and an air gap of 0.008 m in between them. The ambient temperature is given as boundary condition $T_a = 26.85 \text{ }^\circ\text{C}$ which was measured in the laboratory. To calculate the heat transfer to the ambient fluid, a literature value for the heat transfer coefficient of $\alpha = 25 \text{ W}/(\text{m}^2\text{K})$ is used [314], whose variation has no strong impact on the simulation outcome. The fluid and particle bed temperature within the chamber are represented by T_{Fluid} and $T_{Particles}$. The wall temperature has an initial temperature of $30 \text{ }^\circ\text{C}$. After one second no change in temperature can be observed. Due to lower fluid temperatures above the packed bed (compare fig. 13) the increase in temperature is higher for POM than for aluminum. The temperature field within the aluminum oxide glasses is uniform as the thermal conductivity is high with $k = 40 \text{ W}/(\text{mK})$ compared to the conductivity of air $k = 0.03162 \text{ W}/(\text{mK})$. After 90 s the first (left) aluminum oxide glass reaches a steady state temperature of $T_{AlO2_1} = T_a = 26.85 \text{ }^\circ\text{C}$. The temperature of the second (right) glass increases over time. In contrast to both glasses, the temperature distribution within the air gap is non-uniform. Here a temperature gradient influenced by the temperature of the glasses forms out. This temperature gradient shows that the use of an air gap leads to an improvement of the heat insulation.

As a last part of this investigation the impressed energy flows on the wall due to the particle-wall heat conduction and wall-fluid convection are investigated. The summed energies are plotted over time in fig. 15.

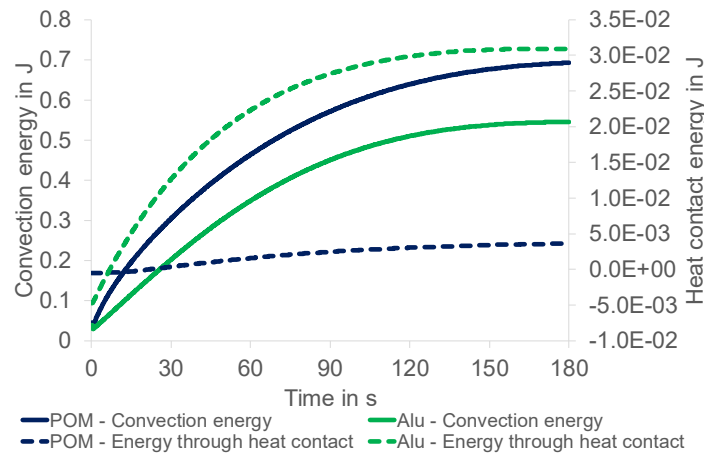


Figure 15: Comparison of transmitted energy out of particle wall contact and convection between wall and fluid over time for the materials POM and aluminum.

Again, no experiments and only the simulation with particle-wall heat conduction is considered. For both materials the energy through convection is more than ten times higher than the energy through particle wall contact. The transmitted convection energy through convection is up to 27% higher for the material POM. In case of aluminum 8.5 times higher particle-wall heat conduction energy rates are transmitted to the wall.

5. Conclusions

The CFD/DEM approach has been extended to include particle-wall heat conduction for spherical particles and to model multidimensional heat transfer within walls. Two test cases are performed to show the relevance of calculating multidimensional heat transfer within walls and to validate the implemented method. The first simulation case is a rotating drum with a constant rotation velocity where the focus is set to the heating of the wall to present a system where 3D heat transfer in walls must be accounted for. The initial temperatures are 326.85 °C for the walls and 25 °C for the particles. Here the CFD solves the heat conduction equation for the walls whereas the DEM used a constant temperature approach for the calculation of the inner particle temperature. For this part the following conclusions can be drawn from this study:

- The simulation mixing temperature of the thermal steady state fits the analytical mixing temperature.
- The heating of the front and back wall is slower compared to the inner cylinder barrel of the rotating drum.
- An evaluation of the wall surface temperatures over time shows an asymmetric temperature distribution within the rotating drum at the beginning which is based on the initial particle height. This effect can be minimized if intended by averaging the simulation results over several simulations with randomly generated packings or by predefining an equal bed height. However, the intentionally given result underlines that the

CFD/DEM framework is able to capture such initial effects in the outcome of a simulation.

- By averaging all radial temperatures in y- and z-direction for one x-coordinate to one value, the temperature distribution within the rotating drum becomes more and more symmetric as the point of the minimum temperature shifts to the center of the geometry.
- The temperature difference between the maximum and minimum value firstly increases from zero at the beginning up to a maximum value of $\Delta T \approx 37.51 \text{ }^\circ\text{C}$ at $t = 5 \text{ s}$ and reaches nearly $\Delta T \approx 0.37 \text{ }^\circ\text{C}$ after $t = 100 \text{ s}$.

In the second part of our investigation we validate the extended CFD/DEM framework through a comparison with experimental results. Here a packed bed consisting of 1461 particles with an initial temperature of $25 \text{ }^\circ\text{C}$ is passed by $100 \text{ }^\circ\text{C}$ heated air from the bottom. Here the novel simulation approach considering particle-wall heat conduction is taken to describe one dimensional heat loss through the wall. In opposite to the first case study, we use a 3D heat transfer model for the calculation of the temperature within the particles. Aluminum and POM, two different materials regarding the thermal behavior, are used. The aim of this part of our investigation is to improve the simulation framework of a previous study by considering particle-wall heat conduction. Therefore, the simulations with and without particle-wall heat transfer are compared against experimental results. In this context the major issues are:

- Both numerical results are in a good agreement with the experimental results for the material POM.
- By comparing the average temperatures of the visible particles, the simulation without particle wall heat conduction shows stronger deviations which increase over time to the experiments. Here the effect of the particle-wall heat transfer is more pronounced due to the higher thermal conductivity of aluminum.
- By comparing the average temperatures of the visible particles behind the aluminum oxide glass the model with particle-wall heat transfer slightly overpredicts the experimental results for aluminum whereas the material POM shows no differences in temperature for the novel method.
- In opposite to that the average fluid temperature directly above the particle packing shows no differences between simulations with particle-wall heat conduction model and experiments for both materials.

The obtained results are restricted to spherical shaped particles. The current state of the heat transfer modelling in the CFD/DEM requires further investigations and model advances. As a first step in that direction Gan et al. [324] performed CFD/DEM simulations of ellipsoidal particles for the determination of the ETC in packed beds. Especially, the heat transfer mechanisms

for non-spherical particles due to contact or and convection between particle and fluid are so far not well understood. For the future the CFD/DEM framework must be extended to consider such phenomena by new models which are required to be validated with experiments. Besides this the new presented model could be also an essential tool for describing fluidized beds with chemical particle reactions, liquids or spray granulation where a resolved temperature model is needed.

Acknowledgements

Financial support by the DFG - KR 3446/6-1 is greatly acknowledged. The support of Saint Gobain Crystals for providing us the aluminum oxide samples is gratefully appreciated. The original form of the DEM-code "DEM-Calc" applied is based on a development of LEAT, Ruhr-Universität Bochum, Germany. The code "DEM-Calc" has then been continuously extended both at Ruhr-Universität Bochum and Technische Universität Berlin, Germany. We thank all who have contributed.

7. Conclusions and Perspective

In the field of energy technology, thermal and mechanical process engineering, a numerical description of the mechanical and thermal behavior of particulate systems is often an essential part for the improvement, operation or design of industrial applications. Typical industrial systems involving particulate granular material are packed beds, fluidized beds, pneumatic conveying systems or drying of particulate solids which is often performed by rotating drums. Many investigations assume spherical shaped particles although real particles are often non-spherical. Especially when sphericity (ratio of surface area of a perfect sphere to the surface area of the particle) and the aspect ratio differ strongly between the spherical assumption and the real particle shape, the geometric shape has a strong influence on the thermal and mechanical behavior [53,324]. This is even more pronounced in systems where particles are passed through, fluidized or entrained by a fluid as the drag force, often dominating in these systems, becomes particle orientation dependent whereas models for spherical particles are orientation independent. For such particle-fluid systems, different detailed modelling approaches can be found in literature. Most commonly used modelling approaches are the resolved and unresolved method, a combination of the continuum approach for the fluid side and the discrete approach which describes the particle motion [3]. However, real systems normally consist of large domains, which makes the resolved method impracticable due to the high number of cells (high computational effort). Therefore, particle-fluid systems are mostly calculated on cells larger than the largest particle by the unresolved method. A modern variant of a DPM is the Discrete Element Method (DEM) which solves the translational and rotational motion of each individual particle and allows to consider non-spherical shaped particles as well as different heat transfer models. In addition to that, the DEM can be coupled with continuum approaches like the Computational Fluid Dynamics (CFD) or equivalent approaches like the Lattice Boltzmann method (LBM). However, DEM investigations are mostly concentrated on spherical shaped particles without heat transfer (see fig. 3). If heat transfer is considered than often only for particles where the temperature distribution within the particle can be assumed as uniform. Because of this, the scope of this cumulative dissertation is to extend the DEM by several models to consider particle-fluid interaction for non-spherical particles and a more general heat transfer formulation which is also valid for an uneven temperature distribution inside a particle. As a model framework the CFD-DEM approach is used with an in-house DEM code and the commercial CFD package ANSYS Fluent.

This dissertation contains seven publications which can be classified in the four simulation areas

1. spherical particles without heat transfer (investigation I)
2. non-spherical particles without heat transfer (investigations II-IV)

3. spherical particles with heat transfer (investigations V-VII)
4. non-spherical particles with heat transfer (investigation V)

The first publication considers no heat transfer equations and in case of the DEM the simpler spherical shape. In this study the third body behavior in wet and dry environments is simulated with the coupled CFD-DEM approach which is extended by a buoyancy as well as a lubrication model. To investigate the system behavior several parameters such as shear velocity, fluid viscosity and orientation of gravity are altered. The third body behavior is mostly influenced by the shear rate, gravity in connection with buoyancy force and sliding friction whereas a variation of the fluid viscosity shows only a marginal effect. Although this investigation focusses on the lubrication and buoyancy force, this work generally shows the application of the mechanical particle-fluid force interaction methods for spherical particles. An accurate description of the mechanical particle-fluid interaction force is essential for all heat transfer studies where the superficial velocity is higher than the minimal fluidization velocity (particles start to move). All remaining studies without heat transfer concentrate mainly on the investigation of non-spherical particles.

Investigation II considers the mechanical mixing analyzed by the Lacey mixing index [148] of non-spherical particles in a model type fluidized bed. Here the CFD-DEM approach is extended by a new particle-fluid interaction force approach and a porosity calculation method to account for non-spherical specific particle properties such as orientation, sphericity, etc. The used particles are represented by clustered spheres as well as polyhedrons within the DEM. Several operating parameters are varied, namely gas inlet velocity, layer arrangement, particle aspect ratio, particle density, sphere quota, cluster approximation accuracy, polyhedron approximation accuracy, grid resolution and particle shape. To quantify the influence on the system behavior, the degree of mixing, the averaged particle heights and the orientation of all particles are analyzed over time for all operating parameters. In general, an increasing inlet gas velocity enhances the degree of mixing as a low velocity can lead to an incomplete mixing due to a stronger influence of the cross-sectional area on the combined particle-fluid force. The results of the layer arrangement show that horizontal mixing is stronger than vertical mixing for the used particle type (ideal cylinder, clustered by 36 spheres). In addition to that, the degree of mixing decreases for particles with low aspect ratios. An increase in particle density leads to a reduced bed expansion due to a higher particle mass which slows down the mixing. Besides this fact, particle segregation can be observed when spherical particles are mixed with non-spherical particles. If non-spherical particles hold an aspect ratio of 1, they tend to mix quicker than spherical particles as variations of the cross-sectional area resulting out of the rotational motion lead to differences in the particle/fluid-forces which enhance the degree of mixing. How-

ever, besides these results this investigation also demonstrates that the accuracy of the approximation method has a strong influence on the mechanical mixing behavior. For both approximation methods (multi-sphere and polyhedron), a variation of the representation accuracy results in different particle weights, crosswise-surface areas, sphericities and inertia tensors which influence the degree of mixing. In case of multi spheres, an increased approximation accuracy impairs mixing whereas mixing is enhanced due to a reduced blockiness for accurately approximated polyhedrons. A variation of the different particle-fluid interaction force models indicates that the mixing between two recently described model frameworks [44] which consider the influence of crosswise particle area on the particle-fluid interaction force is less affected in contrast to model frameworks like [42] without orientation dependent component. A variation in grid accuracy and particle shape (cubes, plates with different aspect ratios) are both attributed to different mixing behaviors. In addition to the main findings of investigation II, two regions, one close to the walls and the other in the interior of the bed, can be observed for the model type fluidized bed. In some cases, the outer wall region influences the overall distribution of orientation angles over time of the particles. In the wall region, particles tend to align in their preferred orientation parallel to the walls of the vessel. In contrast to that, the orientation angles of the particles in the interior region is more distributed. The influence of the wall region on the overall orientation angle distribution can be reduced by elevating the gas velocity and by decreasing sharpness/increasing roundness of the particles. However, for further investigations the CFD-DEM model framework for non-spherical particles should be compared with experimental results to provide a more detailed model validation. Here it should be proofed to which extent CFD-DEM simulation can describe real particle/fluid systems with non-spherical particles. In investigation III the same model type fluidized bed and CFD-DEM approach are used to describe the influences of different shaped non-spherical particles on mixing. In addition to that, the developed CFD-DEM is taken to investigate the mixing behavior of the same particle types during pneumatic conveying. To quantify the differences in the mixing behavior of all considered particle shapes, mixing is investigated qualitatively by snapshots at different moments in time and quantitative by using the Lacey-index. Both numerical setups show that the mixing is strongly influenced by the particle shape. This underlines the importance for using non-spherical particles to describe industrial applications with non-spherical particles. Again, as summarized in study II, the numerical model framework should be compared with experimental results to quantify how precise the CFD-DEM approach predicts the system behavior of non-spherical particles. In investigation IV the CFD-DEM approach is used to simulate a pneumatic conveying system consisting of a horizontal, a vertical pipe and a connecting 90° pipe bend. The numerical setup is based on the work of Chu and Yu [228] who used spherical particles. To investigate the influence of the particle shape on the system behavior, volume equivalent cubes, pyramids, plates and icosahedrons are compared to corresponding spheres.

The numerical results for spheres match the results from the work of Chu and Yu [228]. In addition to that, the CFD-DEM results are validated with empirical models for the bend exit velocities for non-spherical and spherical particles and with the overall pressure drops for spheres. In all performed simulations a rope initiated with the first particle-wall contact forms out. The location of this first particle-wall contact strongly depends on the average particle velocity which is influenced by the particle shape. Furthermore, results show that different particle shapes lead to huge differences in rope structure (length and width), bend exit velocities, particle-particle interaction and particle-wall interaction rates. If simulations assume a spherical shape and the real particle shape is non-spherical, differences in calculated simulation and real particle-particle and particle-wall interactions can be observed. Further studies should investigate if different interactions, result in a different erosion behavior which may lead to significant errors for the design of an industrial application (e.g. deviations in expected lifetime or capacity). In addition to that, experimental setups could be used to figure out how precise the erosion behavior can be described by the CFD-DEM approach. Based on combined experiments and CFD-DEM simulations simpler models can be derived to obtain key features of the fluid, particles and walls. As the CFD-DEM is often too time consuming for the description of systems with many particles, simple models could be used to design and improve such industrial applications.

As described previously, many investigations in literature assume a uniform temperature distribution within the particle but systems with large particle diameters, low particle thermal conductivities or high Biot-numbers often result in a non-uniform temperature profile inside a particle. To close this gap, the DEM is extended by an implicit 3D heat transfer model derived in spherical coordinates for spherical and in a Cartesian formulation for non-spherical particle shapes. As no general analytical solution for the heat transfer equation exists [74] and adequate experimental results are rare, the modelling approach is detailedly compared in parts against the Finite Volume Method (FVM) through the commercial package ANSYS Fluent. With this heat transfer formulation, the following boundary conditions are accounted for: heat transfer by conduction which can be separated in particle-particle contact and particle-fluid-particle contact / non-contact heat transfer, particle-particle radiation heat transfer and particle-fluid heat transfer by convection. Finally, three different simulation cases are performed to demonstrate the advantages of the derived 3D resolved heat transfer model for multi particle systems. In all considered setups, the DEM describes the thermal behavior similarly well as the FVM. Especially the last simulation case where the heat transfer in a packed bed with particle-particle heat conduction is investigated shows noticeable differences between the new 3D heat transfer model and the often-used uniform temperature model. To validate this model approach and to consider particle-fluid systems, the previously described CFD-DEM approach is extended by this resolved 3D heat transfer model and compared with own performed experiments

in a packed bed (investigation VI). To guarantee a more realistic convection heat transfer on the particle surface, a distribution function is used to account for variations of the local heat transfer coefficient on the particle surface. In this study three particle materials, namely wood, aluminum and polyoxymethylene (POM) with different thermal properties are chosen. In addition to the CFD-DEM simulations, a CFD simulation without DEM is performed to quantify the heat loss through the installed aluminum oxide wall and compared against experimental temperature measurements at different locations on the wall. The CFD-DEM results fit the experimental results for the core temperatures of three particles located on three different heights in the middle of the packed bed where the influence of the wall is minimized. In contrast to that, the surface temperatures of the visible particles behind the aluminum oxide wall show noticeable differences between simulation and experiment, especially when aluminum particles with high thermal conductivities are used. Here the heat loss through the wall must be considered. The CFD simulation results additionally underline that a resolved wall model is necessary for the calculation of the heat transfer to reduce the deviation when an aluminum oxide wall is used. Therefore, investigation VII provides a novel method for the calculation of particle-wall heat transfer and for modelling multidimensional heat transfer within walls. Again, the CFD-DEM approach is taken where the DEM calculates the particle-wall heat transfer by conduction and the CFD the wall-fluid convection as well as the intra wall heat transfer. Two test cases are performed, involving a rotating drum without convection and the packed bed system of investigation VI. The rotating drum case is chosen to present a system where an in time and space resolved intra wall heat transfer model becomes necessary to describe the system behavior well. Here the CFD-DEM results fit the analytical solution of the mixing temperature and show a varying temperature profile in space and time. In the second part of this investigation the usage of the novel method reduces the deviations (determined in investigation VI; without particle-wall model) between simulation and experiments by comparing the average surface temperatures of the visible particles behind the aluminum oxide wall for all materials. In addition to that, a good match between novel method and experiments is achieved for the average fluid temperatures directly above the packing. However, a detailed comparison of the surface temperatures without any averaging shows local deviations between experiment and simulation. These observable differences are probably based on inaccuracies in the fluid-wall heat transfer due to convection as no particle bed influence is considered for the calculation of that heat flux. In further investigations models should be derived and implemented in the CFD-DEM approach to proof this.

Based on the main findings of this dissertation, the CFD-DEM approach should be extended to consider non-spherical particles with heat transfer in presence of a fluid. Here different suggestions for future research can be given. To consider the resolved heat transfer within a non-

spherical particle the Cartesian formulation could be used as shown in investigation V. Alternatively, special representation forms like the heat equation in cylindrical or elliptical coordinates are a possible option for describing intra particle heat transfer very precisely without any correction of the particle surface. However, all equations used in this dissertation for the description of the heat transfer by contact conduction assume the contact area as circular flat. In a newer work Gan et al. [324] presented an extension of the particle-particle heat transfer by contact models to describe ellipsoidal particles. Nevertheless, this extended approach is only valid for ellipsoidal particles and it is unclear if these equations can be taken for arbitrary shaped contact areas. In contrast to that a combination of the multi-sphere approach and the three-dimensional heat equation in spherical coordinates for every single clumped sphere would allow the usage of the presented equations for the heat transfer by contact conduction as all contact areas are obtaining the same geometric shape as a single sphere. The drawback of this solution is that all heat transfer nodes of all single clumped particles must be connected to each other to guarantee a simultaneously calculation of every node temperature of the next time step. Here the challenge is to describe the overlapping areas between the respective spheres of the multi-sphere to avoid node doublings. In addition to the heat transfer by conduction, the CFD-DEM approach should be extended to consider particle-fluid heat transfer by convection for non-spherical particles. From the authors point of view, no CFD-DEM investigations exist which provide a general solution of convection heat transfer for non-spherical particles with the influence of the surrounding particles. As presented in investigation V, radiation heat transfer between two particles can be described by using view factors [321]. To be flexible in its application and therefore to provide a suitable solution for the calculation of the view factors between two non-spherical particles, the Ray tracing method [322] could be used. Further investigations should figure out if the DEM framework can be extended by the Ray tracing method without being too CPU-intensive.

To extend the CFD-DEM framework to industrial applications consisting of many particles, up-scaling methods such as the coarse-graining method [3] can be used which may significantly reduce the computational effort. Within the coarse graining method, a set of particles (fine scale particles) is represented by one coarse grained particle (CGP) [333]. To save computational effort the DEM solves only all relevant equations for the CGP. Here all relevant DEM equations are adjusted by different coefficients to model a relationship between the fine particles and the CGPs. Several authors extended their DEM framework by different coarse graining models to represent particle-fluid systems (fluidized beds) [333,334] and showed that the coarse-graining method is able to describe the macroscopic flow behavior such as the pressure drop or bed heights well for low coarse graining ratios s (e.g. $s = 2$ or $s = 3$). The coarse grain ratio $s = d^c/d^f$ describes the ratio of the diameters of one CGP particle d^c and fine particle d^f so that if that ratio is high than many particles are described by one CGP. In a newer

study Lu et al. [335] provide a coarse graining model approach for describing heat transfer in fluidized beds which could be easily adapted to the used CFD-DEM approach of this dissertation. However, from the authors view coarse graining simulations only consider spherical shaped particles and when heat transfer is considered, only a constant temperature profile within a particle. Future investigations should figure out if the coarse graining method can be adapted to non-spherical particle shapes and all heat transfer mechanism including intra resolved heat conduction to extend the CFD-DEM approach for the simulation of industrial applications consisting of many particles.

References

- [1] Shulman, A., Cleverstam, E., Mattisson, T., Lyngfelt, A.: Chemical – Looping with oxygen uncoupling using Mn / Mg - based oxygen carriers – Oxygen release and reactivity with methane. *Fuel* 90, 941–950 (2011)
- [2] Kruggel-Emden, H.: Mischung/Segregation und Wärmeübertragung in fluidisierten Systemen der Energietechnik: Ein Beitrag zur Weiterentwicklung der gekoppelten CFD-Diskreten Elemente Methode für polydisperse Systeme komplexer Partikelgeometrie. DFG Proposal, Ruhr-University Bochum, Bochum (2012)
- [3] Ge, W., Wang, L., Xu, J., Chen, F., Zhou, G., Lu, L., Chang, Q., Li, J.: Discrete simulation of granular and particle-fluid flows: From fundamental study to engineering application. *Rev. Chem. Eng.* 33, 551–623 (2017)
- [4] Bechtel, S.E., Lowe, R.L.: *Fundamentals of Continuum Mechanics*. Academic Press, San Diego (2014)
- [5] Zhu, H.P., Wu, Y.H., Yu, a. B.: Discrete and continuum modelling of granular flow. *China Particuology* 3, 354–363 (2005)
- [6] Zhu, H.P., Zhou, Z.Y., Hou, Q.F., Yu, A.B.: Linking discrete particle simulation to continuum process modelling for granular matter: Theory and application. *Particuology* 9, 342–357 (2011)
- [7] Cundall, P.A., Strack, O.D.L.: A discrete numerical model for granular assemblies. *Géotechnique* 29, 47–65 (1979)
- [8] Zhu, H.P., Zhou, Z.Y., Yang, R.Y., Yu, A.B.: Discrete particle simulation of particulate systems: Theoretical developments. *Chem. Eng. Sci.* 62, 3378–3396 (2007)
- [9] Mahecha-Botero, A., Grace, J.R., Elnashaie, S.S.E.H., Lim, C.J.: Advances in modeling of fluidized-bed catalytic reactors: A comprehensive review. *Chem. Eng. Commun.* 196, 1375–1405 (2009)
- [10] van der Hoef, M.A., van Sint Annaland, M., Kuipers, J.A.M.: Computational fluid dynamics for dense gas-solid fluidized beds: a multi-scale modeling strategy. *China Particuology* 3, 69–77 (2005)
- [11] Hilton, J.E., Cleary, P.W.: The influence of particle shape on flow modes in pneumatic conveying. *Chem. Eng. Sci.* 66, 231–240 (2011)
- [12] Munjiza, A., Latham, J.P., John, N.W.M.: 3D dynamics of discrete element systems comprising irregular discrete elements-Integration solution for finite rotations in 3D. *Int. J. Numer. Methods Eng.* 56, 35–55 (2003)
- [13] Hertz, H.: Über die Berührung fester elastischer Körper. *J. Für Die Reine Und Angew. Math.* 92, 156–171 (1881)
- [14] Di Renzo, A., Di Maio, F.P.: An improved integral non-linear model for the contact of particles in distinct element simulations. *Chem. Eng. Sci.* 60, 1303–1312 (2005)
- [15] Tsuji, Y., Tanaka, T., Ishida, T.: Lagrangian numerical simulation of plug flow of cohesionless particles in a horizontal pipe. *Powder Technol.* 71, 239–250 (1992)
- [16] Walton, O.R.: Numerical Simulation of Inclined Chute Flows of Monodisperse, Inelastic, Frictional Spheres. *Mech. Mater.* 16, 239–247 (1993)
- [17] Walton, O.R., Braun, R.L.: Viscosity, granular-temperature, and stress calculations for shearing assemblies of inelastic, frictional disks. *J. Rheol. (N. Y. N. Y.)* 30, 949–980 (1986)
- [18] Zhou Y.C.: Rolling friction in the dynamic simulation of sandpile formation. *Phys. A Stat. Mech. Its Appl.* 269, Pages 536–553 (1999)
- [19] Iwashita, K., Oda, M.: Micro-deformation mechanism of shear banding process based on modified distinct element method. *Powder Technol.* 109, 192–205 (2000)
- [20] Iwashita, K., Oda, M.: Rolling Resistance at Contacts in Simulation of Shear Band Development by DEM. *J. Eng. Mech.* 124, 285–292 (1998)

- [21] Zhu, H.P., Yu, A.B.: Averaging method of granular materials. *Phys. Rev. E - Stat. Nonlinear, Soft Matter Phys.* 66, 1–10 (2002)
- [22] Kruggel-Emden, H.: Analysis and Improvement of the Time-Driven Discrete Element Method. Dissertation, Ruhr-University Bochum, Bochum (2007)
- [23] Kruggel-Emden, H., Simsek, E., Rickelt, S., Wirtz, S., Scherer, V.: Review and extension of normal force models for the Discrete Element Method. *Powder Technol.* 171, 157–173 (2007)
- [24] Mindlin, R.D., Deresiewicz, H.: Elastic Spheres in Contact Under Varying Oblique Forces. *J. Appl. Mech.* 327–344 (1953)
- [25] Kruggel-Emden, H., Wirtz, S., Scherer, V.: A study on tangential force laws applicable to the discrete element method (DEM) for materials with viscoelastic or plastic behavior. *Chem. Eng. Sci.* 63, 1523–1541 (2008)
- [26] Schäfer, J., Dippel, S., Wolf, D.E.: Force schemes in simulations of granular materials. *J. Phys. I Fr.* 6, 5–20 (1996)
- [27] Van Zeebroeck, M., Tijssens, E., Van Liedekerke, P., Deli, V., De Baerdemaeker, J., Ramon, H.: Determination of the dynamical behaviour of biological materials during impact using a pendulum device. *J. Sound Vib.* 266, 465–480 (2003)
- [28] Zhang, D., Whiten, W.J.: The calculation of contact forces between particles using spring and damping models. *Powder Technol.* 88, 59–64 (1996)
- [29] Dintwa, E., Van Zeebroeck, M., Tijssens, E., Ramon, H.: Determination of parameters of a tangential contact force model for viscoelastic spheroids (fruits) using a rheometer device. *Biosyst. Eng.* 91, 321–327 (2005)
- [30] Gorham, D. a., Kharaz, a. H.: The measurement of particle rebound characteristics. *Powder Technol.* 112, 193–202 (2000)
- [31] Kruggel-Emden, H., Stepanek, F., Munjiza, A.: Particuology A study on adjusted contact force laws for accelerated large scale discrete element simulations. *Particuology* 8, 161–175 (2010)
- [32] Coetzee, C.J.: Review: Calibration of the discrete element method. *Powder Technol.* 310, 104–142 (2017)
- [33] Marigo, M., Stitt, E.H.: Discrete element method (DEM) for industrial applications: Comments on calibration and validation for the modelling of cylindrical pellets. *KONA Powder Part. J.* 32, 236–252 (2015)
- [34] Sudbrock, F., Simsek, E., Rickelt, S., Wirtz, S., Scherer, V.: Discrete element analysis of experiments on mixing and stoking of monodisperse spheres on a grate. *Powder Technol.* 208, 111–120 (2011)
- [35] Elskamp, F., Kruggel-Emden, H., Hennig, M., Teipel, U.: A strategy to determine DEM parameters for spherical and non-spherical particles. *Granul. Matter* 19, 1–13 (2017)
- [36] Li, Y., Xu, Y., Thornton, C.: A comparison of discrete element simulations and experiments for “sandpiles” composed of spherical particles. *Powder Technol.* 160, 219–228 (2005)
- [37] Alonso-Marroquín, F., Ramírez-Gómez, Á., González-Montellano, C., Balaam, N., Hanaor, D.A.H., Flores-Johnson, E.A., Gan, Y., Chen, S., Shen, L.: Experimental and numerical determination of mechanical properties of polygonal wood particles and their flow analysis in silos. *Granul. Matter* 15, 811–826 (2013)
- [38] Ergun, S.: Fluid Flow through packed columns. *Chem. Eng. Prog.* 48, 89–94 (1952)
- [39] Wen, C.Y., Yu, Y.H.: Mechanics of fluidization. *A.I.Ch.E.* 62, 100–111 (1966)
- [40] Hilton, J.E., Mason, L.R., Cleary, P.W.: Dynamics of gas–solid fluidised beds with non-spherical particle geometry. *Chem. Eng. Sci.* 65, 1584–1596 (2010)
- [41] Shimizu, Y.: Three-dimensional simulation using fixed coarse-grid thermal-fluid scheme and conduction heat transfer scheme in distinct element method. *Powder Technol.* 165, 140–152 (2006)

- [42] Di Felice, R.: The voidage function for fluid-particle interaction systems. *Int. J. Multiph. Flow* 20, 153–159 (1994)
- [43] Hold, J.: Charakterisierung der Mischungs- und Segregationsvorgänge in Modellwirbelschichten mit mono- und bidispersen sphärischen Partikelsystemen: Experimente und gekoppelte CFD / DEM-Modellierung. Dissertation, Ruhr-University Bochum, Bochum (2013)
- [44] Rong, L.W., Dong, K.J., Yu, A.B.: Lattice-Boltzmann simulation of fluid flow through packed beds of uniform spheres: Effect of porosity. 99, 44–58 (2013)
- [45] Tomac, I., Gutierrez, M.: Discrete element modeling of non-linear submerged particle collisions. *Granul. Matter* 15, 759–769 (2013)
- [46] Tomac, I., Gutierrez, M.: Fluid lubrication effects on particle flow and transport in a channel. *Int. J. Multiph. Flow* 65, 143–156 (2014)
- [47] Shan, T., Zhao, J.: A coupled CFD-DEM analysis of granular flow impacting on a water reservoir. *Acta Mech.* 225, 2449–2470 (2014)
- [48] Hölzer, A., Sommerfeld, M.: New simple correlation formula for the drag coefficient of non-spherical particles. *Powder Technol.* 184, 361–365 (2008)
- [49] Johnson, S.M., Williams, J.R., Cook, B.K.: Quaternion-based rigid body rotation integration algorithms for use in particle methods. 1303–1313 (2008)
- [50] Nitschke, M., Knickmeyer, E.H.: Rotation Parameters - A survey of techniques. *J. Surv. Eng.* 126, 83–105 (2000)
- [51] Zhong, W., Yu, A., Liu, X., Tong, Z., Zhang, H.: DEM/CFD-DEM Modelling of Non-spherical Particulate Systems: Theoretical Developments and Applications. *Powder Technol.* 302, 108–152 (2016)
- [52] Lu, G., Third, J.R., Müller, C.R.: Discrete element models for non-spherical particle systems: From theoretical developments to applications. *Chem. Eng. Sci.* 127, 425–465 (2015)
- [53] Höhner, D.: Experimentelle und numerische Untersuchungen zum Einfluss von Partikelgeometrie auf das mechanische Verhalten von Schüttgütern mit Hilfe der Diskreten Elemente Methode. Dissertation, Ruhr-University Bochum (2014)
- [54] Kruggel-Emden, H., Rickelt, S., Wirtz, S., Scherer, V.: A study on the validity of the multi-sphere Discrete Element Method. *Powder Technol.* 188, 153–165 (2008)
- [55] Höhner, D., Wirtz, S., Kruggel-Emden, H., Scherer, V.: Comparison of the multi-sphere and polyhedral approach to simulate non-spherical particles within the discrete element method: Influence on temporal force evolution for multiple contacts. *Powder Technol.* 208, 643–656 (2011)
- [56] Barr, A.H.: Superquadrics and Angle-Preserving Transformations. *IEEE Comput. Graph. Appl.* 1, 11–23 (1981)
- [57] Fraige, F.Y., Langston, P.A., Matchett, A.J., Dodds, J.: Vibration induced flow in hoppers: DEM 2D polygon model. *Particuology* 6, 455–466 (2008)
- [58] Wang, J., Yu, H.S., Langston, P., Fraige, F.: Particle shape effects in discrete element modelling of cohesive angular particles. *Granul. Matter* 13, 1–12 (2011)
- [59] Lu, G., Third, J.R., Müller, C.R.: Critical assessment of two approaches for evaluating contacts between super-quadric shaped particles in DEM simulations. *Chem. Eng. Sci.* 78, 226–235 (2012)
- [60] Hogue, C.: Shape representation and contact detection for discrete element simulations of arbitrary geometries. *Eng. Comput.* 15, 374–390 (1998)
- [61] Ting, J.M.: A robust algorithm for ellipse-based discrete element modelling of granular materials. *Comput. Geotech.* 13, 175–186 (1992)
- [62] Lin, X., Ng, T. -T.: Contact detection algorithms for three-dimensional ellipsoids in discrete element modelling. *Int. J. Numer. Anal. Methods Geomech.* 19, 653–659 (1995)
- [63] Ng, T.-T., Lin, X.: A three-dimensional discrete element model using arrays of

- ellipsoids. *Géotechnique* 47, 319–329 (1997)
- [64] Fraige, F.Y., Langston, P.A., Chen, G.Z.: Distinct element modelling of cubic particle packing and flow. 186, 224–240 (2008)
- [65] Cundall, P.A.: Formulation of a three-dimensional distinct element model-Part I. A scheme to detect and represent contacts in a system composed of many polyhedral blocks. *Int. J. Rock Mech. Min. Sci.* 25, 107–116 (1988)
- [66] Nezami, E.G., Hashash, Y.M.A., Zhao, D., Ghaboussi, J.: A fast contact detection algorithm for 3-D discrete element method. *Comput. Geotech.* 31, 575–587 (2004)
- [67] Nezami, E.G., Hashash, Y.M.A., Zhao, D., Ghaboussi, J.: Shortest link method for contact detection in discrete element method. *Int. J. Numer. Anal. Methods Geomech.* 30, 783–801 (2006)
- [68] Incropera, F., Lavine, A., DeWitt, D.: *Fundamentals of heat and mass transfer*. John Wiley & Sons, Hoboken (2011)
- [69] Murakami, T., Xu, G., Suda, T., Matsuzawa, Y., Tani, H., Fujimori, T.: Some process fundamentals of biomass gasification in dual fluidized bed. *Fuel* 86, 244–255 (2007)
- [70] Zhou, Z.Y., Yu, A.B., Zulli, P.: Particle scale study of heat transfer in packed and bubbling fluidized beds. *AIChE J.* 55, 868–884 (2009)
- [71] Rhodes, M.: *Introduction to Particle Technology*. John Wiley & Sons Ltd, Chichester (2008)
- [72] Chen, J.C., Grace, J.R., Golriz, M.R.: Heat transfer in fluidized beds: design methods. *Powder Technol.* 150, 123–132 (2005)
- [73] Collier, A.R., Hayhurst, A.N., Richardson, J.L., Scott, S.A.: The heat transfer coefficient between a particle and a bed (packed or fluidised) of much larger particles. *Chem. Eng. Sci.* 59, 4613–4620 (2004)
- [74] Brosch, B.: *Erweiterung der Diskreten Elemente Methode zur Simulation bewegter und reagierender Feststoffschüttungen mit der Anwendung auf Rostfeuerungs-systeme*. Dissertation, Ruhr-University Bochum, Bochum (2012)
- [75] Wiese, J.: *DEM/CFD-Simulation und experimentelle Untersuchungen von Holzpelletfeuerungen*. Dissertation, Ruhr-University Bochum (2015)
- [76] Ozisik, N.: *Finite difference methods in heat transfer*. CRC Press, Boca Raton (1994)
- [77] Laurien, E., Jr., H.O.: *Numerische Strömungsmechanik*. 4th ed. Vieweg+Teubner Verlag, Wiesbaden (2011)
- [78] Meister, A.: *Numerik linearer Gleichungssysteme*. 3rd ed. Vieweg & Sohn Verlag, Wiesbaden (2015)
- [79] Press, W.H., Teukolsky, S.A., Vetterling, W.T., Flannery, B.P.: *Numerical recipes in Fortran 77*. Cambridge University Press, New York (1992)
- [80] van der Vorst, H.A.: Bi-CGSTAB: A Fast and Smoothly Converging Variant of Bi-CG for the Solution of Nonsymmetric Linear Systems. *SIAM J. Sci. Stat. Comput.* 13, 631–644 (1992)
- [81] Vollmari, K., Kruggel-Emden, H.: Numerical and experimental analysis of particle residence times in a continuously operated dual-chamber fluidized bed. *Powder Technol.* 338, 625–637 (2018)
- [82] ANSYS Inc.: *ANSYS Fluent Theory Guide*. Release 17.2, Canonsburg (2016)
- [83] Rigney, D.A., Karthikeyan, S.: The evolution of tribomaterial during sliding: A brief introduction. *Tribol. Lett.* 39, 3–7 (2010)
- [84] Wimmer, M.A., Loos, J., Nassutt, R., Heitkemper, M., Fischer, A.: The acting wear mechanisms on metal-on-metal hip joint bearings: In vitro results. *Wear* 250, 129–139 (2001)
- [85] Wimmer, M.A., Sprecher, C., Hauert, R., Täger, G., Fischer, A.: Tribochemical reaction on metal-on-metal hip joint bearings. *Wear* 255, 1007–1014 (2003)
- [86] Büscher, R., Täger, G., Dudzinski, W., Gleising, B., Wimmer, M.A., Fischer, A.:

- Subsurface microstructure of metal-on-metal hip joints and its relationship to wear particle generation. *J. Biomed. Mater. Res. - Part B Appl. Biomater.* 72, 206–214 (2005)
- [87] Wimmer, M.A., Fischer, A., Büscher, R., Pourzal, R., Sprecher, C., Hauert, R., Jacobs, J.J.: Wear mechanisms in metal-on-metal bearings: The importance of tribochemical reaction layers. *J. Orthop. Res.* 28, 436–443 (2010)
- [88] Liao, Y., Pourzal, R., Wimmer, M. a., Jacobs, J.J., Fischer, A., Marks, L.D.: Graphitic Tribological Layers in Metal-on-Metal Hip Replacements. *Science* (80-.). 334, 1687–1690 (2011)
- [89] Hahn, M., Bauer, C., Theissmann, R., Gleising, B., Dudzinski, W., Fischer, A.: The impact of microstructural alterations at spray coated cylinder running surfaces of diesel engines - Findings from motor and laboratory benchmark tests. *Wear* 271, 2599–2609 (2011)
- [90] Hahn, M., Theissmann, R., Gleising, B., Dudzinski, W., Fischer, A.: Microstructural alterations within thermal spray coatings during highly loaded diesel engine tests. *Wear* 267, 916–924 (2009)
- [91] Godet, M.: Self-protection of high wear materials. *ASLE Trans.* 22, 56–64 (1979)
- [92] Godet, M.: The third-body approach: A mechanical view of wear. *Wear* 100, 437–452 (1984)
- [93] Stoyanov, P., Romero, P. a., Merz, R., Kopnarski, M., Stricker, M., Stemmer, P., Dienwiebel, M., Moseler, M.: Nanoscale sliding friction phenomena at the interface of diamond-like carbon and tungsten. *Acta Mater.* 67, 395–408 (2014)
- [94] Stoyanov, P., Stemmer, P., Järvi, T.T., Merz, R., Romero, P. a., Scherge, M., Kopnarski, M., Moseler, M., Fischer, A., Dienwiebel, M.: Friction and wear mechanisms of tungsten-carbon systems: A comparison of dry and lubricated conditions. *ACS Appl. Mater. Interfaces* 5, 6123–6135 (2013)
- [95] Zhu, H.P., Zhou, Z.Y., Yang, R.Y., Yu, A.B.: Discrete particle simulation of particulate systems : A review of major applications and findings. 63, 5728–5770 (2008)
- [96] Renouf, M., Massi, F., Fillot, N., Saulot, A.: Numerical tribology of a dry contact. *Tribol. Int.* 44, 834–844 (2011)
- [97] Cundall, P.A., Strack, O.D.L.: Discussion: A discrete numerical model for granular assemblies. *Géotechnique* 30, 331–336 (1980)
- [98] Elrod, H.G., Brewe, D.E.: Paper V (iv) Numerical Experiments with Flows of Elongated Granules. *Leeds-Lyon Symp.* 219–226 (1992)
- [99] Ghaouti, A., Chaze, M., Dubujet, P., Sidoroff, F.: Particulate and granular simulation of the third body behaviour. *Tribol. Ser.* 355–365 (1996)
- [100] Sève, B., Iordanoff, I., Berthier, Y.: A discrete solid third body model: Influence of the intergranular forces on the macroscopic behaviour. *Leeds-Lyon Symp.* 361–368 (2001)
- [101] Iordanoff, I., Seve, B., Berthier, Y.: Solid Third Body Analysis Using a Discrete Approach: Influence of Adhesion and Particle Size on Macroscopic Properties. *J. Tribol.* 124, 530–538 (2002)
- [102] Fillot, N., Iordanoff, I., Berthier, Y.: A Granular Dynamic Model for the Degradation of Material. *J. Tribol.* 126, 606 (2004)
- [103] Iordanoff, I., Fillot, N., Berthier, Y.: Numerical study of a thin layer of cohesive particles under plane shearing. *Powder Technol.* 159, 46–54 (2005)
- [104] Renouf, M., Saulot, A., Berthier, Y.: Third body flow during wheel-rail interaction. III *Eur. Conf. Comput. Mech.* 336–336 (2006)
- [105] Munjiza, A., Xiang, J., Garcia, X., Latham, J.P., D’Albano, G.G.S., John, N.W.M.: The Virtual Geoscience Workbench, VGW: Open Source tools for discontinuous systems. *Particuology* 8, 100–105 (2010)
- [106] Kabir, M.A., Lovell, M.R., Higgs, C.F.: Utilizing the explicit finite element method for studying granular flows. *Tribol. Lett.* 29, 85–94 (2008)

- [107] Tong, J., Mohammad, M.A., Zhang, J., Ma, Y., Rong, B., Chen, D., Menon, C.: DEM Numerical simulation of abrasive wear characteristics of a bioinspired ridged surface. *J. Bionic Eng.* 7, 175–181 (2010)
- [108] Ashrafizadeh, H., Ashrafizadeh, F.: A numerical 3D simulation for prediction of wear caused by solid particle impact. *Wear* 276–277, 75–84 (2012)
- [109] Jerier, J.F., Molinari, J.F.: Normal contact between rough surfaces by the Discrete Element Method. *Tribol. Int.* 47, 1–8 (2012)
- [110] Leonard, B.D., Ghosh, A., Sadeghi, F., Shinde, S., Mittelbach, M.: Third body modeling in fretting using the combined finite-discrete element method. *Int. J. Solids Struct.* 51, 1375–1389 (2014)
- [111] Leonard, B.D., Sadeghi, F., Shinde, S., Mittelbach, M.: Rough surface and damage mechanics wear modeling using the combined finite-discrete element method. *Wear* 305, 312–321 (2013)
- [112] Wang, W., Liu, Y., Zhu, G., Liu, K.: Using FEM-DEM coupling method to study three-body friction behavior. *Wear* 318, 114–123 (2014)
- [113] de Payrebrune, K.M., Kröger, M.: Kinematic analysis of particles in three-body contact. *Tribol. Int.* 81, 240–247 (2015)
- [114] Zhang, H., Tan, Y., Yang, D., Trias, F.X., Jiang, S., Sheng, Y., Oliva, A.: Numerical investigation of the location of maximum erosive wear damage in elbow: Effect of slurry velocity, bend orientation and angle of elbow. *Powder Technol.* 217, 467–476 (2012)
- [115] Gallier, S., Lemaire, E., Peters, F., Lobry, L.: Rheology of sheared suspensions of rough frictional particles. *J. Fluid Mech.* 757, 514–549 (2014)
- [116] Mikulich, V., Nassauer, B., Kuna, M., Brücker, C.: Experimental and numerical study of interaction between particle loaded fluid and a rough wall with micropillars. *Tribol. Int.* 83, 42–50 (2015)
- [117] Joseph, G.G., Hunt, M.L.: Oblique particle-wall collisions in a liquid. *J. Fluid Mech.* 510, 71–93 (2004)
- [118] Yang, F.L., Hunt, M.L.: Dynamics of particle-particle collisions in a viscous liquid. *Phys. Fluids* 18, 1–12 (2006)
- [119] Zhang, W., Noda, R., Horio, M.: Evaluation of lubrication force on colliding particles for DEM simulation of fluidized beds. *Powder Technol.* 158, 92–101 (2005)
- [120] Lian, G., Thornton, C., Adams, M.J.: Discrete particle simulation of agglomerate impact coalescence. *Chem. Eng. Sci.* 53, 3381–3391 (1998)
- [121] Thornton, C., Yin, K.K.: Impact of elastic spheres with and without adhesion. *Powder Technol.* 65, 153–166 (1991)
- [122] Mazzone, D.N., Tardos, G.I., Pfeffer, R.: The behavior of liquid bridges between two relatively moving particles. *Powder Technol.* 51, 71–83 (1987)
- [123] Shan, T., Zhao, J.: A coupled CFD-DEM analysis of granular flow impacting on a water reservoir. *Acta Mech.* 225, 2449–2470 (2014)
- [124] Davis, R.H., Serayssol, J.-M., Hinch, E.J.: The elastohydrodynamic collision of two spheres. *J. Fluid Mech.* 163, 479 (1986)
- [125] Dallavalle, J.M.: *Micromeritics: The Technology of Fine Particles*. Pitman Publishing Cooperation, New York (1948)
- [126] Joseph, G., Zenit, R., Hunt, M., Rosenwinkel, A.: Particle-wall collisions in a viscous fluid. *J. Fluid Mech.* 433, 329–346 (2001)
- [127] Thiel, W.J., Potter, O.E.: The mixing of solids in slugging gas fluidized beds. *AIChE J.* 24, 561–569 (1978)
- [128] Valenzuela, J.A., Glicksman, L.R.: An experimental study of solids mixing in a freely bubbling two-dimensional fluidized bed. *Powder Technol.* 38, 63–72 (1984)
- [129] Rowe, P.N., Nienow, A.W.: Particle mixing and segregation in gas fluidised beds. A review. *Powder Technol.* 15, 141–147 (1976)

- [130] Norouzi, H.R., Mostoufi, N., Mansourpour, Z., Sotudeh-Gharebagh, R., Chaouki, J.: Characterization of solids mixing patterns in bubbling fluidized beds. *Chem. Eng. Res. Des.* 89, 817–826 (2011)
- [131] Shi, Y.F., Fan, L.T.: Lateral mixing of solids in batch gas-solids fluidized beds. *Ind. Eng. Chem. Process Des. Dev.* 23, 337–341 (1984)
- [132] Liu, D., Chen, X.: Quantifying lateral solids mixing in a fluidized bed by modeling the thermal tracing method. *AIChE J.* 58, 745–755 (2012)
- [133] Rhodes, M.J., Wang, X.S., Nguyen, M., Stewart, P., Liffman, K.: Study of mixing in gas-fluidized beds using a DEM model. *Chem. Eng. Sci.* 56, 2859–2866 (2001)
- [134] Kuipers, J.A.M., Van Duin, K.J., Van Beckum, F.P.H., Van Swaaij, W.P.M.: A numerical model of gas-fluidized beds. *Chem. Eng. Sci.* 47, 1913–1924 (1992)
- [135] Ding, J., Gidaspow, D.: A bubbling fluidization model using kinetic theory of granular flow. *AIChE J.* 36, 523–538 (1990)
- [136] van Sint Annaland, M., Bokkers, G.A., Goldschmidt, M.J.V., van der Hoef, M.A., Kuipers, J.A.M.: Development of a multi-fluid model for poly-disperse dense gas-solid fluidised beds, Part I: Model derivation and numerical implementation. *Chem. Eng. Sci.* 64, 4222–4236 (2009)
- [137] van Sint Annaland, M., Bokkers, G.A., Goldschmidt, M.J.V., van der Hoef, M.A., Kuipers, J.A.M.: Development of a multi-fluid model for poly-disperse dense gas-solid fluidised beds, Part II: Segregation in binary particle mixtures. *Chem. Eng. Sci.* 64, 4237–4246 (2009)
- [138] Zhong, H., Gao, J., Xu, C., Lan, X.: CFD modeling the hydrodynamics of binary particle mixtures in bubbling fluidized beds: Effect of wall boundary condition. *Powder Technol.* 230, 232–240 (2012)
- [139] Pirker, S., Kahrimanovic, D., Kloss, C., Popoff, B., Braun, M.: Simulating coarse particle conveying by a set of Eulerian, Lagrangian and hybrid particle models. *Powder Technol.* 204, 203–213 (2010)
- [140] Sun, J., Xiao, H., Gao, D.: Numerical study of segregation using multiscale models. *Int. J. Comput. Fluid Dyn.* 23, 81–92 (2009)
- [141] Xu, B.H., Yu, a. B.: Numerical simulation of the gas-solid flow in a fluidized bed by combining discrete particle method with computational fluid dynamics. *Chem. Eng. Sci.* 52, 2785–2809 (1997)
- [142] Zhong, W.-Q., Zhang, Y., Jin, B.-S., Zhang, M.-Y.: Discrete Element Method Simulation of Cylinder-Shaped Particle Flow in a Gas-Solid Fluidized Bed. *Chem. Eng. Technol.* 32, 386–391 (2009)
- [143] Zhou, Z.Y., Pinson, D., Zou, R.P., Yu, a. B.: Discrete particle simulation of gas fluidization of ellipsoidal particles. *Chem. Eng. Sci.* 66, 6128–6145 (2011)
- [144] Ren, B., Zhong, W., Chen, Y., Chen, X., Jin, B., Yuan, Z., Lu, Y.: CFD-DEM simulation of spouting of corn-shaped particles. *Particuology* 10, 562–572 (2012)
- [145] Ren, B., Zhong, W., Jin, B., Shao, Y., Yuan, Z.: Numerical simulation on the mixing behavior of corn-shaped particles in a spouted bed. *Powder Technol.* 234, 58–66 (2013)
- [146] Tsuji, Y., Kawaguchi, T., Tanaka, T.: Discrete particle simulation of two-dimensional fluidized bed. *Powder Technol.* 77, 79–87 (1993)
- [147] Hoomans, B.P.B., Kuipers, J.A.M., Briels, W.J., Van Swaaij, W.P.M.: Discrete particle simulation of bubble and slug formation in a two-dimensional gas-fluidised bed: A hard-sphere approach. *Chem. Eng. Sci.* 51, 99–118 (1996)
- [148] Lacey, P.M.C.: The mixing of solid particles. *Trans. Inst. Chem. Eng.* 21, 53–59 (1943)
- [149] Bin, Y., Zhang, M.C., Dou, B.L., Song, Y.B., Wu, J.: Discrete Particle Simulation and Visualized Research of the Gas–Solid Flow in an Internally Circulating Fluidized Bed. *Ind. Eng. Chem. Res.* 42, 214–221 (2003)
- [150] Limtrakul, S., Chalermwattanatai, A., Unggurawirote, K., Tsuji, Y., Kawaguchi, T.,

- Tanthapanichakoon, W.: Discrete particle simulation of solids motion in a gas–solid fluidized bed. *Chem. Eng. Sci.* 58, 915–921 (2003)
- [151] Feng, Y.Q., Xu, B.H., Zhang, S.J., Yu, a. B., Zulli, P.: Discrete particle simulation of gas fluidization of particle mixtures. *AIChE J.* 50, 1713–1728 (2004)
- [152] Feng, Y.Q., Yu, a. B.: Assessment of Model Formulations in the Discrete Particle Simulation of Gas–Solid Flow. *Ind. Eng. Chem. Res.* 43, 8378–8390 (2004)
- [153] Chaikittisilp, W., Taenumtrakul, T., Boonsuwan, P., Tanthapanichakoon, W., Charinpanitkul, T.: Analysis of solid particle mixing in inclined fluidized beds using DEM simulation. *Chem. Eng. J.* 122, 21–29 (2006)
- [154] Nakamura, H., Tokuda, T., Iwasaki, T., Watano, S.: Numerical analysis of particle mixing in a rotating fluidized bed. 62, 3043–3056 (2007)
- [155] Tian, F., Zhang, M., Fan, H., Gu, M., Wang, L., Qi, Y.: Numerical study on microscopic mixing characteristics in fluidized beds via DEM. *Fuel Process. Technol.* 88, 187–198 (2007)
- [156] Feng, Y.Q., Yu, A.B.: Microdynamic modelling and analysis of the mixing and segregation of binary mixtures of particles in gas fluidization. *Chem. Eng. Sci.* 62, 256–268 (2007)
- [157] Di Renzo, A., Di Maio, F.P., Girimonte, R., Formisani, B.: DEM simulation of the mixing equilibrium in fluidized beds of two solids differing in density. *Powder Technol.* 184, 214–223 (2008)
- [158] Gui, N., Fan, J.R., Luo, K.: DEM–LES study of 3-D bubbling fluidized bed with immersed tubes. *Chem. Eng. Sci.* 63, 3654–3663 (2008)
- [159] Zhao, Y., Ding, Y., Wu, C., Cheng, Y.: Numerical simulation of hydrodynamics in downers using a CFD–DEM coupled approach. *Powder Technol.* 199, 2–12 (2010)
- [160] Zhao, Y., Cheng, Y., Wu, C., Ding, Y., Jin, Y.: Particuology Eulerian – Lagrangian simulation of distinct clustering phenomena and RTDs in riser and downer. 8, 44–50 (2010)
- [161] Feng, Y.Q., Yu, A.B.: Effect of Bed Thickness on the Segregation Behavior of Particle Mixtures in a Gas Fluidized Bed. *Ind. Eng. Chem. Res.* 49, 3459–3468 (2010)
- [162] Zhang, Y., Jin, B., Zhong, W., Ren, B., Xiao, R.: DEM simulation of particle mixing in flat-bottom spout-fluid bed. *Chem. Eng. Res. Des.* 88, 757–771 (2010)
- [163] Gui, N., Fan, J.: Numerical study of particle mixing in bubbling fluidized beds based on fractal and entropy analysis. *Chem. Eng. Sci.* 66, 2788–2797 (2011)
- [164] Liu, D., Xiao, S., Chen, X., Bu, C.: Investigation of solid mixing mechanisms in a bubbling fluidized bed using a DEM-CFD approach. *Asia-Pacific J. Chem. Eng.* 7, 237–244 (2012)
- [165] Fang, M., Luo, K., Yang, S., Zhang, K., Fan, J.: Computational Fluid Dynamics-Discrete Element Method Investigation of Solid Mixing Characteristics in an Internally Circulating Fluidized Bed. *Ind. Eng. Chem. Res.* 52, 7556–7568 (2013)
- [166] Peng, Z., Doroodchi, E., Alghamdi, Y., Moghtaderi, B.: Mixing and segregation of solid mixtures in bubbling fluidized beds under conditions pertinent to the fuel reactor of a chemical looping system. *Powder Technol.* 235, 823–837 (2013)
- [167] Gopalakrishnan, P., Tafti, D.: Development of parallel DEM for the open source code MFIX. *Powder Technol.* 235, 33–41 (2013)
- [168] Tran-Cong, S., Gay, M., Michaelides, E.E.: Drag coefficients of irregularly shaped particles. *Powder Technol.* 139, 21–32 (2004)
- [169] Hilton, J.E., Cleary, P.W.: Raceway formation in laterally gas-driven particle beds. *Chem. Eng. Sci.* 80, 306–316 (2012)
- [170] Cai, J., Li, Q., Yuan, Z.: Particuology Orientation of cylindrical particles in gas – solid circulating fluidized bed. *Particuology* 10, 89–96 (2012)
- [171] Munjiza, A., Latham, J.P., John, N.W.M.: 3D dynamics of discrete element systems

- comprising irregular discrete elements-Integration solution for finite rotations in 3D. *Int. J. Numer. Methods Eng.* 56, 35–55 (2003)
- [172] Höhner, D., Wirtz, S., Scherer, V.: A numerical study on the influence of particle shape on hopper discharge within the polyhedral and multi-sphere discrete element method. *Powder Technol.* 226, 16–28 (2012)
- [173] Kruggel-Emden, H., Kačianauskas, R.: Discrete element analysis of experiments on mixing and bulk transport of wood pellets on a forward acting grate in discontinuous operation. *Chem. Eng. Sci.* 92, 105–117 (2013)
- [174] Kruggel-Emden, H., Sudbrock, F., Wirtz, S., Scherer, V.: Experimental and numerical investigation of the bulk behavior of wood pellets on a model type grate. *Granul. Matter* 14, 681–693 (2012)
- [175] Höhner, D., Wirtz, S., Scherer, V.: Experimental and numerical investigation on the influence of particle shape and shape approximation on hopper discharge using the discrete element method. *Powder Technol.* 235, 614–627 (2013)
- [176] Launder, B.E., Spalding, D.B.: The numerical computation of turbulent flows. *Comput. Methods Appl. Mech. Eng.* 3, 269–289 (1974)
- [177] Bouillard, J.X., Lyczkowski, R.W., Gidaspow, D.: Porosity Distributions in a Fluidized Bed with an Immersed Obstacle. 35, (1989)
- [178] Richter, A., Nikrityuk, P. a.: Drag forces and heat transfer coefficients for spherical, cuboidal and ellipsoidal particles in cross flow at sub-critical Reynolds numbers. *Int. J. Heat Mass Transf.* 55, 1343–1354 (2012)
- [179] Zastawny, M., Mallouppas, G., Zhao, F., van Wachem, B.: Derivation of drag and lift force and torque coefficients for non-spherical particles in flows. *Int. J. Multiph. Flow* 39, 227–239 (2012)
- [180] Hölzer, A., Sommerfeld, M.: Lattice Boltzmann simulations to determine drag, lift and torque acting on non-spherical particles. *Comput. Fluids* 38, 572–589 (2009)
- [181] Ganser, G.H.: A rational approach to drag prediction of spherical and nonspherical particles. *Powder Technol.* 77, 143–152 (1993)
- [182] Wen, C.Y., Yu, Y.H.: A generalized method for predicting the minimum fluidization velocity. *AIChE J.* 12, 610–612 (1966)
- [183] Rickelt, S., Sudbrock, F., Wirtz, S., Scherer, V.: Coupled DEM/CFD simulation of heat transfer in a generic grate system agitated by bars. *Powder Technol.* 249, 360–372 (2013)
- [184] Deen, N.G., Kriebitzsch, S.H.L., van der Hoef, M.A., Kuipers, J.A.M.: Direct numerical simulation of flow and heat transfer in dense fluid-particle systems. *Chem. Eng. Sci.* 81, 329–344 (2012)
- [185] Oschmann, T., Hold, J., Kruggel-Emden, H.: Numerical investigation of mixing and orientation of non-spherical particles in a model type fluidized bed. *Powder Technol.* 258, 304–323 (2014)
- [186] Xiang, J., McGlinchey, D., Latham, J.-P.: An investigation of segregation and mixing in dense phase pneumatic conveying. *Granul. Matter* 12, 345–355 (2010)
- [187] Kruggel-Emden, H., Wirtz, S., Scherer, V.: An analytical solution of different configurations of the linear viscoelastic normal and frictional-elastic tangential contact model. *Chem. Eng. Sci.* 62, 6914–6926 (2007)
- [188] Mills, D.: *Pipeline Feeding Devices*. Elsevier Butterworth-Heinemann, Oxford, UK (2016)
- [189] Dhodapkar, S., Solt, P., Klinzing, G.: Understanding Bends In Pneumatic Conveying Systems. *Chem. Eng.* 116, 53–60 (2009)
- [190] Hsu, C.-H., Chang, K.-C.: A Lagrangian modeling approach with the direct simulation Monte-Carlo method for inter-particle collisions in turbulent flow. *Adv. Powder Technol.* 18, 395–426 (2007)
- [191] Eskin, D.: Modeling dilute gas-particle flows in horizontal channels with different wall

- roughness. *Chem. Eng. Sci.* 60, 655–663 (2005)
- [192] Pu, W., Zhao, C., Xiong, Y., Liang, C., Chen, X., Lu, P., Fan, C.: Three-Dimensional Numerical Simulation of Dense Pneumatic Conveying of Pulverized Coal in a Vertical Pipe at High Pressure. *Chem. Eng. Technol.* 31, 215–223 (2008)
- [193] Pu, W., Zhao, C., Xiong, Y., Liang, C., Chen, X., Lu, P., Fan, C.: Numerical simulation on dense phase pneumatic conveying of pulverized coal in horizontal pipe at high pressure. *Chem. Eng. Sci.* 65, 2500–2512 (2010)
- [194] McGlinchey, D., Cowell, A., Crowe, R.: CFD investigation of dense phase pneumatic conveying at a pipeline enlargement. *Particuology* 10, 176–183 (2012)
- [195] Behera, N., Agarwal, V.K., Jones, M.G., Williams, K.C.: Modeling and analysis for fluidized dense phase conveying including particle size distribution. *Powder Technol.* 235, 386–394 (2013)
- [196] Behera, N., Agarwal, V.K., Jones, M.G., Williams, K.C.: Modeling and analysis of dilute phase pneumatic conveying of fine particles. *Powder Technol.* 249, 196–204 (2013)
- [197] Laín, S., Sommerfeld, M.: Euler/Lagrange computations of pneumatic conveying in a horizontal channel with different wall roughness. *Powder Technol.* 184, 76–88 (2008)
- [198] Lain, S., Sommerfeld, M., Quintero, B.: Numerical Simulation of Secondary Flow in Pneumatic Conveying of Solid. *Brazilian J. Chem. Eng.* 26, 583–594 (2009)
- [199] Laín, S., Sommerfeld, M.: Effect of geometry on flow structure and pressure drop in pneumatic conveying of solids along horizontal ducts. *J. Sci. Ind. Res. (India)*. 70, 129–134 (2011)
- [200] Laín, S., Sommerfeld, M.: Numerical calculation of pneumatic conveying in horizontal channels and pipes: Detailed analysis of conveying behaviour. *Int. J. Multiph. Flow* 39, 105–120 (2012)
- [201] Alletto, M., Breuer, M.: Prediction of turbulent particle-laden flow in horizontal smooth and rough pipes inducing secondary flow. *Int. J. Multiph. Flow* 55, 80–98 (2013)
- [202] Laín, S., Sommerfeld, M.: A study of the pneumatic conveying of non-spherical particles in a turbulent horizontal channel flow. *Brazilian J. Chem. Eng.* 24, 535–546 (2007)
- [203] Han, T., Levy, A., Kalman, H.: DEM simulation for attrition of salt during dilute-phase pneumatic conveying. *Powder Technol.* 129, 92–100 (2003)
- [204] Ouyang, J., Yu, a. B., Pan, R.H.: Simulation of Gas-Solid Flow in Vertical Pipe by Hard-Sphere Model. *Part. Sci. Technol.* 23, 47–61 (2005)
- [205] McGlinchey, D., Cowell, A., Pugh, J.R., Knight, E.A., Xiang, J., Li, J.: Axial and radial pressure drops of dense phase plugs. *Part. Sci. Technol.* 23, 215–227 (2005)
- [206] Wee Chuan Lim, E., Wang, C.-H., Yu, A.-B.: Discrete element simulation for pneumatic conveying of granular material. *AIChE J.* 52, 496–509 (2006)
- [207] Lim, E.W.C.: Voidage waves in hydraulic conveying through narrow pipes. *Chem. Eng. Sci.* 62, 4529–4543 (2007)
- [208] Fraige, F.Y., Langston, P. a.: Horizontal pneumatic conveying: a 3d distinct element model. *Granul. Matter* 8, 67–80 (2006)
- [209] Strauß, M., McNamara, S., Herrmann, H.J., Niederreiter, G., Sommer, K.: Plug conveying in a vertical tube. *Powder Technol.* 162, 16–26 (2006)
- [210] Strauß, M., McNamara, S., Herrmann, H.J.: Plug conveying in a horizontal tube. *Granul. Matter* 9, 35–48 (2006)
- [211] Zhang, Y., Lim, E.W.C., Wang, C.: Pneumatic Transport of Granular Materials in an Inclined Conveying Pipe: Comparison of Computational Fluid Dynamics–Discrete Element Method (CFD–DEM), Electrical Capacitance Tomography (ECT), and Particle Image Velocimetry (PIV) Results. *Ind. Eng. Chem. Res.* 46, 6066–6083 (2007)
- [212] Kuang, S.B., Chu, K.W., Yu, A.B., Zou, Z.S., Feng, Y.Q.: Computational Investigation of Horizontal Slug Flow in Pneumatic Conveying. *Ind. Eng. Chem. Res.* 47, 470–480 (2008)

- [213] Kuang, S.B., Yu, A.B., Zou, Z.S.: Computational Study of Flow Regimes in Vertical Pneumatic Conveying. 6846–6858 (2009)
- [214] Zhou, Z.Y., Kuang, S.B., Chu, K.W., Yu, A.B.: Discrete particle simulation of particle-fluid flow: Model formulations and their applicability. *J. Fluid Mech.* 661, 482–510 (2010)
- [215] Sturm, M., Wirtz, S., Scherer, V., Denecke, J.: Coupled DEM-CFD Simulation of Pneumatically Conveyed Granular Media. *Chem. Eng. Technol.* 33, 1184–1192 (2010)
- [216] Mezhericher, M., Brosh, T., Levy, A.: Modeling of Particle Pneumatic Conveying Using DEM and DPM Methods. *Part. Sci. Technol.* 29, 197–208 (2011)
- [217] Kuang, S.B., Yu, A.B.: Micromechanic modeling and analysis of the flow regimes in horizontal pneumatic conveying. *AIChE J.* 57, 2708–2725 (2011)
- [218] Kuang, S.B., Zou, R.P., Pan, R.H., Yu, A.B.: Gas–Solid Flow and Energy Dissipation in Inclined Pneumatic Conveying. *Ind. Eng. Chem. Res.* 51, 14289–14302 (2012)
- [219] Li, K., Kuang, S.B., Pan, R.H., Yu, A.B.: Numerical study of horizontal pneumatic conveying: Effect of material properties. *Powder Technol.* 251, 15–24 (2014)
- [220] Levy, A., Mason, D.J.: The effect of a bend on the particle cross-section concentration and segregation in pneumatic conveying systems. *Powder Technol.* 98, 95–103 (1998)
- [221] Schallert, R., Levy, E.: Effect of a combination of two elbows on particle roping in pneumatic conveying. *Powder Technol.* 107, 226–233 (2000)
- [222] Yilmaz, A., Levy, E.K.: Formation and dispersion of ropes in pneumatic conveying. *Powder Technol.* 114, 168–185 (2001)
- [223] Akilli, H., Levy, E.K., Sahin, B.: Gas-solid flow behavior in a horizontal pipe after a 90° vertical-to-horizontal elbow. *Powder Technol.* 116, 43–52 (2001)
- [224] Akilli, H., Levy, E.K., Sahin, B.: Investigation of gas–solid flow structure after a 90° vertical-to-horizontal elbow for low conveying gas velocities. *Adv. Powder Technol.* 16, 261–274 (2005)
- [225] Bernert, K., Frank, T., Schneider, H., Pachler, K.: Numerical simulation of disperse multiphase flows with an application in power engineering. *Int. J. Numer. Methods Fluids* 41, 1253–1271 (2003)
- [226] Quek, T.Y., Wang, C., Ray, M.B.: Dilute Gas–Solid Flows in Horizontal and Vertical Bends. *Ind. Eng. Chem. Res.* 44, 2301–2315 (2005)
- [227] Kuan, B., Yang, W., Schwarz, M.P.: Dilute gas–solid two-phase flows in a curved duct bend: CFD simulation with experimental validation. *Chem. Eng. Sci.* 62, 2068–2088 (2007)
- [228] Chu, K.W., Yu, A.B.: Numerical Simulation of the Gas - Solid Flow in Three-Dimensional Pneumatic Conveying Bends. 7058–7071 (2008)
- [229] El-Behery, S.M., Hamed, M.H., El-Kadi, M.A., Ibrahim, K.A.: CFD prediction of air-solid flow in 180° curved duct. *Powder Technol.* 191, 130–142 (2009)
- [230] Vashisth, S., Grace, J.R.: Simulation of granular transport of Geldart type-A, -B, and -D particles through a 90° elbow. *Ind. Eng. Chem. Res.* 51, 2030–2047 (2012)
- [231] Laín, S., Sommerfeld, M.: Characterisation of pneumatic conveying systems using the Euler/Lagrange approach. *Powder Technol.* 235, 764–782 (2013)
- [232] Martin, H.: *VDI-Wärmeatlas*. Springer Berlin Heidelberg, Berlin, Heidelberg (2006)
- [233] Stieß, M.: *Mechanische Verfahrenstechnik 2*. Springer Berlin Heidelberg, Berlin, Heidelberg (1997)
- [234] Brosh, T., Levy, A.: Modeling of heat transfer in pneumatic conveyor using a combined DEM-CFD numerical code. *Dry. Technol.* 28, 155–164 (2010)
- [235] Wang, J., Qi, H., Zhu, J.: Experimental study of settling and drag on cuboids with square base. *Particuology* 9, 298–305 (2011)
- [236] Lee, L.Y., Yong Quek, T., Deng, R., Ray, M.B., Wang, C.-H.: Pneumatic transport of granular materials through a bend. *Chem. Eng. Sci.* 59, 4637–4651 (2004)

- [237] Muschelknautz, E., Wojahn, H.: Auslegung pneumatischer Foerderanlagen. *Chemie Ing. Tech.* 46, 223–272 (1974)
- [238] Giguère, R., Fradette, L., Mignon, D., Tanguy, P.A.: Analysis of slurry flow regimes downstream of a pipe bend. *Chem. Eng. Res. Des.* 87, 943–950 (2009)
- [239] Huber, N., Sommerfeld, M.: Characterization of the cross-sectional particle concentration distribution in pneumatic conveying systems. *Powder Technol.* 79, 191–210 (1994)
- [240] Lu, Y., Glass, D.H., Easson, W.J.: An investigation of particle behavior in gas–solid horizontal pipe flow by an extended LDA technique. *Fuel* 88, 2520–2531 (2009)
- [241] Yang, W., Kuan, B.: Experimental investigation of dilute turbulent particulate flow inside a curved bend. *Chem. Eng. Sci.* 61, 3593–3601 (2006)
- [242] Yilmaz, A., Levy, E.K.: Roping phenomena in pulverized coal conveying lines. *Powder Technol.* 95, 43–48 (1998)
- [243] Zhou, Y., Chen, X. -p., Liang, C., Xu, P.: Resistance Properties of a Bend in Dense-Phase Pneumatic Conveying of Pulverized Coal under High Pressure. *Chem. Eng. Technol.* 34, 75–80 (2011)
- [244] Schade, K., Erdmann, H., Ha, T.: Experimental and numerical investigation of particle erosion caused by pulverised fuel in channels and pipework of coal-fired power plant. *125*, 242–250 (2002)
- [245] Bilirgen, H., Levy, E.K.: Mixing and dispersion of particle ropes in lean phase pneumatic conveying. *Powder Technol.* 119, 134–152 (2001)
- [246] Idelchik, I.E., Fried, E.: *Handbook of hydraulic resistance: Second edition.* Jaico Publishing House, 3rd. edition Jaico Publishing House (1986)
- [247] Li, J., Mason, D.J.: Application of the discrete element modelling in air drying of particulate solids. *Dry. Technol.* 20, 255–282 (2002)
- [248] Kharaghani, A., Metzger, T., Tsotsas, E.: A Proposal for Discrete Modeling of Mechanical Effects During Drying , Combining Pore Networks With DEM. *AIChE J.* 57, (2011)
- [249] Sudbrock, F., Kruggel-Emden, H., Wirtz, S., Scherer, V.: Convective Drying of Agitated Silica Gel and Beech Wood Particle Beds - Experiments and Transient DEM-CFD Simulations. *Dry. Technol.* 1808–1820 (2015)
- [250] Zhou, Z.Y., Yu, A.B., Zulli, P.: A new computational method for studying heat transfer in fluid bed reactors. *Powder Technol.* 197, 102–110 (2010)
- [251] Gerber, S., Oevermann, M.: A two dimensional Euler-Lagrangian model of wood gasification in a charcoal bed - Part I: Model description and base scenario. *Fuel* 115, 385–400 (2014)
- [252] Zhu, H.P., Zhou, Z.Y., Yu, a. B., Zulli, P.: Stress fields of solid flow in a model blast furnace. *Granul. Matter* 11, 269–280 (2009)
- [253] Krause, B., Liedmann, B., Wiese, J., Wirtz, S., Scherer, V.: Coupled three dimensional DEM-CFD simulation of a lime shaft kiln-Calcination, particle movement and gas phase flow field. *Chem. Eng. Sci.* 134, 834–849 (2015)
- [254] Hou, Q.-F., Zhou, Z.-Y., Yu, A.-B.: Computational Study of the Effects of Material Properties on Heat Transfer in Gas Fluidization. *Ind. Eng. Chem. Res.* 51, 11572–11586 (2012)
- [255] Hou, Q.F., Zhou, Z.Y., Yu, A.B.: Computational Study of Heat Transfer in a Bubbling Fluidized Bed with a Horizontal Tube. *58*, (2012)
- [256] Hou, Q.F., Zhou, Z.Y., Yu, A.B.: Gas-solid flow and heat transfer in fluidized beds with tubes: Effects of material properties and tube array settings. *Powder Technol.* 296, 59–71 (2016)
- [257] Batchelor, G.K., O'Brien, R.W.: Thermal or Electrical Conduction Through a Granular Material. *Proc. R. Soc. A Math. Phys. Eng. Sci.* 355, 313–333 (1977)

- [258] Zhou, Z.Y., Yu, A.B., Zulli, P.: Particle Scale Study of Heat Transfer in Packed Beds. *Mater. Sci.* 46, 1–8 (2007)
- [259] Cheng, G.J., Yu, A.B., Zulli, P.: Evaluation of effective thermal conductivity from the structure of a packed bed. *Chem. Eng. Sci.* 54, 4199–4209 (1999)
- [260] Vargas, W.L., McCarthy, J.J.: Heat conduction in granular materials. *AIChE J.* 47, 1052–1059 (2001)
- [261] Tsory, T., Ben-Jacob, N., Brosh, T., Levy, A.: Thermal DEM–CFD modeling and simulation of heat transfer through packed bed. *Powder Technol.* 244, 52–60 (2013)
- [262] Sun, J., Chen, M.M.: A theoretical analysis of heat transfer due to particle impact. *Int. J. Heat Mass Transf.* 31, 969–975 (1988)
- [263] Zhou, J.H., Yu, A.B., Horio, M.: Finite element modeling of the transient heat conduction between colliding particles. *Chem. Eng. J.* 139, 510–516 (2008)
- [264] Cheng, G.J., Yu, A.B.: Particle Scale Evaluation of the Effective Thermal Conductivity from the Structure of a Packed Bed: Radiation Heat Transfer. *Ind. Eng. Chem. Res.* (2013)
- [265] Holman, J.P.: *Heat Transfer*. McGraw-Hill, New York (1990)
- [266] Li, J., Mason, D.: A computational investigation of transient heat transfer in pneumatic transport of granular particles. *Powder Technol.* 112, 273–282 (2000)
- [267] Li, J., Campbell, G.M., Mujumdar, A.S.: Discrete modeling and suggested measurement of heat transfer in gas–solids flows. *Dry. Technol.* 21, 979–994 (2003)
- [268] Li, J., Mason, D.J., Mujumdar, A.S.: A Numerical Study of Heat Transfer Mechanisms in Gas–Solids Flows Through Pipes Using a Coupled CFD and DEM Model. *Dry. Technol.* 21, 1839–1866 (2003)
- [269] Vargas, W.L., McCarthy, J.J.: Stress effects on the conductivity of particulate beds. *Chem. Eng. Sci.* 57, 3119–3131 (2002)
- [270] Vargas, W.L., McCarthy, J.: Conductivity of granular media with stagnant interstitial fluids via thermal particle dynamics simulation. *Int. J. Heat Mass Transf.* 45, 4847–4856 (2002)
- [271] Zhang, H.W., Zhou, Q., Xing, H.L., Muhlhaus, H.: A DEM study on the effective thermal conductivity of granular assemblies. *Powder Technol.* 205, 172–183 (2011)
- [272] Swasdisevi, T., Tanthapanichakoon, W., Charinpanitkul, T., Kawaguchi, T., Tanaka, T., Tsuji, Y.: Prediction of gas–particle dynamics and heat transfer in a two-dimensional spouted bed. *Adv. Powder Technol.* 16, 275–293 (2005)
- [273] Malone, K.F., Xu, B.H.: Particle-scale simulation of heat transfer in liquid-fluidized beds. *Powder Technol.* 184, 189–204 (2008)
- [274] Di Maio, F.P., Di Renzo, A., Trevisan, D.: Comparison of heat transfer models in DEM–CFD simulations of fluidized beds with an immersed probe. *Powder Technol.* 193, 257–265 (2009)
- [275] Zhao, Y., Jiang, M., Liu, Y., Zheng, J.: Particle-Scale Simulation of the Flow and Heat Transfer Behaviors in Fluidized Bed with Immersed Tube. *AIChE J.* 55, 3109–3124 (2009)
- [276] Sae-Heng, S., Swasdisevi, T., Amornkitbamrung, M.: Investigation of temperature distribution and heat transfer in fluidized bed using a combined CFD–DEM model. *Dry. Technol.* 29, 697–708 (2011)
- [277] Nguyen, V.-D., Benhabib, K., Marie, C., Coorevits, P.: Heat Transfer in a Granular Media Modeled by a Coupled DEM–Finite Difference Method: Application to Fluidized Bed Processes. *Procedia Eng.* 42, 824–832 (2012)
- [278] Patil, A. V., Peters, E. a. J.F., Kolkman, T., Kuipers, J. a. M.: Modeling bubble heat transfer in gas–solid fluidized beds using DEM. *Chem. Eng. Sci.* 105, 121–131 (2014)
- [279] Chaudhuri, B., Muzzio, F.J., Tomassone, M.S.: Modeling of heat transfer in granular flow in rotating vessels. *Chem. Eng. Sci.* 61, 6348–6360 (2006)

- [280] Kwapinska, M., Saage, G., Tsotsas, E.: Mixing of particles in rotary drums: A comparison of discrete element simulations with experimental results and penetration models for thermal processes. *Powder Technol.* 161, 69–78 (2006)
- [281] Shi, D., Vargas, W.L., McCarthy, J.J.: Heat transfer in rotary kilns with interstitial gases. *Chem. Eng. Sci.* 63, 4506–4516 (2008)
- [282] Gui, N., Gao, J., Ji, Z.: Numerical study of mixing and thermal conduction of granular particles in rotating tumblers. *AIChE J.* 59, 1906–1918 (2013)
- [283] Figueroa, I., Vargas, W.L., McCarthy, J.J.: Mixing and heat conduction in rotating tumblers. *Chem. Eng. Sci.* 65, 1045–1054 (2010)
- [284] Laguerre, O., Ben Amara, S., Alvarez, G., Flick, D.: Transient heat transfer by free convection in a packed bed of spheres: Comparison between two modelling approaches and experimental results. *Appl. Therm. Eng.* 28, 14–24 (2008)
- [285] Brosh, T., Levy, A.: Modeling of heat transfer in pneumatic conveyer using a combined DEM-CFD numerical code. *Dry. Technol.* 28, 155–164 (2010)
- [286] Sadhukhan, A.K., Gupta, P., Saha, R.K.: Modeling and Experimental Investigations on the Pyrolysis of Large Coal Particles. *Energy & Fuels* 25, 5573–5583 (2011)
- [287] Schmidt, R., Nikrityuk, P.A.: Numerical simulation of the transient temperature distribution inside moving particles. *Can. J. Chem. Eng.* 90, 246–262 (2012)
- [288] Mahmoudi, A.H., Hoffmann, F., Peters, B.: Application of XDEM as a novel approach to predict drying of a packed bed. *Int. J. Therm. Sci.* 75, 65–75 (2014)
- [289] Zheng, G., List, R.: Convective heat transfer of rotating spheres and spheroids with non-uniform surface temperatures. *Int. J. Heat Mass Transf.* 39, 1815–1826 (1996)
- [290] Dierich, F., Nikrityuk, P.A.: A Numerical Study of the Influence of Surface Roughness on the Convective Heat Transfer in a Gas Flow. 64, 251–266 (2010)
- [291] Shao, X., Shi, Y., Yu, Z.: Combination of the fictitious domain method and the sharp interface method for direct numerical simulation of particulate flows with heat transfer. *Int. J. Heat Mass Transf.* 55, 6775–6785 (2012)
- [292] Niazmand, H., Renksizbulut, M.: Transient three-dimensional heat transfer from rotating spheres with surface blowing. *Chem. Eng. Sci.* 58, 3535–3554 (2003)
- [293] Defraeye, T., Blocken, B., Carmeliet, J.: CFD analysis of convective heat transfer at the surfaces of a cube immersed in a turbulent boundary layer. *Int. J. Heat Mass Transf.* 53, 297–308 (2010)
- [294] Hahn, M., Schwarz, M., Kröplin, B.-H., Wallmersperger, T.: Discrete Element Method for the thermal field: Proof of concept and determination of the material parameters. *Comput. Mater. Sci.* 50, 2771–2784 (2011)
- [295] Terreros, I., Iordanoff, I., Charles, J.L.: Simulation of continuum heat conduction using DEM domains. *Comput. Mater. Sci.* 69, 46–52 (2013)
- [296] Zheng, Q.J., Zhou, Z.Y., Yu, A.B.: Contact forces between viscoelastic ellipsoidal particles. *Powder Technol.* 248, 25–33 (2013)
- [297] Kock, I., Huhn, K.: Influence of particle shape on the frictional strength of sediments - A numerical case study. *Sediment. Geol.* 196, 217–233 (2007)
- [298] Höhner, D., Wirtz, S., Scherer, V.: A study on the influence of particle shape and shape approximation on particle mechanics in a rotating drum using the discrete element method. *Powder Technol.* 253, 256–265 (2014)
- [299] Kruggel-Emden, H., Oschmann, T.: Numerical study of rope formation and dispersion of non-spherical particles during pneumatic conveying in a pipe bend. *Powder Technol.* 268, 219–236 (2014)
- [300] Rhodes, J.M., Peebles, F.N.: Local rates of mass transfer from spheres in ordered arrays. *AIChE J.* 11, 481–487 (1965)
- [301] Gillespie, B.M., Crandall, E.D., Carberry, J.J.: Local and average interphase heat transfer coefficients in a randomly packed bed of spheres. *AIChE J.* 14, 483–490 (1968)

- [302] Jones, L.R.: Diffuse Radiation View Factors Between Two Spheres. *J. Heat Transfer* 87, 421 (1965)
- [303] Cooper, M.G., Mikic, B.B., Yovanovich, M.M.: Thermal contact conductance. *Int. J. Heat Mass Transf.* 12, 279–300 (1969)
- [304] Finney, J.L.: Random Packings and the Structure of Simple Liquids. I. The Geometry of Random Close Packing. *Proc. R. Soc. A Math. Phys. Eng. Sci.* 319, 479–493 (1970)
- [305] Oschmann, T., Schiemann, M., Kruggel-Emden, H.: Development and verification of a resolved 3D inner particle heat transfer model for the Discrete Element Method (DEM). *Powder Technol.* 291, 392–407 (2016)
- [306] Yun, T.S., Dumas, B., Santamarina, J.C.: Heat transport in granular materials during cyclic fluid flow. *Granul. Matter* 13, 29–37 (2010)
- [307] Nguyen, V.D., Cogné, C., Guessasma, M., Bellenger, E., Fortin, J.: Discrete modeling of granular flow with thermal transfer: Application to the discharge of silos. *Appl. Therm. Eng.* 29, 1846–1853 (2009)
- [308] Chaudhuri, B., Muzzio, F.J., Tomassone, M.S.: Experimentally validated computations of heat transfer in granular materials in rotary calciners. *Powder Technol.* 198, 6–15 (2010)
- [309] Kwapinska, M., Saage, G., Tsotsas, E.: Continuous versus discrete modelling of heat transfer to agitated beds. *Powder Technol.* 181, 331–342 (2008)
- [310] Gnielinski, V.: Gleichungen zur Berechnung des Wärme- und Stoffaustausches in durchströmten ruhenden Kugelschüttungen bei mittleren und großen Pecletzahlen. *Verfahrenstechnik* 21, 361–371 (1978)
- [311] Vollmari, K., Oschmann, T., Wirtz, S., Kruggel-Emden, H.: Pressure drop investigations in packings of arbitrary shaped particles. *Powder Technol.* 271, 109–124 (2014)
- [312] Vollmari, K., Jasevičius, R., Kruggel-Emden, H.: Experimental and numerical study of fluidization and pressure drop of spherical and non-spherical particles in a model scale fluidized bed. *Powder Technol.* 291, 506–521 (2016)
- [313] Kruggel-Emden, H., Vollmari, K.: Flow-regime transitions in fluidized beds of non-spherical particles. *Particuology* 29, 1–15 (2016)
- [314] Martin, H.: VDI-Wärmeatlas. Springer Berlin Heidelberg, Berlin, Heidelberg (2013)
- [315] Gui, N., Fan, J.: Numerical study of heat conduction of granular particles in rotating wavy drums. *Int. J. Heat Mass Transf.* 84, 740–751 (2015)
- [316] Komossa, H., Wirtz, S., Scherer, V., Herz, F., Specht, E.: Heat transfer in indirect heated rotary drums filled with monodisperse spheres: Comparison of experiments with DEM simulations. *Powder Technol.* 286, 722–731 (2015)
- [317] Liu, H., Yin, H., Zhang, M., Xie, M., Xi, X.: Numerical simulation of particle motion and heat transfer in a rotary kiln. *Powder Technol.* 287, 239–247 (2016)
- [318] Emady, H.N., Anderson, K. V., Borghard, W.G., Muzzio, F.J., Glasser, B.J., Cuitino, A.: Prediction of conductive heating time scales of particles in a rotary drum. *Chem. Eng. Sci.* 152, 45–54 (2016)
- [319] Xie, Q., Chen, Z., Hou, Q., Yu, A.B., Yang, R.: DEM investigation of heat transfer in a drum mixer with lifters. *Powder Technol.* 314, 175–181 (2017)
- [320] Nafsun, A.I., Herz, F., Specht, E., Komossa, H., Wirtz, S., Scherer, V., Liu, X.: Thermal bed mixing in rotary drums for different operational parameters. *Chem. Eng. Sci.* 160, 346–353 (2017)
- [321] Cheng, G.J., Yu, A.B.: Particle Scale Evaluation of the Effective Thermal Conductivity from the Structure of a Packed Bed: Radiation Heat Transfer. *Ind. Eng. Chem. Res.* 52, 12202–12211 (2013)
- [322] Argento, C., Bouvard, D.: A ray tracing method for evaluating the radiative heat transfer in porous media. *Int. J. Heat Mass Transf.* 39, 3175–3180 (1996)
- [323] Oschmann, T., Kruggel-Emden, H.: Numerical and experimental investigation of the

- heat transfer of spherical particles in a packed bed with an implicit 3D finite difference approach. *Granul. Matter* 19, 1–11 (2017)
- [324] Gan, J., Zhou, Z., Yu, A.: Effect of particle shape and size on effective thermal conductivity of packed beds. *Powder Technol.* 311, 157–166 (2017)
- [325] Mahmoudi, A.H., Besseron, X., Hoffmann, F., Markovic, M., Peters, B.: Modeling of the biomass combustion on a forward acting grate using XDEM. *Chem. Eng. Sci.* 142, 32–41 (2016)
- [326] Mohseni, M., Peters, B., Baniasadi, M.: Case Studies in Thermal Engineering Conversion analysis of a cylindrical biomass particle with a DEM-CFD coupling approach. *Case Stud. Therm. Eng.* 10, 343–356 (2017)
- [327] Baniasadi, M., Baniasadi, M., Peters, B.: Coupled CFD-DEM with heat and mass transfer to investigate the melting of a granular packed bed. *Chem. Eng. Sci.* 178, 136–145 (2018)
- [328] Krause, B., Liedmann, B., Wiese, J., Bucher, P., Wirtz, S., Piringer, H., Scherer, V.: 3D-DEM-CFD simulation of heat and mass transfer, gas combustion and calcination in an intermittent operating lime shaft kiln. *Int. J. Therm. Sci.* 117, 121–135 (2017)
- [329] Lattanzi, A.M., Hrenya, C.M.: A coupled, multiphase heat flux boundary condition for the discrete element method. *Chem. Eng. J.* 304, 766–773 (2016)
- [330] Li, Z., Janssen, T.C.E., Buist, K.A., Deen, N.G., van Sint Annaland, M., Kuipers, J.A.M.: Experimental and simulation study of heat transfer in fluidized beds with heat production. *Chem. Eng. J.* 317, 242–257 (2017)
- [331] Oschmann, T., Hold, J., Kruggel-Emden, H.: Numerical investigation of mixing and orientation of non-spherical particles in a model type fluidized bed. *Powder Technol.* 258, 304–323 (2014)
- [332] Stöcker, H.: *Taschenbuch der Physik*. 2nd ed. Harry Deutsch AG, Frankfurt am Main (2002)
- [333] Hilton, J.E., Cleary, P.W.: Comparison of non-cohesive resolved and coarse grain DEM models for gas flow through particle beds. *Appl. Math. Model.* 38, 4197–4214 (2014)
- [334] Sakai, M., Abe, M., Shigeto, Y., Mizutani, S., Takahashi, H., Viré, A., Percival, J.R., Xiang, J., Pain, C.C.: Verification and validation of a coarse grain model of the DEM in a bubbling fluidized bed. *Chem. Eng. J.* 244, 33–43 (2014)
- [335] Lu, L., Morris, A., Li, T., Benyahia, S.: Extension of a coarse grained particle method to simulate heat transfer in fluidized beds. *Int. J. Heat Mass Transf.* 111, 723–735 (2017)